# Monitoring landslide displacements with passive radio-frequency identification tags, coupled with ambient seismic noise and weather observations

Mathieu Le Breton

Communauté
UNIVERSITÉ Grenoble Alpes

# THÈSE

Pour obtenir le grade de
**DOCTEUR DE LA COMMUNAUTE UNIVERSITE GRENOBLE ALPES**
Spécialité : **Terre Solide (CETSOL)**
Arrêté ministériel : 25 mai 2016

Présentée par
**Mathieu LE BRETON**

Thèse dirigée par **Laurent BAILLET, Professeur, UGA**, et
codirigée par **Eric LAROSE, Directeur de Recherche, CNRS**

préparée au sein du **l'Institut des Sciences de la Terre**
dans **l'École Doctorale Terre, Univers, Environnement**

# Suivi temporel d'un glissement de terrain à l'aide d'étiquettes RFID passives, couplé à l'observation de pluviométrie et de bruit sismique ambiant.

Thèse soutenue publiquement le **28 mai 2019**,
devant le jury composé de :

**M. Christophe DELACOURT**
Professeur, Institut Universitaire Européen de la Mer, Brest, Rapporteur.
**M. Jean-Marc LAHEURTE**
Professeur, ESYCOM, Paris-Est Marne-la-Vallée, France. Rapporteur.
**M. Smail TEDJINI**
Professeur, LCIS, Valence, France. Président.
**M. Jérôme VERGNE**
Physicien, IPG Strasbourg, France. Examinateur.
**M. Laurent BAILLET**
Professeur, ISTerre, Grenoble, France. Directeur de thèse.
**M. Éric LAROSE**
Directeur de recherche, ISTerre, Grenoble. Co-Directeur de thèse.

*Historique: Contrat doctoral démarré le 01/05/2016 ; version intermédiaire du manuscrit soumise aux rapporteurs le 18/04/2019 ; soutenance réalisée le 28/05/2019 en amphithéâtre Kilian, ISTerre ; version finale du manuscrit envoyée à l'école doctorale le 28/08/2019 ; levée de la confidentialité le 1er juin 2019.*

*Ce document est confidentiel jusqu'au 1er juin 2021. Avant cette date, sa consultation nécessite une autorisation écrite par l'auteur, ses encadrants de thèse et la société Géolithe, ainsi qu'un accord de confidentialité.*

*The present document is confidential until 1 June 2021. Before this date, reading this document requires an authorization from the author, his directors and the company Géolithe, as well as a confidentiality agreement.*

# Résumé

La surveillance d'un glissement de terrain vise à anticiper sa rupture pour réduire le risque d'accident. Elle s'opère généralement en mesurant les déplacements du sol. Ce travail propose une nouvelle technique de mesure de déplacement de glissements, flexible et à bas coût, basée sur l'utilisation d'étiquettes d'identification radiofréquence (RFID). La méthode de localisation d'étiquettes par différence de phase à 866 MHz est explorée en conditions extérieures et sur de longues durées. Cette étude a montré une détérioration de la mesure causée par les variations de température, d'humidité, de neige et de végétation. Après application de corrections, la précision de mesure a été améliorée, passant de ±20 cm à ±1 cm en conditions extérieures courantes. Cette technique fonctionne également en conditions neigeuses et en présence d'herbes hautes, mais avec une incertitude de mesure plus élevée (±8 et 4 cm respectivement). Ces erreurs de mesure sont provoquées par des effets de propagation, d'interférence multitrajets, et de per-turbations à proximité des antennes. Un système de mesure en continu a été déployé sur le glissement de terrain de Pont-Bourquin, en Suisse, pendant cinq mois. Ce dispositif a validé l'efficacité de la technique en conditions réelles. De plus, la mesure résiste bien aux intempéries et le dispositif demande peu de maintenance, en comparaison avec les techniques conven-tionnelles (extensomètre, GPS, station totale).

Deux méthodes de mesure complémentaires aux déplacements ont ensuite été étudiées. La méthode de corrélation de vibrations ambiantes est prometteuse, mais n'a pas encore été utilisée en surveillance opérationnelle. Une étude bibliographique souligne plusieurs verrous à lever, tels que la correction des variations saisonnières et journalières, l'augmentation de la résolution temporelle, et le choix des paramètres de traitement adaptés au site surveillé. La méthode qui consiste à inverser une fonction de transfert entre des données de pluie et de déplacements est ensuite étudiée. Une inversion haute résolution de cette fonction est proposée. Elle permet d'identifier des comportements hydrologiques complexes (ex : infiltration à deux vitesses sur le site de Pont-Bourquin) et de mesurer leur évolution. Les avancées de cette thèse vont permettre d'améliorer la surveillance opérationnelle tout en réduisant son coût, répondant aux besoins des collectivités territoriales.

# Abstract

Landslide early-warning systems are based primarily on monitoring the displacement of the landslide. This work develops a new technique for monitoring these displacements, using radio-frequency identification (RFID) passive tags and phase-based location technique. This technique is deployed for the first time outdoors and for several months. Outdoor conditions revealed strong environmental influences due to temperature variations, moisture, snow and vegetation. These can cause a ±20 cm measurement uncertainty over a year, which is too large for landslide monitoring applications. The correction of these effects allows reaching the accuracy of ±1 cm under normal conditions, ±8 cm with snow and ±4 cm with dense high grass. The remaining effects due to snow and grass are explained by the influence of this material on the direct propagation, on the multipath interferences and on the antennas. This measurement system has been deployed on the Pont-Bourquin landslide for five months. The results validate the technique for landslide monitoring applications. The technique also shows the operational benefits of robustness to bad weather, easy maintenance and low-cost material, compared to conventional techniques (extensometer, GPS, total station).

This thesis then studies two complementary monitoring methods that had recently been shown to provide precursors to landslide rupture. First, ambient seismic noise interferometry is used to detect a drop of shear-wave velocity prior to a rupture. The seismic method was studied in the literature to identify what must be developed to use this technique in an operational early-warning system. It requires getting rid of daily and seasonal environmental influences, choosing the processing parameters appropriate to the monitored landslide, and improving the temporal resolution below one day while keeping a stable enough signal. The other method consists of inverting an impulse response between rainfall and displacement rate, with a high resolution. It can shed light on complex infiltration processes (e.g. infiltration with two different delays at Pont-Bourquin) and detect their abnormal evolution across time. These developments should improve landslide operational monitoring with a low budget.

# Avec des mots simples

Les puces « RFID » sont partout : dans les entrepôts logistiques, les conteneurs de marchandise et certains grands magasins. Par exemple, Décathlon les utilise pour remplacer les lecteurs de code-barre lors du passage en caisse. Les articles sont placés tous ensemble dans un bac en plastique et leurs puces sont lues instantanément par radio. Cette thèse propose d'utiliser ces puces pour mesurer des glissements de terrain. Les glissements de terrain représentent parfois plusieurs millions de tonnes de terre qui se met en mouvement. Quand ils accélèrent brutalement, ils détruisent tout sur leur passage. Pour éviter la catastrophe, les autorités surveillent ces glissements et préviennent la population si le glissement se met à accélérer. Pour mesurer ce déplacement, on commence généralement par placer des cibles de mesure sur le glissement. On mesure ensuite leur position en continu en visant tour à tour chaque cible avec un laser orienté par un moteur très précis. Mais ces instruments de précision coûtent cher, et le laser peut être entravé par des flocons de neige ou une branche d'arbre. C'est là que les puces RFID offrent un avantage : elles n'ont pas besoin d'être visées pour être lues et les ondes radio peuvent traverser les obstacles. Fonctionneraient-elles sur un glissement de terrain ? Les résultats de cette thèse l'affirment, et qu'elles fonctionnent même très bien. Leur précision est légèrement réduite quand il neige ou avec de la végétation, mais la mesure continue de fonctionner. Pour mieux éviter les catastrophes, on peut ajouter d'autres mesures sur le glissement. Des laboratoires ont développé de nouvelles techniques prometteuses qui permettraient de mieux prédire les mouvements de terrain rapides. Elles utilisent la relation mathématique entre les vibrations de part et d'autre du glissement, ou encore entre la pluie et la vitesse du glissement. Ces relations restent stables quand le glissement l'est aussi, mais changent de façon anormale plusieurs jours avant la rupture d'un glissement. Ces techniques sont prometteuses, mais encore trop récentes et compliquées pour être adoptées par les autorités. Cette thèse étudie les développements nécessaires sur la méthode de vibration pour qu'elle puisse servir à surveiller des glissements, et approfondit la méthode basée sur la pluie. Ce travail de recherche devrait améliorer la qualité de la surveillance de glissements de terrain, à un coût réduit.

# With Simple Words

This thesis improves the way to monitor landslides, to alert the people if the landslide shows dangerous signs of activities. Measuring landslide displacements is used to detect abnormal activities. A new method is introduced to measure these displacements, using the cheap "RFID" tags that are progressively replacing barcodes in large shops. These tags are read with radio instead of optical light, which has the advantage to work across bags and walls but also tree, fog, and snow. Most of the displacement monitoring techniques do not work under these conditions, and the few techniques that work are very expensive. This thesis demonstrates that this newly introduced "RFID" technique is appropriate for monitoring landslides, at a reasonable cost and even under bad weather. The technique is shown to work under snow or dense vegetation, with only a lower accuracy. Complementary monitoring methods are then studied: they compute the mathematical relation between vibrations measured on the two sides of a landslide, and between the rainfall and the landslide displacement. A strong change in this mathematical relation was detected a few days before a landslide rupture. These methods could be very useful for alerting the people of dangerous landslide activity with more confidence, but are still too new to be used with confidence. This thesis studies what developments need to be done for using the vibration technique in surveillance, and introduced an improvement of the rainfall technique. These techniques are being transferred to the Géolithe company that co-financed this research study, to accelerate their introduction into the standard usage.

À Jean (1940-2018)

# Table of Content

# Introduction

## Raisons de ce travail

Les mouvements gravitaires tels que les glissements de terrain et chutes de blocs rocheux occasionnent des pertes humaines et économiques considérables. Chaque année dans le monde, ils tuent plus de 4000 personnes et coûtent plusieurs dizaines de milliards d'euros en infrastructures détruites. Une stratégie courante pour réduire ce risque consiste à surveiller en continu l'activité des zones concernées pour en restreindre l'accès en cas de rupture imminente.

La fiabilité d'un système de surveillance est vitale. Elle représente l'efficacité à prédire un décrochement, pour alerter les autorités compétentes ou les usagers. La fiabilité dépend avant tout du système de mesure et des indicateurs d'alerte : une panne de capteur, d'alimentation électrique ou de communication de données peut en effet entraver la mesure. Des instruments fiables, simples et redondants permettent de réduire ces problèmes. La fiabilité concerne aussi l'indicateur d'alerte en lui-même : un indicateur fiable doit permettre de déclencher une alerte avant chaque décrochement tout en limitant les fausses alertes. En général, une alerte est déclenchée lorsqu'une valeur mesurée dépasse un seuil prédéfini. Par exemple « si un capteur de position se déplace à une vitesse supérieure à un centimètre par heure, solliciter l'inspection immédiate du personnel d'astreinte et prévenir le comité d'expert ». Le choix d'un indicateur d'alerte dépend du contexte de chaque site et de l'emplacement des capteurs. Un glissement est souvent composé de compartiments qui peuvent s'activer séparément suivant des processus différents. Déployer un maillage resserré de capteurs ou coupler des indicateurs différents (déplacement, pluviométrie, géophysique) peut alors rendre la surveillance plus fiable. Malheureusement, la multiplication des mesures augmente généralement le coût de la surveillance.

Figure 1 : Exemple de glissement de terrain après destruction de la route en aval. La pente instable délimitée en pointillés s'étend sur une largeur de 500 mètres. Pas de l'Ours, Aiguilles, Hautes-Alpes, France, le 27/07/2018.

Le budget alloué pour la surveillance d'un glissement est généralement limité, et nécessite de faire un compromis avec la fiabilité. Pour réduire le risque, la surveillance est souvent préférée à la construction de renforcement ou d'une infrastructure alternative pour son coût plus abordable. Mais les risques de plus faible enjeu, menaçant par exemple des petites routes rurales, pourront rarement bénéficier d'une surveillance de haut niveau (mesure en continue couplant plusieurs observables) et devront choisir des solutions moins coûteuses. Le développement de techniques de surveillance fiables et moins coûteuses représente donc un enjeu réel.

Les déplacements du sol sont généralement mesurés de façon mécanique (extensomètre), par pointage laser (station totale) et par radio (GPS, Radar). Le pointage laser robotisé constitue une mesure de référence pour surveiller de larges zones : l'utilisation de cibles passives permet un maillage de mesure resserré et fournit des données simples à traiter. Cependant, la mesure laser peut être entravée en cas de visibilité réduite causée par de fortes pluies, un brouillard dense, de la neige ou de la végétation, qui réduit donc la fiabilité d'un système de surveillance. Ces obstacles sont bien moins problématiques dans le cas d'ondes radio grâce à leurs longueurs d'onde plus grandes, centimétriques et au-delà. Cependant, il n'existe pas (encore) de technique radio pour mesurer les mouvements du sol basée uniquement sur des cibles passives. Une telle technique permettrait de surveiller un glissement en combinant les avantages de fiabilité à l'alerte d'un maillage resserré, de fiabilité de mesure de la radio et de simplicité des cibles passives. C'est précisément l'objet

d'étude de cette thèse, qui s'appuie pour cela sur la technologie d'identification radiofréquence (RFID).

Des milliards d'étiquettes RFID sont produites chaque année. Elles servent à identifier des objets, de la même façon que les codes-barres qu'elles remplacent peu à peu. Ces étiquettes radio sont activées à distance et n'ont pas besoin de batteries pour fonctionner. Leur énergie est fournie à distance par un dispositif de lecture. Ce dernier envoie une onde électromagnétique (à 866 MHz dans cette étude) qui est rayonnée par une antenne et se propage jusqu'à l'antenne de l'étiquette radio. Une partie de l'énergie reçue par l'étiquette sert à activer ses circuits électroniques. Ces circuits contiennent principalement son code d'identification. Mais ils peuvent implémenter d'autres fonctions, comme des protocoles anticollision pour interroger plusieurs tags à la fois, ou des capteurs intégrés. Une autre partie de l'énergie est rétrodiffusée (comme un écho) à travers l'antenne de l'étiquette radio jusqu'au lecteur. L'étiquette inclut son code d'identification dans l'onde rétrodiffusée par l'alternance entre deux états qui altèrent cette onde (modulation de charge). À 866 MHz, ces étiquettes peuvent être interrogées à plusieurs dizaines de mètres du lecteur. La localisation d'étiquettes RFID fait l'objet de recherches depuis plusieurs années. Les méthodes actuelles les plus précises pour mesurer des déplacements sont fondées sur la comparaison de phase entre le signal envoyé par le lecteur et la réponse reçue de l'étiquette (Nikitin et al., 2010). Ces méthodes ont été développées en espace confiné. Fonctionneraient-elles aussi bien en environnement extérieur, pour surveiller en continu le déplacement de glissements de terrain ?

Par ailleurs, l'utilisation d'indicateurs complémentaires à la mesure de déplacement peut améliorer la fiabilité des alertes et permettre de mieux comprendre chaque site à risque. Le choix de ces indicateurs dépend du contexte géologique et du budget disponible. Sachant que l'eau en sous-sol est le principal déclencheur de glissements de terrain, la mesure directe de hauteur de l'eau souterraine est une donnée intéressante. Mais elle nécessite un forage souvent coûteux et ses mesures spatialement très localisées ne sont pas toujours représentatives de l'ensemble de glissement. Cette eau souterraine provient souvent de l'infiltration d'eau de pluie. Or la quantité de pluie est aisée à mesurer et homogène à l'échelle d'un glissement. En pratique, la combinaison de l'intensité et de la durée d'épisode pluvieux permet d'estimer une probabilité de décrochement. Mais celle-ci reste sujette à de nombreuses fausses alertes dans un dispositif de surveillance. Des approches qui relient mathématiquement les données de pluie et le déplacement existent depuis peu pour

mieux prédire un décrochement (Bernardie et al., 2015). Leur amélioration est étudiée dans cette thèse.

Un troisième indicateur est basé sur l'observation des variations de vitesse sismique au cours du temps. Ces variations sont calculées par corrélation des mesures de bruit sismique ambiant entre deux capteurs placés à proximité du glissement. Elles ont été appliquées récemment sur des glissements de terrain afin de mesurer la baisse de rigidité mécanique dans les couches profondes du glissement. Cette méthode pourrait prédire la rupture d'un glissement de terrain argileux plusieurs jours à l'avance (Mainsant et al., 2012). Cependant, les fluctuations saisonnières de cet indicateur causées par l'environnement (comme la température et la hauteur de l'eau souterraine) peuvent masquer les signaux précurseurs à un décrochement. Peut-on mieux les distinguer des éventuels signaux précurseurs, afin d'utiliser cette méthode dans un système de surveillance opérationnel ?

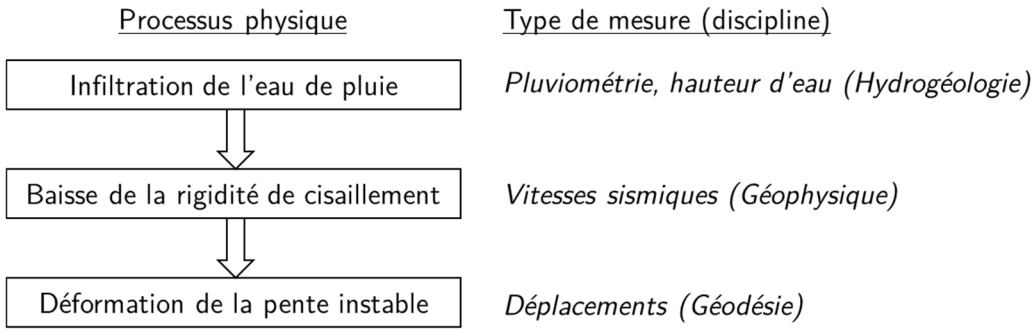


Figure 2 : Processus physiques qui déstabilisent un glissement causé par la pluie.

## Objectifs et déroulement de la thèse

Les objectifs initiaux de cette thèse portaient sur la surveillance de glissements de terrain. (1) Développer une nouvelle technique de mesure de déplacement « low-cost » basée sur des tags RFID ; (2) comprendre le rôle des influences environnementales sur les mesures de variations de vitesse sismiques par corrélation de bruit ambiant en vue d'une utilisation opérationnelle.

Le problème des influences environnementales s'est posé dès les premiers tests en extérieurs sur les mesures RFID : ces influences réduisaient la précision de mesure de façon trop importante pour une surveillance fiable. Elles ont dû être identifiées puis corrigées autant que possible. Pour tester la technique en conditions réelles, une chaîne de mesure a été installée sur un glissement de terrain pendant plusieurs mois. La comparaison des résultats avec des mesures conventionnelles a permis de

valider la technique. Cette dernière s'est avérée très fiable et a atteint une précision d'un centimètre. Le premier objectif était rempli.

Le second objectif était de comprendre les fluctuations saisonnières de vitesse sismiques ($dv/v$) mesurées par corrélation de bruit sismique ambiant, afin de les distinguer de signaux précurseurs à la rupture. Une étude bibliographique a permis d'identifier les influences environnementales qui pouvaient causer ces fluctuations, ainsi que les verrous à lever pour une utilisation opérationnelle en surveillance. L'étude des données de Pont-Bourquin a enfin permis d'explorer une troisième méthode, qui analyse la relation entre les déplacements et l'hydrologie au cours du temps. Les trois méthodes utilisées pour mesurer l'activité d'un glissement de terrain — géodésique, géophysique et hydrologique — ont ainsi été étudiées. (Figure 2)

D'autres projets ont enrichi ce travail. J'ai publié deux articles dans des revues scientifiques internationales, publié un brevet, présenté mes travaux à une douzaine d'évènements scientifiques (avec un poster primé aux conférences EGU et RSS) et contribué à une exposition scientifique grand public (plus de 10 000 visiteurs). J'ai principalement travaillé sur le glissement du Pont-Bourquin (Les Diablerets, Vaud, Suisse) en collaboration avec l'Université de Lausanne. J'ai également participé à la mise en place et à la maintenance d'un système de surveillance au Pas de l'Ours (Hautes-Alpes) avec Géolithe et Myotis, et suivi annuellement le glissement de Valloire (Savoie). Les entraides à ISTerre et Géolithe m'ont fait découvrir les glissements de terrain du Char d'Osset, d'Aletsch, des Gets, d'Harmalière et de Laurichard. Cela m'a fait prendre conscience des enjeux d'une surveillance opérationnelle.

## Organisation du manuscrit

Ce manuscrit se divise en trois parties. L'*État de l'art* présente les techniques utilisées pour surveiller les glissements de terrain, les technologies RFID pour mesurer des déplacements, et la méthode de mesure de vitesse sismique basée sur la corrélation de bruit sismique ambiant. La partie « *Influences environnementales* » identifie les influences de l'eau, de la température, de la neige et de la végétation sur les mesures d'un système RFID. Elle propose des corrections pour réduire la sensibilité de la mesure à ces influences. Enfin, la partie « *Applications au suivi temporel de glissement de terrain* » valide la technique de mesure de déplacement RFID sur le glissement de Pont-Bourquin. Elle comprend également une étude du

couplage entre le déplacement de ce glissement, la quantité de pluie et les variations de vitesse sismique pour mieux comprendre la dynamique de ce glissement.

**Partie I : État de l'art**

Le premier chapitre explique pourquoi et comment surveiller l'activité d'un glissement de terrain. Les contraintes opérationnelles d'un système d'alerte sont ensuite présentées. Enfin, les indicateurs qui ont déjà fourni des signaux précurseurs à une rupture sont présentés : le déplacement, l'hydrologie et la rigidité mécanique.

Le second chapitre identifie les points bloquants de la méthode de corrélation de bruit sismique ambiant pour l'appliquer à un système d'alerte opérationnel. Il rassemble les dernières études de glissements de terrain avec cette méthode, et les présente sous un angle de vue opérationnel.

Le troisième chapitre présente tout d'abord les principes de la RFID. Il synthétise ensuite les études qui ont mesuré des mouvements de terrain avec des tags RFID. Il expose ensuite la technique de localisation basée sur la différence de phase utilisée dans cette thèse.

**Partie II : Influences environnementales sur les mesures RFID**

Le quatrième chapitre identifie expérimentalement les influences environnementales majeures qui détériorent la précision de la mesure de déplacement RFID en conditions extérieures et sur de longues durées : la température et l'humidité. Une chaîne de mesure optimisée est proposée pour réduire ces influences. Elle améliore la précision annuelle de 20 cm à 1 cm, hors conditions neigeuses et végétation.

Le cinquième chapitre identifie les effets de la neige sur la précision de mesure et la portée d'un tel système — correspondant à la phase et la puissance du signal radio reçu. Un ensemble d'expériences met en évidence l'effet de la neige sur les antennes, sur la transmission d'ondes directes et sur l'interférence des trajets réfléchis au sol. Le rôle primordial de l'humidité et de la densité de la neige est aussi montré.

Le sixième chapitre identifie les effets de la végétation basse sur la puissance et la phase du signal, avec une approche similaire à celle utilisée pour la neige. Les principaux effets proviennent de la perturbation de l'onde directe qui se propage dans la végétation, et de l'altération des trajets multiples qui interfèrent avec le

trajet direct. Ces effets dépendent de la densité de végétation, de son contenu en eau et de sa conductivité.

**Partie III : Applications au suivi temporel de glissements de terrain**

Le septième chapitre présente le déploiement du système de mesure de déplacement RFID sur un glissement de terrain (Pont-Bourquin, Suisse). Il valide son fonctionnement pendant cinq mois. Le dispositif présente une robustesse exceptionnelle pour un prototype, et atteint une précision de mesure de 1 cm pour une portée maximale de 60 mètres. En cas de neige, le système continue de fonctionner, mais avec une portée légèrement diminuée et une précision détériorée de 8 cm. Ce chapitre apporte une nouvelle technique pour mesurer les déplacements surfaciques de glissements de terrain. Ce dispositif combine la simplicité de déploiement des systèmes à cible passive avec la robustesse des communications radio en cas d'intempéries.

Le huitième chapitre propose une méthode d'analyse combinée de déplacements et de pluviométrie. Elle repose sur l'inversion d'une fonction de transfert entre ces deux observables, qui est fortement liée au délai d'infiltration. Sur le site de Pont-Bourquin, elle indique une infiltration à deux vitesses, phénomène jusque-là observé uniquement par une étude hydrogéologique poussée. L'évolution de cette fonction de transfert dans le temps semblerait également reliée avec les variations de vitesse sismique (dv/v) et les fortes pluies. Cette méthode pourrait apporter un nouvel indicateur pour surveiller l'activité d'un glissement de terrain lent et comprendre ses interactions avec l'infiltration d'eau, à faible coût.

# Part 1—State of the art

# Chapter 1
# Landslide early warning systems

**Contents**



## 1.1 Summary


This chapter reviews the main methods used within landslide early-warning systems. A first section presents the principles of landslide risk and mitigation. The next sections present three monitoring methods providing precursors to a landslide rupture, based on geodesy, hydrology and passive seismology. The geodesic method consists of measuring the deformation of the ground. The hydrologic approach consists of monitoring precipitations and their infiltration in the subsurface. The seismological approach consists of measuring indicators of mechanical damaging and rigidity loss.

## 1.2 Landslide risk mitigation

### 1.2.1 Landslide hazard

Slope destabilization occurs in many regions of the world (

Fig. 1-1), imposing a heavy cost in life loss, properties and infrastructure. In the last decade, more than 40 fatal landslides and 4000 casualties due to landslides were recorded per year (Froude and Petley, 2018). Their annual economic cost has been estimated to $4, $2.6-5 and $3.6 billion only for Japan, Italy and the United States, respectively (Alimohammadlou et al., 2013). Besides, their occurrence is increasing due to human activities (Froude and Petley, 2018) and climate changes, particularly in alpine and polar regions where ice and permafrost melting create instabilities (Gariano and Guzzetti, 2016).

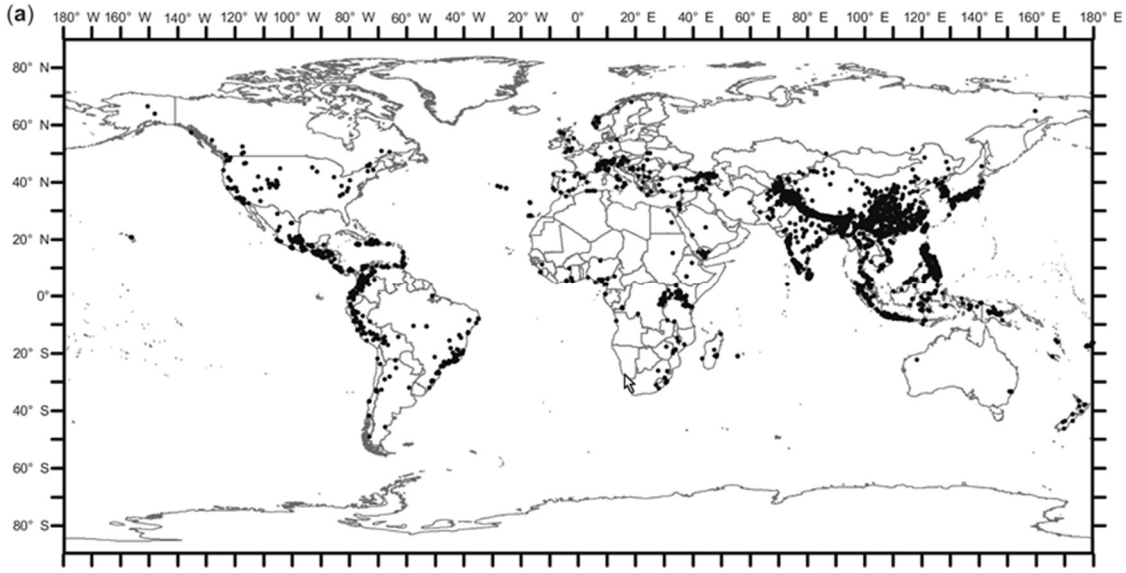


Fig. 1-1: Map of fatal landslide occurrence from 2004 to 2016. Each point represents a fatal landslide. From (Froude and Petley, 2018)

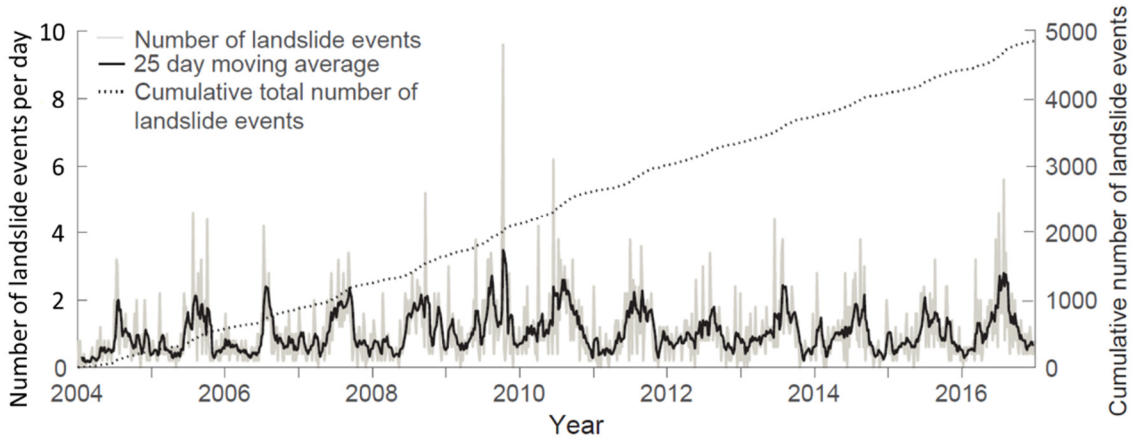


Fig. 1-2: Occurence of fatal non-seismically triggered landslide events from 2004 to 2006, and cumulative total of recorded events. Modified from (Froude and Petley, 2018)

Physical processes involved in landslides are numerous, driven by tectonics (Bennett et al., 2016), human activity (Petley et al., 2007), earthquakes (Marano et al., 2010), volcanoes (Scott et al., 2001) and climate (Moreiras, 2005). Climate has caused more than 70% of the fatal landslides (Froude and Petley, 2018). Climate-induced landslides are due to heavy rainfalls, snow melting or permafrost melting, which can decrease the ground rigidity and increase its stress. Landslides also involve very different type of movements (fall, topple, slide, spread, flow), geological materials (from solid rock to soft clay) and velocities (centimeters/year to meters/seconds), which are inventoried in (Cruden and Varnes, 1996; Hungr et al., 2014) (Fig. 1-3).

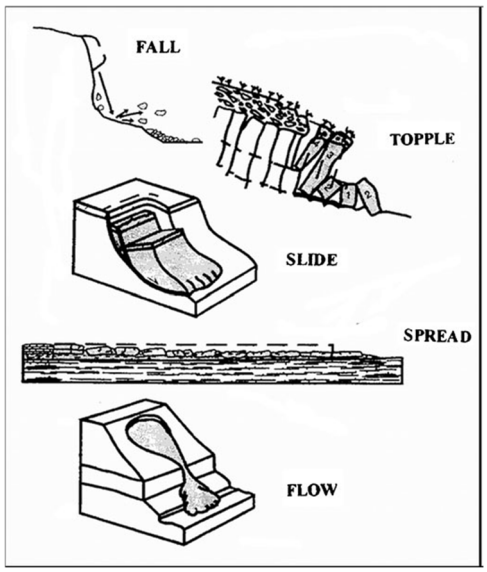


Fig. 1-3: Landslide movements illustration. From (Cruden and Varnes, 1996; Hungr et al., 2014).

### 1.2.2 Risk Mitigation

Landslide risks are determined from the hazard, the vulnerability of the community and infrastructure, and their exposure to the risk. The landslide risk $R$ can be expressed quantitatively as an annual loss of property value or life depending on the probability $P$ of a rupture event, its spatial and timely probability of impact (timely probability=1 for a permanent infrastructure), the vulnerability in case of an impact, and the value of the loss (Dai et al., 2002; Morgan et al., 1992):

$$\text{Risk} = P_{\text{Hazard}} \times P_{\text{Impact}}(\text{space}) \times P_{\text{Impact}}(\text{time}) \times \text{Vulnerability} \times \text{Value} \quad (1\text{-}1)$$

Risk management can reduce these values with three types of mitigation measures (Dai et al., 2002), illustrated in Fig. 1-4. Planning control consists of avoiding building infrastructure in an exposed zone based on risk assessment knowledge (Guzzetti et al., 1999) or replacing infrastructure. Engineering solutions stabilize the slope (landslide geometry corrections, water draining or retaining structures) or install protecting structures. Finally, early-warning systems reduce the probability of an impact in time by forecasting landslide failure and anticipating for a response. An identified risk can be reduced rapidly at a decent cost by implementing an early-warning system.

The cost of mitigation is fundamental to decide which measures to operate. Since budgets depend on the risk, a landslide that threatens a small road in a low-populated area may receive only minimal—if any—mitigation. Therefore, the availability of low-cost solutions is important. In this regard, early-warning systems are often the cheapest mitigation.

### 1.2.3 Early Warning Systems

Early warning system is defined by the United Nations Office for Disaster Risk Reduction (UNISDR, 2016) as *an integrated system of hazard monitoring, forecasting and prediction, disaster risk assessment, communication and preparedness activities systems and processes that enables individuals, communities, governments, businesses and others to take timely action to reduce disaster risks in advance of hazardous events.* Landslides early warning systems include four principal stages: design, monitoring, forecasting and education (Fig. 1-5) (Intrieri et al., 2013, 2012).

The education stage consists of communicating to the population and anticipating the actions that would have to be taken (e.g., block the road) if a rupture were

imminent (Basher Reid, 2006). This stage is essential, but out of the scope of this study.

In the design stage, the landslide hazard and risks are analyzed to choose the adequate monitoring strategy. Any information about the landslide is valuable here. A geological observation would help to delimit the landslide boundaries and understand its potential dynamics. Geotechnical measurements would assess the stability limits of the landslide material. Hydro-geological investigation would help to understand water infiltration, which is often the triggering factor. Historical deformation data would help to understand the landslide dynamics, set warning thresholds. All this knowledge would help to install the right monitoring instruments at the right position. The design and monitoring often require trade-offs depending on the available budget (Intrieri et al., 2013). Again, low-cost methods can be essential for monitoring sites with moderate risks and budgets.

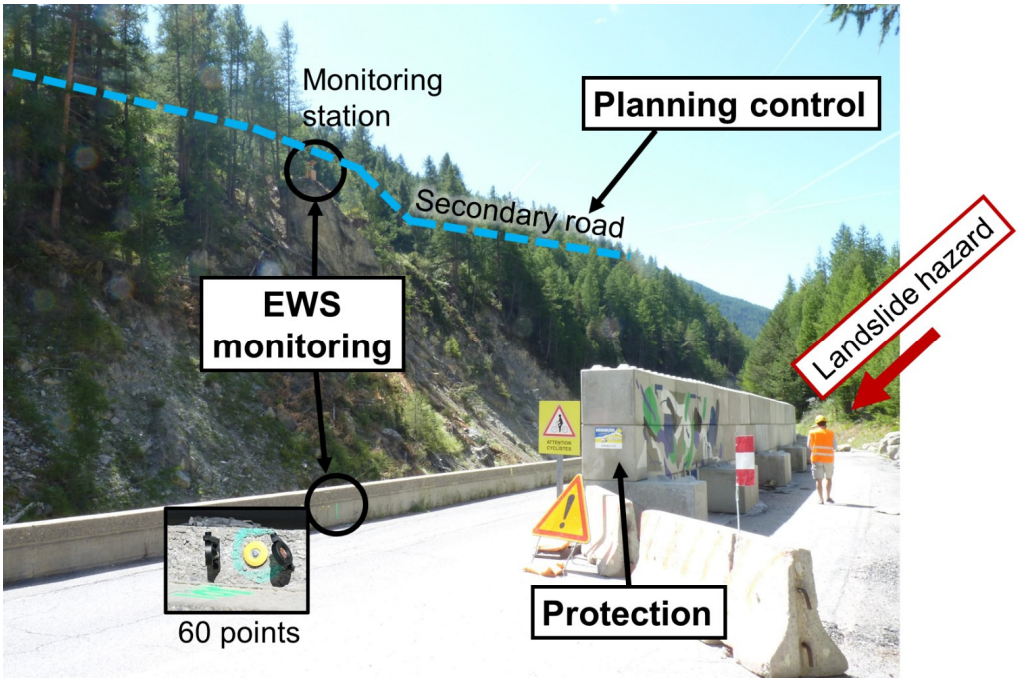


Fig. 1-4: Mitigation measures at the Pas de l'Ours landslide: Planning control led to building an emergency road, protections against mudflows were installed, and a real-time deformation monitoring system was installed for early warning.

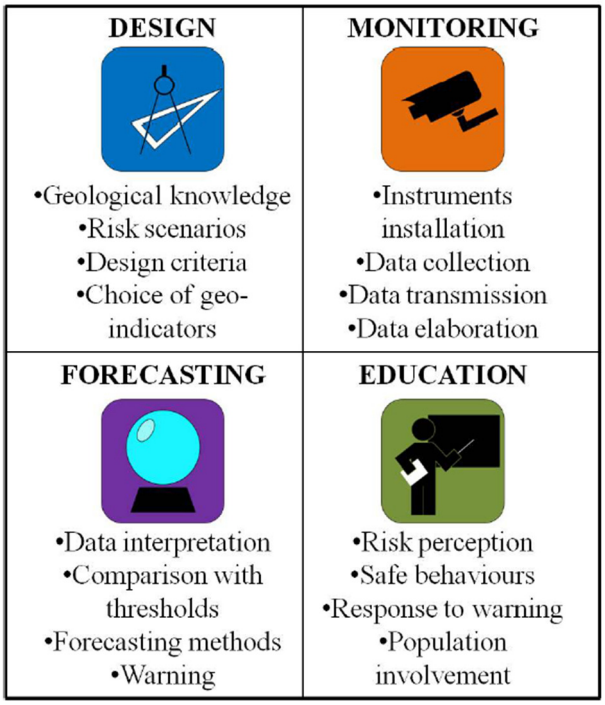


Fig. 1-5: Stages of a landslide early warning system, from (Intrieri et al., 2013)

Monitoring stage consists of installing instruments and ensuring the correct acquisition, transmission and processing of data. Monitoring is crucial for an early-warning system, but also to investigate mass movements in general to better understand their dynamics and physical processes. The monitored data usually consist of ground deformation (geodesy), water infiltration (hydrogeology and meteorology) and subsurface alterations (geophysics/seismology), each one providing complementary insights landslide processes. The key factor for a good monitoring is robustness, followed by accuracy and rapidity of the data workflow. Data quality must be high enough for raising automatic or manual warnings, and every technical problem encountered must be resolved. The list of potential problems in the field is long and includes energy shortage, loss of telecommunication network or material destruction due to animals, thunder, theft, strong wind or a tree falling (all experimented during this research work…). Some measurement (particularly optical and mechanical displacement) can be blocked by snow, heavy rain, heavy fog or vegetation, and halt the surveillance. When such event occurs, it must be discriminated from potential landslide failure and corrected rapidly, requiring maintenance efforts. A discontinued surveillance would strongly increase the risk, and may require to block the infrastructure usage. Therefore, the robustness of the measurement is a key for a good monitoring. In that regard, radio technologies (GPS, radar) are more robust than optical and mechanical techniques. Similarly, techniques that do not require

powering a full instrument on every measurement points are easier to maintain (e.g., remote sensing techniques, or localization of optical reflectors with a laser).

Rapid workflows are valuable to increase the lead time (time between a warning and a failure). Anticipating the rupture is indeed essential to take adequate protective measures. Furthermore, the confidence of the forecasting is usually higher just before the event, and monitoring until the last minute gives a higher chance to avoid a false warning. Fast and robust workflow transmit lightweight data, and can process the data and raise warnings without human intervention.

Forecasting phase requires analyzing the data provided by the monitoring, and deciding to raise warnings and to take actions or not. The decision may be human, or automatic when lead-times are very short (e.g., a rock is falling and will hit a road within seconds). Automatic warnings are raised when a monitored value exceeds a pre-defined threshold. Threshold value is defined to balance the risk of false warning (which should not occur too often) against missed warning (which should never happen), depending on the confidence level required in the warning. There are several ways to increase the confidence. First, the processing should reduce the noise level and reject outliers due for example to a local motion. Accurate and redundant measurements are useful at this step. Warnings should then be given a confidence level. Combining different observations would increase the confidence and reduce false warnings (Intrieri et al., 2013). The appropriate observation for predicting and understanding landslide activation may depend on the geological context. Such observations include surface displacement, rainfall and groundwater level, geophysical monitoring, and optionally earthquakes and vibrations. However, monitoring with multiple methods needs a higher budget. Again, lower-cost monitoring techniques are useful in this regard. This work addresses the problem by introducing a new displacement monitoring technique that is both low-cost and robust.

## 1.3 Displacement rate

### 1.3.1 Inverse velocity to predict failures

Measuring a landslide velocity of displacement is the main way to monitor its activity and to set warning threshold. Landslide velocity follows three stages before failure: it decreases in the primary stage, remains constant in the secondary stage, and increases rapidly until failure in the tertiary stage. Saito (1965) proposed to forecast the time of failure from its velocity time series (or strain rate after distance

normalization) by extrapolating the future velocity from the past measurements. However, the results strongly depended on the choice of the extrapolating algorithm. Fukuzono (1985) proposed to predict the time of failure with a simple method based on the inverse of the velocity of the tertiary phase (Fig. 1-6). The inverse velocity (1/V) was shown to decrease almost linearly until the failure, which strongly simplified its extrapolation. The mechanical theory supporting this technique is summarized by Federico et al. (2012).

Like any forecasting method, the difficulty of the inverse velocity technique is to predict all the failures (no missed warnings) and avoiding false warnings. However, scientific studies mostly present successful warning and rarely false warnings. The results of inverse velocity extrapolations also depend on the period in which the extrapolation is made, and using shorter or longer periods would result in different predictions (see Fig. 1-7). Predictions should also be confirmed by observing the velocity continuously until the last moment, when the confidence of the prediction is higher. For this reason, warnings should be given with gradations depending on their stage, lead time and levels of confidence. External parameters can also influence the observed trend, such as rainfall, snow melting or earthquake. These effects should be monitored also, to have more confidence in the observed trends. In terms of monitoring technique, the inverse velocity method requires accurate measurements and appropriate data filtering to avoid outliers (Carlà et al., 2017), and spatial redundancy to avoid local effects.

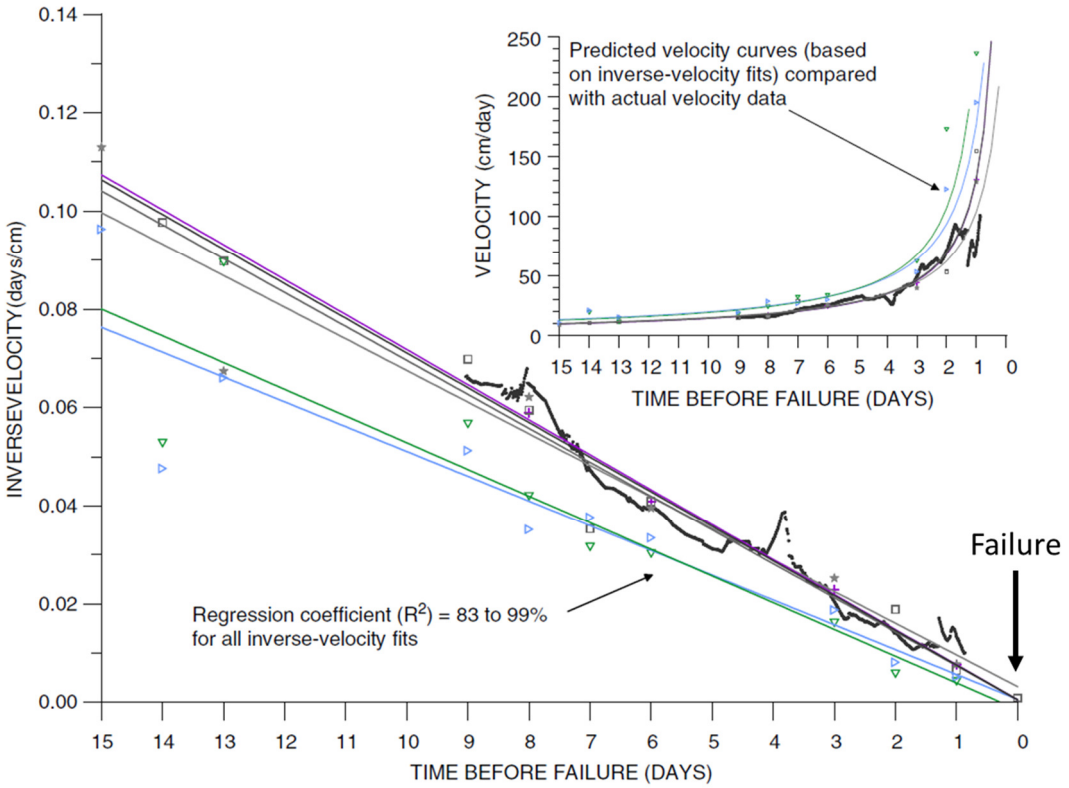


Fig. 1-6: Example of inverse velocity application on an open-pit mine. Daily manual surveys are in color and continuous extensometer monitoring in black. From (Rose and Hungr, 2007)

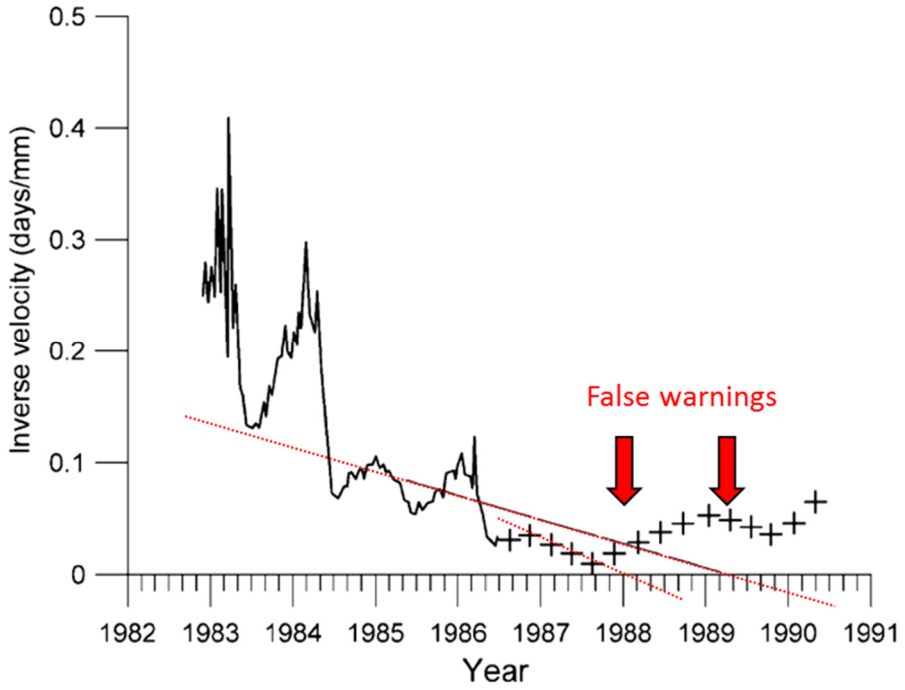


Fig. 1-7: Example of false positives at La Clapière landslide. Two false warnings would have been made in 1988 and 1989. From (Vibert et al., 1988; Rose and Hungr, 2007).

### 1.3.2 Displacement monitoring techniques

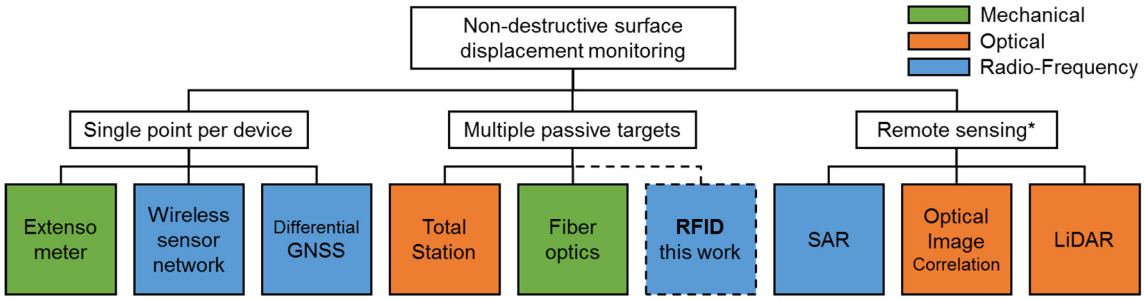


Fig. 1-8: Existing techniques to monitor landslide displacements. This review focus on surface techniques, and present the problems addressed by the proposed RFID technique. *Remote sensing is made from the ground, air or satellite and can also use passive targets.

The accurate and automatic monitoring of ground surface displacements is of paramount importance to forecast potential landslide failures. The existing monitoring techniques are reviewed in (Angeli et al., 2000; Baroň and Supper, 2013; Casagli et al., 2017; Uhlemann et al., 2016) and shown on Table 1-1. Their advantage and limitation strongly depend on the physical principles behind the measurement. These principles are usually mechanical, optical or radio frequency (Fig. 1.8). The number of local sensors also influences the cost of installation and maintenance. Some techniques require installing one complete sensor per measured point (e.g., GPS); other techniques need simply to install passive targets (e.g., laser total stations); remote sensing technique does not require any material installed on the monitored zone.

Mechanical techniques consist of attaching a wire (Angeli et al., 2000), a bar, or an optical fiber (Higuchi et al., 2005; Iten et al., 2008; Zhang et al., 2018) between two points to measure their relative displacement. This wire is easily destroyed by anything that crosses it or by a rapid landslide motion. It is also inefficient under the snow. Burying the wire underground reduces these problems, but at a higher cost and difficult maintenance. Optical techniques such as LIDAR (Favorskaya and Jain, 2017; Jaboyedoff et al., 2012), total station or optical image correlation (Travelletti et al., 2012), can monitor large zones without any fragile mechanical bounding. However, they still require an optical line of sight, which is vulnerable to precipitations, fog, vegetation, or snow. That is problematic for ensuring the continuity of the early-warning system under any weather conditions, particularly when the triggering factors are snow melting and rainfall. Radio-frequency techniques use larger wavelengths (centimeters) which can cross small obstacles and resolve this

problem. The drawback is the need to handle the reflected waves on the ground that interferes with the direct wave, called multipath. Radio-frequency techniques include GPS (Gili et al., 2000; Benoit et al., 2015; Squarzoni et al., 2005), interferometric radar or GB-SAR (Monserrat et al., 2014) and radio-based ranging devices (Intrieri et al., 2018a; Kenney et al., 2009; Lucianaz et al., 2015). Radio-frequency techniques provide the best robustness to natural disturbances.

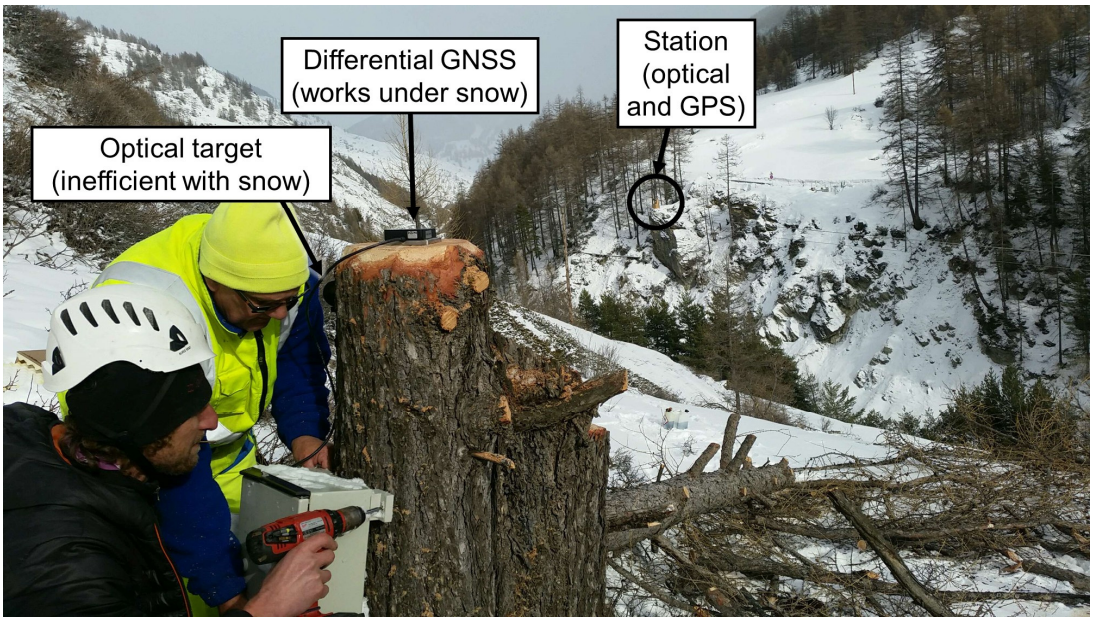


Fig. 1-9: At the Pas de l'Ours landslide, the optical monitoring was regularly discontinued in winter due to the snow and ice, and required a lot of maintenance. Low-cost differential GPS (Benoit et al., 2015) were installed in complement because the radio signal is less perturbed by snow. That allowed for 24/24h monitoring under any weather. However, their cost and energy consumption allowed monitoring only a few points, and the instruments were removed when the landslide became too active to avoid their destruction.

Many displacement monitoring techniques require installing one sensor on every point that is monitored (extensometers, GPS, radio-ranging devices). Such sensors are convenient on small installations, but the cost of the instruments, power sources and maintenance does not scale with hundreds of densely spaced points, despite recent developments to reduce their cost (Benoit et al., 2015; Intrieri et al., 2018a). On the contrary, ground-based remote techniques (optical images or interferometric radar) can monitor large zones with a high spatial density and do not require to install material on difficult to access areas. However, radar stations are expensive, and remote techniques generate large data flow that increases the complexity of real time monitoring. Sometimes, remote sensing monitoring is combined with the installation of a few passive targets on the monitored zone, to improve its accuracy and processing. Remote sensing also includes satellite (Intrieri et al., 2018b; Milillo

et al., 2014; Lacroix et al., 2018) and airborne remote sensing (Reigber and Scheiber, 2003), including a recent development of measurements from unmanned aerial vehicle (UAV, or drones) (Casagli et al., 2017; Lucieer et al., 2013; Niethammer et al., 2012). These can monitor very large areas for a reasonable cost. However, their temporal resolution is limited today to a few days which does not fit for continuous monitoring. Yet, their temporal resolution is likely to increase in the future with new satellite launch, and with improvements of material, data processing and automated guidance systems of drones. A last category of techniques uses only passive targets, which offers a trade-off between remote and one-sensor-per-point techniques. Laser total stations are very common for measuring displacement and use this approach. Still, they are based on an optical laser that requires a full optical line of sight and is sensitive to weather. This study introduces a new RFID technique that combines the scalability of passive targets with the reliability of radio-frequency techniques.

Table 1-1: Methods for automatic monitoring of landslide displacements

| Type of tracking | Method | Physical principle | Vulnerability | Typical Range | Typical Accuracy [g] | 1–3D | Sampling period | Cost [f] | References |
|---|---|---|---|---|---|---|---|---|---|
| Single point | Extensometer | Mechanical | Wire broken, snow cover, ice | ~100 m | 1 cm | 1D | | 2 k€ for 1 point | (Angeli et al., 2000) |
| | Differential GNSS | Radio | Satellite reception, atmospheric water content, multipath | 1 km | 0.1-1 cm | 3D | Real time (but limited by battery) | 2–5k€ for 1 point | (Benoit et al., 2015; Gili et al., 2000; Squarzoni et al., 2005) |
| | RF sensor network | Radio | Snow cover | 300 m | 0.3 cm / 5 cm [d] | 1D | | 1–2k€ for 1 point[b] | (Intrieri et al., 2018a; Kenney et al., 2009) |
| Surface, from a satellite | Optical image correlation | Optical | Clouds, vegetation, illumination | 800 km | 100 cm [c] | 2D | a few days | free[c] / paid | (Bontemps et al., 2018) |
| | InSAR | Radio | Snow cover | 800 km | 0.5 cm | 1D | | | (Colesanti et al., 2003; Intrieri et al., 2018b; Monserrat et al., 2014) |
| Surface, ground-based | Lidar | Optical[a] | Snow, rain, fog, snow cover, vegetation | 1 km | 1 cm | 1D | 5–100 minutes | 100 k€ for a zone | (Jaboyedoff et al., 2012) |
| | Optical image correlation | Optical | Snow, rain, fog, snow cover, vegetation, night, illumination, change of surface state | 500 m | 1–5cm | 2–3D | 1 day[e] | 2–10k€ for a zone | (Travelletti et al., 2012) |
| | GB-SAR | Radio[a] | Snow cover. For slow movements. | 30 m - 5 km | ~ 0.1 cm | 1D | ~1 minute | 100 k€ for a zone | (Herrera et al., 2009; Noferini et al., 2007; Pieraccini et al., 2003) |
| | Doppler radar | Radio | Snow cover. For fast movements. | km's | na | 1D | real time | 20 k€ for a zone. | (Gauer et al., 2007) |
| Multiple points, passive targets | Optical Fiber | Mechanical | Large landslide displacements | km's | 10% | 1D | seconds | 100k€ | (Habel and Kreb-ber, 2011) |
| | Laser tacheometer | Optical[a] | Snow, rain, fog, snow cover, vegetation, target rotation | 1 km | 0.5 cm | 3D | 10 s / target | 50 k€ for 100 points | (Abellán et al., 2009) |
| | Passive RFID | Radio | Snow cover, target rotation, multipath | ~100 m | 1 cm | 1–3D | 0.01 s / target | 10 k€ for 100 points | This work |

(a) Also requires an accurate motorization

(b) The cost is approximated, because the device was developed only for research purpose.

(c) This concerns data from SENTINEL-1 (SAR) and SENTINEL-2 (Optical).

(d) The higher accuracy is obtained with the phase-based technique presented by Kenney et al. (2009).

(e) Travelletti et al., 2012, reports a sampling period of 4 days. A sampling period below one day would be complicated, because of the weather and sun irregularity.

(f) The cost concerns only the material, and not the cost of maintenance, data retrieving, and processing.

(g) The typical accuracy is estimated for a range of 50 m, except for satellite techniques, for which the range is not relevant.

The typical range reflects the average distance between a base station, and the measured surface, or between different instruments in the case of a sensor network.

## 1.4 Rainfall and water infiltration

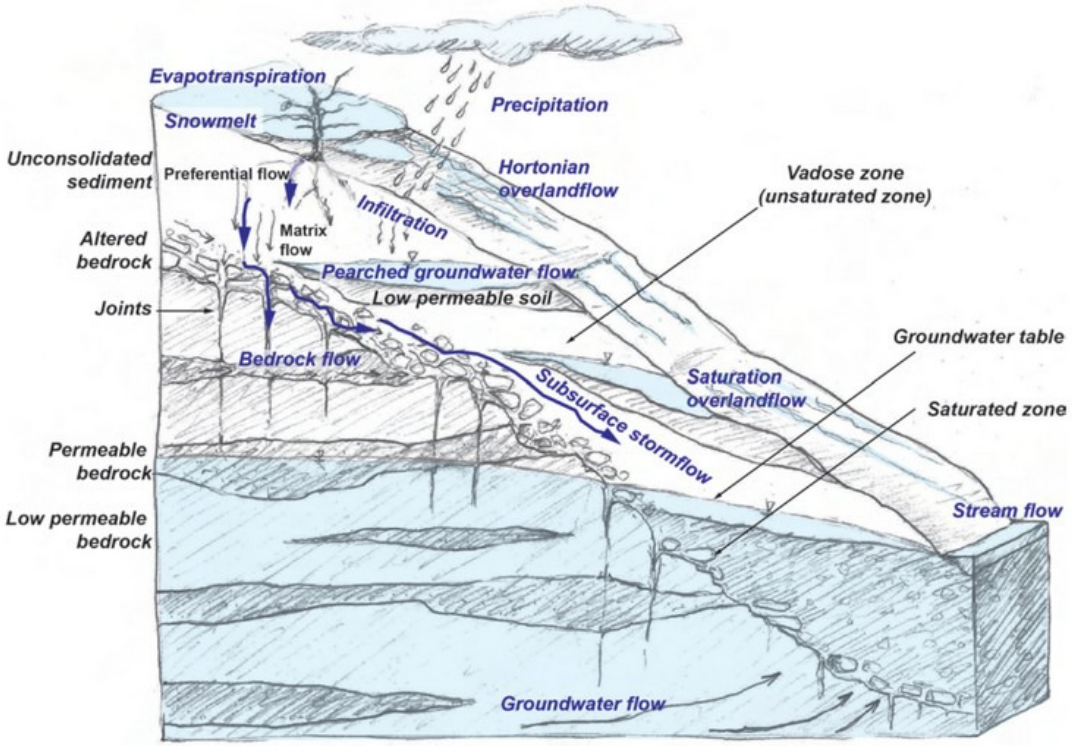


Fig. 1-10: Representation of the infiltration processes on a hill slope, from (Brönnimann, 2011)

### 1.4.1 Failure probability estimation

Climate-induced landslides are triggered by the infiltrated water (illustrated in Fig. 1-10) that follow precipitation episodes (Iverson, 2000). Therefore, some early-warning systems use a threshold based on the quantity and duration of rainfall events (Caine, 1980; Keefer et al., 1987; Aleotti, 2004; Baum and Godt, 2010). That raise alerts (e.g., low/moderate/high) when the measured or forecasted precipitation exceeds a pre-defined threshold. This statistical threshold varies between region and on landslides (Guzzetti et al., 2007) (Fig. 1-11) and defining it correctly is essential to avoid too many false warnings. Many parameters can influence this threshold, such as the geology or the slope angle (Montgomery and Dietrich, 1994). At a regional scale, this indicator is useful to raise the level of awareness of the authorities, but it can only estimate the probability of failure.

The relation between rainfall and rupture probability can be improved by accounting for the infiltration process across time and using local groundwater level measurements. The increase in groundwater levels due to rainfall can be computed by convolving the rainfall with a response function that has the shape of an infiltration curve (Iverson, 2000). The groundwater level data (measured or modeled)

then serve to compute the time and dynamics of the landslide rupture using a mechanical model (Iverson, 2000). However, using purely physical models (hydrological and mechanical) leads to strong discrepancies with the true rupture, and require numerous in-situ measurements to constrain the hydro-mechanical properties of the landslide. At the opposite, the relation between rainfall and rupture can be modeled empirically using an impulse response $\Psi(t)$ which, when convoluted with the rainfall time series, gives a mobility function $Y(t)$ that is representative to the probability of failure when exceeding a threshold (Capparelli and Versace, 2011). This generalizes several existing approaches that estimate the probability of failure, depending on the shape of the curve chosen for the impulse response. For example, the intensity-duration threshold introduced above would have the shape of a constant flat response. This technique has been tested with many different shapes of impulse responses (Luca and Versace, 2017) (Fig. 1-12) defined by 3 to 5 parameters using a 40+ year's historical dataset. The lowest rate of false/missed warnings were provided by mixed impulse response shapes using 5 parameters, showing the superiority of this approach compared to the rainfall-intensity duration that uses a 1-parameter flat shape. However, this technique is based only on failure events, which rarely occur. Moreover, optimizing more parameters require larger historical dataset of recorded failure events (curse of dimensionality), which are not available on recent landslides.

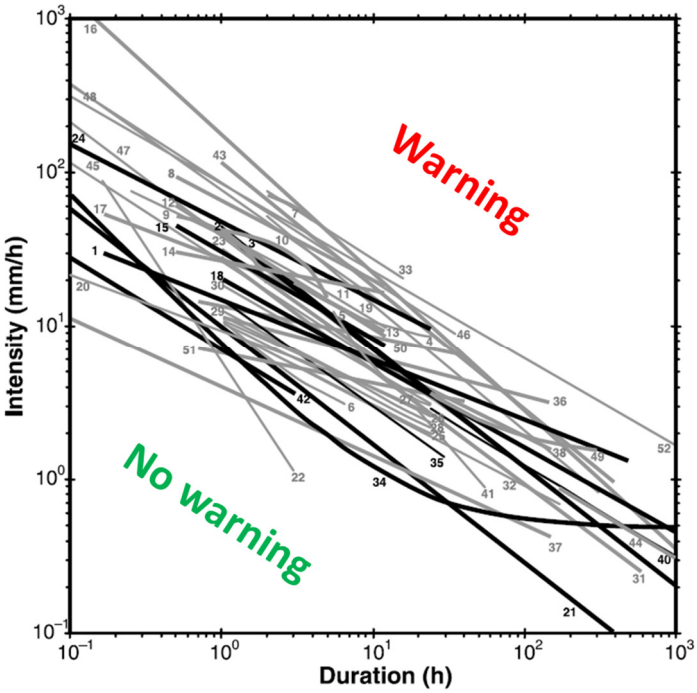


Fig. 1-11: Rainfall intensity-duration thresholds estimated in 52 regions of Europe. Modified from (Guzzetti et al., 2007).

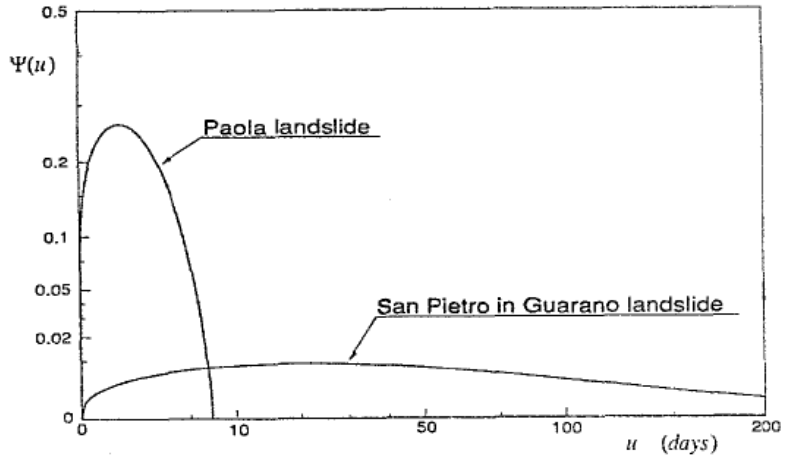


Fig. 1-12: Impulse response Ψ(t) of landslide mobility optimized on two different landslides. This impulse response is convolved with the rainfall time series to provide a mobility function that defines the probability of failure. From (Sirangelo and Versace, 1996)

### 1.4.2 Slow displacement prediction

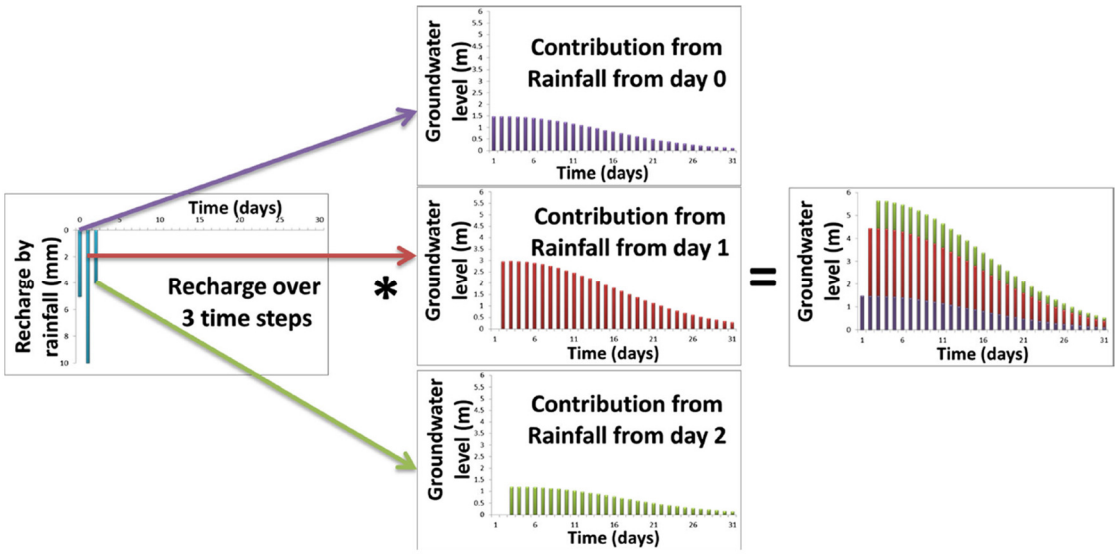


Fig. 1-13: Framework to compute the response of the groundwater level, by convolving the rainfall to a response function. From (Bernardie et al., 2015).

Slow reactivated landslides move regularly without failure in response to rainfall events. Recording their displacement provides a much larger dataset than recording only their failures. That allows computing an impulse response rapidly between rainfall (input) and displacement data (output), which would predict slow linear displacements (Belle et al., 2012). Physically this impulse response represents mostly the infiltration process. Indeed, the impulse response approach had been initially proposed to relate rainfall (input) to spring water (output) using a parameter inversion (Pinault et al., 2001). This study computed a full impulse response without a priori on its shape (such as a theoretical infiltration curve), to represent the complexity of the infiltration processes along time (Fig. 1-14). The direct relation (when no failure occurs) between groundwater level and landslide velocity (Fig. 1-15) justifies using an impulse response to estimate slow landslide movements from rainfall inputs. However, using effective rainfall input may require to correct for effects such as evapotranspiration, water running on the surface (Bièvre et al., 2018) and snow melting (Matsuura et al., 2003, 2017).

A short time series of effective rainfall and landslide velocity can then be used to predict the slow displacements of a landslide empirically based only on rainfall inputs. That was made firstly with a black-box neural network approach (Mayoraz and Vulliet, 2002). The use of an impulse response was then proposed. It was computed either once from a multi-year time series (Helmstetter and Garambois, 2010),

as the sum of two impulse responses that represent the slow/rapid infiltration (Belle et al., 2014), by integrating displacement data from multiple sensors (Lévy et al., 2017), and by computing the impulse response over a moving window (Bernardie et al., 2015). These resulted in overall good predictions of slow landslide motions. However, a landslide early-warning system aims at predicting rapid and harmful non-linear failures, for which the impulse response approach does not work. During such event, the landslide would accelerate far above the rainfall-based linear prediction. With this consideration, Bernardie et al. (2015) proposed to use the difference between the predicted and measured velocity as a potential failure indicator. Over 8 years, this indicator correctly anticipated the two failures occurring on Super-Sauze landslide (Fig. 1-16) without any false warnings, contrarily to the inverse velocity method. The present study pushes this method forward, by computing and studying a fully-inversed impulse response proposed by Pinault et al. (2001)(Fig. 1-14) for purely hydrologic studies, and comparing it with geophysical observations to better understand infiltration processes without requiring any hydrological measurement.

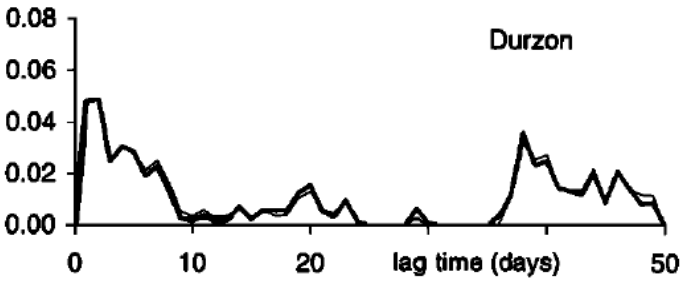


Fig. 1-14: Example of an impulse response inversed from the time series of rainfall (the input) and the amount of infiltrated rainwater measured on a spring (output), on a karstic region. From (Pinault et al., 2001)

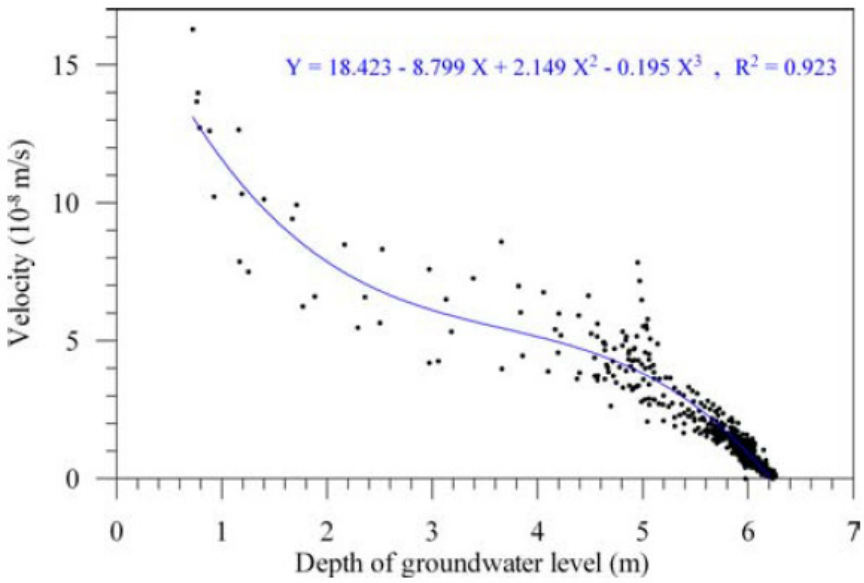


Fig. 1-15: Nearly linear relation between the depth of the groundwater level measured with a piezometer, and the velocity of the Vallcebre landslide. From (Corominas et al., 2005).

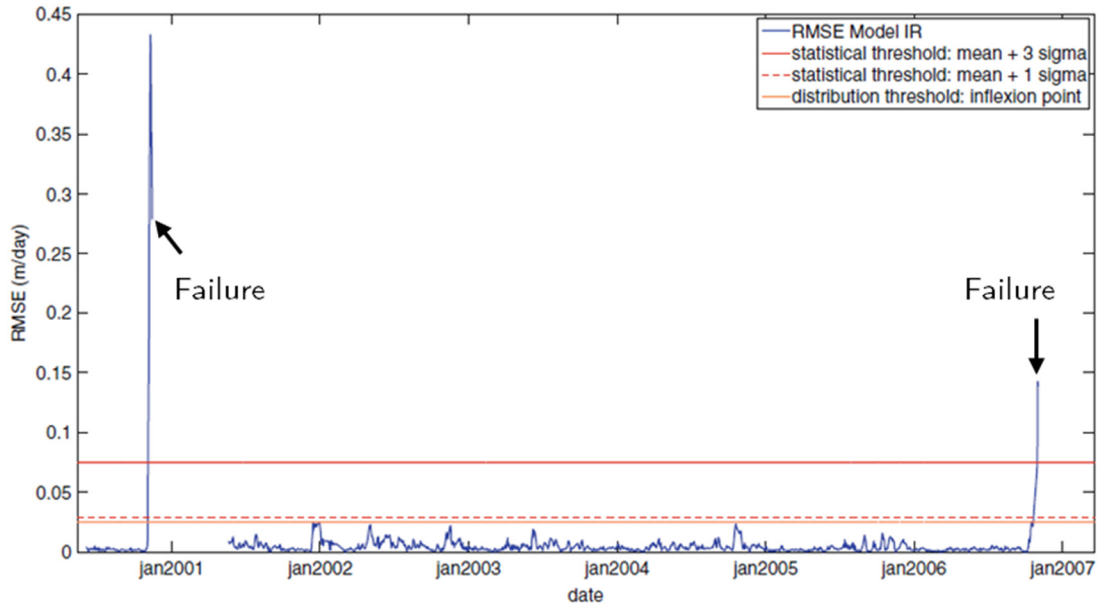


Fig. 1-16: RMSE difference between the velocity predicted from an impulse response and rainfall, with the measured velocity. This indicator strongly increased several days before the two failures, without false or missed warnings. From (Bernardie et al., 2015)

## 1.5 Geophysical Methods

Geophysics measure contrasts of physical properties of the subsurface such as conductivity, permittivity, mass density, rigidity or electrical potential. By imaging those contrasts spatially, geophysical methods can provide insights about landslide structure, hydrology and mechanical properties (Jongmans and Garambois, 2007)

and their dynamic across time using monitoring techniques (Fig. 1-17) (Whiteley et al., 2018).

These monitoring techniques provide either hydrological or mechanical indicators as their dominating sensitivity parameter of interest. Electrical methods are mostly sensitive to the bulk volume, salinity and circulation of water, and give useful insights to understand landslide hydrological dynamics. However, if groundwater levels measured directly with piezometers cannot alone predict a rupture, its indirect estimation using geophysics is unlikely to provide better precursors. Quadrature conductivity measurements (Flores Orozco et al., 2018; Gallistl et al., 2018) provide indicators on intrinsic electrical properties of the solid matrix that could suggest its alteration (Revil et al., 2017a, 2017b). However, the technique is operationally difficult for permanent and accurate monitoring: it did not provide precursory signals up to now.

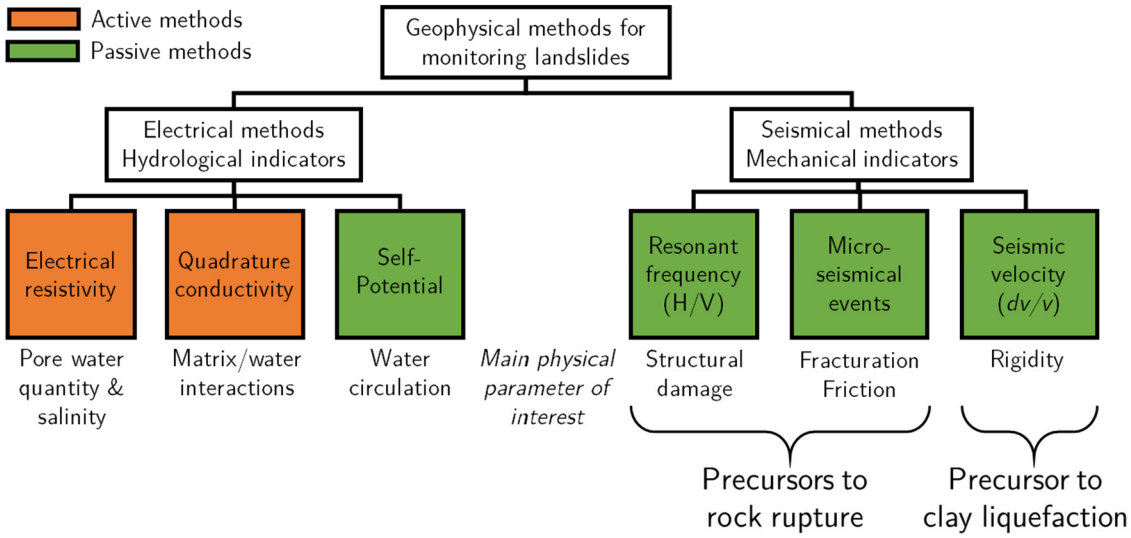


Fig. 1-17: Geophysical methods used for monitoring landslides, inspired by (Whiteley et al., 2018).

Passive seismic is the only geophysical method that has shown clear precursory signals several hours to days before a failure (Larose et al., 2015; Snieder and Larose, 2013). The damaging of a rock column was shown to increase its micro-seismic activity several hours before its rupture (Amitrano et al., 2005; Senfaute et al., 2009) and to reduce its resonant frequency several weeks earlier (Lévy et al., 2010). On clayey landslides, acoustic events are less energetic and more attenuated and such technique did not work. However, clay is subject to a strong shear-wave velocity drop before its fluidization. Such drop has been measured several days before a rupture using ambient noise interferometry (Mainsant et al., 2012b)(Mainsant et

al., 2012b) using passive ambient noise interferometry (Sens-Schönfelder and Wegler, 2006, p.). That led the way to a new type of precursors. The challenges for integrating this technique into an operational landslide early-warning system are reviewed in the next chapter.

# Chapter 2
# Ambient noise interferometry on landslides

**Contents**



## 2.1 Summary


This chapter reviews the applications of ambient noise interferometry applied to landslides, and study its challenges for implementing this method in an operational early-warning system. Environmental influences on the measured value are identified as groundwater, temperature and freezing/melting. The different techniques in the processing workflow are also reviewed, and indications to choose the appropriate processing parameters are given. The choices concern the investigation depth that must be investigated for a correct monitoring, the tradeoffs between stability and temporal reactivity, and the uncertainty assessment to increase the confidence of potential warnings.

## 2.2 Ambient noise interferometry for landslide monitoring

### 2.2.1 Ambient seismic noise interferometry

The idea of the ambient noise interferometry is to reconstruct an approximation of the transfer function (or Green's function, GF) of a medium to an impulse excitation, by cross-correlating the noise measured passively between two sensors. That has been done on an ultrasonic receiver (Weaver and Lobkis, 2001), on a larger scale using the diffused energy from an earthquake coda (Campillo and Paul, 2003) and finally using ambient seismic noise (Shapiro and Campillo, 2004). Ambient seismic noise has the advantage of relying not on a localized and timely source of energy, but instead on diffused noise from multiple sources. That allows for a more stable reconstruction of the GF. These studies retrieved the early and high-energy part of the correlations, which represent direct surface waves. They used it to measure the phase velocity and make a tomography of the seismic velocity of the materials at depth. These could also use late arrivals, but in a static way (Larose et al., 2006). Sens-Schönfelder and Wegler (2006) then proposed to monitor the later part of the correlations, also named coda, along time. The coda is mostly influenced by the scattering of waves between the two sensors. Its monitoring allows measuring apparent velocity variations that result from a small velocity perturbation in the bulk caused by geological events. This velocity was observed to increase slightly before a volcano eruption (Brenguier et al., 2011, 2008b, 2016; Obermann et al., 2013a; Nakata et al., 2016), to decrease abruptly during an earthquake then to increase slowly during a recovery phase (Wegler and Sens-Schönfelder, 2007; Brenguier et al., 2008a; Rivet et al., 2011; Hobiger et al., 2016), and to decrease even more strongly after an earthquake in a volcanic area (Brenguier et al., 2014; Taira and Brenguier, 2016).

Smaller scale objects have also been monitored. Velocity decreases were observed due to a seepage on dams or levees (Olivier et al., 2017; Planès et al., 2017, 2016) or to seasonal thawing of permafrost (James et al., 2017). Another approach has consisted of monitoring the decrease of coherence between the correlations along time. Such decorrelation was observed for example during the filling/drainage of a glacier-dammed lake (Preiswerk and Walter, 2018; Walter et al., 2015) or during the fluid injection on a geothermal site (Obermann et al., 2013a).

### 2.2.2 Applications to landslide monitoring

On landslides, ambient noise interferometry firstly served to image the subsurface using surface waves dispersion (Renalier et al., 2010b). Apparent surface wave velocity monitoring (Renalier et al., 2010a) attracted much interest after detecting a clear velocity drop five days before the catastrophic acceleration of a shallow clayey landslide (Mainsant et al., 2012b). It led to a new technique for predicting landslide failures. This drop of velocity, that reached 7% before the failure (Fig. 2-1), was attributed to clay fluidization at the base of the moving layer due to the material accumulation and pore pressure increase. Indeed, clay fluidization due to stress and pore saturation has been shown in laboratory conditions to strongly decrease the clay shear-wave velocity before its fluidization (Carrière et al., 2018, 2018; Dong Yi and Lu Ning, 2016; Mainsant et al., 2015, 2012a).

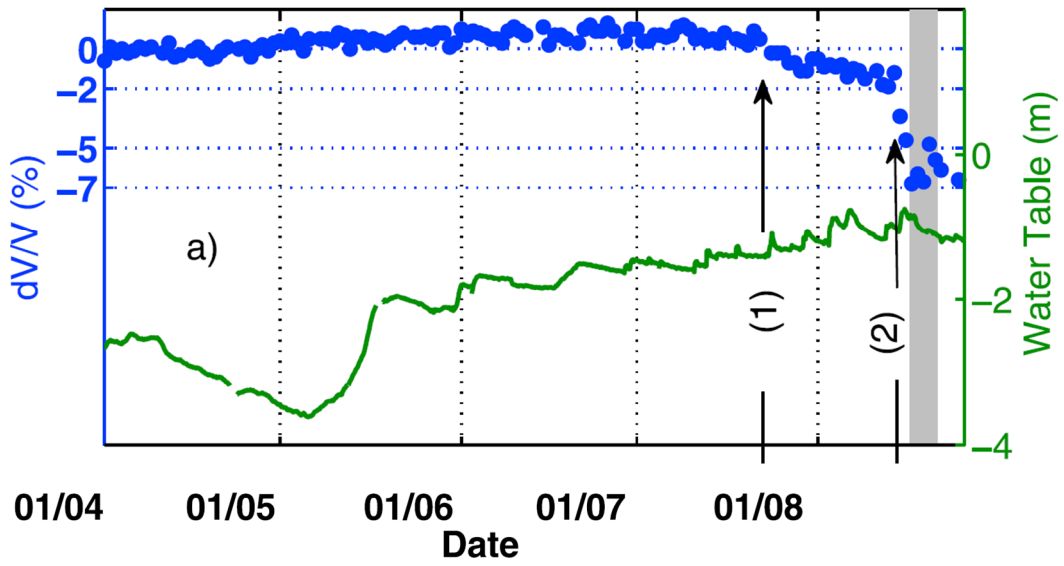


Fig. 2-1: On the Pont-Bourquin landslide, the apparent surface wave velocity (in blue) was monitored before the major failure of 19 August 2010 (in gray). Vertical line 1: the first velocity reduction starts after rainfall on 23 July and represents a drop of 2% developing over 20 days. Vertical line 2: the major drop starts after rainfall on 14 August, with a total decrease of 7% over the 5 days preceding the landslide. The water table height (green) was not sufficient to predict a failure. From (Mainsant et al., 2012b)

Several landslides have been monitored since then (), including deep-seated landslides (Bontemps et al., in preparation; Voisin et al., 2016), a rock glacier (Guillemot et al., in preparation), a rockfall/slide (Colombero et al., 2018) and the use of seismic arrays to study spatiotemporal variations during a few months (Chtouki et al., 2017; Harba and Pilecki, 2017). However, these studies did not lead to the detection of a precursory signal, simply because the landslides that were studied have not been subjected to a failure yet. The potential of $dv/v$ precursory signal has recently been confirmed on a

rotational slide (Fiolleau et al., in preparation), in a different configuration: a seismic sensor was placed on a prone-to-failure earth column, and its recordings compared with a sensor placed on stable grounds. The degradation of the material did not permit monitoring velocity variations correctly, but led to a progressive decrease of correlation coherence 20 days before the failure (explained by the rear-fracture progressive opening).

Table 2-1: Landslide monitoring based on ambient noise interferometry

| Landslide | Technique (a) | Precursor | Seasonal variation | Duration (yr.) | Stations | Sliding depth (m) | Slide class (Hungr, 2014) | References |
|---|---|---|---|---|---|---|---|---|
| Avignonet, France | *dv/v* | na | ±0.5 % | 2.5 | 2 | 10–16 and 42–47 | Clay/silt compound slide | (Renalier et al., 2010a) |
| Pont-Bourquin, Switzerland * | *dv/v* | 2–7% in 5d | ±2% | 6 | 6 | 10 | Clay planar slide-earthflow | (Bièvre et al., 2018; Larose et al., 2015; Mainsant et al., 2012b) |
| Utiku New Zealand | *dv/v* | na | ±2% | 1.1 | 4 | 300 (Massey et al., 2013) | Planar rockslide/earthflow | (Voisin et al., 2016) |
| Madonna del Sasso, Italy | *dv/v*<br>$f_0$ | na | ±10%<br>2.7-3.3Hz | 2.3 | 4 | 15 and 16 | Rock fall-slide | (Colombero et al., 2018) |
| Harmalière, France | CC<br>$f_0$ | 0.8–0 in 20d<br>9–6 Hz in 8h | na<br>na | 0.3 | 2 | 3 | Earth rotational slide | (Fiolleau et al., 2018, in preparation) |
| Gugla, Switzerland | *dv/v*<br>CC | na<br>na | ±1.5%<br>1-0.5 | 3 | 2 | 2 to 15 | Rock slope deformation/solifluction | (Guillemot et al., in preparation) |
| Maca, Peru | *dv/v* | na | ±1% | 3 | 1[(b)] | 50 | Clay/silt compound slide | (Bontemps et al., in preparation) |

* exploited in the present study

(a) *dv/v* stands for temporal relative velocity variations based on the coda of the green function and CC stands for Coherence Coefficient of the green function. $f_0$ (also called H/V) use ambient noise—but not interferometry—to monitor the horizontal resonant frequency, normalized by vertical component or horizontal component of another sensor.

(b) Auto-correlation between vertical and horizontal polarization of the ambient noise, on one single sensor.

### 2.2.3 Potential and limitations for an early-warning system

Ambient noise interferometry presents multiple advantages for an early-warning system. Firstly, it measures directly the loss of rigidity in the bulk of the material that causes the failure, in contrast to the later surface displacement or the earlier rainfall infiltration. It is therefore complementary to existing monitoring techniques. Secondly, it provides the ability for a continuous and very robust monitoring. Indeed, ground seismic waves propagate even with rain, snow, vegetation or without line of sight. Furthermore the sensors can be partially buried to avoid

their deterioration. Finally, it is non-destructive and does not require expensive drilling.

However, forecasting a rupture before it occurs—and not after—requires 1) to validate statistically the precursory signals compared to false warnings 2) to know before the event which processing parameter will highlight the precursor and 3) to be reactive enough to raise a warning before the event. Up to now, precursory signals were observed at Pont-Bourquin and Harmalière landslide (Mainsant et al., 2012b; Fiolleau et al., in preparation). Bièvre et al. (2018) recently showed four additional years of monitoring on this site for which no failure occurred, and highlighted seasonal velocity variations that remained below ±2%, suggesting this threshold would be sufficient to avoid false warnings. Statistical relevance should then be assessed on multiple landslides and new ongoing studies (Table 2-1) should validate it.

Prior knowledge of the landslide is important to set proper parameters in the processing workflow. A depth sensitivity analysis should constrain parameters of frequency and time window (detailed in subsection 3), requiring first to investigate the sliding surface depth and the seismic velocities in the unstable mass. A learning time would also be valuable, to observe the landslide behavior in regard to environmental influences and set a threshold that would avoid false warning.

Effective lead time is of paramount importance to anticipate a failure, and give enough time to make decisions and take actions. That means to automatize fast processing and warning system with minimum manual intervention, to reduce the time resolution below a day, and maybe to correct for environmental influences to increase the sensitivity to the precursor.

## 2.3 Environmental influence on the $dv/v$

### 2.3.1 Seasonal variations on landslides

Environmental influences on apparent relative seismic velocity ($dv/v$) are clearly visible on Fig. 2-2. Understanding and predicting these variations would allow discriminating them from true precursory signals, thus reducing false warning rates and increasing the lead time. Seasonal variations on the Pont-Bourquin landslide were clearly highlighted in (Larose et al., 2015), and later interpreted in (Bièvre et al., 2018) and (Voisin et al., 2016) for shallow and deep-seated landslides, respectively.

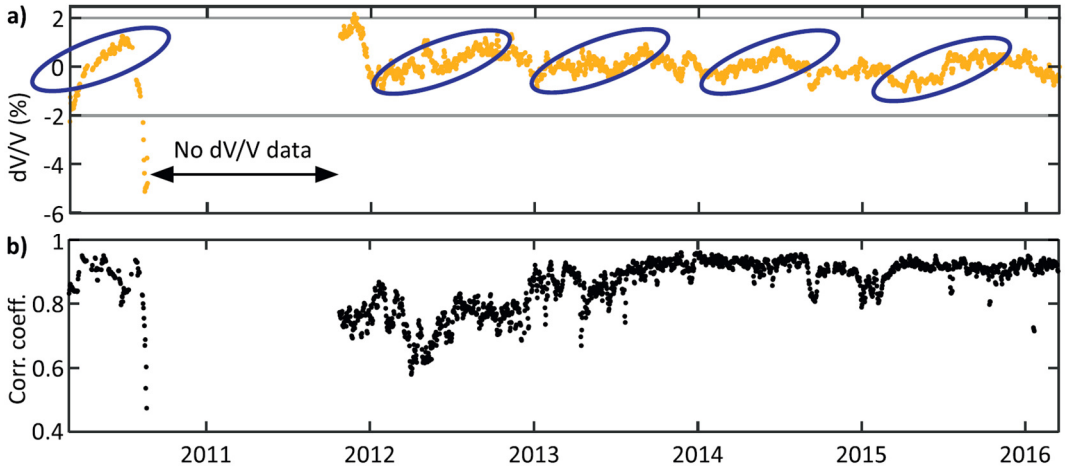


Fig. 2-2: (a) Relative velocity changes *dv/v* at Pont-Bourquin landslide between March 2010 and March 2016, for the frequency range 8–12 Hz. The horizontal gray lines represent the proposed threshold of ±2% and the blue circles highlight seasonal increases. (b) The associated correlation coefficient. From (Bièvre et al., 2018; Larose et al., 2015)

On Utiku landslide (Voisin et al., 2016) the *dv/v* clearly appeared negatively correlated with a measured groundwater level (Fig. 2-3.a), suggesting its predominance on the *dv/v* control. On the Pont-Bourquin landslide (Bièvre et al., 2018), the *dv/v* appeared negatively correlated to rainfall with 2–5 days of lag (Fig. 2-3.b), positively correlated to air temperature with 30–50 days of delay (Fig. 2-4), and positively correlated with cold peaks in winter. That suggests a possible control of groundwater, shallow soil temperature (±2% for both) and frost (±1%). While the influence of rainfall/water table should control rapid variations of *dv/v*, it seems unsure whether the long-term seasonal variations are controlled by temperature and/or water elevation at Pont-Bourquin. To better understand seasonal effect then requires to enlarge the study scope to non-landslide investigations.

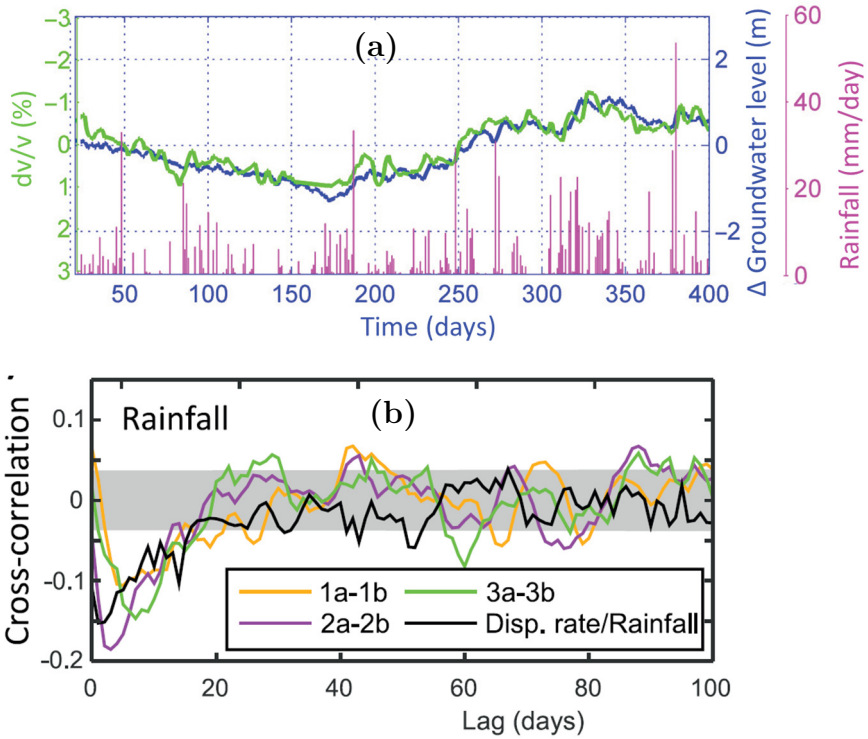


Fig. 2-3: Influence of water shown two landslides. (a) On Utiku landslide, the measurements of dv/v over a year show a clear negative correlation with the measured groundwater level—modified from (Voisin et al., 2016) (b). Pont-Bourquin landslide, the cross-correlation between *dv/v* and rainfall over four years shows a clear peak of negative correlations 2–5 days after the rainfall event, due to the infiltration delay.

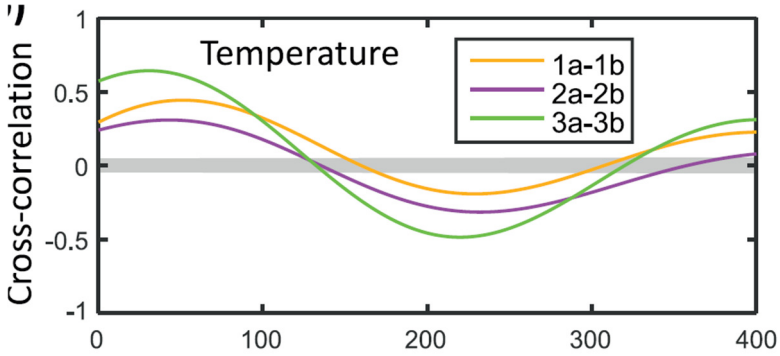


Fig. 2-4: Correlation between *dv/v* and air temperature on the Pont-Bourquin landslide time series, filtered for periods higher than 300 days. It shows that temperature increases are followed by velocity increases with a lag of 30–40 days, which suggests a causal relation due to thermo-elastic stress. From (Bièvre et al., 2018).

### 2.3.2 Seasonal variations in general

Seasonal variations of *dv/v* were observed on various sites (Table 2-2) including volcano, sedimentary basin, landslide, groundwater storage, CO2 storage, and even lunar soil, glacier and ice sheet. A first look at these studies reveals that the amplitude of seasonal variations varies by a factor 200 between studies, from 0.03%

(Lecocq et al., 2017; Wang et al., 2008) to 6% (James et al., 2017). This suggests very heterogeneous behaviors between studies. However this discrepancy can mostly be explained by the different investigation depths. Indeed, when comparing the studies together, the seasonal amplitude appears to follow a trend with the central frequency $f$ chosen for filtering the correlation (Fig. 2-5). The trend relation $\Delta v/v_{\max} \sim f^{3/2}$ appeared respected for all the study sites, on the moon (Sens-Schönfelder and Larose, 2008) and Greenland ice sheet (Mordret et al., 2016). This trend suggests that near-surface soil would be more sensitive to seasonal variations than deep material, because lower-frequency surface waves are sensitive at greater depth. Inter-station distance and time window also followed a trend with the seasonal variation amplitude (not shown here). This is explained because all these parameters are in practice mutually correlated to investigation depth. In fact, multiple studies have observed an increase of seasonal variations with early time windows (Hillers et al., 2015b; Richter et al., 2014; Sens-Schönfelder and Wegler, 2006), shorter inter-station distance (Meier et al., 2010) and higher frequencies (Richter et al., 2014; Voisin et al., 2016). Only one study observed a decrease of seasonal variation when increasing the frequency (Hillers et al., 2015a), which was explained by the sensitivity of deep rock to thermo-elastic strain.

Two conclusions appear from this trend. First, the ratio between frequency and seasonal velocity variations follow the same trend even in different regions and materials (except for the Moon and Greenland ice sheet, which are very different contexts). The same seasonal influences should then occur on landslides. Secondly, investigating a shallow landslide should lead to stronger seasonal variations than a deep-seated landslide.

Table 2-2: Environmental variations of seismic velocity observed on the long-term (monthly, yearly and multiple years) in different studies

| Study | Frequency (Hz) | Amplitude (%) | Context | Suggested governing influence |
|---|---|---|---|---|
| (Sens-Schönfelder and Wegler, 2006) | Broadband >0.5 | 4 | Volcano, Merapi, Indonesia | Groundwater level (–) |
| (Sens-Schönfelder and Larose, 2008) | 6–11 | 0.15 | Lunar soil, Apollo 17 | Temperature (+, 7d) |
| (Meier et al., 2010; Tsai, 2011) | 0.1–2 | 0.1 | Basin, Los Angeles, USA | Groundwater level (–) |

| | | | | |
|---|---|---|---|---|
| (Voisin et al., 2016) | 6–8<br>3–20 | 2.2<br>6 | Landslide, Utiku | Groundwater level (–) |
| (Bièvre et al., 2018; Larose et al., 2015) | 8–12 | 3 | Landslide, Pont-Bourquin, Switzerland | Rainfall (–), temperature (+, 40d), frost (+) |
| (Wang et al., 2017) | 0.15-0.9 | 0.03 | Whole Japan, Hi-net | Pore pressure (–), snow depth (+), sea level/tide (+), *Temperature (+, 40d)* |
| (Miao et al., 2018) | Broadband<br><30 | 0.3 ms | East Japan, Kik-net | Rainfall (–) |
| (Lecocq et al., 2017) | 0.1–0.8 | 0.04 | Ground water storage, Gräfenberg Array, Germany. | Temperature (+)<br>and groundwater level (–) |
| (Clements and Denolle, 2018) | 0.5–2 | 0.3 | Groundwater basin, San Gabriel Valley, California | Groundwater level (–) |
| (Hillers et al., 2015a) | 0.5–2 | 0.2 | San Jancinto Fault, California, USA | Temperature (+, 20d) |
| (Hillers et al., 2015b) | 2–8 | 0.3 | Mountain, San Jancinto Fault Area, Piñon Flat Observatory, California, USA | Tidal strain (–) |
| (Hillers et al., 2014) | 1–4 | 0.3 | Chelungpu fault, Taiwan | Precipitations/groundwater level (–) |
| (Richter et al., 2014) | 4–6<br>9–11 | 0.29<br>2 | Northern Chile | Temperature (+, 33d) |
| (Mordret et al., 2016) | 0.1–0.3 | 0.1 | Ice sheet, western Greenland | Ice mass (–, 2 months) |
| (Preiswerk and Walter, 2018) | 2–8 | 10 dB SNR | Glacier, Aletsch, Switzerland | Source variation |
| | 4–16 | CC drop | Glacier, Plaine Morte, Switzerland | Source variation due to drainage/filling of a glacier-dammed lake |
| (James et al., 2017) | 13–17 | 6 | Permafrost, Poker Flat Research Range, Alaska | Soil freezing (+)/melting (–) |
| (Guillemot et al., in preparation) | 4–10 | 3 | Rock glacier, Gugla, Switzerland | Soil freezing (+)/melting (–) |
| (Gassenmeier et al., 2015) | 1.5–3 | 0.8 | CO2 storage site, Ketzin, Germany | Groundwater level (–), Frost (+) |
| (Rivet et al., 2014) | 0.1–2 | 0.50 | Volcano, Piton de la Fournaise | |
| (Hobiger et al., 2016) | 0.25–0.5<br>0.5–1<br>1–2 | 0.02–0.04<br>0.04–0.12<br>0.08 | Earthquakes in Japan | Curve fitting with a sinusoidal function |

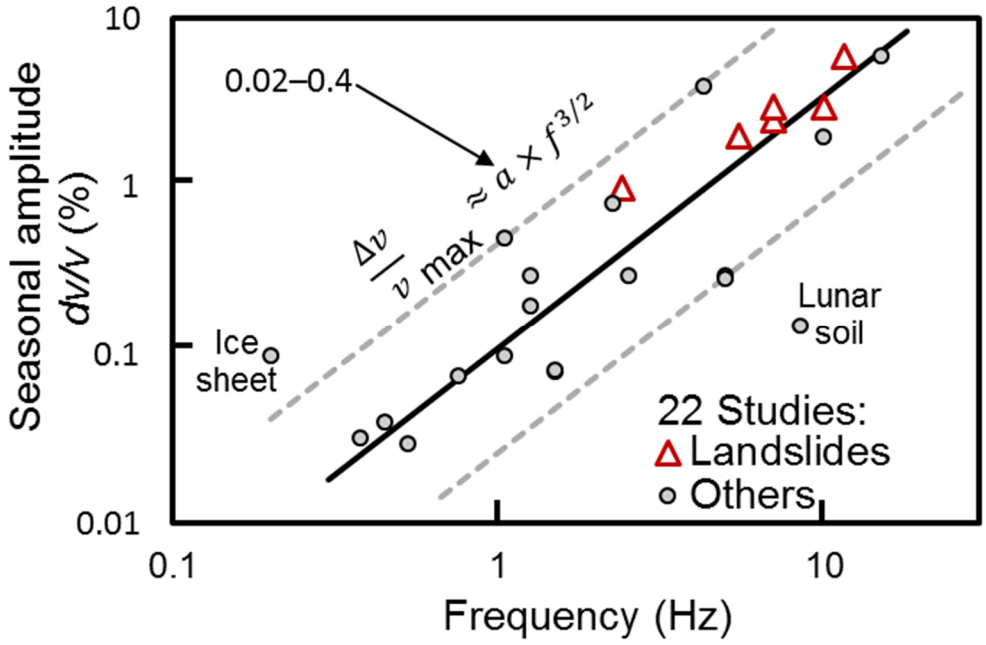


Fig. 2-5: Amplitude of the seasonal variation of relative velocity versus central frequency. Coefficient a = 0.11 (dashed lines: 0.02 and 0.4).

The different governing causes suggested in studies from Table 2-2 may appear contradictory on a first look. Temperature and groundwater level are often suggested, but are often mutually correlated over a year and difficult to discriminate. Furthermore, rainfalls that increase groundwater level can also reduce soil temperature. Temperature is usually observed to vary a few days before the *dv/v*. Depending on the study, that lag would either discard the temperature influence, or confirm it, due to thermal diffusion in the soil. Tide level would affect crustal stress (Luttrell and Sandwell, 2010) but could also increase the groundwater level near the coast. Snow load would increase the stress and apparent velocity (Wang et al., 2017), but its melting also increases the groundwater level.

In addition to that complexity, seasonal variations would differ on a regional scale (Wang et al., 2017) and their influence parameters may have to be estimated locally. When trying to discriminate seasonal effects from exceptional events, a pragmatic approach is then to take into account the multiple effects together and fit coefficients to account for their different importance (Wang et al., 2017).

At the pore scale, these influences can be separated between mechanical strain (thermo-elastic, tidal, atmospheric, groundwater load and snow load) and pore sat-

uration. Environmental variations on the crustal scale can influence both the mechanical strain and the pore saturation, at the pore scale. For example, tide can both induce stress changes and modify the groundwater level. Groundwater level in turn affects pore saturation and material strain.

Despite some disagreements on the governing cause, every study agree on the sign (positive/negative) of those suggested influences on the apparent velocity: groundwater elevation decreases the apparent velocity and temperature increases it. In cold conditions, soil freezing increases the velocity and soil melting decreases it.

The influence of temperature was clearly discriminated from groundwater in Richter et al. (2014) and Sens-Schönfelder and Larose (2008), because the measurements were situated respectively in an arid desert and on the moon without water, and still displayed cyclic variations corresponding to the temperature cycle.

The influence of groundwater level is of particular importance for studying rainfall-induced landslides because groundwater elevation decreases the $dv/v$ under normal conditions (for example on Fig. 2-6). This environmental dv/v drop should then be discriminated from the drop due to clay liquefaction prior to a failure (Mainsant et al., 2012b). A better understanding of groundwater influence is therefore essential, and should be studied at the time scale of the early warning: a few days.

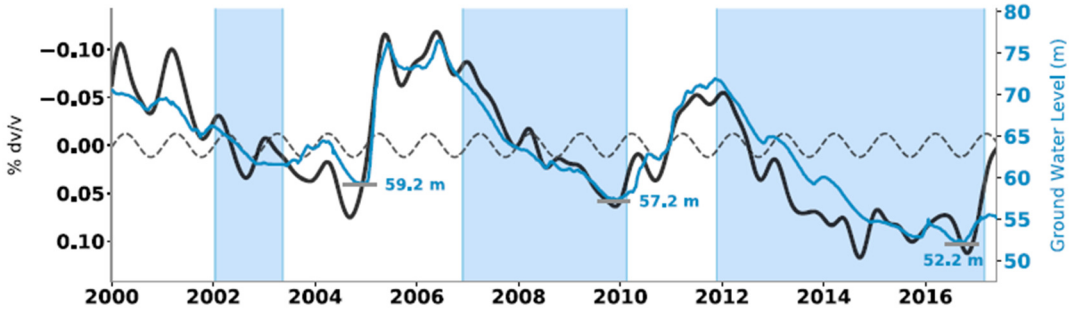


Fig. 2-6: Relating seismic wave speed temporal perturbations (in black) to groundwater level (in blue) and modeled thermoelastic strain (dashed) in the Baldwin Park Key Well, in California Basin. From (Clements and Denolle, 2018)

### 2.3.3 Daily variations

Daily time scale has been less studied than seasonal variations, for multiple reasons. Sub-daily correlations are noisier, less stable, and prone to daily source insta-

bility and soil variations, compared to correlations stacked over several days. Observing deep geological structure requires a high accuracy to spot small *dv/v* and a resolution of one or several days is sufficient in most of the studies anyway.

On the contrary, the observation of shallow layers is likely to raise strong *dv/v* variations (several %) and tolerate a lower signal-noise ratio. The first meters of soil could show variation within a few hours due to temperature variation, rainfall, frost or simply source variation (e.g., road traffic) that would vary along the day. Understanding these rapid variations is valuable to distinguish them from a potential precursor, but also to improve the time resolution to a few hours and therefore increase the lead time. Observing sub-daily data should also help to understand the daily environmental influences from only a few days of data, instead of the multiple years required to understand them from seasonal variations.

Few studies have worked on daily variation of the *dv/v* (see Table 2-3). Because of the difficulties cited above, each one had to adapt its processing to the observation of sub-daily raw data. Takano et al. (2014) computed noisy correlation functions every minute between 2 a.m.—4 p.m. and averaged them over three months. It resulted in one correlation function during tidal dilatation and another during contraction, which were then compared. Planès et al. (2017) and Voisin et al. (2017) used the energetic early arrivals of the correlation after verifying the source stability and azimuth, and discarding unstable sources. Mao et al., (2019) denoised the correlation with a Wiener filter (Moreau et al., 2017), averaged the *dv/v* over 1225 pairs and studied the resulting time series in the frequency domain. Richter et al. (2014) computed a dv/v between each hourly correlation and their average over the same day, then computed the average *dv/v* over 1557 days separately for each hour of the day. James et al. (2017) presented only the amplitudes of daily variations without detailing its specific processing and Preiswerk and Walter (2018) showed the abrupt loss of coherence between two consecutive daily correlation functions due to a source change.

Suggested daily influences are the same as seasonal ones. Daily temperature variation is positively correlated to *dv/v* within the arid desert of Atacama, probably due to thermo-elastic stress (Richter et al., 2014). Sea level/tide appeared negatively correlated with *dv/v* in two studies (Planès et al., 2016; Takano et al., 2014). However, the suggested causes are different. In mountainous and volcanic regions, the variations of 0.2% (Fig. 2-7) are suggested to originate from the Earth tide. On a coastal levee, a stronger variation of 5% variation fitted perfectly to the measured

variations of groundwater level caused by the tide (Fig. 2-8) demonstrating the effect of groundwater. The causality of groundwater influence was demonstrated (Voisin et al., 2017) by injecting water in a water storage site, which again showed a clear negative correlation between the groundwater level and the apparent $dv/v$ (Fig. 2-9)

Table 2-3: Daily variations of $dv/v$ observed in different applications.

| Study | Frequency (Hz) | Amplitude of $dv/v$ (%) | Context | Suggested governing influence |
|---|---|---|---|---|
| (Takano et al., 2014) | 1–2 | 0.19 | Volcano, Iwate, Japan | Tidal strain (decrease of velocity during dilatational episodes) |
| (James et al., 2017) | 13–17 | 0.2 | Permafrost, Poker Flat Research Range, Alaska | No suggestion for daily variations (only seasonal) |
| (Planès et al., 2017) | 5–20 | 5 | Sea levee, Colijnsplaat, Netherlands | Pore water pressure (–) [due to tide level] |
| (Preiswerk and Walter, 2018) | 4–16 | CC drop | Glacier, Plaine Morte, Switzerland | Source variation, due to drainage/filling of a glacier-dammed lake |
| (Mao et al., 2019) | 1–5 | 0.02 | Volcano, Piton de la Fournaise, La Réunion | Tidal strain, temperature |
| (Voisin et al., 2017) | 5–12 | 3 | Groundwater storage, Crépieux-Charmy, France | Groundwater level (–) controlled by fluid injection. |
| (Richter et al., 2014) | 4–6 | 0.09 | Northern Chile | Temperature (+, 3h) |

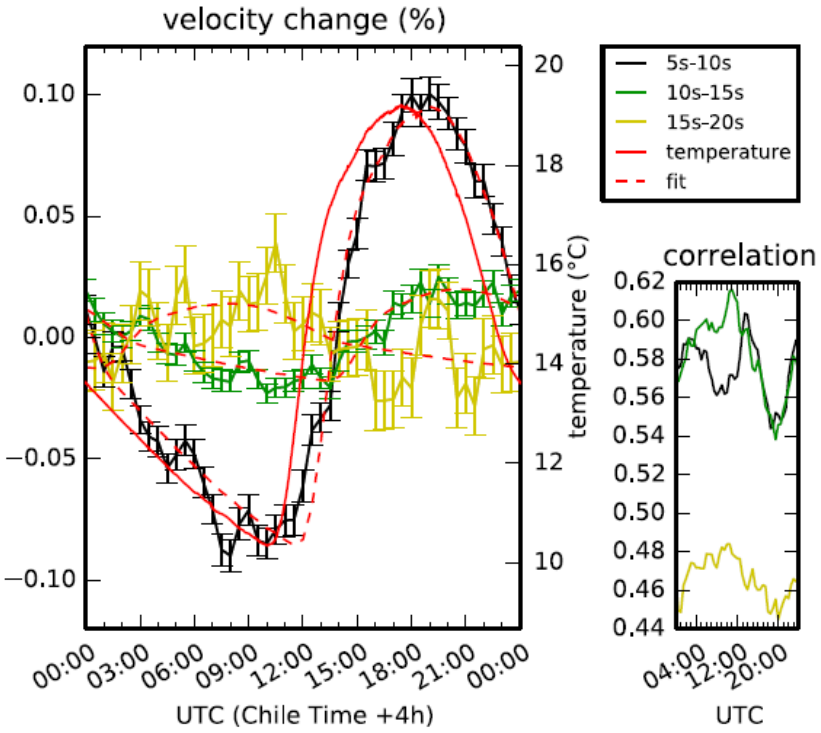


Fig. 2-7: Highlighting the effect of daily temperature variation at Atacama Desert. From (Richter et al., 2014)

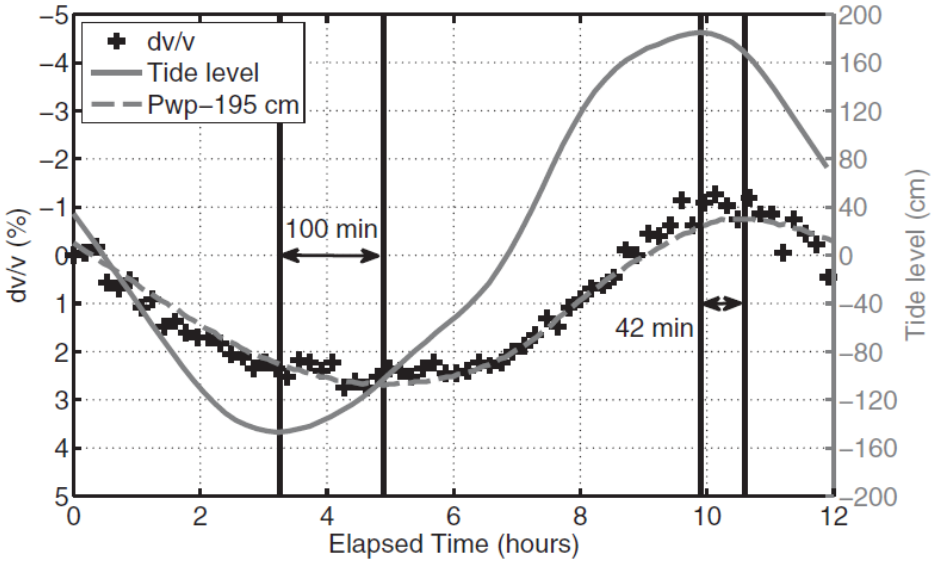


Fig. 2-8: Highlighting the correlation between *dv/v*, tide and groundwater level on a coastal levee. From (Planès et al., 2017)

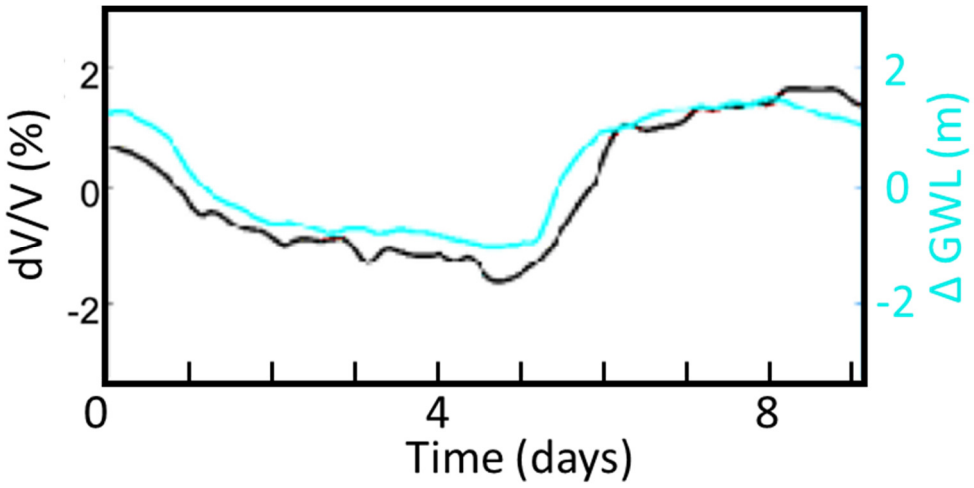


Fig. 2-9: Ground water levels compared to daily-smoothed *dv/v* at 3–20 Hz during a controlled fluid injection, which proves the causal link from water level to *dv/v*. From (Voisin et al., 2017).

## 2.4 Adapting the method to an early-warning system

### 2.4.1 General processing workflow

A general processing workflow is presented in Fig. 2-10. For an early warning system, the workflow should rapidly detect changes of *dv/v* and raise a warning with the shortest possible lead time. However, increasing the reactivity may deteriorate the signal-to-noise ratio and lead to false early warnings. A tradeoff should then be found between reactivity and stability (in blue). The precursor should also be detected automatically with a minimal human intervention and prior knowledge about the landslide. The process should constrain the parameterization as much as possible with minimal manual tuning. A prior knowledge of the structure of the landslide at depth and a seismic velocity profile would help to constrain the choice of the frequency band, time window and optionally sensor pair selection (in yellow). The steps of the processing are presented in the following sections.

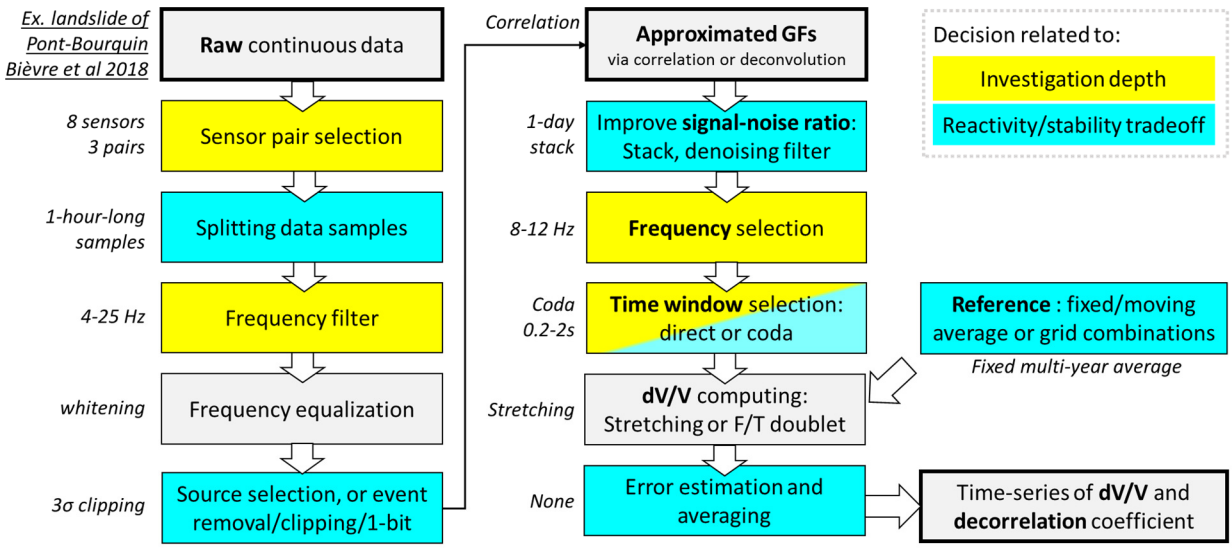


Fig. 2-10: General workflow to process ambient seismic noise correlation and extract daily relative velocity changes *dv/v* and decorrelation coefficients. Modified after (Larose et al., 2015).

The workflow starts by preparing the raw continuous data recorded by the seismometer, or "traces". Traces consist of ground vibration measurements in 1 or 3 directions (vertical or 3D). Data is typically sampled every 1–10 milliseconds and accurately timed by a GPS-synchronized clock. Sensors are selected by pairs that are within the area of investigation. Their traces are split in time by samples of equal size and time base. The length of the samples, typically one hour, defines the minimal resolution of the *dv/v*. The traces frequencies are then normalized and filtered around the desired frequency/depth of investigation. This can be done in the frequency domain with an apodization window $A^{f_{\min},f_{\max}}(\omega)$ to filter the selected bandwidth $[f_{\min}, f_{\max}]$ and shows a smooth transition from 0 out of the bandwidth to 1 within the selected bandwidth:

$$S_i^{\text{filtered}}(\omega) = \frac{S_i^{\text{raw}}(\omega)}{\left|S_i^{\text{raw}}(\omega)\right|} A^{f_{\min},f_{\max}}(\omega) \tag{2-1}$$

The correlation of two traces $a(t)$ and $b(t)$ gives an approximation of the GF $h_{AB}$ between their two sensors (it is possible also possible to exploit one single sensor using autocorrelation):

$$h_{AB}(t) \approx ccf_{AB}(t) = \int a(\theta)b(t+\theta)d\theta \tag{2-2}$$

The resulting cross-correlation functions (CCF) can be normalized by the traces energy $\sqrt{(\sum a^2(t))(\sum b^2(t))}$, or instead be computed with a deconvolution (Nakata and Snieder, 2012), not discussed here.

CCFs are then stacked and filtered in frequency. A reference CCF is chosen (often the average CCF over the whole period), and each CCF is compared with the reference within a defined time window to extract their *dv/v*. The choice of processing steps and parameters such as averaging, frequency filtering, reference selection and time window depend on the investigation depth and on the appropriate tradeoff between stability and reactivity. These are discussed in the next section.

Computing the *dv/v* between two CCF uses either the stretching or doublet method. These were compared by Hadziioannou et al. (2009). The doublet method measures the time shift $\Delta t$ between two CCFs on a narrow moving window in the time or frequency domain, and extracts the slope $\Delta t/t$ (Fig. 2-11). The stretching method (Sens-Schönfelder and Wegler, 2006) consists of testing several possible velocity changes of *dv/v* by resampling the time of the CCF $h(t) \to h\left(t\left(1-dv/v\right)\right)$. The optimum velocity change *dv/v* at a given date maximizes the correlation coefficient computed between the stretched and reference CCF:

$$CC\left(\frac{dV}{V}\right) = \frac{\int h\left(t\left(1+dV/V\right)\right) h_{ref}(t)dt}{\sqrt{\int h\left(t\left(1+dV/V\right)\right)^2 dt \int h\left(t\right)^2 dt}} \tag{2-3}$$

When compared, the doublet would better eliminate localized decorrelations outliers, spot non-linear velocity variation along the time windows, and provide the same contribution from every part of the CCF whatever their amplitude. On the other hand, the stretching would work with a lower signal-noise ratio and requires less parametrization, which seems preferable for an automatic early-warning system. To equalize the contribution from the different times in the CCF, we propose to normalize its amplitude before applying the stretching method.

Finally, if the dv/v is computed over multiple pairs, that can serve to localize the velocity change spatially (Brenguier et al., 2008b), or to compute an averaged *dv/v* and a standard deviation.

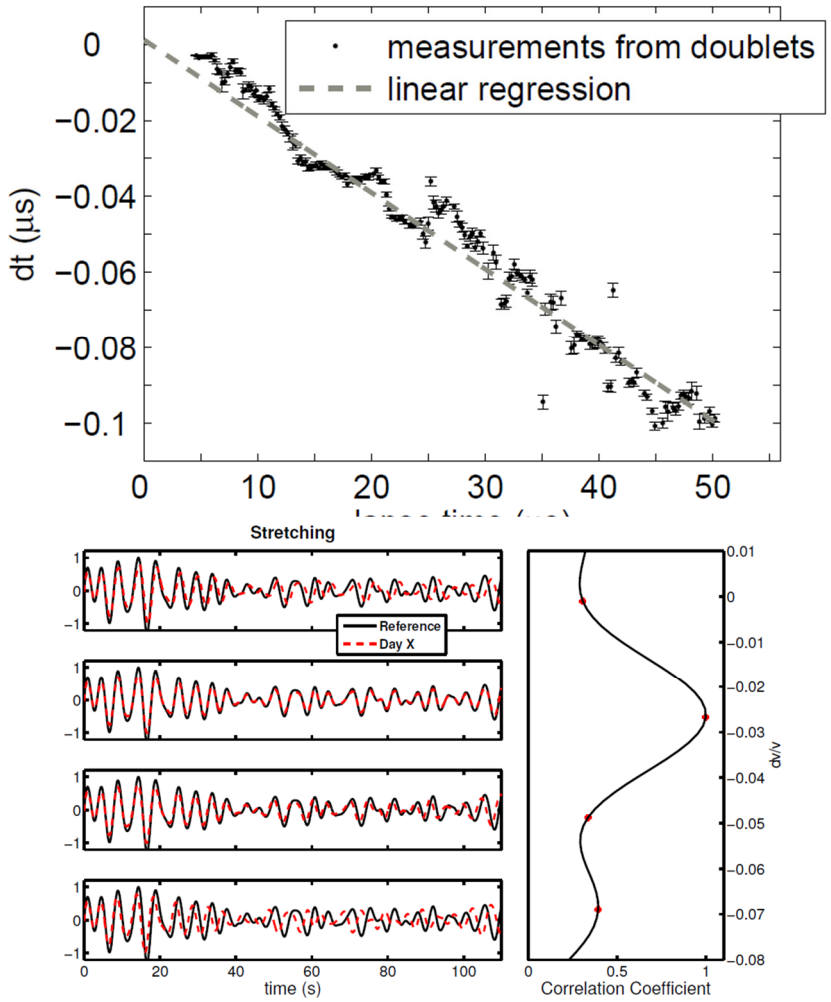


Fig. 2-11: Illustration of the method of (top) doublet and (bottom) stretching, from (Hadziioannou, 2011; Hadziioannou et al., 2009)

### 2.4.2 Investigation depth

Ideally, a CCF would reconstruct the response of a pulse originating from sensor A and measured on sensor B, after a complex propagation in the medium. This propagation consists in surface waves and scattered surface and/or body waves, with a mutual conversion between them. Each propagation mode will exhibit different sensitivity to depth, wave frequency, time response and material properties (Obermann et al., 2013b).

Surface waves phase velocity and penetration depth depend on their frequency and on the bulk P and S velocities of the subsurface layers. The choice of frequency to filter the CCFs is then crucial, and depends on the depth and material that needs to be monitored (Fig. 2-12).

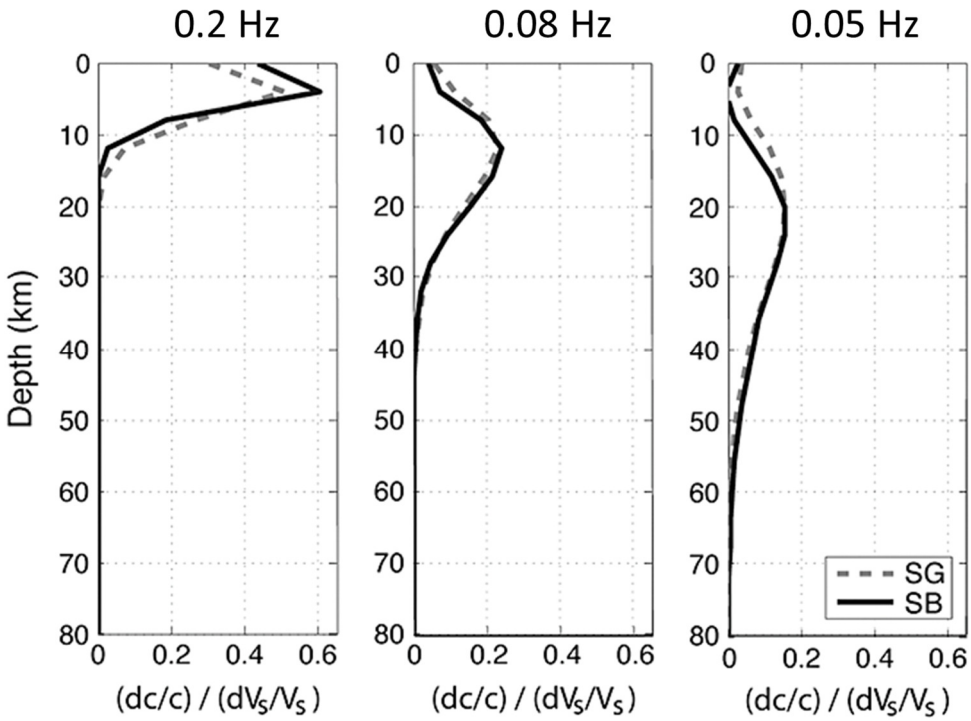


Fig. 2-12: Sensitivity of the Rayleigh phase velocity c to a shear velocity perturbation $dV_s$ in Wenchuan region, for different frequencies, highlighting the dependence of the depth of investigation to frequency. SG and SB correspond to two different sites. From (Froment et al., 2013).

Scattered body waves can propagate much deeper than the sensitivity depth of surface waves, and therefore be sensitive to deeper material. Their sensitivity depth depends mostly on the observed time window in the coda (late times correspond to waves that traveled deep in the subsurface). But it also depends on the inter-station distance, on the velocity of the medium and on its scattering properties (which in turn depends on the wavelength/frequency). All these parameters are mutually dependent, for example increasing the inter-station distance will necessarily require to increase the time window.

A sensitivity depth has been modeled by Obermann et al., (2013b) (Fig. 2-13) to separate the contribution of surface waves (in red) and body waves (in blue) to the apparent velocity change $dv/v_{app}$ in response to a bulk velocity change $dv/v_{bulk}$ of a layer placed at a variable depth. The figure shows that surface wave sensitivity is quite shallow (approximately half a wavelength) compared to scattered body waves that travel at a much greater depth.

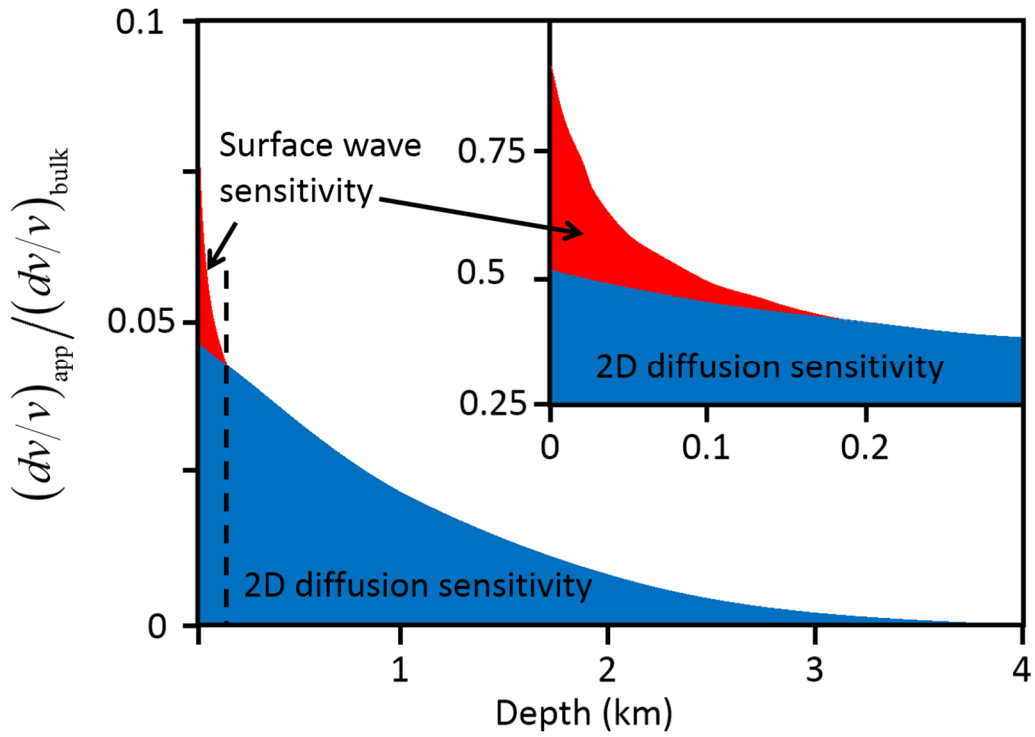


Fig. 2-13: Model of the apparent velocity response to a change of bulk velocity of a layer depending on its depth (layer thickness=200m, P-wavelength=340m, frequency=20 Hz, time window=2.8-4.4s). The surface waves are sensitive to changes near the surface (in red, up to approximately half the wavelength) and the diffused waves (in blue) are sensitive to much deeper changes (in blue) which mostly depend on the medium scattering and inter-station distance. Redrawn from (Obermann et al., 2013b).

The repartition between body and surface waves sensitivity depends not only on depth, but also on the choice of the time window, and on the scattering properties of the medium (Fig. 2-14). In early times, surface waves dominate, at late times bulk waves do. Medium scattering is expressed by the mean travel time/distance of a propagated ray before being scattered. Medium with a higher degree of heterogeneities means more scattered waves and smaller transport mean free time/path (Table 2-4). Surface-wave observation, and therefore short time window is preferred in shallow near-surface landslides. Ideally, constraining the limit of the time window would require to estimate the transport mean free path which is rarely measured. However in practice, the time window is set between the end of the high-amplitude direct surface waves, up to either 5–10 wavelengths or the limit before the CCF become too noisy. This favors the role of surface waves for our analysis on landslides.

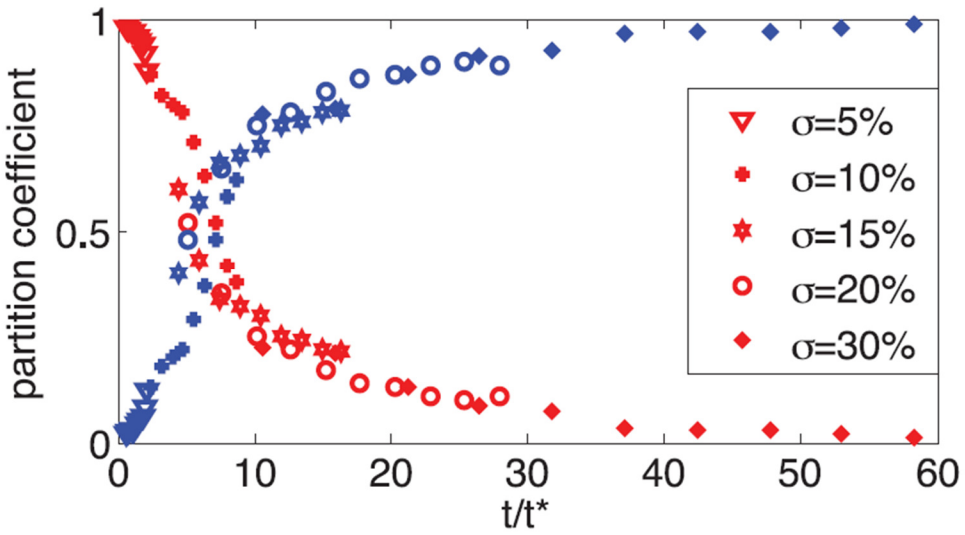


Fig. 2-14: Ratio between the surface waves (red) and body waves (blue) sensitivity, depending on the choice of the time window for a perturbed layer at a depth of 500 m. The time window is normalized by the transport mean free time $t^* = l^* / c$ , with $c$ the bulk wave velocity and $l^*$ the mean free path length between two scatterings which depends on the level of heterogeneity $\sigma$ . Surface waves dominate for the six mean free times. From (Obermann et al., 2013b).

Table 2-4: Scattering mean free path and transport mean free path calculated experimentally for models with different amounts of heterogeneity for the model presented in (Obermann et al., 2013b).

| Model | Scattering mean free path ($\ell$) | Transport mean free path ($\ell^\star$) |
|---|---|---|
| $\sigma$ = 5 per cent | 10 000 m ±10 per cent | 13 000 m ±15 per cent |
| $\sigma$ = 10 per cent | 2200 m ±7 per cent | 2700 m ±15 per cent |
| $\sigma$ = 15 per cent | 1200 m ±5 per cent | 1500 m ±10 per cent |
| $\sigma$ = 20 per cent | 900 m ±5 per cent | 940 m ±5 per cent |
| $\sigma$ = 30 per cent | 500 m ±2 per cent | 450 m ±3 per cent |

### 2.4.3 Stability, reactivity and signal-noise ratio

Processing the correlation function will face tradeoffs. The first tradeoff is between using defined strong sources or eliminating their contribution (Fig. 2-15). Cross-correlation interferometry was firstly applied to the coda (=late arrivals) of earthquake events, well localized in time. For continuous monitoring, repeated smaller sources are preferred such as small earthquakes, ice quakes, cars or artificial sources. However reconstructing a GF would require either a source aligned with the two sensors, perfectly distributed sources around the sensors, or a highly scattering medium (scatterers act as secondary sources). In practice these conditions are rarely respected. Nevertheless, an approximated but stable GF is sufficient for

monitoring (Hadziioannou et al., 2009). So using localized and often active sources requires to study and to select the sources to ensure their stability (stability in position, not in time). Another approach is to use only diffuse and weak sources, which are scattered multiple times before arriving on the sensor. Scattered sources will ensure a better spatial repartition of the pseudo-sources (scatterers should be surrounding the sensors) as well as a better stability (underground scatterers rarely move). In practice, scattered pseudo-sources are continuous in time but with low amplitude, as opposed to short-time events with strong amplitude. Events can be removed from the traces or shrunk by clipping it to a maximum value, such as 3 or one-bit reduction (Larose, 2004). Such process will strongly increase the contribution of scattered waves (very stable) and continuous weak sources (often stable) and improve the source stability. Clipping provides stable correlations and fits well with an automatic processing.

Similarly, waves that travel between two sensors are either direct or scattered, corresponding in the correlation to early and late arrivals, respectively. Direct waves are more energetic, but again, depend on the source directionality and would be more impacted by a minor change of the soil at the surface just between the sensors, such as a crack (Fig. 2-15). The emergence of scattered waves in the correlation again requires a better signal-noise ratio and a longer time of observation, but provides more stability. Furthermore, velocity variations is easier to measure with long coda of scattered waves (10+ wavelengths) than with early arrivals, for two reasons. First, computing velocity variations over several wavelengths instead of using only one maximum estimation is more accurate and resilient to noise. Second, the direct waves arrive very close to t=0 for sensors installed at short distance, so an error on the estimation of $dt$ is manified when computing $dt/t$.

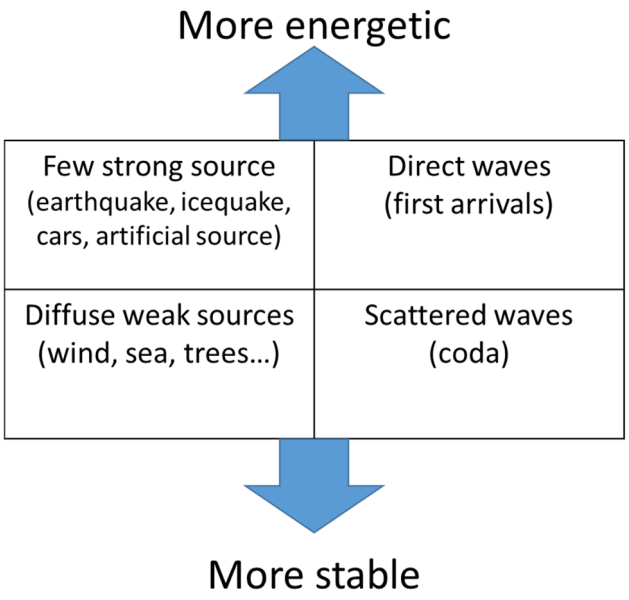


Fig. 2-15: Tradeoff between stability of the GF and its level of energy.

Improving the correlation stability requires longer recording times to balance the low signal amplitude, which deteriorates the time resolution of the method. On a landslide, correlations are typically computed every hour and then averaged over 24h to improve the signal-noise ratio and to eliminate daily variations due to source and subsurface variations. 24-hour averaging appears sufficient for detecting $dv/v$ variations of the order of a few percent (see Fig. 2-7). Still, that may not be sufficient for a landslide early-warning system. A shorter resolution, such as hourly, would strongly increase the effective lead time (precursory signals are often required for redundancy before making a warning). However that would require handling daily cyclic variations of potentially several % (Fig. 2-8) and working with noisy correlations. To handle the daily variations, we propose first to continue averaging correlations over 24h, but using an hourly moving window to increase the resolution without affecting the stability of the CCF. To be more reactive, daily variations could be handled by comparing correlations at the same time of the day between different days, as a variant of the method used in Richter et al. (2014). Noise reduction could be operated by using the SVD-Wiener filter introduced by Moreau et al. (2017) that exploits the coherence from one correlation to the other, in order to remove the noise that is not coherent between correlations.

The reference CCF chosen to compute the *dv/v* affects the reactivity to detect strong variations. Most studies use the average correlation over the whole investigated period or over a stable period. Averaging ensures weak noise and reference uniqueness ensures coherence between all the computed *dv/v*. However, strong changes of the sources or propagating medium over time would result in a loss of coherence compared to the averaged reference, and therefore prevent the good quality of the measured *dv/v*. On permafrost for example, the melting strongly alters the correlation over time. In that case, computing the reference over a moving window averaged over 3 to 10 days allows resolving large velocity variations (James et al., 2017), at the cost of a lower signal-to-noise ratio and a long-term drift (easily compensated). In extreme cases, the *dv/v* can be computed between every possible couple of dates $i, j$ from the same sensor, resulting in a 2-D grid of $\delta v_{i,j}$. The optimal 1-D time series of $\delta v_i$ is then inverted to minimize every $\delta v_{i,j} = \delta v_j - \delta v_i$ and provide a *dv/v* time series that best fits the grid (Brenguier et al., 2014; Machacca et al., 2019, 2017). A comparison with the standard stretching technique is provided in Fig. 2-16. The inverted dv/v is tested with different inversion parameters $\beta$. This parameter is the characteristic length of correlation between the model parameters. The choice of $\beta$ will either smooth the *dv/v* time series or provide a higher temporal resolution with stronger variations. This technique compensate for the higher noise by the matrix inversion. It allows detecting rapid changes by comparing correlations that are close in time. It gives a lower weight to the couples that have a low coherence. And the method resolves the problem of drift that exists when using a moving-window reference, by comparing also correlations that are distant in time. This results in a better reactivity/stability tradeoff on landslides, at the cost of a higher computational complexity and cost.

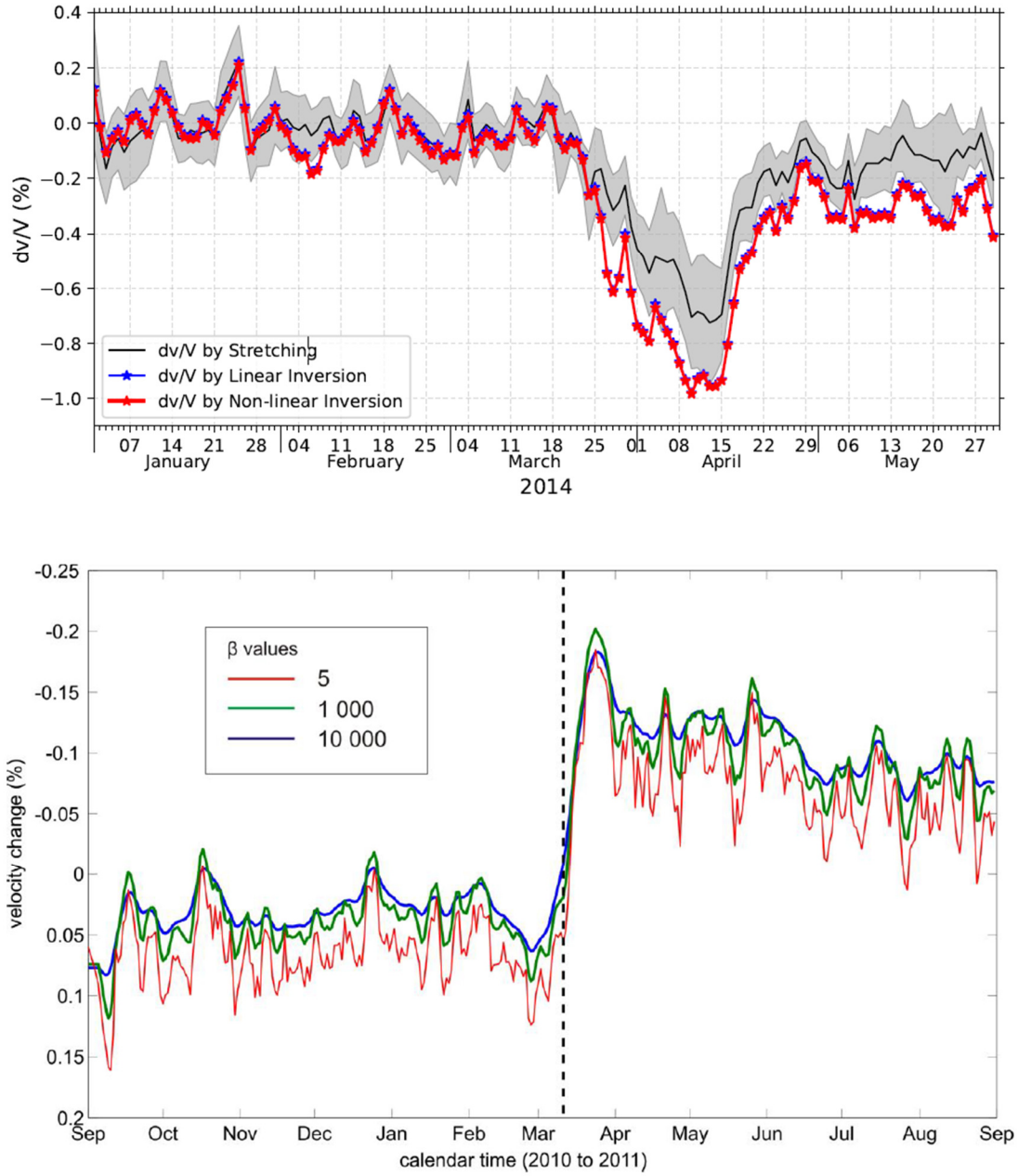


Fig. 2-16: (top) Comparison of an inverted *dv/v* time series with the standard stretching method, and (bottom) different time series obtained, depending on $\beta$ the characteristic length of correlation between the model parameter $\delta v$. From (Machacca et al., 2017) and (Brenguier et al., 2014, supp. material), respectively.

### 2.4.4 Assessing the uncertainty

Estimating *dv/v* uncertainty would increase the reliability of a warning system. Lower coherence coefficients between the CCF and the reference or between each pair of CCF (Fig. 2-17) are often used to discard meaningless *dv/v* computations. However, deciding the coherence threshold that discard couples of *dv/v* (often 0.6) is a rough and approximate process. Furthermore, precursory drops of *dv/v* were shown to be accompanied by a drop of coherence (Fig. 2-2.b), and lower coherence

could be a precursory signal in itself (Fiolleau et al., 2018, in preparation). Therefore, correlation coherence should instead remain as a valuable indicator.

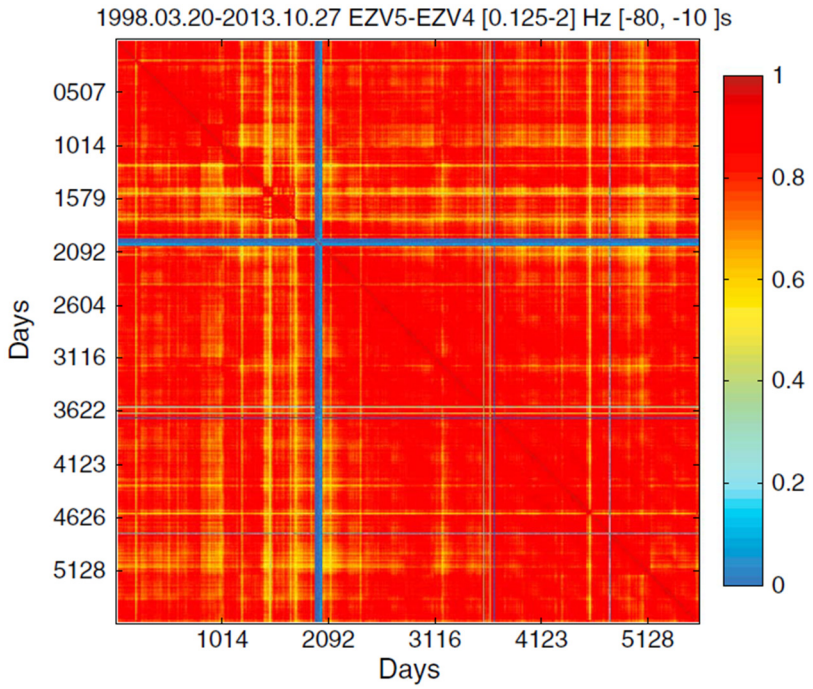


Fig. 2-17: Matrix of coherence coefficient between different every possible combination of correlation on the same sensor for 15 years at Merapi Volcano. The correlation coefficients < 0.6 were discarded. From (Lesage et al., 2014).

A mathematical approach was introduced to compute an error based on the maximized correlation coefficient $CC(dv/v)$ between the stretched and reference correlation. The error also depends on frequency bandwidth $1/T$, on the time window [$t_1, t_2$], and on the central pulsation $\omega_c$ (Weaver et al., 2011):

$$rms\left(\frac{dv}{v}\right) = \frac{\sqrt{1-CC(dv/v)^2}}{2CC(dv/v)}\sqrt{\frac{6\sqrt{\frac{\pi}{2}}T}{\omega_c^2\left(t_2^3-t_1^3\right)}} \quad (2\text{-}4)$$

More empirically, the *dv/v* can be computed for different configurations (e.g., multiple time windows and/or multiple sensor pairs) in order to extract their average, standard deviation or probability density function. For the best possible robustness, both approaches should be combined. The averaging approach would increase the robustness but would also reduce the impact of a precursory signal that would be localized only on one pair of sensors. Therefore, warning threshold should be set on the average *dv/v* value, the statistical standard deviation over multiple pairs or time windows, and the *rms* computed from the *CC*, all at the same time.

# Chapter 3
# Measuring ground motions with passive RFID

**Contents**



## 3.1 Principles of passive RFID

Billions of passive targets, or tags, are produced by the RFID industry every year (Das, 2017) to identify goods remotely. That led to numerous research and business applications (Ngai et al., 2008; Tzeng et al., 2008). Technically, the technology relies on a forward and backward communication between a reader and a tag (Fig. 3-1). During the forward link, a reader emits a radio-frequency carrier wave towards a tag. This wave creates a current in the tag antenna that powers its electronic circuits. The wave can contain data to give instructions to the tag. During the backward link, the tag modifies the wave by load modulation to send back its own identification data to the reader.

Passive RFID tags are often replacing barcode optical identification. Their main advantage is to be readable even without direct optical line of sight and under different orientations. Their major disadvantage is their higher cost per tag (0.01-10€) than barcodes. However for earth science this cost is negligible, and several orders of magnitudes below conventional sensors.

The different categories of passive tag are presented on Fig. 3-2, and illustrated in Fig. 3-3. We firstly separate them by the logic that store and restitute their identifiers. Chipless tags do not contain electronic chips and restitute their identifier

directly through physical means, using for example electromagnetic resonators or electroacoustic conversion (Preradovic and Karmakar, 2010). However this study focuses on tags with chips, which represent by far the largest RFID production today. Tags with chips have several advantages. For example, they are easily reconfigured, can store large identifiers, and comprise anticollision algorithms to read hundreds of tags in the same zone. Mostly, these are produced on a large scale which allows for buying commercial reliable devices and use interoperable standards.

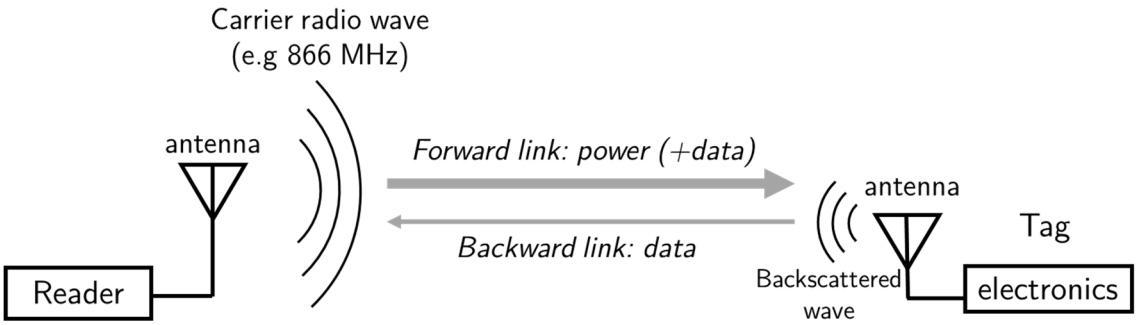


Fig. 3-1: General principle of reading microwaves backscattering RFID tags

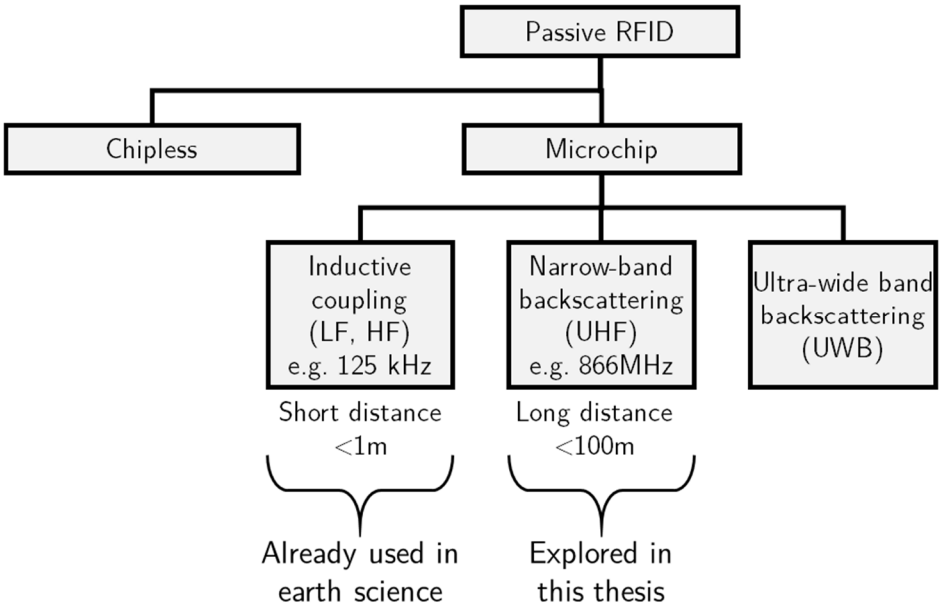


Fig. 3-2: Major categories of passive RFID tags.

Chip tags can then be categorized on their electromagnetic communication: magnetic coupling and narrow or wide band backscattering. At lower frequency (125 kHz–13MHz), the tags communicate with magnetic coupling with the reader.

Except for the data communication, the physical principle is similar to metal detectors and Slingram geophysical method. The power of this communication decreases rapidly with the distance, and this technique is commonly used at distances well below the wavelength.

The backscattering communication (Stockman, 1948; Koelle et al., 1975) allows reading tags at distances of several wavelengths. The propagation principle is the same as for radars. The mainstream tags use standardized communication protocols (*EPC Gen2*, 2015) operated at UHF microwave frequencies. Today, the devices in Europe use the 865–868 MHz frequency band (recently expanded 915–921 MHz) defined by regulations (*ETSI-EN 302-208*, 2016).

UHF tags provide multiple advantage to be deployed for years over large remote areas, which is a classical context of earth sensing. First, the low cost of the tag (0.01-20 €) allows for deploying numerous tags with very small budget restrictions. A station costs 1–10 k€, which is comparable to the cost of one single conventional instrument (i.e., differential GPS, long-range extensometer). Second, anticollision protocols allow identifying hundreds of tags present in the same zone (*EPC Gen2*, 2015; Klair et al., 2010). The tags are interrogated one by one at a rate of 30 to 800 tags per second (1–30 ms per tag). Third, the tags do not have a battery (or can comprise a battery assistance that lasts 10+ years) and can remain functional for several years at the same location with minimal maintenance. That can be useful for earth observation, where several years or decades of data are often useful, but sensor maintenance across this timescale is often problematic.

An RFID system can provide data about the detection of a tag in a large zone, a tag location or displacement, and the sensing of the tag environment. The classic usage of RFID is to detect the presence of a tag in a zone, remotely. That can give a rough estimation of the tag localization. Precise localization of a tag is still a topic of research. It can be useful for measuring ground displacements, which is used in this thesis. Lastly, tags can provide sensing capabilities. Sensing is made either with a dedicated sensor, or using a tag antenna that is sensitive to its near environment. In this thesis, sensing data is secondary compared to displacement data. But it could be used as a primary data.

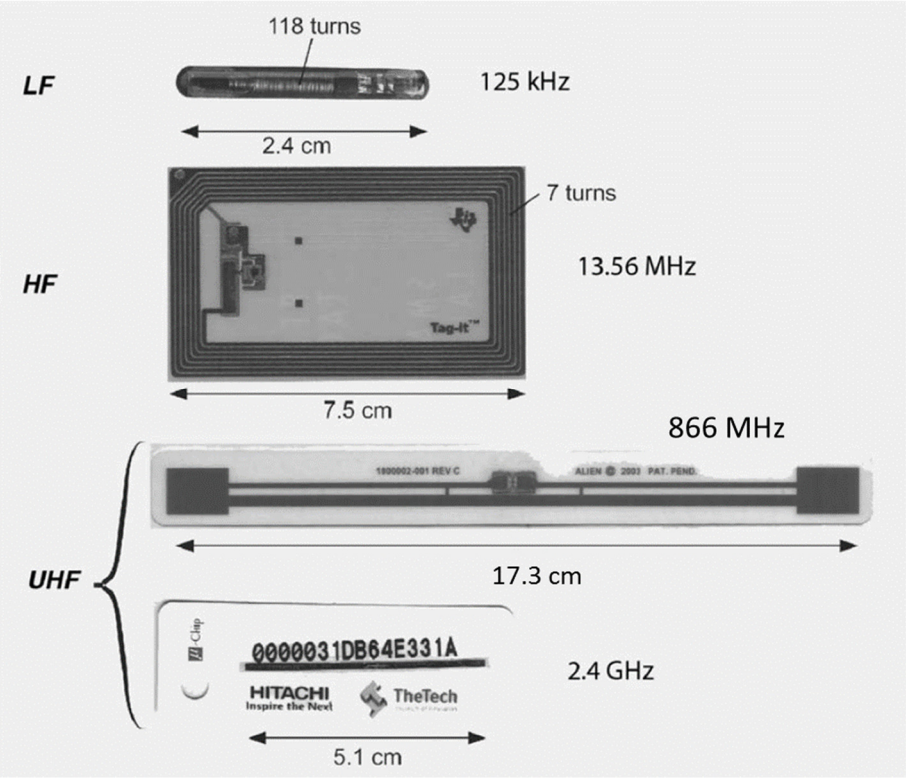


Fig. 3-3: Examples of tags and antennas that operate at different frequencies. At low and high frequencies (LF/HF), tags use coil antennas that are interrogated by inductive coupling at short distances. At higher frequencies, UHF tags are interrogated using propagation at large distances. Modified from (Dobkin, 2008)

## 3.2 Measurement of ground motion

### 3.2.1 Manual tag detection (125 kHz)

RFID tags were firstly used in earth science to manually trace the displacement of sediments in a river. The sediment position was determined by manual surveys. Gravel and pebble heavy sediments are moved by rivers through a process called bedload. To obtain in situ experimental data on this bedload process, researchers have deployed gravel-like particles with controlled sizes in rivers, and traced their displacement. Methods used in the past had several constraints: painted particles could not be recovered once buried, magnetic particles could be detected underground but their identification required to excavate them. Active radio-frequency tracers greatly improved the recovery and identification. But they were more expensive (problematic when deploying 1,000+ particles), could not trace small particles due to their large size, and their usage was limited in time by their battery.

River investigations using passive tags (also called PIT for passive integrated transponders) have then been introduced to track sediments in rivers (Lamarre et al., 2005; Nichols, 2004). Their small size, small cost, and ability to be identified

underground (up to 0.5 meters) proved useful for such studies (Fig. 3-4). Since then, the technique has been used for numerous riverine applications (i.e., Bradley and Tucker, 2012; Lamarre and Roy, 2008, 2008; Liébault et al., 2012). These applications were reviewed by Chapuis et al. (2014), and Piegay et al. (2016) specifically for large rivers. Many new riverine applications have emerged since these reviews (Bradley, 2017; Dell'Agnese et al., 2015; Dépret et al., 2017; Mao et al., 2017; Olinde and Johnson, 2015; Plumb, 2017; Rainato et al., 2018; Raso, 2017).

RFID tags were also used to trace wood sediments transportation by rivers (Kim et al., 2006; MacVicar et al., 2009; Ravazzolo et al., 2013; Santos et al., 2014; Schenk et al., 2014; Jochner et al., 2015; Allen et al., 2015) and coastal sediments (Allan et al., 2006; Benelli et al., 2009; Curtiss et al., 2009; Bertoni et al., 2010; Dickson et al., 2011; Miller et al., 2011; Osborne et al., 2011; Bertoni et al., 2013; Ford, 2014).

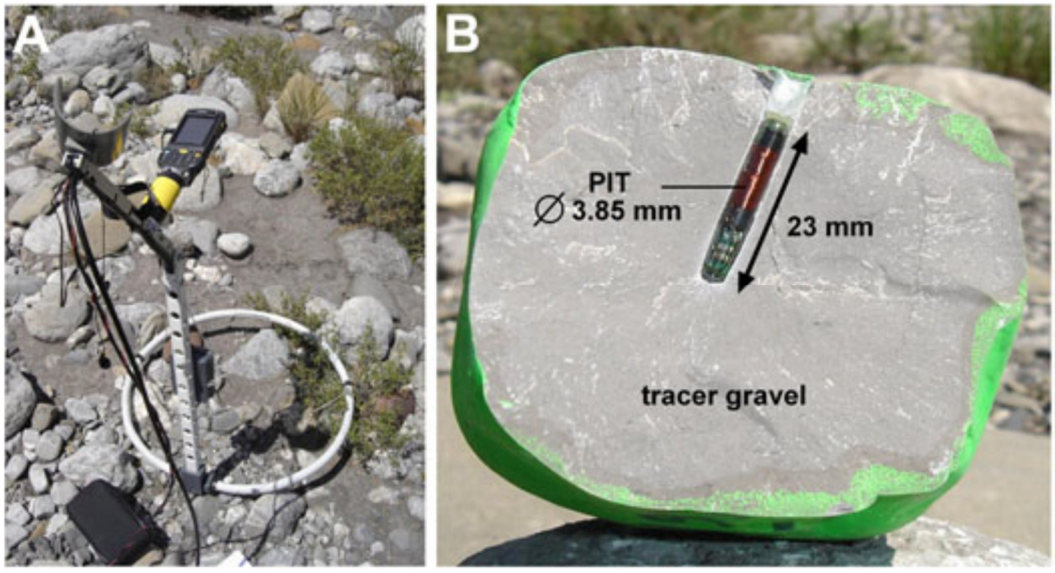


Fig. 3-4: (a) RFID detection system manually moved along the river bed (b) stone marked with an RFID (or PIT) tag. From (Liébault et al., 2012).

Other interesting application include monitoring sediments near engineered structures, such as dam walls (Gilet et al., 2018; Shahmirzadi et al., 2016), bridges (Lauth and Papanicolaou, 2008) or flow deflectors (Biron et al., 2012; Carré et al., 2007). It has also been used to study geohazard processes such as tsunami (Goseberg N. et al., 2016), floods (Rainato et al., 2018) or debris flow (Graff et al., 2018). Unusual contexts include frozen rivers (Tremblay et al., 2014), and sediments moved by… rodents (Amundson and Reed, 2009).

The scale of these studies, particularly the riverine studies, has increased in time, space and number of sensors. Today, studies reach 1000+ tags deployed for several years. That provide large and useful data (for example on Fig. 3-5), but recovering tags manually over large zones is tedious. A single survey can take weeks to operate, which strongly limits the time resolution of the data.

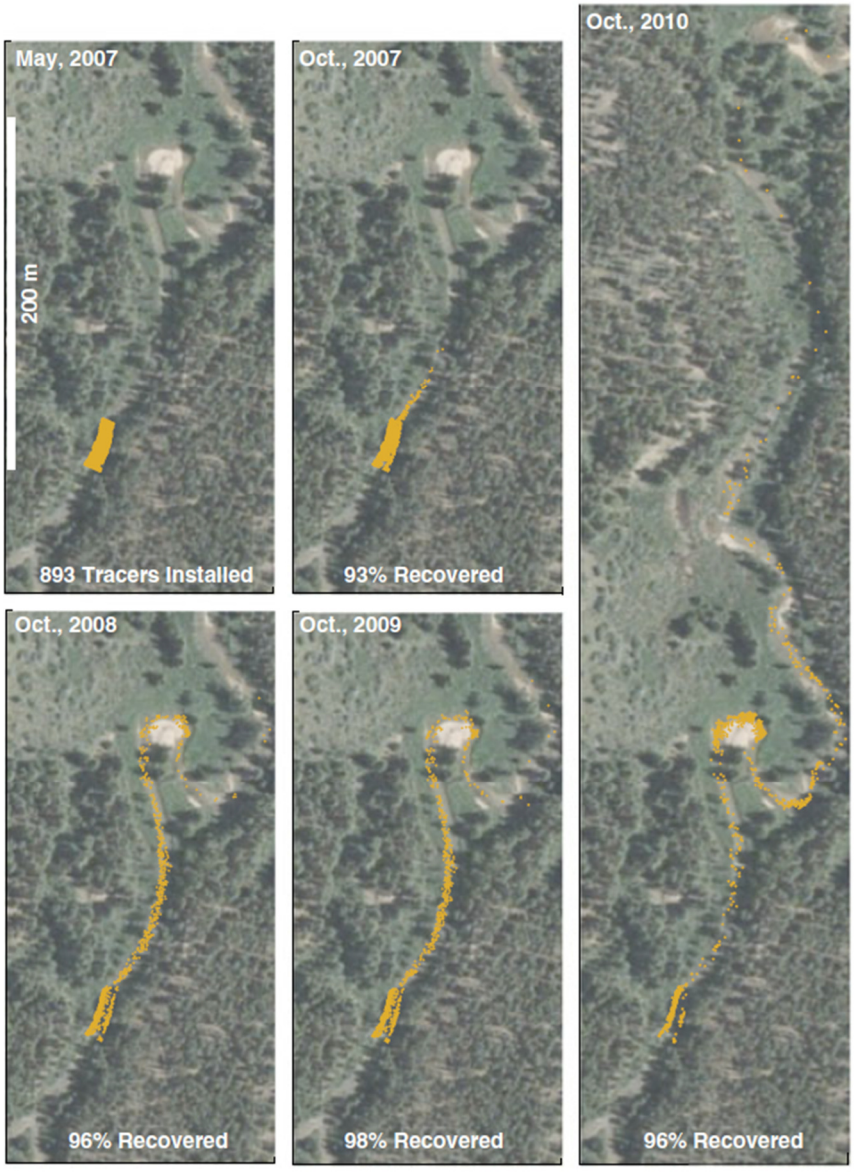


Fig. 3-5: Displacement of 893 RFID tracers for 3 years, over 200-meter large area. From (Bradley and Tucker, 2012)

### 3.2.2 Automatic detection with a fixed station (125 kHz)

To detect tags at a high temporal resolution, Schneider et al. (2010) proposed to install a semi-permanent station in a river. They installed a large coil antenna on the river bed, that would automatically detect a tag passing near this antenna (Fig. 3-6). This has been later been used in mountain streams (Olinde, 2015) (Mao et al., 2017), to track wood debris in urban waterways (Allen et al., 2015). This technique provided high-resolution data, but at a very low spatial resolution (tags were detected only when passing near the station). This spatial resolution was slightly increased by combining several stations (Hufnagel, 2016), (Mao et al., 2017). Two stations allowed computing at least an average velocity between the stations, and more stations provided it with a better resolution.

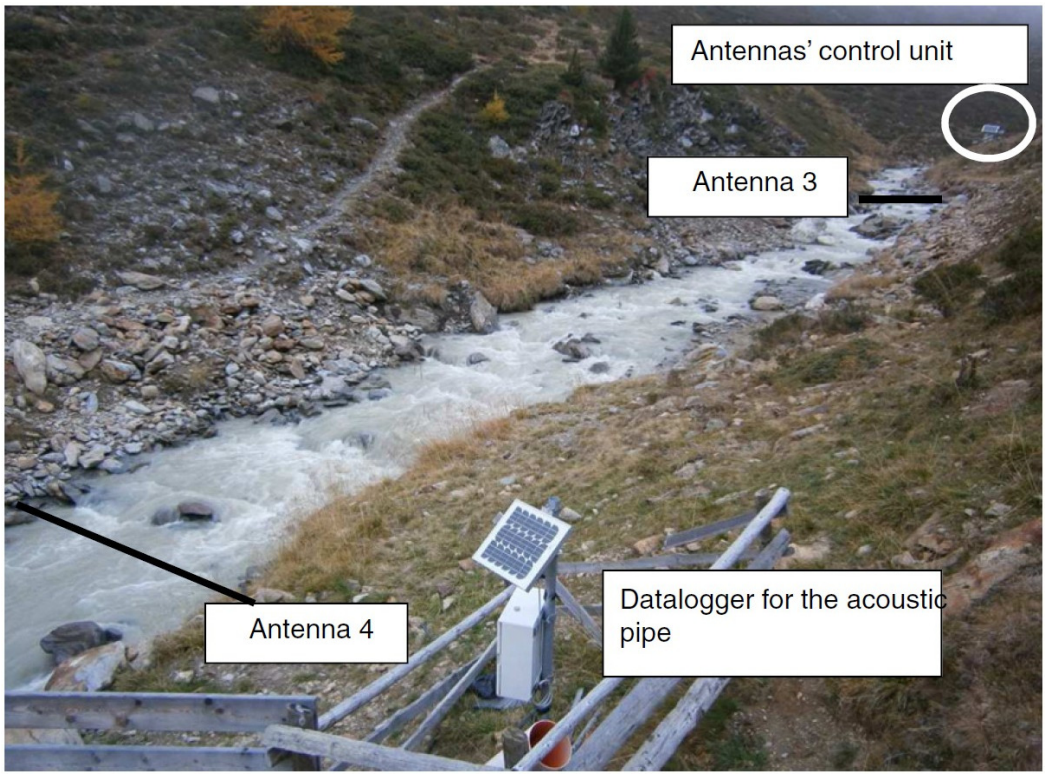


Fig. 3-6: Stationary antenna loops installed within the river, from (Mao et al., 2017).

The transport of sediments by rivers is not linear in time. It typically alternate between quasi-static position and rapid motion, for example during a flood. But fixed stations or manual surveys only allow for computing an average velocity, from the data between two surveys or between two stations. To better understand the dynamics of these displacements would require to combine both a high temporal and spatial resolution. That could be done by combining the high time resolution of fixed stations, with the much larger reading range of UHF tags (10–100 m). That

has been done with 433 MHz active tags (Cassel et al., 2017). However, active tags have the inconveniences of higher costs and shorter life due to their battery consumption, already discussed. Passive tags at 866 MHz have recently received preliminary investigations for riverine tag detection, particularly concerning underwater usage or interrogation from a drone (Tedjini et al., 2015) but no results were published. The technical challenge of underwater interrogation is not a problem for an application on a landslide. Furthermore, landslide move typically by a few centimeters to a few meters per year, which do not need a drone to be interrogated, and should fit very well for being interrogated from a fixed station. But measuring a slow displacement requires a high accuracy for tracking tag location. Fortunately, high-accuracy localization techniques have been developed in the last years by RFID researchers.

### 3.2.3 Long-range localization using the phase (866 MHz)

The localization of passive RFID at frequencies near 900 MHz has been subject to many research (Miesen et al., 2011). These methods usually estimate the 1D range or displacement between a tag and a station antenna, and optionally locate the tag in 2D or 3D using multiple station antennas. These ranging techniques are based on the Received Signal Strength (Griffin and Durgin, 2009; Ni et al., 2003), the Phase Difference of Arrival (Vossiek and Gulden, 2008; Nikitin et al., 2010) or more recently the Time of Flight (Arnitz et al., 2010; Arthaber et al., 2015). Currently, phase-based methods are compatible with commercial readers and offer the best accuracy. Several studies used the phase to localize tags with the accuracy of one centimeter or less (Scherhäufl et al., 2015; Wang et al., 2016; Zhou and Griffin, 2012).

The principles of phase difference of arrival (that we will simply call "phase") is illustrated in Fig. 3-7, in the complex In-phase/Quadrature plane. The continuous wave emitted by the reader is radiated through an antenna. The wave $\mathbf{V}_{\text{channel}}$ represent the wave backscattered by the enviroment and instruments back by the reader, and $\mathbf{V}_{\text{tag}}$ represents the additional contribution of the interrogated tag. The total wave received by the reader is then the sum of $\mathbf{V}_{\text{tag}} + \mathbf{V}_{\text{channel}}$. Under the hypothesis of a stable environmental response $\mathbf{V}_{\text{channel}}$ during the time of an RFID message (typically 1–30 ms), the changes in the wave received by the reader is mostly controlled by the tag contribution $\mathbf{V}_{\text{tag}}$. During that time, the interrogated tag alternates its load impedance—and therefore the wave backscattered by its antenna—between two states (data 0 and 1) to include data in the backscattered

wave. This alternation is detected in the whole wave received by the reader (channel + tag) to read the tag identifier. The phase $\varphi_{measured}$ and amplitude $A_{measured}$ of this alternation can also be retrieved. With a stable environment, a constant phase shift induced by the tag modulation between $V_{tagData0}$ and $V_{tagData1}$, and a fixed tag and reader antenna in space, the phase and amplitude remains constant. A modification of the tag–reader distance would induce a phase variation , that we will commonly call *phase* for convenience. Both the signal phase and amplitude can be used for localization purpose.

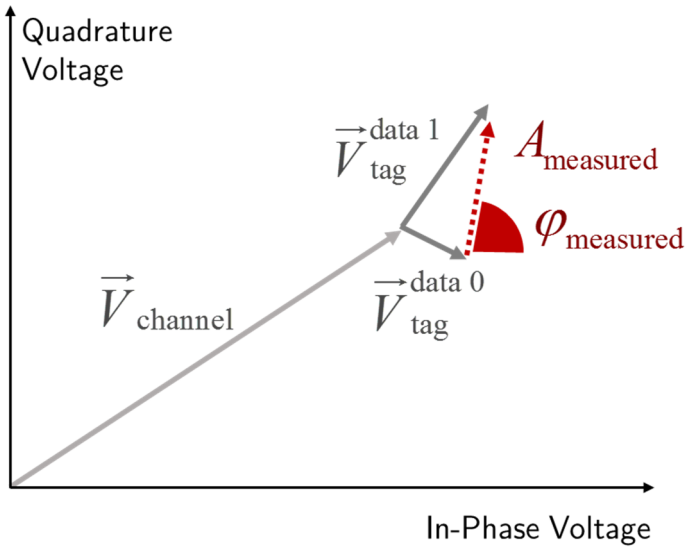


Fig. 3-7: Total backscattered signals received by the reader in complex representation. The phase $\varphi_{measured}$ and amplitude $A_{measured}$ is measured from the modulated signal of a message backscattered by one tag. The voltage from the environment channel is supposed to be stable during this message.

The relation between the phase variation $\delta\varphi$, the displacement $d$ and the relative radial displacement $\delta r$ is illustrated in Fig. 3-8. The relative radial displacement $\delta r$ of a backscattering tag can be computed in free space using (Nikitin et al., 2010):

$$\delta r = -\frac{v}{4\pi f}\delta\varphi \tag{3-1}$$

Where $v$ represents the velocity of the wave ($\approx 2{,}998 \times 10^8$ m/s in the air) at the central carrier frequency $f$ (typically 866 MHz). This technique was never applied outdoors on large range and long times, and such usage may pose some challenges.

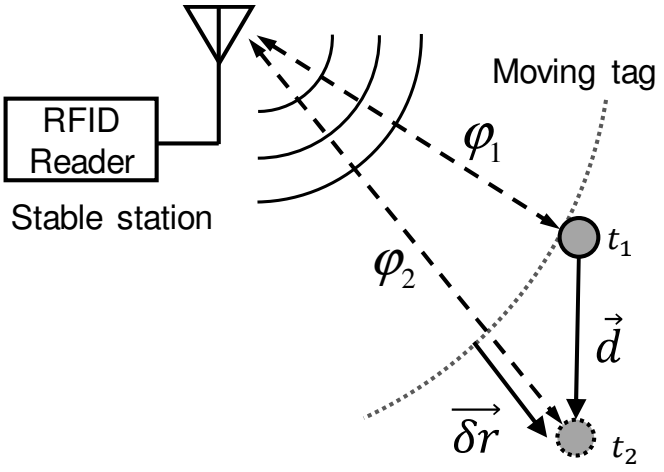


Schematic representation of how tag displacement is tracked by a station. The phase variation measures the radial displacement **r** between two acquisitions.

## 3.3 Challenges

### 3.3.1 Wide areas: drone and long-range tags

Earth science requires data over wide and wild areas. That is a major challenge for RFID applications. Surveying large areas manually consumes a lot of time. Frequent surveys would be very expensive and cannot be afforded. That severely restrains the temporal resolution of the data. Semi-automatic surveying would allow for more frequent surveying with fewer efforts. The usage of Unmanned Aerial Vehicles (drones) is increasing rapidly to evaluate landslide deformations (Casagli et al., 2017; Lucieer et al., 2013; Niethammer et al., 2012). New developments are being made to read tags from UAV (Casati et al., 2017; Greco et al., 2015a) and localize tags accurately (Buffi et al., 2017). Yet, even semi-automatic reading would not provide a high enough temporal resolution for operational landslide early warning.

Permanent monitoring stations could provide a high enough temporal resolution for an operational early-warning system. Wild and harsh conditions pose technical difficulties for permanent station, which require complicated remote maintenance. A common problem comes from the instrument powering. Robust and low-consumption material is highly advised to overcome this technical difficulty. Wide area is a major challenge, due to the limited reading range of fixed stations. With 125 kHz magnetic coupling tags, this range hardly above one meter, and only allows for detecting a tag passing very close to the station antenna. At 866 MHz, the wave propagation allows for reading a tag at larger distances. The range is mainly limited

by legislation that limits the maximum emitted power within given bandwidths (*ETSI-EN 302-208*, 2016). Constructors provide material adapted to these limits. Commercial devices allow a reading range typically up to 10 meters, and claim to reach up to 60 meters with high sensitivity tags (but that may be enthusiastic, see appendix 3). This reading range is increasing with technological improvements. Today, the technical limitation of the range is usually the tag sensitivity. Research literature states range above 100 meters and even 1 kilometer using high-sensitivity tag chip. However, these chips are not standard nor produced commercially yet. The range can be increased using standard tag chips with custom directive antennas. However that requires large antennas, that would strongly increase the cost of the tag and allow its interrogation only in a given direction. Such tags would be contradictory to the needs of RFID mainstream applications, and are not available commercially.

### 3.3.2 Environmental influences and sensing

Tags are also sensitive to their environment. That is exploited for sensing applications, but could create problems for their usage outdoors. The sensing can be realized with dedicated sensors (in that case the tag serves as a powering source and communication medium). Standard commercial tags can also be used as sensors, by exploiting the influence of the environment on the tag antenna. The environment can influence the received power (related to the signal amplitude $A$ in Fig. 3-7) (Occhiuzzi et al., 2013). The influence of environmental factors on the received power can be problematic because a too low power would not allow reading the tag. Such influence should be reduced as much as possible. A change in the tag antenna properties would also influence the phase ($\varphi$ in Fig. 3-7). Such influence is less problematic for general RFID usage and allows for a more accurate sensing with fewer constraints than using the received power (Caccami et al., 2015). However it is highly problematic when monitoring the displacement of the tag using the phase. Another approach was proposed very recently to estimate the change of antenna impedance, by directly measuring the change of tuning frequency using self-tuning tags (Caccami and Marrocco, 2018). The measurement of this detuning would be independent from the tag position. It can provide an indication of the antenna parameters change, more accurately than any other antenna-based technique. This measurement could also be used to correct for environmental influences on the phase, as all these measurements are related (Grosinger et al., 2016).

There are numerous applications of antenna-based sensing (Occhiuzzi et al., 2013). These can be improved by using specific sensing materials (Amin et al., 2014b; Caccami et al., 2015). Applications include the measurement of temperature (Manzari et al., 2014a; Occhiuzzi et al., 2018), humidity and moisture (Manzari et al., 2012), pH or gas, light (Amin et al., 2014a), biochemical sensing (Croux et al., 2013; Yuan et al., 2015; Caccami et al., 2015; Caccami and Marrocco, 2018; Manzari and Marrocco, 2014; Manzari et al., 2014b), proximity to objects (Batchelor et al., 2014; Vera et al., 2016). Structural health monitoring (Zhang et al., 2017) applications include sensing strain, crack (Caizzone and DiGiampaolo, 2015) and corrosion. Applications of particular interest for sensing soil moisture (Pichorim et al., 2018; Aroca et al., 2018), 1-bit vibration sensing (Occhiuzzi et al., 2010; Todd et al., 2009; Vora et al., 2015), vibration sensing with an integrated sensor (Jayawardana et al., 2016).

Two conclusions are drawn from these sensing applications. Firstly, they could provide an interesting way for sensing the earth over several years with a large number of low-cost and batteryless sensors. Secondly, the variations of environmental influence factors such as temperature and humidity could create environmental drift when measuring the displacement of tags outdoors for long periods using their phase.

## 3.4 Conclusion

RFID has a strong potential for observing the earth over large areas and for long times. It has been already used for tracking sediment transportation in rivers and on the coasts, using inductive coupling tags (125 kHz) interrogated at short ranges (<1 m). Their detection with manual surveys provided data at a high spatial resolution, and their automatic detection with a fixed station provided data at high temporal resolution. To accurately observe the displacement velocity would require both a high spatial and temporal resolution. For this goal, we suggest deploying passive backscattering tags (866 MHz) on a moving landslide, and interrogating them automatically from a fixed station installed on stable grounds. Their displacements would be estimated using phase measurement. The technique may be limited by its reading range to work over large areas, and by potential environmental influence factors, such as temperature and moisture, studied in the next part.

# Part 2 — Environmental influence on RFID

# Chapter 4
# Influence of water and temperature on RFID

*Published as Le Breton, M., Baillet, L., Larose, E., Rey, E., Benech, P., Jongmans, D., Guyoton, F., 2017. Outdoor UHF RFID: Phase Stabilization for Real-World Applications. IEEE Journal of Radio Frequency Identification 1, 279–290. https://doi.org/10.1109/JRFID.2017.2786745*

*The discussion section (1.6) has been added after publication, thanks to the thesis reviewers suggestions.*

## Contents



## 4.1 Summary

The present study investigates meteorological factors that affect the phase of RFID passive tags at 868 MHz, in outdoor conditions. The study identifies the effect of water on the tag and base antennas, the effect of temperature on the cables,

tags, and base antenna, the effect of the tag support moisture, and the effect of atmospheric conditions on wave velocity. Combined, these effects could lead to over 8.1 radians phase drift over a year, in a typical environment. In a tag location tracking application, that would correspond to an error of 22 centimeters. This article proposes techniques to correct these effects and to increase the phase stability. These techniques are applied to a new RFID system, which is tested in outdoor conditions, for five months. The new system optimize the material used, and makes numerical correction based on temperature and humidity measurements. It improves the phase stability for rainy days, dry days, and long-term drift by a factor of 3, 12 and 5 respectively. After corrections, the long-term drift was reduced to below 0.05 radians per month; the equivalent to 1.5 millimeter per month, which is within the acceptable boundary of 1 cm for the targeted landslide application.

## 4.2 Introduction

Backscatter tag radio-frequency identification (RFID) techniques (Heidrich et al., 2010) have considerably developed in the last decade, by adding location tracking (Miesen et al., 2011) and environment sensing (Marrocco, 2010) capabilities.

We aim to track low-cost tag location for monitoring the stability of structures prone to slow motions, such as landslides, volcanoes, and civil infrastructures. Those structures typically move from a few centimeters to a few meters over a year, requiring an accuracy of ten centimeters or less per year. There are already solutions on the market, such as GPS (Gili et al., 2000), optical laser (Abellán et al., 2009), photogrammetry (Travelletti et al., 2012), radar interferometers (Herrera et al., 2009), or radar nodes (Kenney et al., 2009). However, passive RFID tags offer a lower-cost alternative in terms of installation and maintenance. Real-time monitoring of tag grids would provide dense data, both in space and time, at reasonable cost.

Most location techniques are based either on the received signal strength indication (RSSI), or on the phase shift (Nikitin et al., 2010). Phase variation measurement is more accurate than RSSI and less perturbed by geometric parameters (tag height, polarization angle, antenna orientation). Phase-based tag location techniques (Nikitin et al., 2010) are claimed to reach centimeter to millimeter accuracy, when combined with multiple frequencies (Zhou and Griffin, 2012), signal strength and accelerometric data (Akbar et al., 2015a), a synthetic aperture moving antenna

(Miesen et al., 2013a), a moving tag with multiple antennas (Wang et al., 2016), and multiple tags and antennas (Scherhäufl et al., 2015).

In RFID sensing, the tag is equipped with a sensor, but the analog to numeric conversion is realized either at the tag level when it has a dedicated sensor (Want, 2004), or by the interrogator when the sensed data is within the backscattered wave properties (Occhiuzzi et al., 2013). The former is more accurate, whereas the later keeps simpler electronic circuits and consumes less energy. In this last case, the tag antenna itself acts as a sensor, and modifies the properties of the backscatter link. This modification is measured by the reader through signal strength, tuning frequency or phase. Phase-based sensing is recent and has the advantage of not necessarily deteriorating the signal strength, which improves the tag reliability, reading distance, and resolution. It has been used for sensing crack opening (Caizzone et al., 2014) and air humidity (Caccami et al., 2015).

Phase-based experiments from existing literature were conducted indoors or lasted less than one hour. In such conditions, the phase offset $\varphi_0$ is assumed constant and removed from measurements through calibration. However, during long, outdoor experiments (typically from days to months), meteorological variations may cause significant phase offset drifts. Such drifts should be removed for location and sensing applications.

Literature on outdoor tag location includes locating objects on a construction field (Song et al., 2007; Razavi and Haas, 2011; Valero et al., 2015; Li et al., 2016; Valero and Adán, 2016), locating tags in rivers (Chapuis et al., 2015; Miller et al., 2011; Tsakiris et al., 2015), glaciers (Rorato et al., 2014), and landslides (Lucianaz et al., 2015), testing a location method on a roof (Akbar et al., 2015b), and tracking motions of a person (Polivka et al., 2009), a train (Yang et al., 2015), or an unmanned aerial vehicle (Greco et al., 2015b).

Existing literature shows environmental variations as either parameters that are measured, sources of energy loss, or sources of device deterioration. From this study's point of view, they are all considered as sources of drift. Such variations include temperature (Babar et al., 2012; Gutierrez et al., 2013; Lahokallio et al., 2014; Mazur et al., 2014; Merilampi et al., 2014; Qiao et al., 2013; Yang et al., 2014; Yu et al., 2016; Zhenzhong et al., 2011), air humidity (Chang et al., 2007; Manzari et al., 2012; Merilampi et al., 2014; Saarinen et al., 2014; Virtanen et al., 2011), moisture (Bauer-Reich et al., 2014; Gao et al., 2011; Hasan et al., 2015; S. Kim et

al., 2014; Prasad et al., 2011; Siden et al., 2007; Toivonen et al., 2013), snow (Nummela et al., 2008), light (Amin et al., 2014a), object proximity (Alarcon et al., 2012; Dobkin and Weigand, 2005; Griffin et al., 2006; Mercer et al., 2011), and mechanical strain (Alarcon et al., 2012; Babar et al., 2013; Gutierrez et al., 2013). Over long observation times, (Ni et al., 2011) shows a signal strength drift in static laboratory conditions over eight hours, and (Watkins et al., 2007) studies tags durability outdoors over a six-year period. However, those studies are based on energy levels and do not study the phase.

The effect of meteorological conditions on environmental phase drift has rarely been addressed for two reasons. Firstly, radio-identification location has been developed by electronic and radio laboratories for indoor tag location tracking. Secondly, global navigation satellite systems (GNSS) already provide a robust outdoor localization. However, the recent developments in RFID techniques now allow for phase measurement with off-the-shelf and low-cost interrogators, which increases the accessibility of phase-based RFID applications for research, and its robustness for outdoor applications.

This paper aims to identify and correct the meteorological effects on the phase. Firstly, it quantifies the effect of the following meteorological variations over the phase shift: 1) water presence over a tag or a base antenna; 2) temperature of the cable, tag and base antenna; 3) moisture content of a tag wood support; and 4) atmospheric conditions of the air. Secondly, it proposes techniques to reduce those effects, and apply them on a new acquisition system. Finally, it tests this system outdoors for five months, to evaluate its accuracy and validate the corrections under real, natural conditions.

## 4.3 Method and experimental protocol

In free space, the phase shift related to the direct propagation of a two-way backscattered wave is given by

$$\varphi_{air} = -\frac{4\pi f}{v} r \tag{4-1}$$

where

$\varphi_{\text{air}}$ phase shift resulting from the propagation in the air;

$r$ radial distance between the base and the tag;

$v$ RF wave velocity in the medium;

$f$ carrier frequency.

In real conditions, the measured phase also includes the propagation in the instruments, as in:

$$\varphi_{\text{total}} = \varphi_{\text{base}} + \varphi_{\text{air}} + \varphi_{\text{tag}} \tag{4-2}$$

where

$\varphi_{\text{total}}$ phase shift measured by the interrogator;

$\varphi_{\text{base}}$ phase shift resulting from the propagation in the reader, cable, and base antenna;

$\varphi_{\text{tag}}$ phase shift resulting from the tag backscattering.

Each of these terms is prone to variations:

$\varphi_{\text{air}}$ is influenced by the propagation environment between the base antenna and the tag, such as the transmitting medium, reflectors, and scatterers. This term is almost independent from the RFID instruments, and its variations differ between each tag. This term is useful for localization applications.

$\varphi_{\text{tag}}$ variations mostly depend on the tag electronics and on the antenna properties. The environmental conditions may influence it, from coupling/detuning effects, or impedance variation with temperature. These effects may be different for each tag. This term is useful for phase-based sensing.

$\varphi_{\text{base}}$ variations depend on the reader electronics, cable properties, and base antenna. This effect is the same for all tags, and can be corrected by a reference tag. However, since $\varphi_{\text{tag}}$ and $\varphi_{\text{air}}$ are different for each tag, that would add uncontrolled variations.

The first challenge for outdoor applications is to account for the changes in meteorological parameters (rain, air moisture, temperature), which vary over time, and are likely to strongly influence phase measurements. Indeed, each instrument part (tag, cable, antennas) or medium (air and materials near the antennas) may react to meteorological changes, modifying the three phase terms in equation (4-2).

Our purpose is to evaluate in a systematic way the effect of the meteorological conditions (mainly water and temperature) on the phase variations related to instruments, antenna detuning, and direct propagation. Multipathing, which is the combination of direct and indirect propagation, is not studied here. The experiments are designed to minimize its effect, by studying short-time variations and by using highly directive antennas.

In this article, the term *variation* represents a fluctuation of a measurable quantity over time, which includes a true variation of the measured quantity together with an added error. An *error* comes either from a bias or from random noise. A *bias* is an error that is systematic and repeatable over a short interval of time. A *drift* is a bias that is influenced by an uncontrolled parameter that varies over long periods of time. The *precision* is an indicator of random noise, the *accuracy* is an indicator of bias, and the *stability* is an indicator of drift. The scope of this article is focused on methods for improving phase stability. The precision and accuracy are not studied because results are averaged and present only relative phase variations, respectively.

The next section presents several experiments to quantify the effect of each meteorological factor on the phase. The experiments were performed outside and in a rural area, (see Fig. 1.a,b), to exclude indoor multipathing and reduce human interactions. Each experiment consisted in varying one meteorological parameter (temperature, water) and studying its effect on one element of the measurement system (cable, tag, tag support, base antenna). The experimental durations were short enough to limit the effect of other meteorological drifts, and a control measure was used to verify that there was no drift from uncontrolled parameters..

The material used in the experiments is presented in Fig. 1.c,d. Each tag (Confidex Survivor B) consisted of a quarter-wavelength patch antenna, separated by a foam insulator, protected by a hard-plastic casing, and based on a battery assisted chip (EM 4325 from EM Microelectronic). In term of lifetime, the tag's battery may last 5 to 20 years under continuous reading, given the cell of 290 mAh and the typical micro-circuit current of 1.7–6 µA (*EM 4325 Spec.*, 2015). The tag chip has an internal temperature sensor, with 0.25 °C resolution and 1 °C accuracy. We chose a commercial, off-the-shelf, monostatic interrogator with four channels (Impinj SR420), controlled by a custom software based on the manufacturer toolkit (Octane SDK Java). Each tag interrogation acquired the phase shift, the reader internal temperature, the interrogator's time, and the temperature of the tag. We

performed preliminary tests, showing that the phase was not sensitive to the interrogator temperature between -10 °C and 50 ° C.

This article used data from three different systems that we will name the *initial*, *intermediate*, and *new system*. The initial system was composed of a horizontally polarized slot antenna (Impinj Threshold, 5 dBi), an 8-m-long coaxial cable (type RG-58-C/U) with solid, polyethylene insulator and a 40-cm-high wood stake to support the tag. The intermediate system was composed of a Yagi-Uda antenna (14 dBi, 1-m-long), a 15-m-long coaxial cable (type RF 240) with polyethylene foam insulator and the same wood supports. It was mostly used because of its higher read range outside. The new system was composed of a 5-m-long phase-stable cable (PhaseTrack LS240, from Time Domain), a radome-protected panel antenna (Kathrein 80010643, 21 dBi, X-Pol, 3-dB radiation angle of 8° vertical and 35° horizontal), non-porous tag support (0.9-m-high fiber-glass stakes, planted 0.25m below the ground), and super-hydrophobic coating on the tag (Neverwet). This system was designed to reduce the phase drift from meteorological factors, and was tested in outdoor conditions for five months. The use of the highly-directive 21 dBi base antenna, combined with tags placed at a short distance, contribute to reduce the impact of the ground-reflected path: its orientation is 28° downwards (Fig. 4-1.b), which is out of the 8° main lobe of the antenna radiation pattern.

The interrogator was configured on 30 dBm output power, 865-868-MHz carrier frequencies (*EPC Gen2*, 2015)(*ETSI-EN 302-208*, 2016), with approximately 20 asynchronous readings per second. During the processing, the phase was wrapped within [0, π], and initialized at zero to quantify the drift. A meteorological station (Davis Vantage Pro 2) measured relative humidity, rainfall, pressure, and air temperature.

The instrument position was measured at different dates over four months using a scanning Lidar (Riegl VZ 400), to monitor instrument motions, with an error estimated at 6 mm. The motion of the instruments had also been measured with an infrared laser theodolite (Leica TCR805), placed 14m behind the tags for two hours with a precision measured at 1 mm.

Each experiment was repeated two to five times, using the same device, with slight modifications of the experimental protocol, and showed reproducible results.

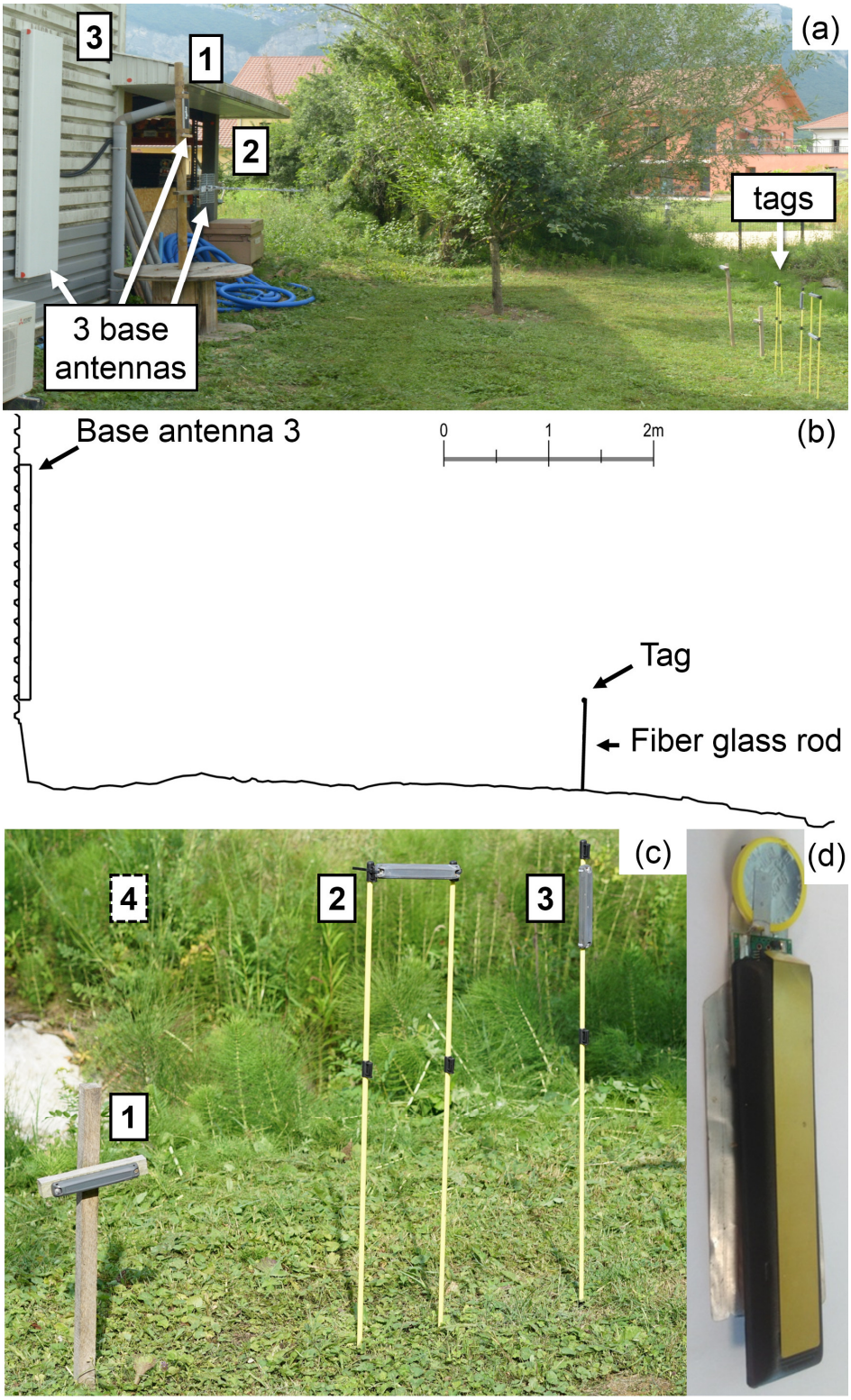


·1. System deployed outdoors, with (a) initial, intermediate and new system side by side, ɛnted respectively with antenna 1,2 and 3, (b) two-dimensional profile of the new system ɔy terrestrial laser scanning, (c) tags on their support, with tag 1 from the initial system and tags 2-3 (4 was added later) from the new system, and (d) a tag under its casing.

## 4.4 Experimental Results

### 4.4.1 Effect of the tag temperature

To evaluate the effect of the tag temperature on the phase, a hydrophobic tag was first immersed in water, at 60°C for 20 minutes, to stabilize the tag temperature. We used water for its high calorific capacity and temperature stability. Then, we rapidly removed the tag from the water, dried it and placed it on a wooden, outdoor support. The tag remained motionless. Its temperature decreased and stabilized around 0°C after 35 minutes. The meteorological conditions were dry, with no sun and 0°C air temperature. Fig. 2 shows the phase, depending on the temperature measured by the tag. The phase shows a linear relationship with the temperature, with a negative slope of 5.3×10-3 rad/°C.

To estimate a yearly phase drift, we evaluate a yearly tag temperature range from 0°C to 60 °C, affected by air temperature and radiative heating. Such a temperature variation corresponds to a possible phase error of 0.37 rad, which represents a relative ranging error of 10 mm.

This instrumental and detuning effect is not characterized by constructors of tags and microcircuits, and may differ between tag constructions. It may originate from the tag's antenna (Yadav et al., 2013), printed circuit board (Zhang et al., 1997) or integrated circuit. It could be cancelled by a specific tag conception, or by calibrating the effect and measuring the tag temperature.

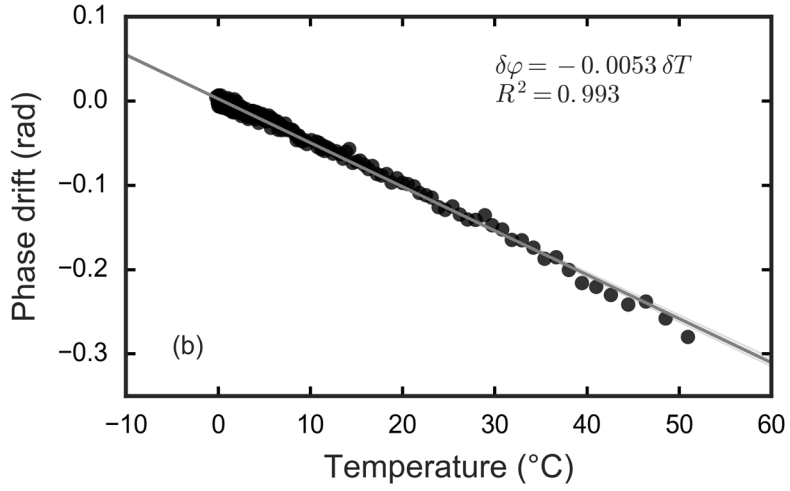


'hase drift versus temperature, during the cooling down of a tag, with a linear slope of -5.3 mrad/°C.

### 4.4.2 Effect of the RF cable temperature

The effect of temperature on the characteristics of coaxial transmission cable has been previously studied (Arbuthnott et al., 1960; Czuba and Sikora, 2011; Dhawan, 1992). It was first shown that temperature has an impact upon the cable electrical length, resulting from thermal expansion of the cable assembly, and change in dielectric permittivity of the insulator material, such as polyethylene or Teflon-PTFE. (Slack, 2017)

To evaluate the effect of temperature on different cables, we plunged a large portion of each cable into a recipient of tap water. The water was initially mixed with ice, to remain at a temperature of 0°C, and then heated step by step by adding boiling water. The temperature was measured at each heating step and during its natural decrease, and is associated to a phase averaged over 10s.

Fig. 3 shows the bivariate representation of the phase and temperature, at each temperature measurement. The RG58 cable shows a quadratic relation with temperature, and the RF240 and PT240 show linear relationship, which are summarized in Table I.

The relative wave velocity is 66% in the RG58 (from the relative permittivity $\varepsilon_r = 2.3$ of solid polyethylene (Lanza and Herrmann, 1958)), and 83% in the RF240 and PT240 (from specifications). To compare the results independently from frequency, the relative electrical length variation is calculated by using (4-1) after correcting the total electrical length with the relative wave velocity. The relative electrical length variation reported in Table I, for the PT240 cable, is coherent with the specifications. However, for the solid-polyethylene-based cable, the literature reports a value that is twice smaller than the one we measured, at 400 MHz for the 25-55°C temperature range (Arbuthnott et al., 1960). The different cable assembly may explain the difference.

A typical yearly temperature variation of 0-60°C, over an 8-m-long cable, would induce a phase drift between 4.7 radians and 0.13 radians, respectively with RG58 and PT240 coaxial cable.

This is an instrumental effect, characterized by constructors of phase-stable cables, and independent from the tag. It could be reduced by choosing an appropriate cable assembly, by keeping the cable as short as possible, by estimating the cable temperature, or by limiting the temperature variation, either passively, for example by burying the cable, or with a temperature control.

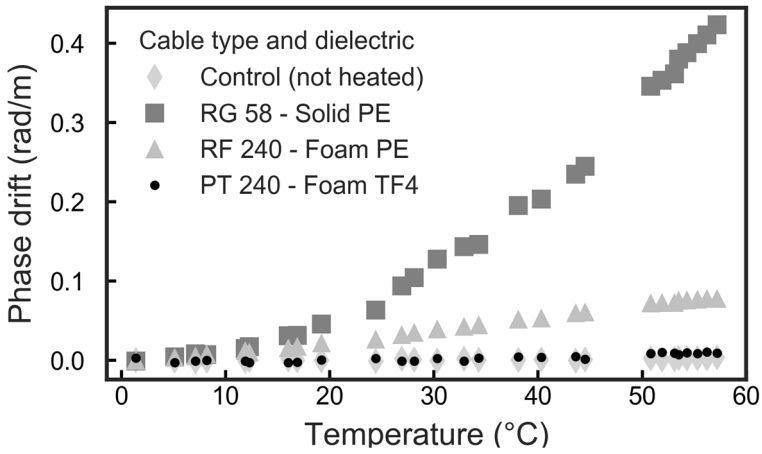


Phase drift versus temperature, normalized to 1-m-cable-length, for three
ent types of coaxial cables, and one control cable that was not heated.

ble 4-1: Comparison of the phase variations from temperature, for different coaxial cables

| Cable | Phase variation (mrad/m) | Electrical length variation (ppm/°C) | Variation, from literature / specs (ppm/°C) |
|---|---|---|---|
| RG58 | 0.13 x T2 | 181 (25-55°C) | 87 (25-55°C) |
| RF240 | 1.5 x T | 34 | - |
| PT240 | 0.21 x T | 5.3 | 5 (0-60°C) |

### 4.4.3 Effect of the base antenna temperature

To evaluate the effect of the antenna temperature on the phase, a fixed Yagi-Uda antenna was heated with a heat gun (P = 2 kW) for one minute, with regular movements over the whole antenna, holding the gun at an approximate distance of 10 cm. The antenna temperature started at 12 °C, and reached approximately 50 °C, evaluated from the same procedure applied on an independent temperature sensor. A control antenna remained 30 cm away from the heat gun. After heating the antenna, the operator went away.

Fig. 4 shows the phase measured through the two antennas over time. A negative phase drift of 0.03 rad is observed while heating the antenna (t = 7.5-8.5 min). The phase drift progressively goes back to null after 7 minutes, while the antenna cools down. In a linear approximation, this variation represents $-8\times10^{-4}$ rad/°C.

A temperature antenna of 0-60°C would create a phase error of 0.05 radians, or 1.3 mm relative ranging error, which we consider negligible for our application

This instrumental effect is not characterized by constructors, and it is independent from the tag. It may vary significantly depending on the antenna, especially if it contains temperature-sensitive dielectric materials. It could be corrected by calibrating and measuring the temperature antenna.

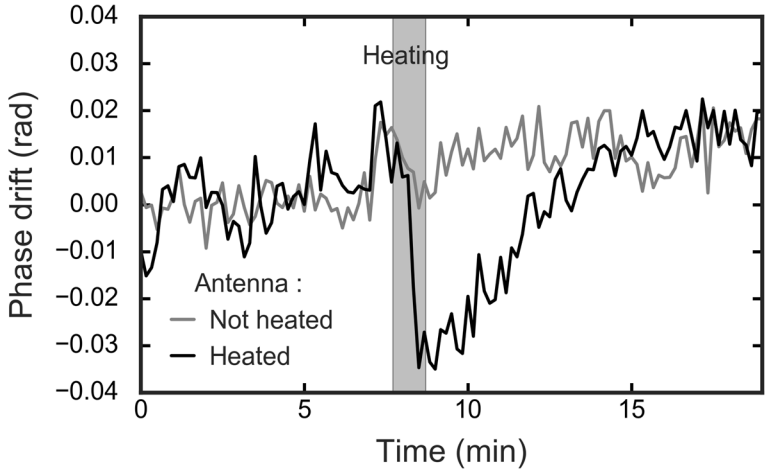


4. Phase drift versus time when heating an aluminium Yagi antenna. The
ith an unheated antenna is shown for comparison. The y-axis scale is smaller
than on other figures.

### 4.4.4 Atmospheric conditions on wave velocity

Wave velocity in the low troposphere at ultra-high frequency depends on atmospheric conditions (Gage and Balsley, 1980), with a celerity ratio $n$ given by:

$$n - 1 = 77.6 \times 10^{-6} \frac{P}{T} + 3.73 \times 10^{-1} \frac{e}{T^2} \tag{4-3}$$

where

$P$ atmospheric pressure (hPa);

$e$ water vapor partial pressure (hPa);

$T$ absolute temperature (K);

As this value depends on several parameters, we will estimate its real drift over a year, with real meteorological data, obtained from a local station (Le Versoud, France). The partial vapor pressure $e$ is derived from the saturated vapor pressure calculation in (Murray, 1967), using

$$e = RH \times 6.1078 \exp\left[\frac{17.2693882(T - 273.16)}{T - 35.86}\right] \tag{4-4}$$

Where RH is the relative humidity (no unit), provided from the meteorological station.

The resulting variation in air velocity is shown in Fig. 5. The velocity variation is converted as a phase drift, normalized for one-meter distance between the tag and antenna. A typical application with 10 m free air range between the tag and base antenna, would imply a yearly phase drift of 0.03 rad, or 0.8 mm relative ranging. This effect is negligible at such a distance, but should be taken into account for larger distances. This effect concerns direct and indirect propagation. It is generalizable for air transmission, but not other mediums such as water, vegetation or snow. As soon as the air is the only propagation medium, this effect can be corrected, by measuring the atmospheric condition with a meteorological sensor, and estimating the absolute tag range.

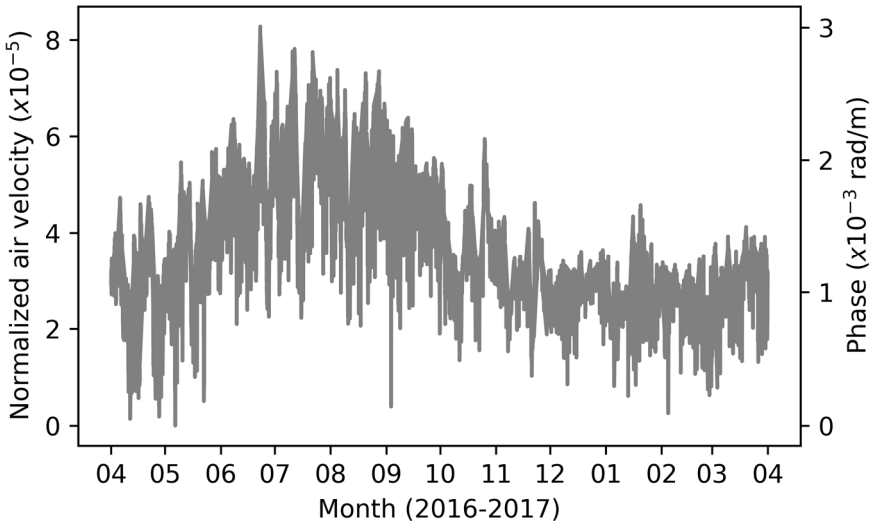


Model of the relative variation of air velocity, and phase variation per distance between the antenna and tag, for a year, based on meteorological data.

### 4.4.5 Effect of water over the base antenna

The presence of droplets or a thin layer of water on antennas, resulting from rain or condensation, is a well-known problem in radar (Kurri and Huuskonen, 2008), as it attenuates the signal but also modifies its phase. To reduce this effect, radomes are commonly used in combination with various types of hydrophobic surfaces (Salazar et al., 2014).

To simulate the effect of rain or condensation, an operator poured a jar of 1000 ml of tap water everywhere over two motionless Yagi-Uda base antennas, in 10 seconds. The first antenna was unprotected, whereas the radiating element of the

second antenna was protected with a radome coated with a super-hydrophobic layer (Simpson et al., 2015) (Neverwet). This outdoor experiment lasted four minutes, fast enough to consider other meteorological parameters as constants. The air relative humidity was 46%, and the temperature was 29°C (air) and 35°C (tags).

The phase-time curves are shown in Fig. 6, for the antennas with and without protection. Water is poured on the unprotected antenna at t = 0.45 min, and shortly after on the protected antenna. For the antenna protected with a hydrophobic radome, a short positive phase drift of about 1 radian is observed, which results from the presence of the operator. After 0.7 min, the curve is perfectly flat. In contrast, with the unprotected antenna, there is a total communication loss from 0.45 min to 0.8 min, followed by a strong negative phase drift peak of about 2 rad, which decreases rapidly until reaching 0.3 rad at t = 1.6 min. Then, the phase regularly increases, and returns to a null value after 2.5 min. The fast decrease corresponds to water that drips and form droplets, whereas the slow decrease corresponds to water evaporation, which was rapid due to elevated temperature and low humidity.

Using (4-1) these effects corresponds to a temporary ranging error of 55 mm for the maximum peak, and 8 mm for the slower decrease.

This detuning and tag-independent effect is not characterized by traditional constructors. This experiment highlights the efficiency of an hydrophobic radome to protect the antenna from water and cancel its effect.

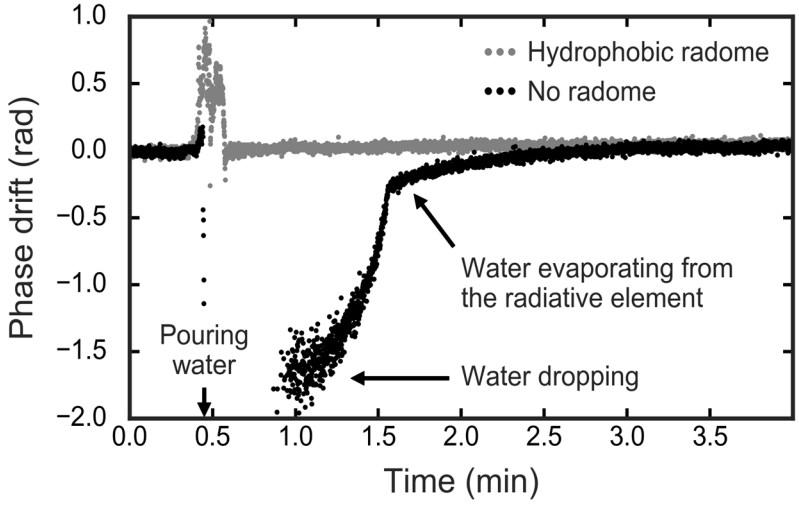


hase drift versus time when pouring water on a base antenna that is unprotected, or that is protected with a hydrophobic radome.

### 4.4.6 Effect of water over tags

To simulate the effect of rain or condensation on tags placed outside, an operator dropped 25 ml of distilled water at ambient temperature (T = 7±1 °C, no sun), on two hard-cased tags, either unmodified, or coated with a super-hydrophobic layer (Neverwet). Later (t = 70 min), the operator gently dried the tag with a disposable tissue. The tags were attached on a hydrophobic plastic stick to avoid water on the support. A third tag remained dry for control. The operation of dropping water lasted 10 sec. The relative humidity was measured at 74±2 % during the whole experiment.

Phase measurements on Fig. 7 reveals that water induced firstly a negative phase peak of 2.1 radian on the standard tag (equivalent to 58-mm ranging error), followed by a slow decrease starting from 0.5 rad (14 mm) while the water slowly evaporated. The return to zero was obtained after the operator dried the tag. Visual control showed that water formed a thin layer over the surface just after pouring water, which rapidly aggregated into droplets, that almost did not dry (compared to Fig. 6) because of cold and humid conditions. The phases of the control tag and hydrophobic tag remained stable.

This detuning and tag-dependent effect is not characterized by tag constructors. An external water protection could cancel the effect independently of the tag type. This experiment again shows the efficiency of the super-hydrophobic coating that removes the effect of water on the tag, as in (Ghahremani et al., 2016).

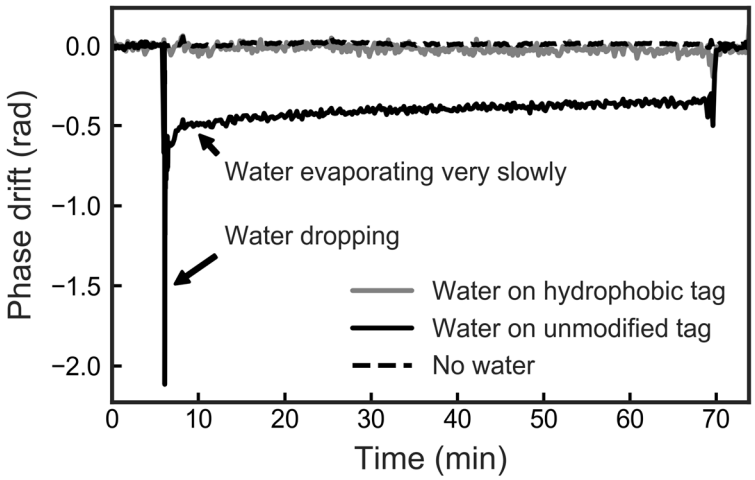


Phase drift versus time when pouring water on a hydrophobic and non-hydrophobic ncapsulated tag. The phase variation for a dry tag is shown for comparison.

### 4.4.7 Moisture of the material supporting the tag

In outdoor conditions RFID tags have to be attached on a stake, made of non-metallic material, to avoid affecting antenna performance (Griffin et al., 2006) or increase multipathing complexity. Many RFID experiments use wood stakes that are inexpensive and easy to shape. However, wood is porous and contains moisture. Moisture varies with rain, air humidity and temperature, and may be inhomogeneous over the wood volume. The moisture content is defined as the ratio between the mass of water and dry wood. It typically varies between 10 to 25% within a year outdoors (Niklewski et al., 2016), and by 2% per day on the first centimeter of the material, when exposed to high air humidity (Droin et al., 1988). The moisture content modifies the dielectric properties of wood (James, 1975) and thus shifts the phase. This effect is exploited in (Gonçalves et al., 2015), to track the moisture content of a cork wine-bottle-cap with a tag.

The following experiment investigates the effect of the moisture content on the phase. A piece of pine-wood (dimension 35x35x125 mm, density = 0.40) was oven dried at 105 °C for one hour, and a second identical piece was saturated with water in a vacuum chamber. Their moisture content was respectively 0.3 % and 44 %, measured by weight difference after drying the pieces in a 105-°C oven for 24h. On step one, a tag was fixed on a plastic support, designed to leave free space behind the tag. On step two, we placed the dried wood behind the tag, in contact with its plastic casing, without moving the tag. On step three, we removed the dried wood and placed the saturated wood instead. On the last step, we removed the wood, to return to the initial conditions.

Fig. 8 shows the phase shift, while changing the tag background sequentially with air (t = 0), dry wood (t = 2 min), saturated wood (t = 4.3 min), and air again (t = 8 min). The presence of dry wood behind the tag shifts the phase by 0.3 rad, and the 44% moisture content shifts the phase by another 0.5 rad. In a linear approximation, that corresponds to a variation of 12 mrad per percent of moisture content. After removing the background material, the phase returns to its initial state.

It is difficult to estimate a typical variation of moisture content over a year: this parameter has different dynamics depending on the depth considered, and varies from one material to another. As an estimate of a maximal yearly drift, we will use the phase difference between dry and saturated wood in our experiment, which is 0.5 rad. That is equivalent to 14 mm in relative ranging.

This detuning effect is similar to the effect of water on the tag. It could be eliminated by changing the tag support, whatever the tag. To correct this effect, one may use non-porous support, or separate the tag from its support with a metallic reflector.

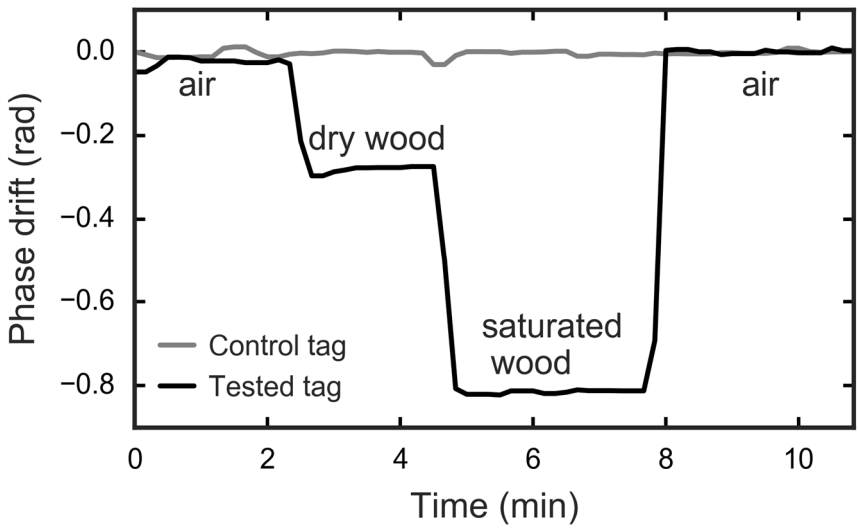


Phase shift versus time with different moisture contents of the support material placed behind the tag: free air, and wood with 0% and 44% water content.

## 4.5 Validation

### 4.5.1 Overview of the new system

To validate the experimental results and the efficiency of the corrections, a static installation was set outside, for one month. It compares the evolution of the phase, between an initial system, and a new system that corrects for phase drift.

The initial system is composed of a standard slot antenna, a coaxial cable provided by the interrogator manufacturer, and a hard-cased tag attached on a wood support. In comparison, the new system is numerically corrected for tag temperature (from a temperature sensor on the tag), and physically corrected for cable temperature (with temperature-stable cables), moisture of the tag support (with fiber glass stakes), water on the tag (with super-hydrophobic coating), and water on the base antenna (with radome-protected antenna).

Fig. 9.a presents the phase drift over one month, and Fig. 9.b-d presents rain, dew indicator and tag temperature, obtained from a meteorological station on site, and from a temperature sensor within the tag. The phase varies from 0.50 to -2.50 radians (3.0 rad total) on the initial system, and from 0 to -0.95 radians on the new

system. The accuracy of the new system has improved by a factor of 3 over the whole period. However, this accuracy may depend on the period considered. It is separated in the next sections into water-related drift, temperature-related drift, and residual unidentified slow drift.

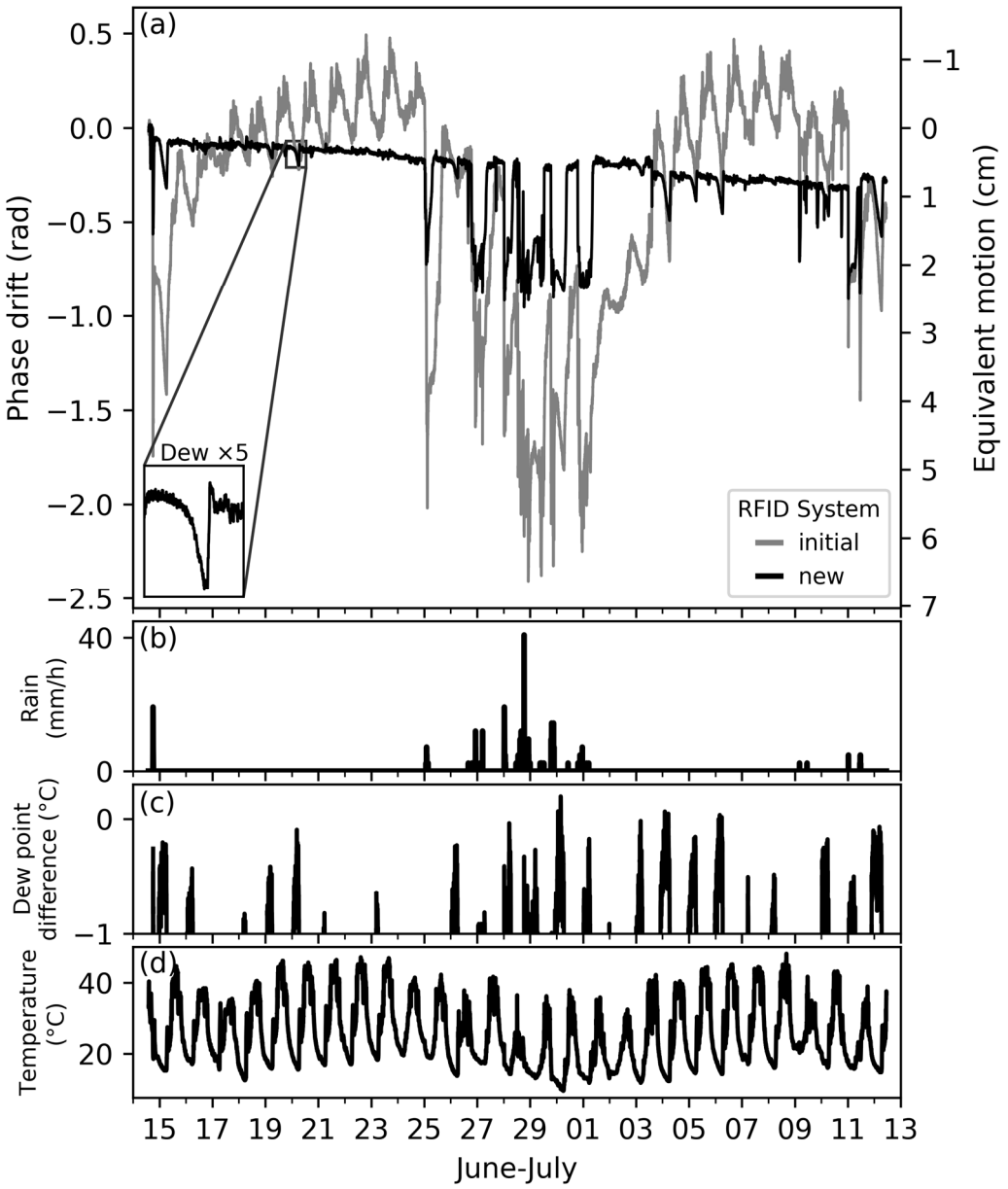


'ariation over one month of (a) the phase for different RFID systems, for initial (tag 1, antenna 1) and new tag 2, antenna 3), along with (b) the measured rain rate, (c) the difference between tag temperature and ›int, that suggest the condensation of a water film when above a certain point, and (d) the temperature measured by the tag sensor.

### 4.5.2 Water effect

Rain forms a water layer on the tags and base antenna, which impacts the phase. The rain on Fig. 9.b shows a strong and systematic impact over the phase. For example, during heavy rain on June 28$^{th}$, the phase decreases of up to 2.3 radians on the initial system, and up to 0.7 radians on the new system. Besides, heavy rain creates a negative phase offset on the initial system, which takes a day or more to decrease, as observed after the rain episodes of June 14$^{th}$ and 29$^{th}$. This offset comes from the moisture of the wood tag support, that is slow to dry, and influence the phase, as shown in Fig. 8.

Dew forms a water layer on the tags and base antenna, when radiative heat loss decreases their temperature below the dew point. It happens mostly outdoors at night, from radiative heat loss. Fig 9.c shows the difference between the tag temperature and the dew point, provided by the meteorological station. A positive difference (within the 1°C accuracy of the tag sensor) indicates dew formation on the tags, and on objects with the same temperature. This indicator clearly correlates with negative phase peaks on Fig 9.c, which often appears between 24h-6h. The dew effect varies from almost no variation, like on the zoom of 20$^{th}$ at 6am), to 0.7/0.25 rad (former/new system) on June 15$^{th}$, just after a rain episode.

The effect of water was reduced by a factor of 3, both for rain and dew formation, between the initial and new system. This residual effect results from the observed water accumulation on the tag and antenna, even with the new system. Also, it was observed (not presented) that the water effect amplitude on the vertically-polarized tags 3 and 4 was reduced by a factor of 2, simply because the vertical shape accumulates less water on top of the tag**.** A specific design of the tag and its casing may better correct this effect, which is out of this study scope.

### 4.5.3 Temperature effect

Fig 9.d. shows the temperature measured by the tag, which differs from air temperature by radiative heat transfers. The temperature shows a positive correlation with the phase of the initial system, and no visible correlation on the new system, which is a good improvement.

The phase-temperature ratio was previously measured at -5 mrad/°C for the tag (Fig. 2) and 0.13 mrad/°C$^2$/m for the solid polyethylene cable (Fig. 3). Within a 15-45°C temperature interval, the expected daily drift on the initial system is 1.4 radians, however, Fig. 9 shows only a drift of 0.8 radians. The cable temperature is

prone to less daily variations, due to lower sun exposition, which may explain the difference.

### 4.5.4 Slow drift

Apart from rain and temperature effect, the phase on the new system seems to show a slow drift, of approximately 0.3 rad over the month. To further investigate this residual slow phase drift, the phase was observed for five months, with three hydrophobic tags attached on non-porous stakes (tags 2-4 on Fig. 1.c). The tag 2 was used in the new system, presented on Fig.9. It was attached with two fiber-glass stakes and a horizontal polarization. The tag 3 was vertically polarized and attached on one single stake, to see if the tag polarization had any effect on the phase drift. Finally, the tag 4 was sealed in a 70-cm-deep and 10-cm-large hole, filled with concrete, and vertically polarized. It replaced tag 1 on July 14$^{\text{th}}$, to reduce a potential motion of the stakes.

Fig. 10 shows the slow drift of those three tags, by showing the daily 95$^{\text{th}}$ percentile. A previous test showed no meaningful change on the result between the 90$^{\text{th}}$ and 98$^{\text{th}}$ percentile, which proves the method robust on this dataset, to remove the residual effect of rain and dew, and focus on slow drift.

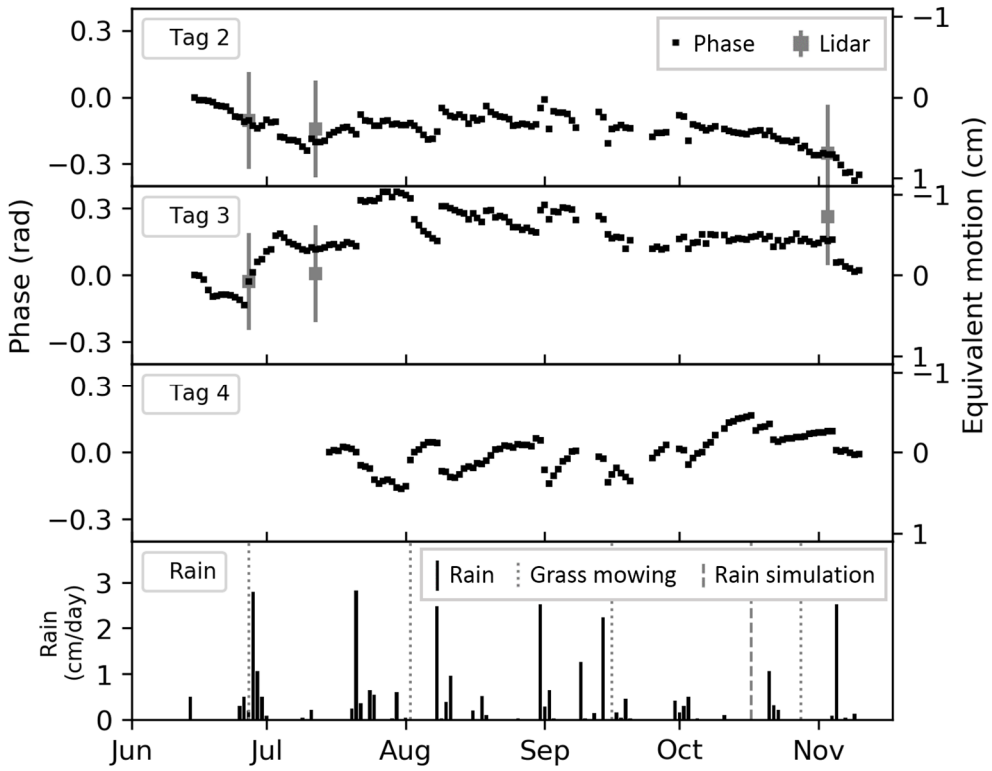


. Daily phase (95th percentile), and motion estimated by LiDAR scanning, for three different tags, months, along with the daily rainfall. The four dotted vertical lines represent the intervention of a er to mow the grass, and the dashed vertical line on October 17th represents a rain simulation.

**5-month trend**

The phase drifted by an average amplitude of 0.05-0.11 rad (1.4-2.8 mm) per month over five months, depending on the tag considered. The phase of tag 2 slowly decreased by 0.28 rad the first month, plateaued the following three months and decreased by 0.22 rad during the last month. The phase of tag 3 increased steeply by 0.5 rad the first month, decreased by 0.09 rad/month until September 27th and finished by a plateau. The phase of tag 4 showed no clear trend. It is globally hard to see any relation between the very slow drift of each tag.

**No multipathing influence from vegetation**

The dotted lines on Fig. 4-10 show the intervention of a gardener, who mowed the grass. Those interventions did not have significant effects on the phase, either on the long-term or by zooming on the event (not presented here), except on August 2nd when the tags 3 and 4 moved during the operation. A special care was taken on July 27th, where the grass was weighted (1.3 kg/m2 wet, 0.20 kg/m2 dried, height

below 30 cm) and measured by Lidar, and the gardener operation carefully reviewed, but the phase did not change. It changed only a few hours later, with the rain.

**Motion of the tags detected by Lidar measurement.**

A scanning Lidar acquired the geometry of the environment in 3 dimensions, on June 27th, July 12th, and November 3rd, that allowed for comparison across time. The comparison showed no significant translation or tilt of the base antenna, compared to immobile reference targets. There was, however, a motion of the tag, quantified from a tilt of the stake, and a variation of distance with the base antenna. This motion influences the phase, and as a consequence, the slow variation is explained partly by a residual undesirable drift and partly by a true motion.

**Influence of the rain**

The slow variation of the phase was clearly impacted by rain, especially observed during important episodes. The most impactful event, on July 21th, changed the phase by +0.09, +0.2 and -0.06 rad, respectively on the tags 2,3, and 4. On tag 2, the rain had no consistent effect on the phase. On tag 4, the rain consistently decreased the phase. On tag 3, the rain increased the phase until July 21st and decreased it after this date. To conclude, the rain had an effect on the phase, but it was not consistent over time and between tags. A part of this variation could have been caused by a tag motion: a changes of rigidity, shape or pressure of the soil, may result from water content variations (Mainsant et al., 2015) or variations in the roots network, and induce a tilt of the tag stakes.

The next section presents an experiment to test if the rain can move the tags, which would explain this influence on the phase.

**Motion induced by simulated rain**

To better understand the rain-related slow-drift, we simulated the effect of rain on the soil. On October 17th (showed by a dashed line on Fig. 10), we poured 50L of water (conductivity 32 mS/m, temperature 19.1 °C), equivalent to 5 cm of rain over $1m^2$, at the base of the stakes that support the tags, without wetting the tag. The tag position was measured regularly with a laser theodolite. Prior tests showed that wetting the environment and the potential reflectors (vegetation, ground) had no significant effect on the phase, which again confirmed that ground-reflected paths were negligible in this specific experimental design (to observe the effect of ground reflexion under other experimental designs, see sections 5.7 and 6.4.3).

Fig. 4-10 shows that dropping high quantities of water near the stakes had a clear effect on tag 4, a slight effect on tag 3, and no significant effect on tag 2. The phase of tag 4 progressively dropped by 0.06 rad (2 mm), from 17h40 to 18h05, right after pouring the water on the tag stake. A similar 2-mm-decrease was observed independently with the theodolite, which confirms the displacement. This phase variation is also visible as a jump on Fig. 10, which effect remained for several days. Furthermore, the following important rain events, on October 21st and November 5th, also decreased the phase by a similar magnitude, which suggests that the motion of the tag 4 was a major cause of rain-related phase drift. From this experiment it can be concluded that water can move the stakes that support the tags, even with a 70-cm-deep concrete sealing, and that this effect has the same magnitude as the slow drift that happen during rain events.

The motion of the tag is therefore an important part of the slow drift. There remains an unidentified contribution, which can be estimated at a maximum of 6 mm over the 4-month interval of Lidar measurement, deduced from the Lidar precision. This corresponds to a maximal drift (not related to motion) of 0.05 rad/month, of 1.5 mm/month

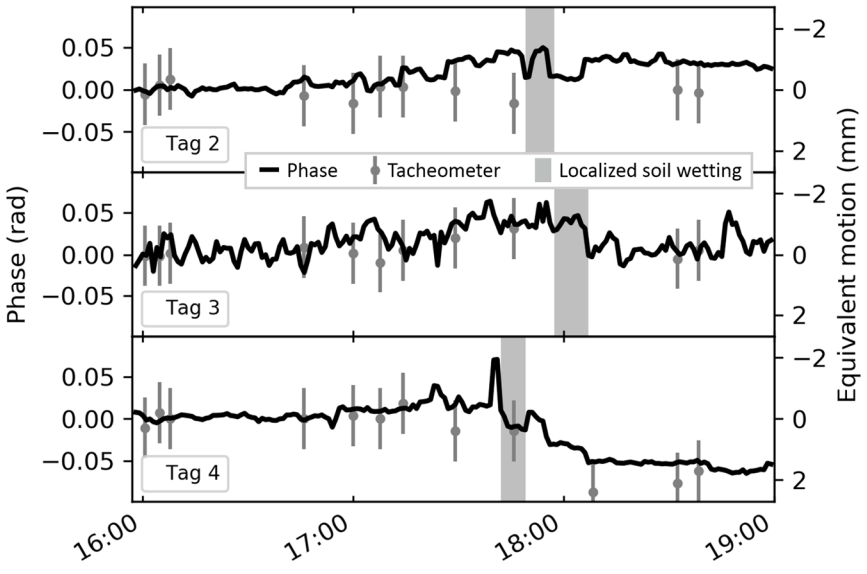


. Phase along time, for all the tags tested, when simulating a rainfall event, along with motion measured by an independent tacheometric device. The grayed zones represent ɔuring higher quantity of water at the base of the stakes that support the tags.

## 4.6 Discussion

This section discusses firstly the additional environmental effects that may influence the phase delay, and secondly the types of ground motion that could be monitored with the new acquisition system that is introduced.

Long-term irreversible aging of the material (cables, electronics, antenna, radomes) may influence the phase or even destroy the equipment by changing the material mechanical structure or dielectric permittivity. Such deterioration could occur from multiple sources, such as chemical processes, UV radiation or mechanical deterioration (wind, animals, freeze/melt cycles). In the present study, temperature showed almost no effect on the reader, and a reversible effect on the tag. However, on the long-term, temperature could also be a factor for accelerated aging. Studying these variations may require either very long observation times, or accelerated aging in artificial laboratory conditions.

Mountainous areas are subject to extreme cold (Nummela et al., 2008) and humidity (Saarinen et al., 2014) conditions. These may accelerate the aging process and add additional phase delays, for example due to frost formation on the tags (see section 5.5.3). Since many landslides occur in mountain areas, it could be useful to test the equipment in similar conditions.

Hydrometeors and aerosols may also add a propagation phase delay. These effects were reviewed by Solheim et al. (1999) at GPS frequencies of 1.2–1.6 GHz close to UHF RFID, and summarized in Table 4-2. Atmospheric air conditions have the strongest influence, with a yearly delay fluctuation of 80 mm/km at ground level already studied in section 4.4.4. The effect of particles in the air depends on the particle diameter, volume density and refractive index (or dielectric permittivity). The strongest particle effects would be triggered by events of strong sandstorms (18 mm/km), rainfall (2–15 mm/km) and hail (7 mm/km). Such effects might be visible on the RFID system we used for distances >100 m. All the other effects due to particles in the air should be completely negligible for RFID applications, with, however, three comments. First, a strong reactivation of a landslide or rockfall may create aerosols in the air, which might result in a phase delay with an amplitude between volcanic ash and a sandstorm. Second, the table considers only the effect of dry snow, but watery snow may increase the delay by more than 5 times (Sadiku, 1985) due to the higher refractive index of liquid water. Third, the attenuation due

to the particles should be negligible in any case (e.g. <0.01 dB/km for strong rainfall) (Oguchi, 1983, fig. 33).

Table 4-2: Phase delay induced by atmospheric constituents for GPS waves., along with diameter and volume density of the particles. Note that the effect of dry air and vapor is superior for the whole atmospheric layer than near the ground only (computed as 80 mm/km in section 4.4.4). From (Solheim et al., 1999).

| Source | Diameter, ≤mm | Density, ≤g $m^{-3}$ | Delay, ≤ mm $km^{-1}$ |
|---|---|---|---|
| Dry air | $10^{-7}$ | 1400 | 290 |
| High vapor | $10^{-7}$ | 25 | 140 |
| Low vapor | $10^{-7}$ | 2.7 | 15 |
| Cloud | 0.1 | 5 | 8 |
| Radiation fog | 0.05 | 0.1 | 0.2 |
| Advection fog | 0.05 | 0.3 | 0.3 |
| Haze | 0.001 | 0.01 | 0.02 |
| Drizzle | 0.5 | 0.1 | 0.2 |
| Steady rain | 4 | 1 | 2 |
| Heavy rain | 6 | 7.5 | 15 ($L_2$) |
| Hail | 20 | 7 | 7 ($L_2$) |
| Snow | 15 | .75 | 0.75 ($L_2$) |
| Aerosols | 0.01 | 0.1 | 0.1 |
| Sand | 1 | 60 | 18 |
| Volcanic ash | 0.2 | 0.03 | 0.01 |

Finally, multipath may be the major residual source of inaccuracy. This effect is particularly problematic for short-term localization studies indoor (Wang and Katabi, 2013), due to the presence of many reflectors. The effect is also influential outdoors, due mostly to ground-reflected waves (Skolnik, 2008, chap. 16). The present study reduced this effect by using highly directive antennas at a close distance from the tag, but that does not correspond to field requirements to monitor landslides. This effect is reduced on high-quality GPS by using expensive geodetic antennas that attenuate the signal coming from the ground, but that is hardly feasible for RFID tags. This effect is also difficult to model and mitigate numerically, as it strongly depends on the environment that is complex, unique and variable over time. Ground-reflected multipath is influenced by multiple environmental parameters (Larson, 2016) such as ground topography (appendix 2), soil moisture (Larson et al., 2010), snow (chapter 5) or vegetation (chapter 6) that are studied in the following chapters.

Another discussion concerns the landslide velocities measurable by the RFID technique. Cruden and Varnes (1996) classify landslide velocities from extremely rapid (5 m/sec) to very slow (16 mm/year) to extremely slow. With a residual slow

drift of 2–3 cm per year, the RFID technique should allow monitoring velocities >10 cm/year, corresponding to landslides between slow and very slow. This accuracy could be improved by measuring and correcting for the tag tilt. For rapid motion, the problem would come from phase ambiguity. When the landslide direction is known, the maximum displacement between two measurements should < 8.6 cm (=quarter wavelength). The interrogator we used with the most accurate configuration allowed for about 25 interrogations per seconds. Therefore, the fastest measurable velocity for N tags should be about 2/N $m.s^{-1}$. Faster velocities might be attained by measuring Doppler frequency shift, but that is out of the scope of this study. To conclude, the technique may allow monitoring motions from 10 cm/year to 0.01–1 m/s for 1–100 tags, therefore covering the majority of landslide velocities (Cruden and Varnes, 1996) excepting very slow / extremely slow and extremely rapid landslides.

## 4.7 Conclusion

We identified significant meteorological effects on the phase measurements, the magnitude of which is given in Table II. For a typical installation with an 8-m-long polyethylene cable, 10-m range between tag and base antenna, and 60 °C of object temperature variation under the sun, the factors of greatest influence are the water layer over the base antennas and tag (4.1 rad) and the cable temperature (3.7 rad). Factors with smaller influence are the tag temperature (0.3 rad) and the material moisture (0.5 rad). The temperature of Yagi antenna temperature (0.05 rad), and the meteorological variations of the air (0.03 rad) have a negligible influence. Some effects are opposed, such as the temperature of the tag and of the cable, and might be partially cancelled. Combining the different effects shown in table II may lead to an error of up to 8.1 rad within one year of operations, where the drift reaches its minima for high humidity and low temperature, and maxima for the opposite. In terms of positioning, one may expect a drift of about 22 cm in relative ranging over a year from meteorological effects, which is to be compared with the centimeter accuracy reported in the literature for absolute ranging indoors during short times. In terms of sensing, this is far beyond the sensor dynamic reported in the literature (Caizzone et al., 2014; Occhiuzzi et al., 2013), which is typically from 1 to 2 rad.

Table 4-3: Sources of phase drift outdoors

| Effect | Variations (mrad) | Yearly drift (rad) | Yearly drift (mm) | Solution |
|---|---|---|---|---|
| Water on base antenna. | -2000 | 2.0 | 55 | Hydrophobic radome. |
| Water on tag. | -2100 | 2.1 | 58 | Hydrophobic radome. |
| Cable temperature (Polyethylene). | 0.13 /°C²/m | 3.7 | 102 | Phase-stable short cable. |
| Tag temperature. | -5 /°C | 0.3 | 10 | Temperature sensor. |
| Wood stake moisture. | -12 / % | 0.5 | 14 | Impermeable material. |
| Antenna temperature (Yagi) | -0.8 /°C | 0.05 | 1.3 | Temperature sensor. |
| Air refractive index. | 3 /m | 0.03 | 0.8 | Meteorological data. |

Specific solutions have been proposed for each identified effect to reduce the phase drift. A hydrophobic and hermetic radome avoids the creation of a water film from rainfall and condensation. The cable temperature effect is reduced by using shorter cable with phase-stable assembly and insulator. The tag temperature effect is corrected by using an integrated circuit that includes a temperature sensor. The problem of moisture content is reduced by attaching the tag to a non-permeable material such as plastic or fiber glass. The variation of wave velocity in the air is corrected by measuring the air temperature, pressure and relative humidity over the area. Finally, the antenna temperature is corrected by installing a temperature sensor near or within the antenna. These corrections are independent of the tag construction, except for the water protection, the efficiency of which depends on the tag design, and for the temperature correction which requires the calibration of each tag.

All these solutions were implemented in a new acquisition system, which was compared for 1 month outdoors to the initial system. The new system improved the phase stability by a factor of at least 3 for the whole period, as shown in table III. It made negligible the influence of temperature, and reduced the influence of water by a factor of 3. The stability over one dry day was improved by a factor of 12, to reach 0.05 rad.

There remained slow variations over long periods, partly related to a motion of the tags, and partly related to a residual unidentified drift. This residual drit was estimated at a maximum of 0.20 rad (6 mm) within the four month interval of

Lidar campaign, which corresponds to an average of 0.05 rad per month, or 1.5 mm per month.

The measured slow drift now fits with our application requirements to monitor movements between 10 centimeters and a few meters per minutes, corresponding to slow to very rapid landslides. Since a significant part of the phase variation came from parasitic ground-related tag motion, which may be expected to be even stronger on a landslide application, it is not worth further stabilizing the phase for slow motion monitoring.

Future works may require to better understand the impact of the multipathing on the phase outdoors, which is prone to complex and slow variations (shape and liquid water content of the soil, vegetation, and snow), and to mitigate this effect. Other instrumental challenges may also be studied, especially under extreme temperature or humidity. A real outdoor experiment on a landslide site will be implemented to address these questions.

4: Comparison of the phase variations with the initial and newly developed systems during the 1-month experiment

| Period considered | Initial phase variation (rad) | New phase variation (rad) | Gain in accuracy |
|---|---|---|---|
| Whole period. | 3.0 | 0.95 | 3 |
| A dry day. | 0.6 | 0.05 | 12 |
| Rain event. | 2.3 | 0.7 | 3 |
| Dew event. | 0.7 | 0.25 | 3 |

## 4.8 Acknowledgment

Authors thank Q. Barbier for the Lidar acquisition and processing, and H. Taylor for proofreading the manuscript.

# Chapter 5
# Influence of snow on RFID

**Contents**



## 5.1 Summary

In the mountains, many landslides are triggered by melting snow. The ability to monitor their movements in the presence of snow is critical. However, radio methods such as GPS or radar are deteriorated by snow. This chapter shows that snow also influence RFID phase and signal strength with three types of effects: proximity effects, direct propagation and multipath. All these effects are also influenced by snow density and liquid water content. Each effect is studied from the literature and put in evidence with one or two experiments outdoors. Proximity effects are

induced by snow situated near tags (usually at a distance<wavelength). These effects are shown by accumulating snow on a tag and by approaching a tag near the snowpack surface. Snow liquid water content and dry density control the snow dielectric permittivity. Variation of liquid content is observed during daily cycles of snowpack melting/freezing and of frost deposition/melting/evaporation on the tag. The phase velocity and attenuation of bulk propagation depend directly on the snow in-phase and quadrature permittivity, respectively. The relation with phase velocity is demonstrated by changing the thickness of a snow volume placed between a tag and a station antenna. Multipath represents the interferences that occur from summing the direct path between the tag and station antenna, with indirect reflected paths (mostly reflected on the ground). Its influence is demonstrated observing a strong variation of phase and signal strength when removing a thin layer of snow from the ground at the reflexion point. The validity of the experiments is then discussed, due to the very heterogeneous conditions on the snow, and because each experiment ends up being influenced by different effects which can be difficult to discriminate. Finally, these effects should lead to potential problems when using RFID tags in snowy environment, for which potential solutions are suggested.

## 5.2 Introduction

Radio-Frequency Identification (RFID) tags are mostly used to identify goods indoors (Ngai et al., 2008). New usages have been presented outdoors, such as monitoring a construction field (Song et al., 2007; Valero et al., 2015), tracking wood logs (Björk et al., 2011), monitoring a landslide (Le Breton et al., 2019; Pichorim et al., 2018) or monitoring structures (Zhang et al., 2017). In cold regions or seasons, these applications would have to deal with frost and snow. Frost and snow can deteriorate tags (Gutierrez et al., 2013), reduce their reading range (Li et al., 2011; Nummela et al., 2008) or reduce their localization accuracy (Le Breton et al., 2019). Snow would reduce the signal strength—critical for reading a tag—and modify the phase, reducing the accuracy of phase-based localization and sensing. In the literature, active transponders at 315 MHz have been used below snow to communicate the measurement of dedicated sensors (Rorato et al., 2014) but without studying the impact of snow on the communication. RECCO® passive tags have been used for snow avalanche rescuing for decades (Grasegger et al., 2016). These passive tags are excited at 866 MHz like the RFID tags presented in this study. However,

their signal is discriminated from the environmental by doubling the carrier frequency of the backscattered wave, and does not transmit data. However very little literature exists on these devices and no study of the effects of snow on RFID tags has been proposed yet.

In a snowy outdoors environment, four major factors are expected to influence the phase and signal strength of the signal backscattered by an RFID tag. Firstly, tag antennas are affected by the presence of material in their vicinity that has a different dielectric permittivity than the air (Dobkin and Weigand, 2005; Le Breton et al., 2017a), such as snow (Nummela et al., 2008). Such material would affect the signal strength (Occhiuzzi et al., 2013), phase difference of arrival (Caccami et al., 2015), and tag tuning (Caccami and Marrocco, 2018). Secondly, snow permittivity—typically 1 to 3.5 (Tiuri et al., 1984)—depends on its density and volume ratio of liquid water. These properties are heterogeneous in space and time due to snow deposits, melting, freezing, compaction and many more phenomena's (Fig. 5-1) (Fierz et al., 2009). This effect on antennas is exploited to measure snow properties with microwave devices (Kinar and Pomeroy, 2015; Techel and Pielmeier, 2011). Thirdly, a wave transmitted across snow would be slowed and attenuated, depending on its permittivity. This is used for example to measure the properties of a snowpack with a ground-penetrating radar (Bradford et al., 2009; Marshall and Koh, 2008). Snow appeared to influence the phase outdoors even with a tag above the snow surface, inducing distance measurement errors of up to 8 cm (Le Breton et al, 2019). Fourthly, snow on the ground may affect the ground-reflected paths that interfere with the direct path (Fuschini et al., 2008). The influence of a snowpack on multipath propagation at microwave frequencies is exploited for example with GPS, which can be used to measure the snow depth (Larson et al., 2009).

Other effects exist, but we considered them minors and did not study them. The scattering due to snow heterogeneity, measured by polarimetric radars, should be negligible at 866 MHz, because the wavelength (34 cm) is much longer than most of the heterogeneities. Snowflakes in the air also induce attenuation and depolarization, measured by meteorological radars (Matrosov, 1998, 1992) but these effects start to be visible at distances of several kilometers. Using multiple layers should help to model the effect of multipath with more accuracy. However such modeling is too complex and requires too much data, so we stayed with the first-order approximation of a single layer. Snow generates passive emission of electromagnetic

waves, but such emissions are much smaller than the readers (>30dBm) and tags radiations (>-30 dBm).

This study aims to demonstrate that snow affects RFID signal mostly by proximity effects, direct propagation and multipath. The intensity of these should be influenced mostly by the snow density of liquid and solid water and by the height of the snowpack. Section 5.3 present the material used for the measurements. Each effect is studied separately in sections 5.4 to 5.7: Sections start with a literature study to make suppositions on the expected effects. They are followed by 1–2 experiment(s) to show these effects empirically. They finally end up with a short discussion to validate the expected effects and to suggest hypothesis about the few unexpected observations. Conclusions and limits of these experiments are summarized in section 5.8. Practical concerns for implementing RFID in the snow are suggested, followed by perspectives of using RFID for sensing the snow properties.

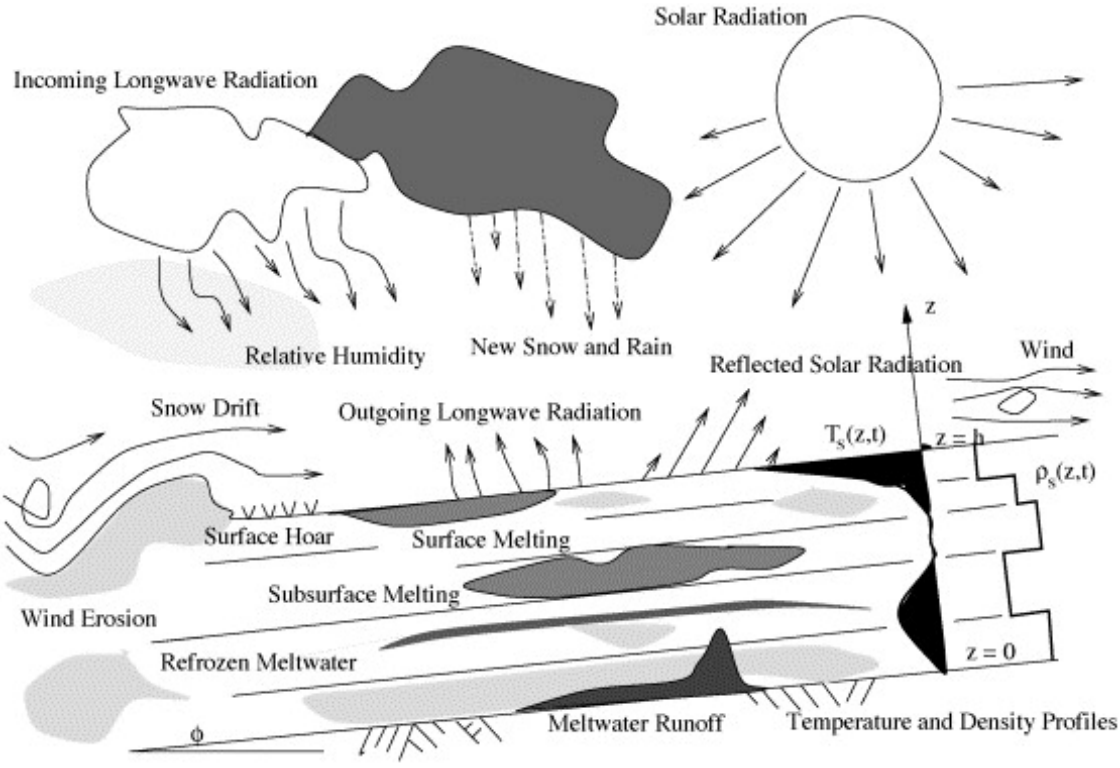


Fig. 5-1: Physical processes that affect snow depth, density and liquid water content within different layers. From (Bartelt and Lehning, 2002)

## 5.3 Snow Characterization and RFID Material

This study shows six experiments that demonstrate specific effects of snow on the phase and signal strength when reading a tag. The experiment 5.7.3 consisted of removing a thin layer of snow on the ground. It was realized at Crolles, France, on

27 January 2017. The snow was not characterized. The experiment 5.5.3 showed the effect of daily frost deposition and melting on tags. It was realized at Crolles, France, on 8–9 December 2016. The RFID results were complemented by local meteorological station measurements (Davis Vantage Pro2) and tag temperature sensors. The experiments 5.4.2, 5.4.3, 5.6.2 and 5.5.2 showed the effect of the proximity of a tag to the snow surface, the effect of daily snow melting and the effect direct wave transmission in a snow volume, respectively. These experiments were realized at Chamrousse, France, on 21 March 2017. The snow permittivity and density were regularly characterized during the day. In-phase permittivity was measured with a standard instrument using a cavity filled with snow which resonant frequency depends on snow permittivity, and density was estimated by mass weighting (see Fig. 5-2). The vertical profiles were measured at the height of 0.05, 0.2, 0.4, 0.6 and 0.8 m. The snow surface was 0.8 m above the ground on average.

Every experiment used an RFID system that comprised an interrogator (SR420 from Impinj) emitting at 865.7 MHz and battery-assisted passive tags with temperature sensors (Survivor B from Confidex). The signal was radiated and received by a Yagi-Uda antenna (gain ≈14 dBi) or by a slot antenna (Impinj Threshold, 8 dBi), depending on the experiment.

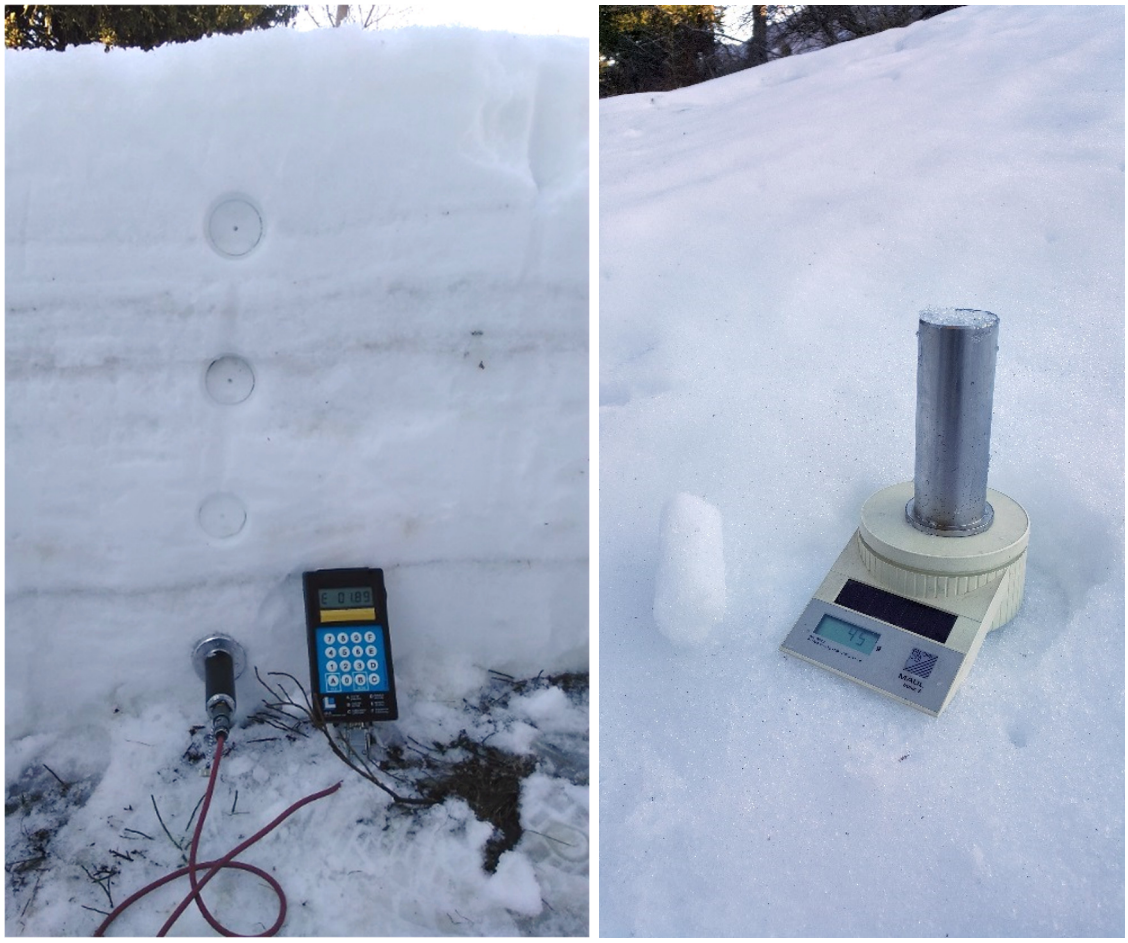

Fig. 5-2: Pictures of the snow characterization at Chamrousse, to measure (left) the snow in-phase permittivity using a resonating cavity instrument and (right) the snow density by mass weighting. Measurements were repeated along the day at the same location.

## 5.4 Proximity effects

### 5.4.1 Studies with water near tags

Aqueous materials at a few centimeters from a tag can influence signal strength (Dobkin and Weigand, 2005; Occhiuzzi et al., 2013), phase difference of arrival (Caccami et al., 2015; Le Breton et al., 2017a) and tuning frequency of a tag (Caccami and Marrocco, 2018). These effects are summarized in Table 5-1. The suggested causes are the reduction of electric field amplitude (Dobkin and Weigand, 2005) or the change of tag antenna impedance that affects the tuning frequency (Caccami and Marrocco, 2018). Other causes could be a change of antenna radiation pattern, a reduction of radiated power due to capacitive coupling (i.e., ground effect), an interference with surface waves, or a partial/full reflexion just before the tag antenna. These effects would depend on the tag design, on the tuning frequency of the tag, on the permittivity of the material near the tag, on the material thickness, and on its distance from the tag.

Many studies have shown the influence of water near an RFID tag on the received signal strength (the list presented on Table 5-1 is not exhaustive). The effects on the signal strengthwere either positive or negative, depending on the tag design and tuning frequency. Increasing the water content of a material placed near a tag should lower its resonant frequency (Capdevila et al., 2012). A resulting resonant frequency closer or further to the carrier frequency should increase or decrease the signal strength, respectively. The effect on the phase seems more consistent, with in general a phase decrease with the presence of water. However, few studies were realized using phase-based sensing and more studies could result in more discrepancies in the results. The measurement of antenna detuning with self-tuning tags (Caccami and Marrocco, 2018) is very recent and shown for the completeness of the review and for perspectives.

The only study that tested to place snow on tags (Nummela et al., 2008) observed a signal strength variation of -7 dB to +10 dB depending on the tag. However, the tags were not designed for outdoor usage and the snow was not characterized. The outdoor-designed Survivor B tags were only tested with a water cover and in contact with a dry/saturated wood. These resulted in a signal strength increase of +1 dB to +4 dB, and a phase decrease in -0.25 rad to -2.1 rad (Le Breton et al., 2017a). Another experiment placing a piece of wood with a volume water content of 17% near a tag, decreased the phase by -0.8 rad. Therefore, the effect of placing snow (typical water content <15%) near a tag should should affect the phase within -0.25 and -0.8 rad. We also expect the amplitude of these effects to increase for snow placed closer to the tag, and for thicker snow volumes (Dobkin and Weigand, 2005).

Table 5-1: Effect of water and snow nearby tags

| Influence material | Thickness | Proximity | Tags | Resulting variation | Reference |
|---|---|---|---|---|---|
| | | | | **Signal strength** | |
| Snow | ≈1 mm | 0 | 5 low-cost tags | -7 to +10 dB | (Nummela et al., 2008) |
| Water in a container | >5 cm | 0 to 4 cm | 5 low-cost tags | -20 to +1 dB | (Dobkin and Weigand, 2005) |
| | >5 cm | <1 mm | Low-cost tag | -15 dB (0.8 dB/cm) | (Bhattacharyya et al., 2010) |
| | >5 cm | <1 mm | Commercial tags | -20 dB | (Capdevila et al., 2011) |
| Water in concrete | >5 cm | <1 mm | Commercial tags | 10 dB (-2.4 dB/ ε ' )<br>-40 dB | (Suwalak et al., 2012)<br>(Capdevila et al., 2012) |
| Air humidity (RH) | >5 cm | 0 | Custom tag with sensitive material | -23 dB (-0.44 dB/%RH) | (Manzari and Marrocco, 2014) |
| Water (parse/a lot)<br>Wood (dry/wet) | <1 mm<br>3.5 cm | 0 | Survivor B tag, from Confidex. | +1 / +1 dB<br>+3 / +4 dB | Unpublished data from (Le Breton et al., 2017a) |
| | | | | **Phase** | |
| Air humidity (RH) | >5 cm | 0 | Custom tag with sensitive material | -1.4 rad (-20 mrad/%RH) | (Caccami et al., 2015) |
| Water (parse/a lot)<br>Wood (0/17% moisture) | <1 mm<br>3.5 cm | 0, all around<br>0 | Survivor B tag, from Confidex. | -0.5 / -2.1 rad<br>-0.25 / -0.8 rad | (Le Breton et al., 2017a) |
| Natural snow outdoors | n.a. | On the tag and ground | Survivor B tag, from Confidex. | ±2.9 rad. Mix of proximity and multipath effects. | (Le Breton et al., 2019) |
| | | | | **Detuning** | |
| Water | <1 mm | 0 | Dogbone, from Smartrack (Magnus S3 chip) | Sensor code = 30 to 4 from air to water. | (Caccami and Marrocco, 2018) |

### 5.4.2 Snow accumulation on a tag

To quantify the near-field influence of snow on the commercial tags of this study, we placed a pack of snow on the tag, then removed it (Fig. 5-3), and observed its influence on the RSS and phase. The presence of snow increased the RSS by 2 dB (Table 5-2), and decreased the phase by –0.65 rad. Both the phase and signal strength reversed to their original value when removing the snow.

Fig. 5-3: Picture of snow placed on a tag

This experiment confirms the influence of snow that couples with the tag antenna, by simulating a snow accumulation on a tag resulting from snowfall. The observed effect is within the expected bounds for the signal strength (+1 to +4 dB) and for the phase (-0.25 to -0.8 rad) defined from Table 5-1.

To improve this experiment, the thickness of the snow layer should be increased progressively to observe the influence of the thickness, and the experiment should be repeated with different density and liquid water content of the snow. The effect of the distance to the snow surface and the effect of burying tag completely in the snow would also be observed, which is presented in the next section.

Table 5-2: Proximity effect of snow placed on the top of the tag

| Effect on signal strength | Effect on phase |
|---|---|
| +2 dB | -0.65 rad (+1.8 cm) |

### 5.4.3 Proximity to the snowpack surface

What happens when the height of a snowpack increases until reaching a tag? To simulate the variation of snow height relatively to a tag, we moved a tag from +80 cm to −20 cm relatively to the snow surface (Fig. 5-4). The station antenna was placed 30 cm above the snow surface and 3 m away from the tag. The surface of the snow was measured with a relative dielectric permittivity of 3.2, a total density (liquid+solid) of 0.42 and volume liquid water content of 9.1%.

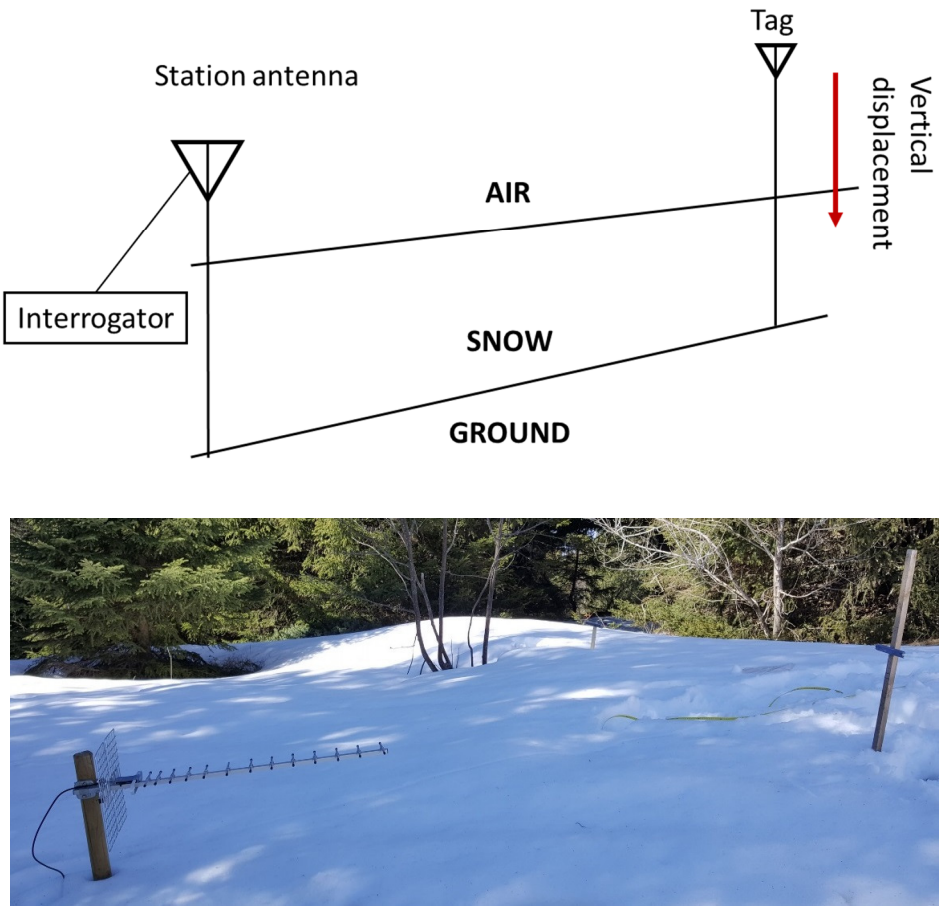


Fig. 5-4: (top) Sketch and (bottom) picture of the experiment that moves the tag vertically from 80 cm above to 20 cm below the snow surface

The resulting phase and signal strength were clearly influenced by the distance between the tag and the snow surface (Fig. 5-5). This influence can be categorized in four stages. When the tag was sufficiently above the snow (>20 cm), the phase followed a geometric hyperbole model and the RSS varied slowly. In this situation, the influence of the snow cover remained minor on the communication. When the tag approached the snow surface (0–20 cm), the signal strength started decreasing rapidly and the phase started diverging from its expected value in free space. When the tag went below snow (0 to −10 cm), the signal strength remained at a nearly constant low value (−75 to −80 dBm) while the phase increased rapidly. Finally, when the tag went deeper into the snow (<-10 cm), the RSS started to increase again and the phase passed an inflexion point. At h=−15 cm, the phase progressively stabilized, at +7.5 rad above its theoretical value in free space.

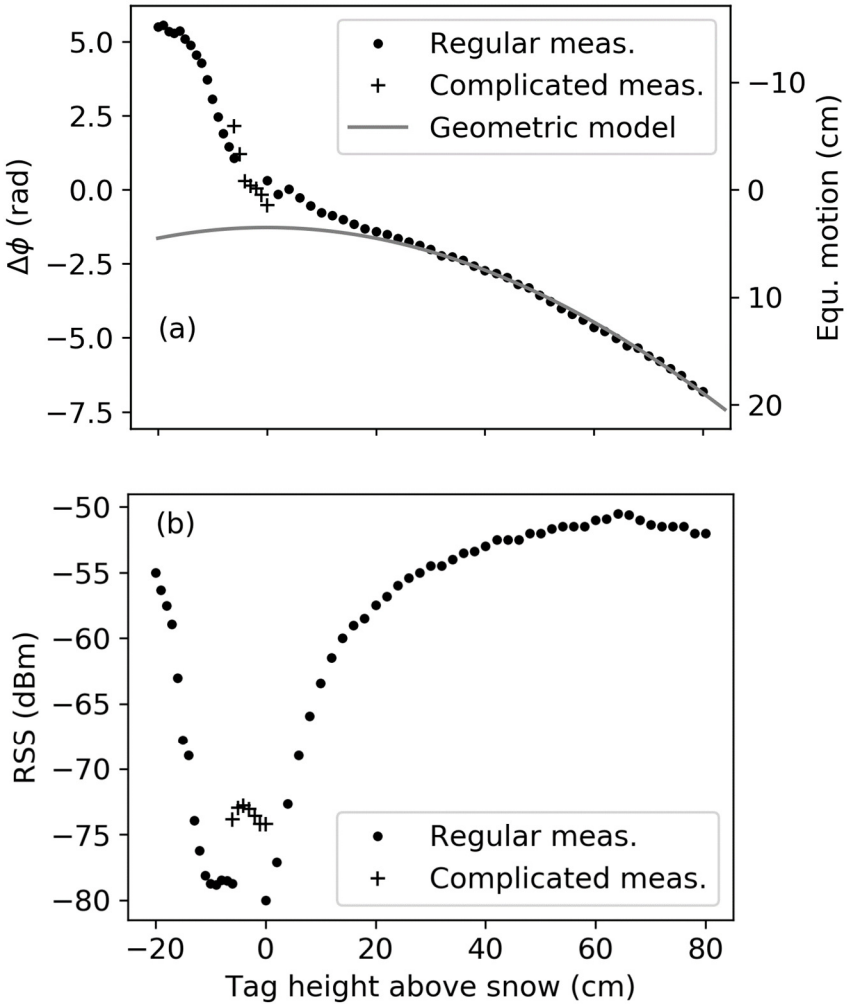


Fig. 5-5: Variation of (a) phase and (b) signal strength when moving the tag vertically above and below the snow cover surface.

The results showed an unexpected effect when the tag passed the transition from +20 cm to -20 cm above the snow surface. The phase was expected to decrease due to the slower propagation in snow and to the proximity effect on the tags shown in the previous section. Yet, it increased by +7.5 rad. The RSS also strongly decreased during this transition, passed a plateau, and increased back to its initial value after this plateau. The strong decrease of signal strength near the snow surface had been consistently observed with two other types of tags during preliminary experiments (not shown here). The following paragraph proposes and eliminates several hypotheses that could explain this effect.

On a first look, this effect could result from multipath (see section 5.7). Indeed, a snow permittivity of 3 and an incident angle of 70° would result in a reflexion coefficient R=−0.7 (the phase of the reflected ray is inverted due to the negative sign). The sum of the direct and snow-reflected path would lead to a relative signal

amplitude of 0.3, equivalent to −21 dB loss over the two-ways propagation. However, interferences from a ray reflected by the snow surface should result in $\pm\pi$ of phase variations at maximum, and disappear once the tag goes below the snow. In the experiment, the phase variations were above this value, and the signal strength loss showed a plateau when the tag was below the snow, which is contrary to the effect expected only from multipath. The effect should not have been caused by tags in contact with the snow either, because the phase and signal strength started to diverge 20 cm above snow. It might have been caused by slow surface waves near the air/snow interface (Balanis, 2012, section 5.3.4), from a coupling effect between the tag antenna and the snow surface (similar to ground effect) or from several combined effects. This hypothesis could be tested experimentally by placing a tag on the snow surface, and progressively moving it away from a station antenna while remaining above the snow surface. If the communication were dominated by the snow surface, the resulting phase velocity should be different from direct propagation in the air. Another possible effect is the modification of the phase and amplitude diagram of the tag antenna when placed near a dielectric material such as snow.

## 5.5 Solid/liquid water content

### 5.5.1 Theoretical permittivity from liquid/solid density

Snow accumulation on the ground forms snowpacks. Snowpack properties, such as density or liquid water content, are heterogeneous in space and time (Fierz et al., 2009). That results in spatiotemporal contrasts of electromagnetic properties (Tedesco, 2015). In particular, the dielectric permittivity of snow is controlled mostly by the snow density and by its volume of liquid water (Tiuri et al., 1984). The quantity of liquid water can be defined by its volume ratio of liquid water. A volume of snow $V_S$ can be considered as a mixture of moist air, solid ice crystals and liquid water, with volume ratios ($\theta = V / V_S$) of $\theta_a, \theta_i$ and $\theta_w$, respectively (Bartelt and Lehning, 2002) and the relation:

$$\theta_a + \theta_i + \theta_w = 1 \tag{5-1}$$

Snow liquid water content is heterogeneous in space and time. It fluctuates mostly at the top of a snowpack, because of melting/freezing due to heat exchanges with the environment (this fluctuation is reduced in deeper layers due to the thermic

insulation provided by the upper layers). Snow can be considered as a porous medium that stores liquid water. With low water content ($\theta_w$ <8%), the pores are not connected and snow is in a "pendular" regime. With more liquid water, the snow enters a "funicular" regime with free water and connected pores (Denoth, 1980) (see Table 5-3), with a water content that can reach 40% on soaked snow. The equations presented in this section are applicable for a pendular regime.

The density $\rho$ of each component of snow (ice, liquid water and air) depend on their volume ratio and intrinsic density. For example, dry snow density $\rho_d$ is:

$$\rho_d = \theta_i \times \rho_{\text{pure ice}} \tag{5-2}$$

Dry snow density $\rho_d$ is typically 0.05-0.5, with a typical value of 0.1 for newly fallen snow (Doesken and Judson, 1997). Temperature can differentiate wet and dry snow: wet snow is constrained to $T_{\text{wet}} = 0°\text{C}$ by the energy required for ice melting, whereas dry snow temperature can be lower. T=0°C is the only temperature considered in this study.

Table 5-3: Liquid water content of snow, from (Fierz et al., 2009)

| Term | Description | $\theta_w$ (%) |
|---|---|---|
| dry | Usually $T_s$ is below 0 °C, but dry snow can occur at any temperature up to 0 °C. Disaggregated snow grains have little tendency to adhere to each other when pressed together, as in making a snowball. | 0 |
| moist | $T_s = 0$ °C. The water is not visible even at 10× magnification. When lightly crushed, the snow has a distinct tendency to stick together. | 0–3 |
| wet | $T_s = 0$ °C. The water can be recognized at 10× magnification by its meniscus between adjacent snow grains, but water cannot be pressed out by moderately squeezing the snow in the hands (pendular regime). | 3–8 |
| very wet | $T_s = 0$ °C. The water can be pressed out by moderately squeezing the snow in the hands, but an appreciable amount of air is confined within the pores (funicular regime). | 8–15 |
| soaked | $T_s = 0$ °C. The snow is soaked with water and contains a volume fraction of air from 20 to 40% (funicular regime). | >15 |

At 866 MHz, radio propagation in snow depends mostly on its dielectric permittivity

$$\varepsilon = (\varepsilon' + j\varepsilon'')\varepsilon_0 \tag{5-3}$$

With $\varepsilon_0$ the constant dielectric permittivity of vacuum (=8.854×10$^{-12}$ Farad / m) and $\varepsilon', \varepsilon''$ the relative in-phase and quadrature permittivity of the snow propagating medium, respectively. The in-phase and quadrature permittivity influence respectively the wave velocity and attenuation. This study names "permittivity" the relative complex dielectric permittivity.

In-phase permittivity $\varepsilon_s'$ of wet snow at 10–1000 MHz in the pendular regime depends on its liquid water content $\theta_w$ and dry density $\rho_d$ (Tiuri et al., 1984) using:

$$\varepsilon_s' = 1 + 1.7\rho_d + 0.7\rho_d^2 + 8.7\theta_w + 70\theta_w^2 \quad (5\text{-}4)$$

Quadrature permittivity of wet snow $\varepsilon_s''$ depends on liquid water content $\theta_w$ and wave frequency $f$ (Hz). At 0.5-1 GHz, they are related using:

$$\varepsilon_s'' = \frac{f}{10^9}(0.9 \times \theta_w + 7.5 \times \theta_w^2) \quad (5\text{-}5)$$

To understand these influences visually, a diagram resulting from the equations (5-4) and (5-5) is presented on Fig. 5-6. Snow in-phase permittivity would be within 1–3.5 (light and dry snow – dense and wet snow), depending on the snow density and liquid water content. The following two sections show the influence of melting water on RFID communication, due to 1) snow melting during the day, and 2) frost deposition, melting and evaporation over 24h in winter.

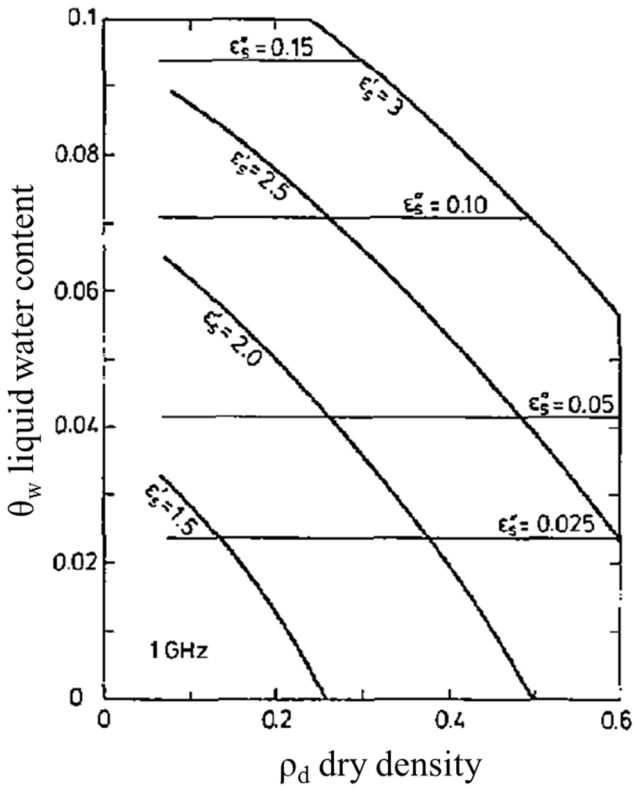


Fig. 5-6: Nomograph for determining the wetness and density of snow from its complex dielectric constant at 1 GHz. From (Tiuri et al., 1984).

### 5.5.2 Melting at the Snowpack Surface

To observe the influence of snow liquid water content on the RFID signal, we installed three tags near the snow and interrogated them continuously. The three tags were installed at a height of +1.5/+0.2/-0.20 m relatively to the snow surface (Fig. 5-7), and horizontal distances of 1/6/5 m from the station antenna. The measurements were made from 8 a.m. to 5 p.m. The snow was dry at 9 a.m. due to previous night solidification, and melt progressively during the day. Snow melting was the only major environmental parameter that had varied during the day. The effect of temperature on the tags (about -5 mrad/°C) was corrected (Le Breton et al., 2017a), and the coaxial cables remained below the snow at a constant temperature of 0 °C.

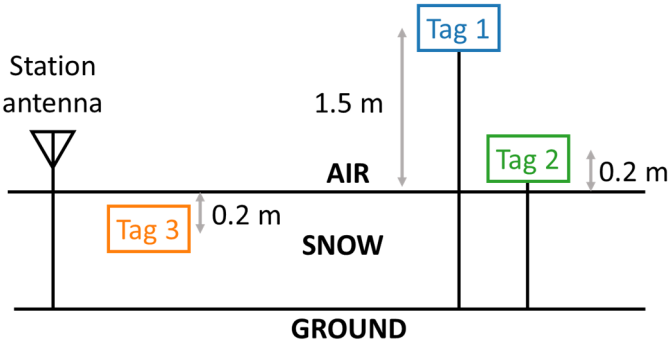


Fig. 5-7: Installation to observe the effect of superficial snow melting over the day.

The permittivity of the superficial layer of snow increased from 1.8 in the morning (8–10 a.m.) to 3.2 in the middle of the day (2 p.m.) due to melting (Fig. 5-8, black curve). The influence of snow melting on the phase and signal strength was dependent on the tag height (Fig. 5-8). The tag n° 1 placed well above the snow (+1.5 m) was almost not influenced by the snow melting. The greater distance between this tag and the snow surface should prevent from the occurrence of proximity effects. The minor variations observed on this tag may be due to multipath and to other uncontrolled variations. On the tag n° 2 just above the snow surface (+0.2 m), the phase increased by about +0.8 rad and the signal strength decreased by -8 dB. Such effects, not observed on tag n° 1, should be due to snow surface proximity.

On the tag just below the snow surface (−0.2 m), the phase progressively decreased down to −2.2 rad at 17h, while the signal strength decreased irregularly down to −8 dB at 17h. This tag should be influenced by proximity effects, but also by other effects: The propagation across snow should affect the phase (see section 5.6) and the transmission at the air-snow surface should affect the signal strength (see section 5.7). The phase decrease is explained by the propagation within the superficial layer. An increase of permittivity from 1.8 to 3.2 over a 20 cm layer should reduce the phase by −3 rad, equivalent to a motion of +9 cm (see section 5.6). The measured phase decreased only by −2.2 rad, so the +0.8 rad of difference should represent the proximity effects. This is the same value as the proximity effects observed on the tag n° 2.

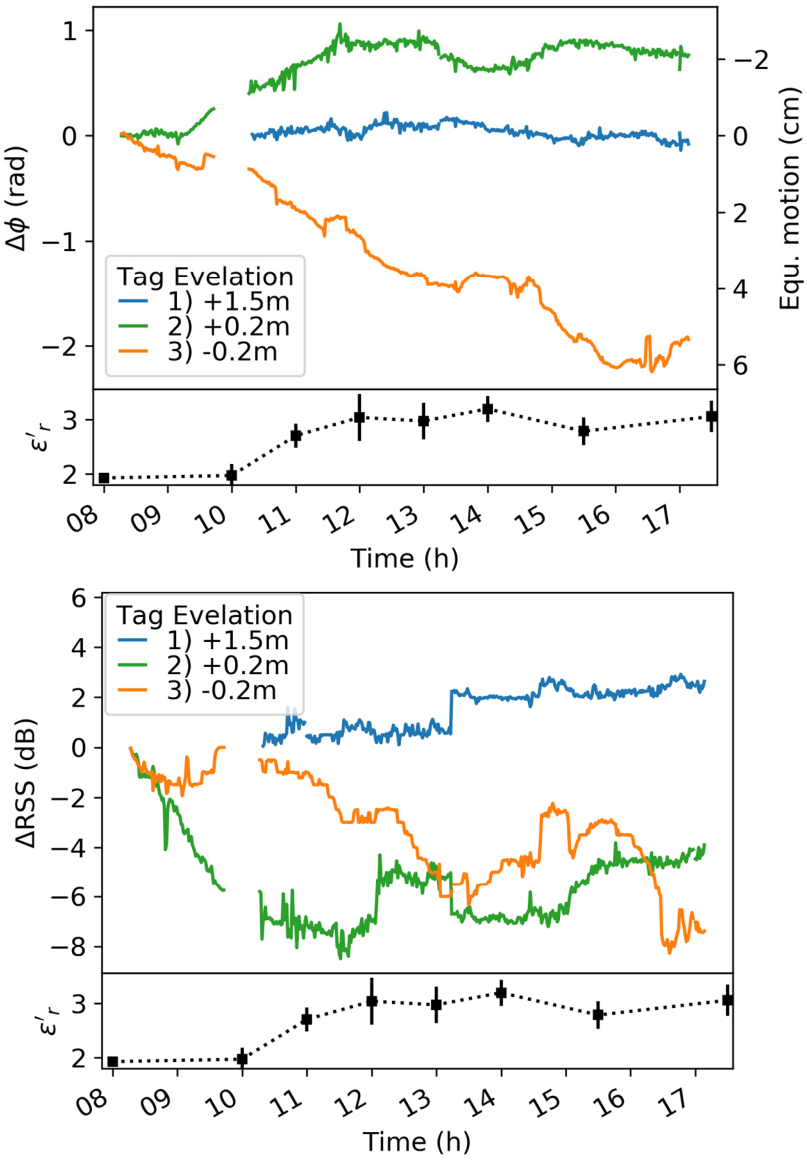


Fig. 5-8: Variation of (top) the phase and (bottom) RSS for 10 hours on tags installed at 3 different elevations relatively to the snow surface. The in-phase relative permittivity of the snow surface is also displayed.

To conclude, this section shed light on the effect of snow at the proximity of RFID tags, on the phase (+0.8 rad in the experiment) and on the signal strength (down to -8 dB). These effects depend on the distance between the tag and the snow: they are visible at 20 cm, but not at 1.5 m. They also depend on the liquid water content of snow, which controls the snow permittivity. Liquid water content can vary strongly within a few hours due to snowpack superficial melting during the day.

### 5.5.3 Frost Deposition and Melting on a Tag

Frost may also induce proximity effects on tags, due to liquid⇔solid water transition. To observe this effect, a tag was placed outdoors in December 2016 in a humid place near a creek, 6 m away from a station antenna. The station antenna was 1.5-meters high, and the tag was placed 0.4 m above the ground on a wooden stick. A meteorological station recorded humidity, temperature and air pressure, to calculate the dew point. The dew point (or frost point with negative temperatures) indicates the possibility of dew/frost precipitation on objects. An object at a temperature below or equal this point should have a precipitation of dew/frost at its surface. The object temperature would decrease faster than the air in the night due to radiative heat transfer. However, its temperature may be maintained equal to the dew point because of the heat gained from the precipitation process. The meteorological station also measured the solar radiation, which would provide energy to melt the frost and evaporate the resulting liquid water.

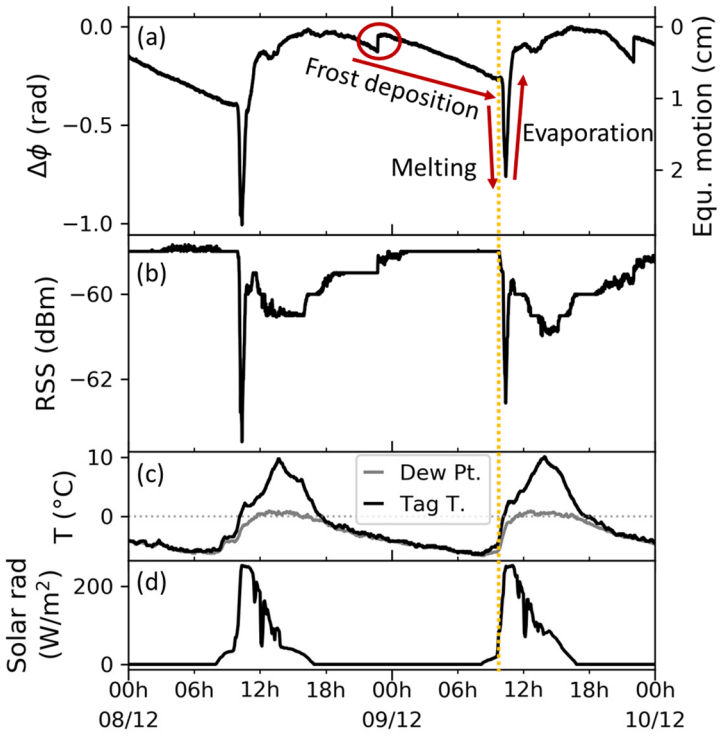


Fig. 5-9: Effect of frost deposition and melting on the (a) phase and (b) RSS of a tag placed 12 m away from the station antenna for two days. (c) Tag temperature below 0 °C and equal to the dew point indicates frost deposition. (d) Solar radiation, which heats and melt the ice. The dashed yellow vertical line indicates the solar radiation arriving on the tags. The red circle highlight an event discussed in the text.

The measured phase and signal strength show a cyclic behavior every 24h (Fig. 5-9). In the early morning, the tags were covered with frost, with no sun and a tag

temperature almost equal to the dew point. When the sun arrived on the tags, the frost layer melted rapidly. That decreased the phase (−0.7 rad) and the signal strength (−4 dB). This liquid water then evaporated within an hour, which increased the phase (+0.9 rad) above its initial value before melting. The phase and signal strength then remained approximately stable for a few hours (12–18h) while the tag remained dry. When these measurements were done, the RFID system had not been corrected yet for temperature effects (Le Breton et al., 2017a), which explains the residual phase variations. Around 18h, the tag temperature started to follow the dew point temperature, suggesting a potential precipitation of water. The phase started to decrease shortly after, confirming the potential water deposition. At this point, water gradually deposited on the tags, slowly decreasing the phase.

Around 23h, the phase increased abruptly by about +0.1 rad (discussed in the next paragraph). After that time, the phase decreases at a constant rate (−0.3 rad in 9h) while the signal strength remains constant. The slow phase decrease is explained by the accumulation of frost deposited on the tag. Finally, in the early morning (8h30), the frost stops accumulating on the tags, the sun arrives, and the cycle starts again.

The abrupt phase increase during the night has been observed on other tags installed in the same zone, but at different hours and amplitudes (Fig. 5-10). The phase increased slowly by +0.2 rad between 19 and 21h on tag n° 0, increased abruptly by +0.1/+0.05/+0.03 rad at 23h/20h30/21h15 on tags n°1/3/4, and did not increase on tags 2&5. The cause of this increase is not obvious. It could be explained by a freezing of the soil that would modify the multipath, by the solidification of gaseous water trapped within the tag casing, or by the freezing of the wood supporting the tag. To understand this effect would require determining if the variations between tags depend on the tag itself, on its supporting material, or on its position.

In conclusion, the effect of ice melting is observed not only with snow, but also with frost. Solid ice on the tag would slowly decrease the phase (−0.3 rad over the night), and the melting of this layer followed by its evaporation would increase then decrease the phase rapidly (+0.7/−0.9 rad). This effect seems difficult to avoid: it happens at any height above the ground and hydrophobic coatings used in Le Breton et al. (2017) are inefficient with frost. It could be corrected numerically

after estimating frost thickness with a self-tuning sensor tag (Caccami and Marrocco, 2018).

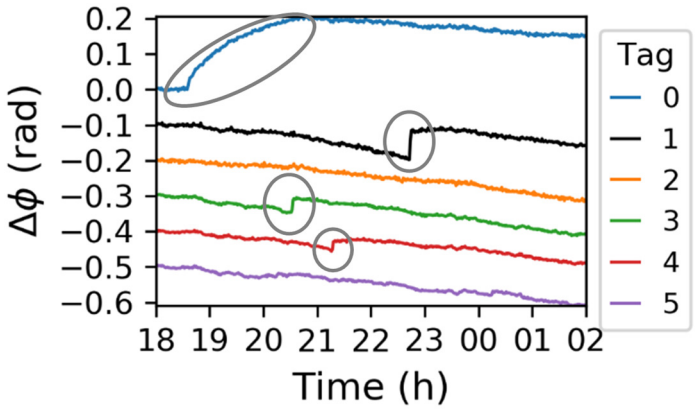


Fig. 5-10: Abrupt phase increases (circled in grey) observed on tags installed on the same zone. The tag observed on Fig. 5-9 is in black (n°1).

## 5.6 Direct propagation

### 5.6.1 Theoretical slowness and attenuation

This section presents the basic theory of microwave propagation in a dielectric medium (Balanis, 2012), applicable for snow at 866 MHz. We approximate the propagation as rays, and snow as a linear, isotropic and homogeneous low loss dielectric medium. That is partly valid up to about 2 GHz (Bradford et al., 2009). At higher frequencies, the scattering due to heterogeneities would have played a more important role, and radiative transfer theories would have been more appropriate (Picard et al., 2018; Tsang et al., 2007). For plane waves, the monochromatic propagating electric field $E$ (Volt / m) depending on the initial electric field $E_0$ and the distance of propagation $r$ in a linear isotropic material is given by:

$$E(r,t) = E_0 e^{-\alpha r} e^{-j(\beta r - \omega t)} \tag{5-6}$$

In which $\alpha$ and $\beta$, related respectively to the attenuation and velocity, depend on the complex absolute permittivity $\varepsilon^*$, permeability $\mu^*$, and conductivity ($\sigma = \sigma' + j\sigma''$) using: (Balanis, 2012)

$$\alpha = \omega \sqrt{\frac{\varepsilon^* \mu^*}{2} \left( \sqrt{1 + \left( \frac{\sigma}{\varepsilon^* \omega} \right)^2} - 1 \right)} \tag{5-7}$$

$$\beta = \omega \sqrt{\frac{\varepsilon^* \mu^*}{2} \left( \sqrt{1 + \left( \frac{\sigma}{\varepsilon^* \omega} \right)^2} + 1 \right)} \tag{5-8}$$

To simplify these equations (Bradford, 2007) we use the formulation of in-phase effective permittivity ($\varepsilon_{eff} = \varepsilon' - \sigma''/\omega$) and conductivity ($\sigma_{eff} = \sigma' + \varepsilon''\omega$) that appear when resolving Maxwell's equations. Snow can be considered as nonmagnetic ($\mu = \mu_0$), with a negligible conductivity ($\sigma' \approx 0, \sigma'' \approx 0$) and low-loss approximation ($\sigma_{eff} \ll \varepsilon_{eff}\omega$) . This leads to express the wave velocity $v$ and attenuation coefficient $\alpha$ as a function of the snow permittivity $\varepsilon$, the pulsation $\omega$, and the velocity in a vacuum: $c$ ($\approx 2.998 \cdot 10^8$ m/s) (Bradford et al., 2009)

$$v = \frac{c}{\sqrt{\varepsilon'}} \tag{5-9}$$

$$\alpha = \frac{1}{2c} \frac{\varepsilon''}{\sqrt{\varepsilon'}} \omega \tag{5-10}$$

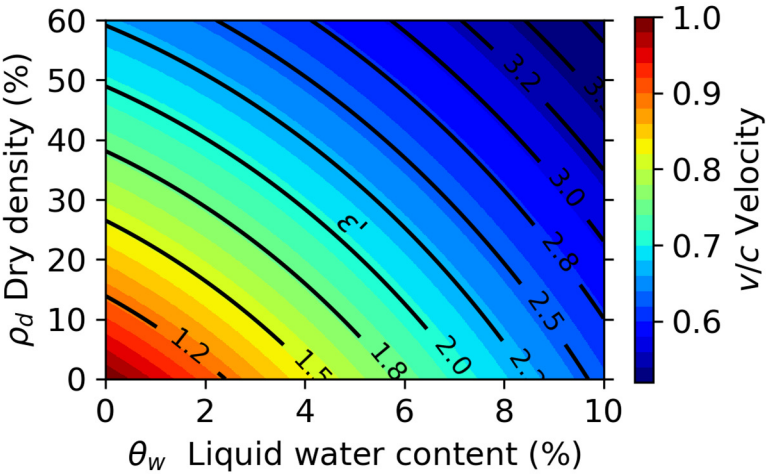


Fig. 5-11: Wave velocity (color) and in-phase permittivity (contours) of snow depending on its dry density and liquid water content at 10–1000 MHz.

The wave velocity in snow can be computed based on snow dry density and liquid water content (or density) by combining equations (5-4) and (5-9). The resulting velocity can vary strongly depending on snow properties (Fig. 5-11). In dry and low-density snow, waves would be slightly slower than in the air, whereas in dense and wet snow, the velocity would be half the velocity in the air. Over their typical range, dry and liquid volume densities would have a similar influence on velocity.

In RFID, the velocity mostly influences the phase difference of arrival. The phase is measured by the interrogator and depends on the carrier frequencies $f$ (= 865.7, 866.3, 866.9 or 867.5 MHz) *(ETSI-EN 302-208,* 2016), following the relation:

$$\varphi = -\frac{4\pi f}{v} r + \varphi_0 \tag{5-11}$$

Where $\varphi_0$ represents the propagation through the instruments (cable, electronics) and the phase shift imposed by the antenna impedances. The conversion to distance is influenced by the velocity in the volume, and $\varphi_0$ by the medium near the tag antenna (Caccami et al., 2015). In practice the phase is measured within [0, [ so it is only useful as a relative difference across time, frequency or space (Nikitin et al., 2010). This phase difference should remain within ]-π/2, π/2[ to be unwrapped without ambiguity.

The wave attenuation coefficient $\alpha$ in snow can be computed using the dry/solid snow density and the equations (5-4), (5-5) and (5-10). The loss of signal strength per path length $L$ (dB/m) and the resulting loss $\Delta P_{dB}$ depending on the distance $r$ followed by both the forward and backward path are converted to decibels using:

$$L_{dB} = -\frac{20}{\ln(10)} \alpha \tag{5-12}$$

$$\Delta P_{dB} = L_{dB} \times 2r \tag{5-13}$$

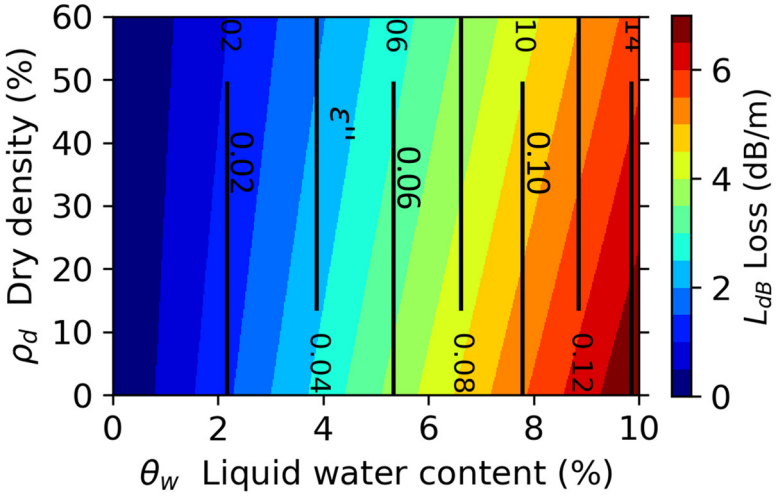


Fig. 5-12: Power attenuation (colors) and quadrature permittivity (black lines) of snow depending on its dry density and liquid water content at 866 MHz.

To conclude, the effect of snow on the phase and signal strength should depend on the thickness of snow in which the wave propagates, and on its dry density and liquid water content.

### 5.6.2 Snowpack thickness

This section verifies the influence of snow thickness and permittivity on RFID propagation experimentally. In this goal, a tag and station antenna are placed on each side of a snow volume which thickness is progressively reduced (Fig. 5-13). The resulting phase and signal strength variations are compared with a vertical profile of snow permittivities.

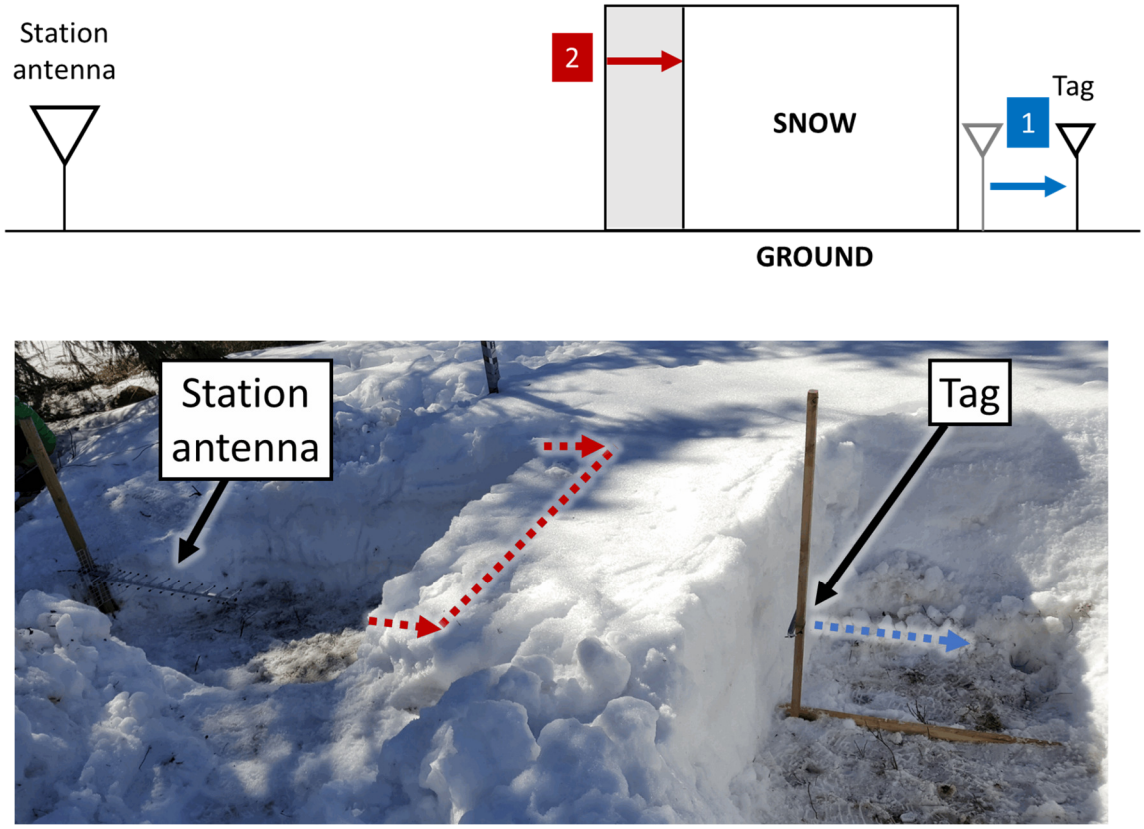


Fig. 5-13: This experiment firstly moved the tag away from the snow mass to provide a reference, then reduced the thickness of the snow between the tag and the station antenna.

The snow volume was 0.8-m-high and 1.2-m-thick, and the tags and station antenna were placed at a height of 0.4 m above the ground, initially at a distance of 3.2 m. We firstly moved the tag away from 0.1 m to 0.5 m from the vertical surface of the snow volume (stage 1, in blue) within the air, to verify that the wave velocity in the air was correctly measured. The tag then remained at a fixed distance of 0.5 m from the wall. Then, we reduced the snow wall thickness from 1.2 m to 0.9 m by consecutive slices of 0.03 m (stage 2, in red), to observe its difference of wave

velocity with the air. After this operation, the permittivity and density of the snow were measured at different heights of the volume, on the side that had just been sliced, with four repetitions at each height. The in-phase permittivity measured around 17 MHz was also used at 866 MHz, being nearly constant in the 10–1000 MHz frequency range (Denoth, 1989). We started digging snow at 15h, moving the tag at 16h20, slicing the snow volume at 16h50, and measuring its snow properties at 17h30. Each experiment lasted 20 minutes, which should be short enough for approximating a constant liquid water content.

The profile of snow permittivity and density realized at the end of the day allowed for computing a liquid water content (Table 5-3). The liquid water content was 0–2 % at 0-0.4m and increased up to 9% at the surface of the snowpack. The snow temperature measured at 0 °C at any depth confirmed that the whole snowpack was partially wet (this was true at 17h, but not at 8h). Following Eq. (5-9), permittivities of 1.8 ± 0.1 to 3.1 ± 0.2 correspond to a slowness factor $c / v$ of 1.34 ± 0.4 to 1.76 ± 0.6 at the bottom and top of the snowpack, respectively.

When moving the tag in the air, the phase varied following the air velocity, as expected (Fig. 5-14.a, in blue). A deviation to the theoretical value was observed on the first 10 measurements. That resulted from an insufficient fixation of the tag on its support, which slightly reduced the tag vertical position between each measurement. When correcting for this effect at the distance of 24 cm, the phase went back to its expected value.

When reducing the snow volume thickness, the phase varied at a rate corresponding to the slowness of 1.29 ($R^2$=0.95). The corresponding permittivity of 1.7 (using Eq. (5-9)) is consistent with permittivity measured at 2.0 ± 0.3 at the height of the tag. The snow volume near its vertical surface may have slightly melted after one hour of direct exposition to the air. That should explain why the permittivity measured at the vertical surface was slightly higher than the bulk permittivity estimated by the RFID experiment.

Table 5-4: Characterization of the snow wall

| Height (m) | In-phase permittivity ε' | | Liquid water content $\theta_w$ (%) | |
|---|---|---|---|---|
| | Mean | σ | Mean | σ |
| 0.8 | 3.1 | 0.2 | 8.7 | 1.0 |
| 0.6 | 2.4 | 0.5 | 4.9 | 3.4 |
| 0.4 | 2.0 | 0.3 | 1.9 | 2.1 |
| 0.2 | 1.8 | 0.1 | 0.0 | 0.9 |
| 0.05 | 1.9 | 0.1 | 0.9 | 1.0 |

ittivity measurement was repeated four times. The density was measured as 0.41 with ·iations of ±0.05 that were uncorrelated to depth. The temperature was measured as any depth. The measurements were made at 17h30, two hours after having dug the initial snow wall, and 15 minutes after the last snow slicing.

The attenuation expected from a snow density of 0.4 and a liquid water content of 0–2% should be $2 \times L_{dB} = 0$ to 2 dB/m (Fig. 5-12), corresponding to a signal strength increase up to 0.6 dB when removing 30 cm of snow. This increase is too small to be measured, compared to the 0.5 dB instrumental resolution and to potential multipath effects. Results showed indeed a signal strength decrease of -14 dB when reducing the snow thickness (Fig. 5-14.b, in blue). This drop is also observed when moving the tag at 20 cm from the wall, with a comparable steepness. However, the drop observed when moving the tag is temporary, and the signal strength increases back after the drop. This looks like a destructive multipath interference that would have occurred on both experiments. Similar patterns with negative peaks of signal strength had already been observed on preliminary experiments (not shown here). Multipath interferences may therefore play a major role on the signal strength, in the presence of snow.

In conclusion, this section shows that RFID has no problem propagating within a few meters of dry or almost-dry snow with an incidence angle perpendicular to the snow surface. It validates that the propagation delay within a snowpack depends on its thickness, with a velocity that can be estimated from the snow in-phase permittivity. To unwrap the phase without ambiguity, the experiment required to reduce the snowpack thickness by steps of maximum 3 cm. That is opposed to the variations of several meters needed to measure the snow attenuation properly. As a result, the attenuation was not measured. The signal strength was instead dominated by multipath effects, which we study in the following section.

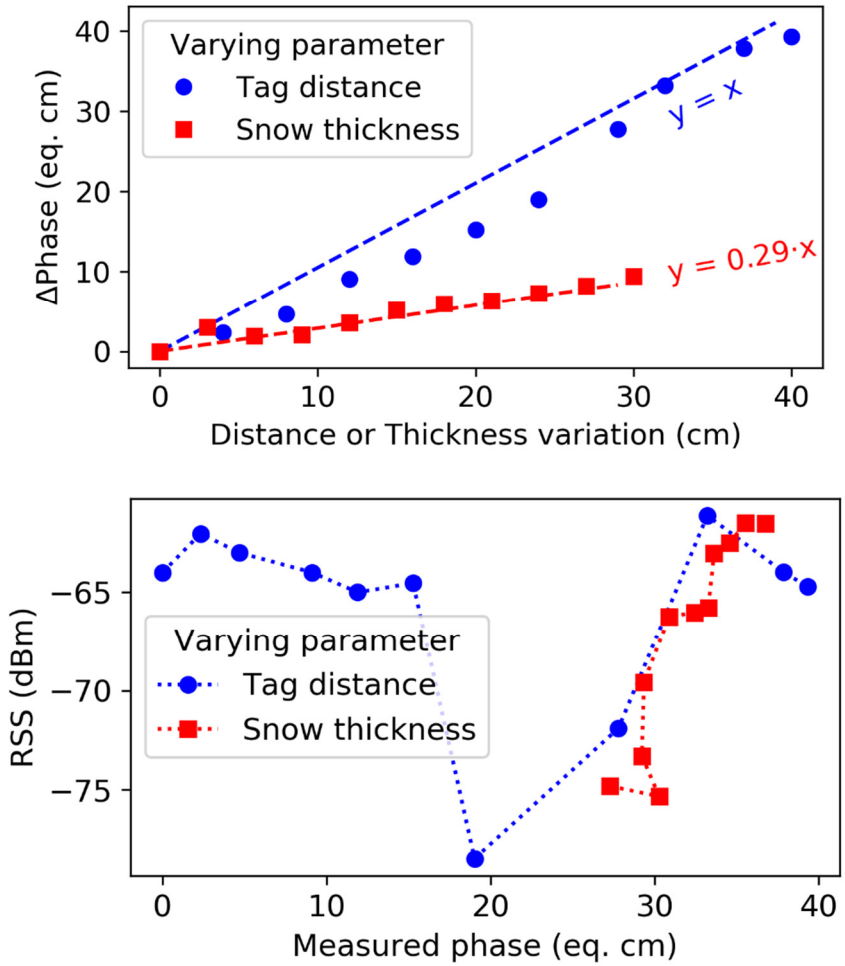


Fig. 5-14: (top) Phase and (bottom) signal strength variations while moving the tag or changing the wall thickness. The negative peak of signal strength is very probably due to unwanted ground interferences, and is observed both when moving the tag or reducing the wall. Note that the x-axis of the RSS red curve represents the equivalent electrical length using the coefficient obtained from the phase curve. (Δelectrical length= 0.29 x Δwall thickness)

## 5.7 Multipath

### 5.7.1 Theory of reflexion, transmission and interferences

This section presents the basic theory behind multipath interferences using the ray approximation. That includes the transmission and reflexion of microwaves at the interface between two medias, and the variations of the phase and signal amplitude during the propagation.

When crossing a flat horizontal interface from a medium 1 to a medium 2 (

Fig. 5-15), a wave is partly reflected in the medium 1 and partly transmitted in the medium 2. With an oblique angle of incidence $i$ , the wave partly reflects with the same angle $i_r = i$ and partly transmits with a refraction angle $i_t$, following well-known Snell-Descartes's law:

$$\sin i = n \sin i_t \tag{5-14}$$

Where $n$ is the velocity ratio $v_1/v_2$. The relation between velocity and permittivity $v = c/\sqrt{\varepsilon'}$ (5-9) in a nonmagnetic material leads to $n = \sqrt{\varepsilon_2'/\varepsilon_1'}$

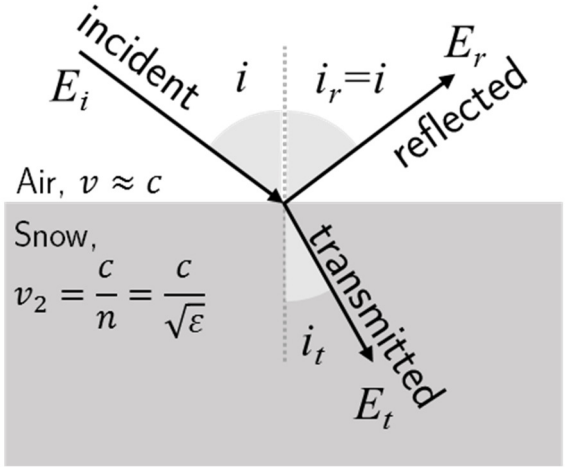


Fig. 5-15: Reflexion and transmission of a ray at the interface between air and a "perfect" snow.

The amplitude ratio between the incident electric field $E_i$ and the reflected and transmitted electric fields $E_r, E_t$ are the reflexion and transmission coefficient $R = \frac{E_r}{E_i}$ and $T = \frac{E_t}{E_i}$. These can be computed for horizontal and vertical polarization using (Balanis, 2012):

$$R_{\text{horizontal}} = \frac{\cos i - n\sqrt{1 - \frac{\sin^2 i}{n^2}}}{\cos i + n\sqrt{1 - \frac{\sin^2 i}{n^2}}} \quad R_{\text{vertical}} = \frac{-\cos i + \frac{1}{n}\sqrt{1 - \frac{\sin^2 i}{n^2}}}{\cos i + \frac{1}{n}\sqrt{1 - \frac{\sin^2 i}{n^2}}} \tag{5-15}$$

$$T_{\text{horizontal}} = \frac{2\cos i}{\cos i + n\sqrt{1 - \frac{\sin^2 i}{n^2}}} \quad T_{\text{vertical}} = \frac{\frac{2}{n}\cos i}{\cos i + \frac{1}{n}\sqrt{1 - \frac{\sin^2 i}{n^2}}} \tag{5-16}$$

The reflexion and transmission coefficients depending on the incident angle are displayed on Fig. 5-16, for either vertical (dashed lines) or horizontal polarization (plain lines). The permittivities of 1.2 to 3.2 correspond to typical snow, and 20 correspond to a typical wet soil (Hallikainen et al., 1985). The point at which the reflexion coefficient equals zero in vertical polarization is called the Brewster angle

$i_{Brewster}$. The reflexion coefficient is shown in absolute value. It is always negative for horizontally polarized waves, which means that the phase is inverted at the reflexion. The reflexion coefficient is also negative for $i<i_{Brewster}$ and positive for superior incident angles. The sign of the reflexion coefficient plays a major role in the interference pattern when summing the direct and reflected ray.

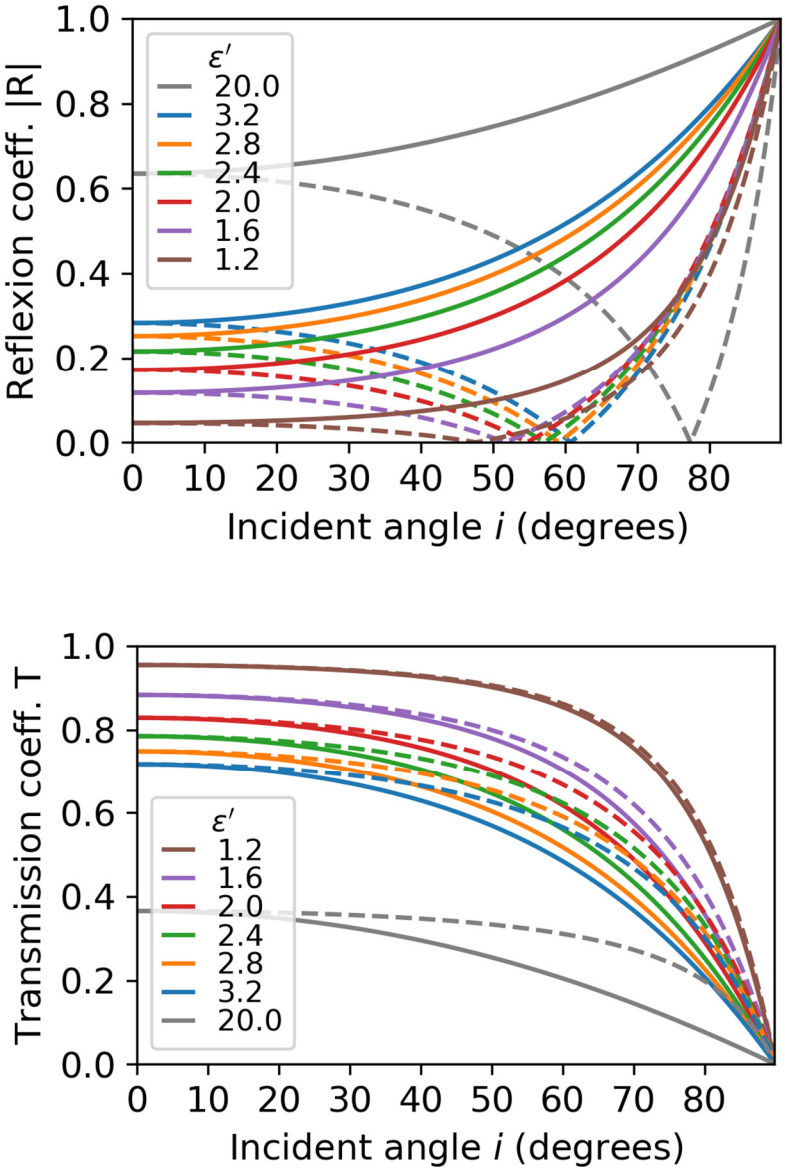


Fig. 5-16: (top) reflexion coefficients in absolute value and (bottom) transmission coefficient when arriving at the interface from air to snow, for different snow permittivities. Horizontal polarization is in plain lines, and vertical polarization is dashed. $R_H$ is always negative, $R_V$ is negative when $i<i_{Brewster}$ and positive when $i>i_{Brewster}$. Typical permittivities are in color for snow, and in gray for a wet soil.

In the case of a short-range RFID communication, the tag would receive the sum of the direct wave, the wave reflected on the ground, and waves reflected elsewhere. These multiple waves will interfere with the direct wave in a process called multi-path, illustrated in Fig. 5-17. In most of the situations outdoors, the reflected waves have a lower amplitude than the direct wave. In such case, the amplitude of $E_{total}$ would fluctuate within the maximum $E_{direct}+E_{reflected}$ when $\Delta\varphi_{reflected}=0$ and the minimum $E_{direct}-E_{reflected}$ when $\Delta\varphi_{reflected}=\pi$. The variation of phase $\Delta\varphi_{tot}$ due to the interferences would fluctuate within $[-\pi/2,+\pi/2]$ and would be null when $\Delta\varphi_{reflected}=0$ or $\pi$. The resulting effects would be applied twice to account for the forward and backward link.

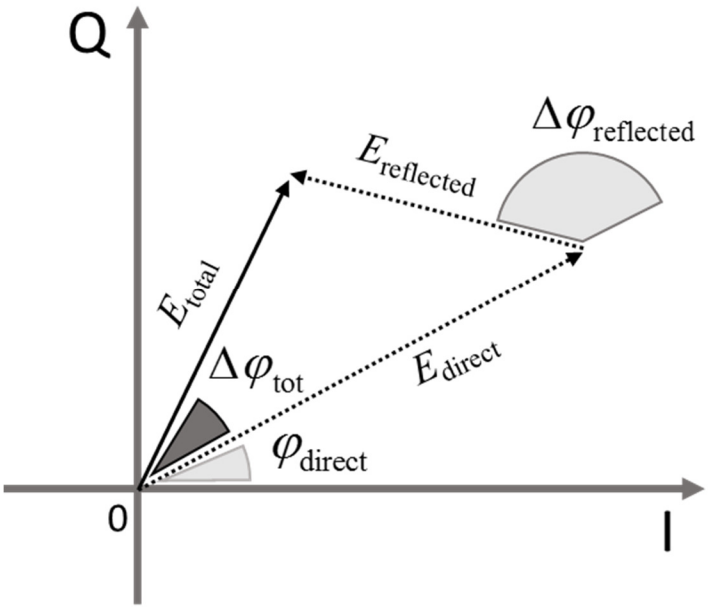


Fig. 5-17: Representation of the influence that a reflected path can have over the total signal, in the in-phase/quadrature representation. The total signal phase is shifted by $\Delta\varphi_{tot}$ compared with the ideal direct signal in free space. Its amplitude is also modified.

Radiofrequency communications are often expressed in power value instead of signal amplitude. The energy received by an antenna $P_r$ (typically a tag) depends on the radiated energy $P_t$, the gain of the transmitting and receiving antenna $G_t(i)$ and $G_r(i)$ in the direction $i$, the wavelength $\lambda$ and the distance $r$ using the Friis formula:

$$P_r(r) = \left(\frac{\lambda}{4\pi r}\right)^2 \times P_t G_t(i) G_r(i) \tag{5-17}$$

Combining the plane wave propagation equation (5-6) with the Friis formula (5-17), we can write the voltage received on the tag antenna due to the direct wave as (Pozar, 2000, section 4.5):

$$V(i,r) = \sqrt{P_{\mathrm{r}}\left(i\right)Z_0}e^{-jkr} = \frac{\sqrt{P_0 Z_0 G_{\mathrm{t}}\left(i\right)G_{\mathrm{r}}\left(i\right)\lambda^2}}{4\pi r} = V_0 \times A\left(i,r\right) \times C \times e^{-jkr} \quad (5\text{-}18)$$

With a constant $C = \lambda/4\pi$ , the receiver load impedance $Z_0$ , the initial voltage $V_0 = \sqrt{P_0 Z_0}$ , and the amplitude gain *A(i)* defined as following:

$$A(i,r) = \frac{1}{r}\sqrt{G_{\mathrm{t}}\left(i\right)G_{\mathrm{r}}\left(i\right)} \quad (5\text{-}19)$$

For a reflected wave, the amplitude gain would be adapted by computing the distance of propagation $r_{reflected}$ geometrically, and by accounting for the reflexion coefficient *R(i)* in the amplitude gain:

$$A_r(i) = \frac{1}{r}R(i)\sqrt{G_{\mathrm{t}}\left(i\right)G_{\mathrm{r}}\left(i\right)} \quad (5\text{-}20)$$

The signal can be normalized for calculation convenience:

$$s(i,r) = \frac{V(i,r)}{V_0} = A\left(i,r\right) \times C \times e^{-jkr} \quad (5\text{-}21)$$

The resulting signal arriving on the tag due to the forward propagation would be expressed as the sum of the direct and reflected rays:

$$s_{\mathrm{tot}}\left(i,r\right) = \sum_{\mathrm{n}} s_{\mathrm{n}}(i,r) \quad (5\text{-}22)$$

The wave would then be backscattered from the tag to the station, following the same path and with the same amplitude gain due to the reciprocity of the antennas gain for emitting or receiving a signal. After accounting for the modulation efficiency of the tag $L_t$ (typically -5dB), the signal $s_{full}$ received by the station antenna would be:

$$s_{\mathrm{full}} = s_{\mathrm{tot}}^2 \times L_t \quad (5\text{-}23)$$

Finally, the expected phase and signal strength resulting from the two-ways multipath are:

$$\varphi_{\mathrm{full}} = \mathbf{Arg}\left(V_{\mathrm{full}}\right) + \varphi_0 \quad (5\text{-}24)$$

$$P_{\text{full}} = \left( s_{\text{full}} \times s^{*}_{\text{full}} \right) \times P_0$$

These formulas can serve for modeling snow impact on multipath, studied in the next section.

### 5.7.2 Thin layer of snow on the ground: model

This section models the influence of removing a thin snow layer on the phase and signal strength, due to the multipath modification:

$$\Delta\varphi = \varphi_{\text{no snow}} - \varphi_{\text{snow}} \;;\; \Delta P_{\text{dB}} = P_{\text{dBm, no snow}} - P_{\text{dBm, snow}}\,.$$

The model reproduces the experiment presented in the next section. A generic illustration is shown on Fig. 5-18. The station antenna is installed at a height of $h_{station}$=1.5 meters above the ground, and a tag at $h_{tag}$= 0.4 m. The horizontal distance between the tag and station antenna is variable: x=0 to 40 meters. The incidence angle *i(x)* and the ray length *r(x)* are defined geometrically from the variable parameter x. The tag gain is 0 dBi in its preferential direction, with a radiation pattern reproduced from the Survivor B data sheet (Confidex, 2014). The station antenna is a 14dBi Yagi array antenna with 13 elements. The Yagi and tag antennas are oriented horizontally, and polarized horizontally. The snow is defined with a height of $h_{snow}$=8cm. The permittivity of the snow is fixed arbitrarily at $\varepsilon$'=2.0, which could correspond for example to a dry density of $\rho_d$=0.3 with a liquid water content $\theta_w$=4% (see Fig. 5-11). The permittivity of the soil is fixed $\varepsilon$'=20, corresponding to a typical wet soil. The attenuation within snow is neglected, due to the small thickness of the snow layer. The snow is considered homogeneous, isotropic, linear, perfectly flat and without scattering. The proximity effects of snow presented in sections 5.4.3 and 5.5.2, and the potential diffractions are not considered.

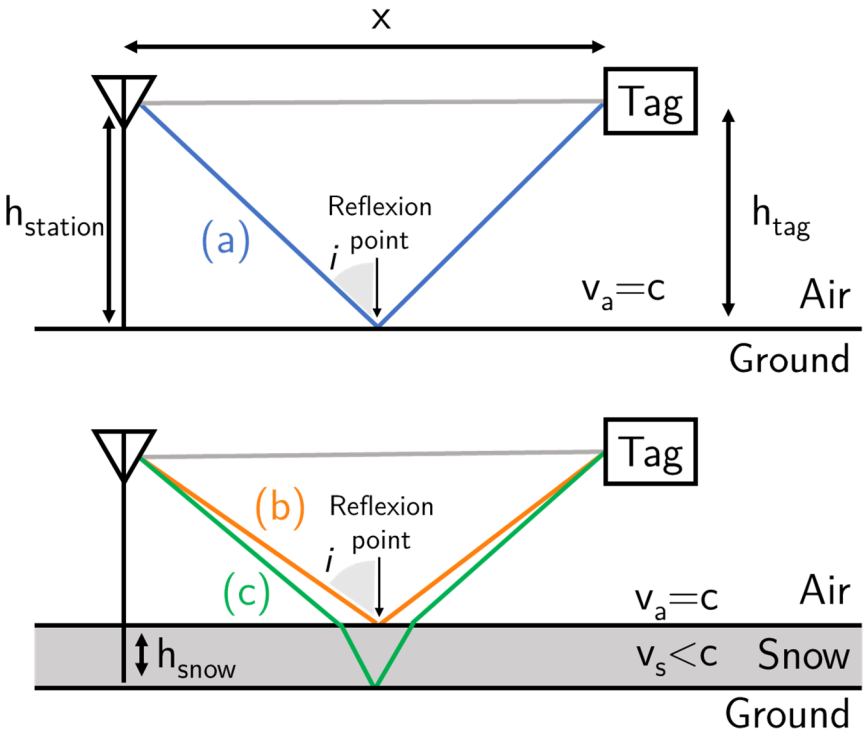


Fig. 5-18: Propagation scenarios using the ray approximation. (top) Without snow, the direct ray (in grey) interferes with (a) a ray reflected on the ground. (bottom) With a snow layer, the direct ray interferes both with (b) a ray reflected on the snow surface, and with (c) a ray transmitted in snow then reflected on the ground.

The reflected rays considered—ignoring potentially guided rays—are shown in colors on Fig. 5-18. Their amplitude depends on $A_r(i,t)$ (5-19). Computing their signal amplitude requires determining the term $A_r(i,r)$. In equation (5-20), this term depends on the reflexion coefficient $R(i)$, the antenna gain $G(i)$ and the path length $r$. The incidence angle and path length are computed geometrically as a function of x:

$$i = \text{Arctan}\left(\frac{x}{h_{station} + h_{tag} - 2h_{snow}}\right) \tag{5-25}$$

$$r = \sqrt{(h_{station} + h_{tag} - 2h_{snow})^2 + x^2} \tag{5-26}$$

Without snow ($h_{snow}$=0) only one reflected path on the ground is considered (Fig. 5-18.a). The presence of a snow layer would induce two reflected rays. The first ray would reflect on the snow surface (Fig. 5-18.b). The second ray would transmit in snow and reflect on the ground (Fig. 5-18.c) with an effective reflexion coefficient $R_{eff}$ and an effective velocity $v_{eff}$:

$$R_{\text{eff}} = T_{\text{air}\rightarrow\text{snow}} \times R_{\text{snow}\rightarrow\text{ground}} \times T_{\text{snow}\rightarrow\text{air}} \quad (5\text{-}27)$$

$$v_{eff} = v_a - \frac{2 \times h_{snow}}{h_{tag} + h_{base}} \left( v_a - v_s \right) \quad (5\text{-}28)$$

The reflexion coefficients *R(x)* are computed using equations (5-15) and (5-16) for these three rays (Fig. 5-19).

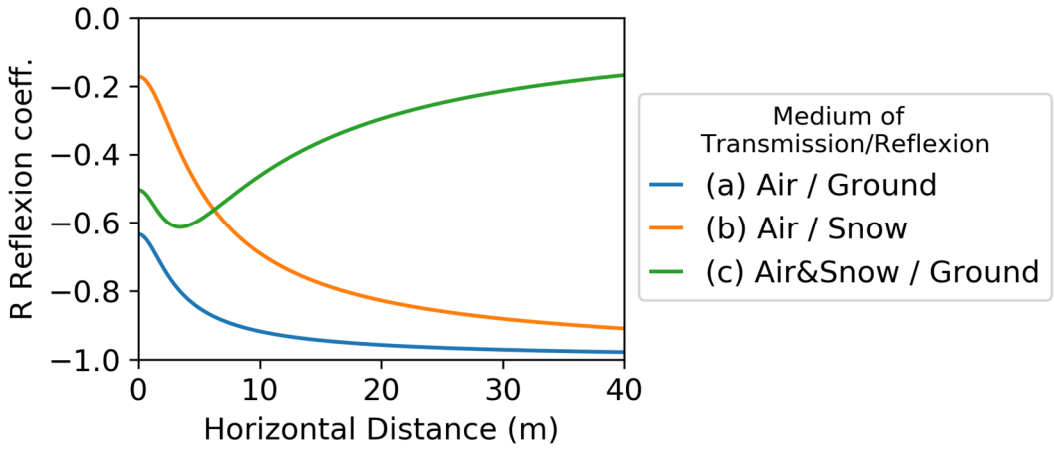


Fig. 5-19: Accounting for the reflexion coefficient of air/snow/ground interface. Without snow, we consider (a) one reflected ray on the ground. With snow, we consider two reflected rays, (b) reflected on the ground and (c) transmitted in snow and reflected on the ground. Negative reflexion coefficient represents a phase inversion.

Antenna gains depend on the radiating angle (radiating angle *i'* is related to the incidence angle $i$ with $i' = \frac{\pi}{2} - i$ ). The tag radiation pattern was retrieved from the tag constructor datasheet (Confidex, 2014) and interpolated using a polynomial regression within [-90°,90°], and the radiation pattern of the base station was computed with the script of Ilma (2016). The resulting radiation patterns are shown depending on the angle *i'* (Fig. 5-20.a) and transposed to tag horizontal positions $x$ (Fig. 5-20.a). The resulting signal gain *A(t)* is smoothed along $x$ to account for the imperfect Yagi antenna, and multiplied by the arbitrary coefficient of 0.95 to account for losses in the reflexion, for example due to rugosity. This makes the resulting interference peaks smoother and with a more realistic amplitude. The amplitude coefficient resulting from the antenna gain and ground reflexion are presented in Fig. 5-21. These are used to compute the amplitude of rays separately, before summing them.

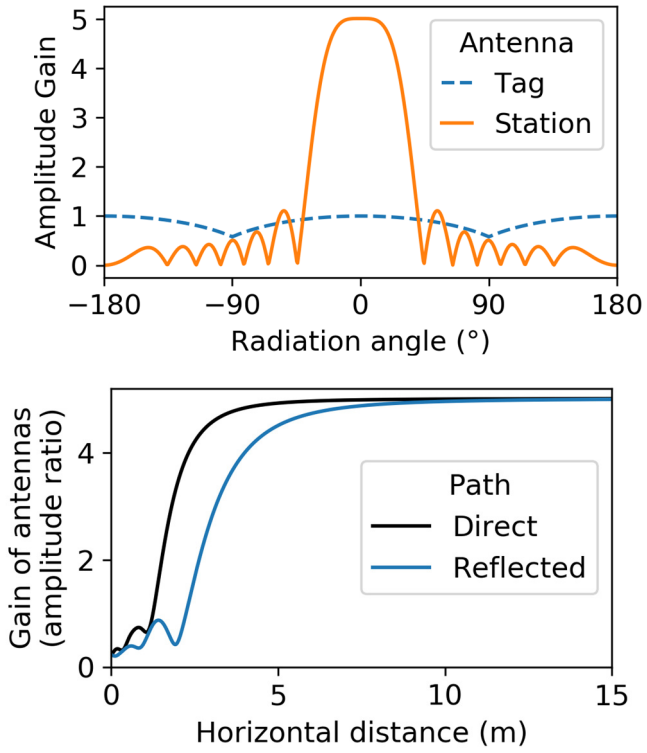


Fig. 5-20: Accounting for the directivity of the antennas. (top) Gain of the tag patch antenna and of the 14-dBi Yagi-Uda station antenna depending on the radiation angle. (bottom) Combination of the tag and station antenna gains for the direct and reflected ray, depending on the tag position.

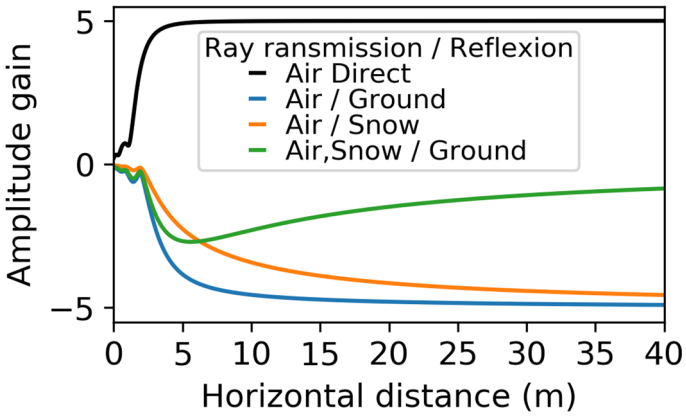


Fig. 5-21: Gain in amplitude combining antenna gain and reflexion coefficients, depending on the tag position.

The interferences of each reflected ray on phase $\Delta\phi = \phi_{\text{multipath}} - \phi_{\text{direct}}$ and signal strength $\Delta P_{\text{dB}} = P_{\text{dB,multipath}} - P_{\text{dB,direct}}$ are first presented separately (Fig. 5-22). The reflected rays on the ground and snow surface represent a typical interference pattern with one single ray. The phase error varies in the first meters

within [-π,+π]. It reaches its last negative peak when the direct and reflected path lengths differ by half a wavelength. After that, the phase error converges to zero as the reflected and direct path lengths also converge. The difference between (a) and (b) lies firstly in their amplitude, because the higher permittivity of the wet soil induces a higher reflexion coefficient. Less noticeable, the interference peaks shown on (a) are a little bit stretched compared to (b), because the tags and station antennas are slightly closer to the snow surface than to the soil. Generally, antennas far above the ground would stretch the interference peaks to great distances, and antennas close to the ground would reach the asymptote at shorter distances. The interference of (c) is different, because it oscillates with a regular period without reaching any asymptote. That is explained by the slower propagation within snow than within air. The reflected wave would be slower on average (by about 3% in this model), and moving the tag away from the antenna would regularly create interferences. A slower average velocity of the reflected path due to a higher density, liquid water content or snowpack depth would compact these oscillations in space. On the contrary, a smaller velocity difference would increase the spatial period of the oscillations. Furthermore, the amplitude of the oscillations decreases with distance on (c), due to the transmission coefficient at the snow-air surface that converges to zero when the incident angle increases (Fig. 5-16). The combined interference of two reflected rays with a snow layer (d) includes the contribution of the ray reflected on the snow surface and on the ground.

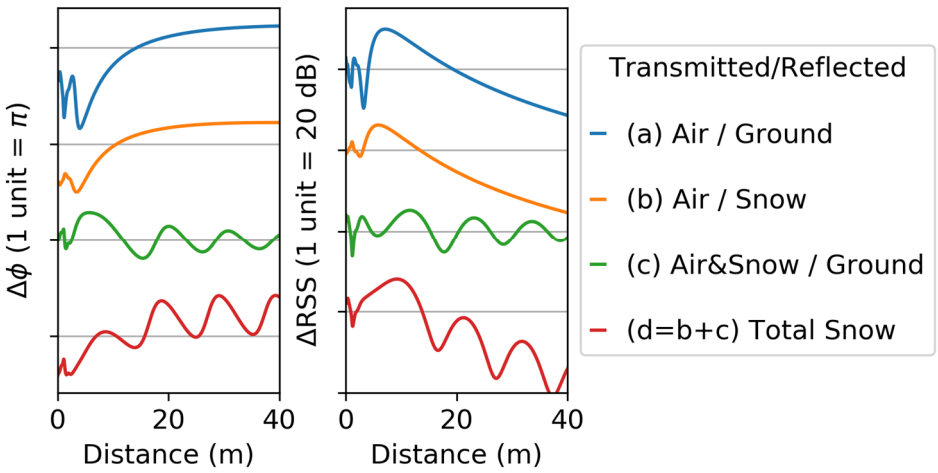


Fig. 5-22: Influence of each reflected ray on the direct ray (a) without snow and (b,c,d) with a thin snow layer. The oscillations on (c) are due to the slower propagation in the layer of snow than in the air.

The variations of phase and signal strength when adding a layer of snow should then be the difference of the curve of Fig. 5-22.d minus the curve of Fig. 5-22.a. This difference (Fig. 5-23) reveals potentially large variations of the phase (ex: -1.5 rad at 6m) and signal strength (±12 dB, and +3.3 dB at 6m). These variations are stronger in the first few meters. However, spatial oscillations of the phase and signal strength are still observable at large distance, meaning that the effect of removing a layer of snow would strongly depend on the distance between the station and the tag. In this model, the phase variation remains ≥0 at larger distances, but in real situations with non-flat topography and rugosity the influence of the phase could probably be either positive or negative.

To conclude, the influence of snow on multipath is complex, with positive or negative variations of phase and signal strength depending on the tag position. Even with all the simplifications made in the model, (homogeneous layer, flat ground and surface snow, no rugosity, and more…) the resulting interferences remain complicated. These should be even more complex in a real situation. That is studied experimentally in the next section.

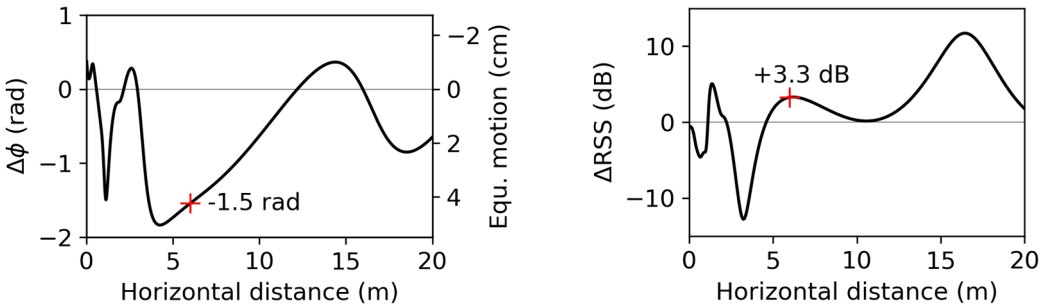


Fig. 5-23: Expected multipath effect when removing a thin snow layer (thickness of 8cm), on the phase $(\Delta\phi = \phi_{\text{no snow}} - \phi_{\text{snow}})$ and signal strength $(\Delta RSS = RSS_{\text{no snow}} - RSS_{\text{snow}})$.

### 5.7.3 Thin layer of snow on the ground: experiment

This section verifies the influence of snow on multipath interferences experimentally, under similar conditions to the model presented in the previous section. That model should be quantitatively inexact due to the many approximations compared to the reality. Therefore, the experiment leads to qualitative conclusions, to (1) validate that the multipath effect is mostly influenced by the material at the reflexion point; (2) validate the strong effect on the phase and signal strength; and (3) discriminate the multipath effect from proximity effect.

To observe the influence of snow on reflected propagation, we progressively removed a natural snow cover between a station antenna and a tag (Fig. 5-24). The snow cover was approximately 8 cm high, with unknown dielectric permittivity. The station antenna and tag were 1.5 m and 0.4 m above the ground, respectively. Their horizontal spacing was 6 m (Fig. 5-23). The snow was removed by slices from the antenna to the tag, at the distance of 4, 5.25, 5.5, 5.75, 6, 6.25 and 6.5 m from the station antenna. The reflexion point using the ray approximation would be situated at a horizontal distance of 4.8 m and 5.0 m, respectively with and without the snow layer.

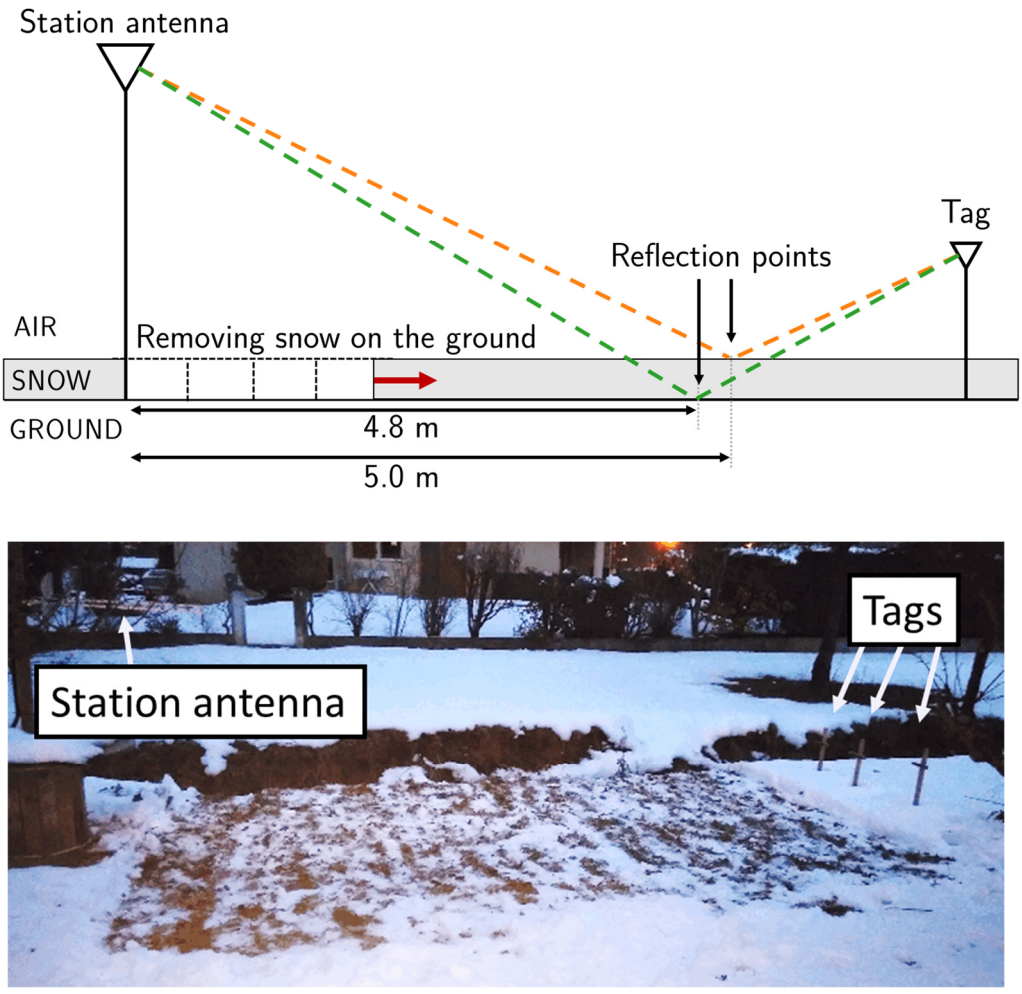


Fig. 5-24: (top) sketch and (bottom) picture of the experiment of removing snow on the ground

The phase and signal strength are shown on Fig. 5-25. Long pauses >1 minute with stable measurements are annotated with their positions, unstable measurements caused by the operator are removed. A change of colors means snow has been partially removed. The largest phase and signal strength variations, of +6 dB and -1.6$\pm k\pi$, occurred when removing the snow at the reflexion points near 4.8 m (marked as 2). That confirms that multipath has a major role in explaining the phase and signal strength variations caused by a layer of snow on the ground. The measured values are also close to the expected values of the model presented in the previous section (-1.5 rad and +3.3 dB).

The signal also varied when removing snow approximately one meter below the station antenna (+0.2 rad and -3 dB, marked as 1) and one meter near the tag (-0.4 rad and +1 to 2 dB, marked as 3). That suggests the occurrence of proximity effects not explained by the ray multipath. These should be explained by coupling

between the antenna and the surface of the ground or snow, or by a stronger contribution of scattering near the antennas. Such an effect was expected for the tag placed only at 32 cm from the snow, but not on the Yagi antenna placed one meter above snow. We suggest that the large size of the Yagi (1-meter-long, installed horizontally) may induce a higher sensitivity to coupling effects.

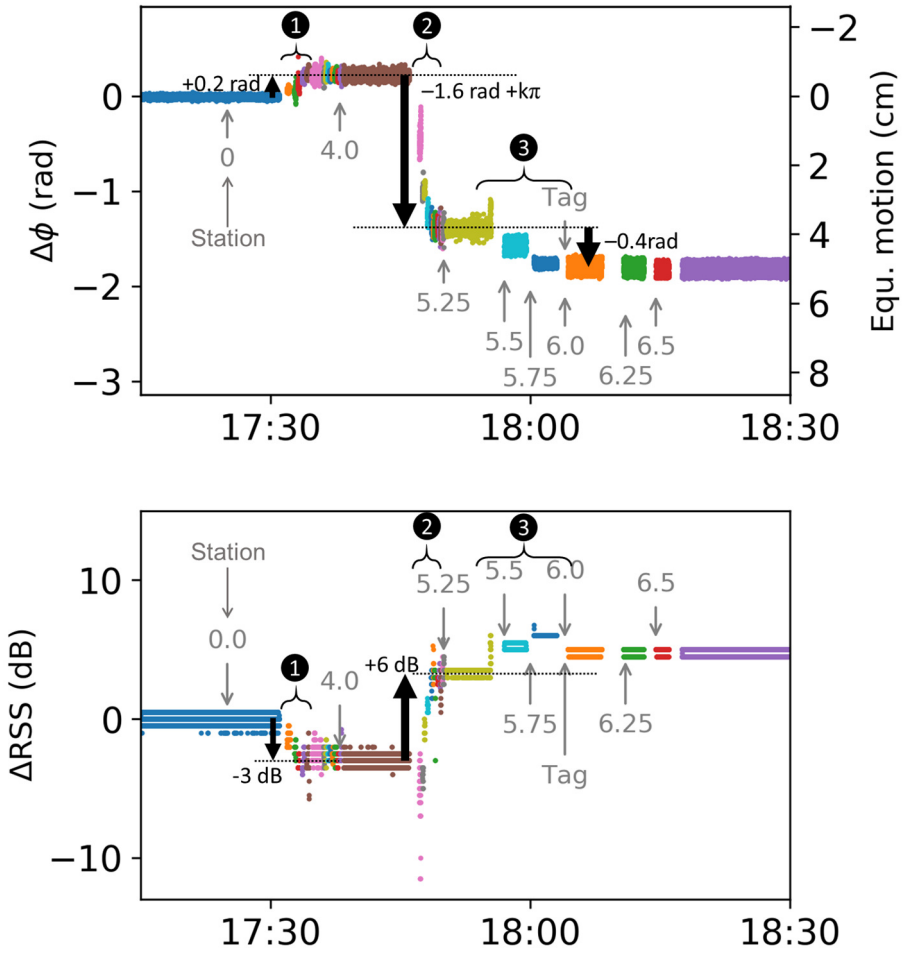


Fig. 5-25 : (top) Phase and (bottom) signal strength variations, when progressively removing an 8 cm high snow cover from the ground. The black arrows and numbers represent the length of snow remaining between the tag and the base antenna in centimeters (negative values mean that snow is removed behind the tags).

Removing snow between the reflexion point and the tag decreased the phase. In that case, the hypothesis of interference from scattered waves seems more probable, due to the large radiation pattern of the tag antenna. Moreover, the proximity effects of the tag with the snow or ground should affect the phase, due to the short distance between the tag and snow surface (0.32 m). It must be noted that removing snow behind the tag had no visible effects. That may be more favorable to the hypothesis of the scattering multipath.

This experiment could be improved, to validate the model with more confidence. Several tags should be installed at different distances from the station antenna, in order to observe the spatial oscillations of the interferences predicted in the model. Proximity effects should be reduced and better discriminated by installing the tag and station antenna higher above the snow surface. A different station antenna, such as a panel antenna, could reduce the coupling effect compared to Yagi-Uda antennas. A more advanced experiment could use two directive antennas: the first one directed towards the ground and the second towards the tag. Installing vertically and horizontally polarized tags and antennas could also validate the influence of polarization and maybe provide an indicator of depolarization due to scattering.

In conclusion, the experiment showed two effects when removing the snow: Proximity effects near the station antenna (+0.2 rad / –3 dB) the tag (–0.4 rad / +1 dB), and a multipath effect near the ground reflexion point (+1.6 rad / +6 dB). The measured multipath effect corresponds well to the previous multipath model results (+1.5 rad / +3.3 dB) with, however, a possible phase ambiguity. That validates the strong influence of snow on the ground due to multipath, even with a thin snow layer situated well below the tags and station antennas.

## 5.8 Conclusions

This study demonstrates that snow can influence RFID communication with proximity effects, direct propagation within snow and multipath. Proximity effects were measured as +2 dB and -0.65 rad when placing snow on “Survivor B” tag, but such effect strongly depends on the tag design. Proximity effects were also seen when removing a small layer of snow on the ground up to 1–2 meters from the tag (+0.2 rad / -3 dB) and station antenna (-0.4 rad / +2 dB). The proximity of the tag within 20 cm of the snow surface created an effect of +7.5 rad and -30 dB, strongly reducing the ability to read tags placed on the snow surface. This effect could be due to slow surface waves or to coupling between the tag antenna and the snow surface.

Propagation within a snow volume increased the phase wave slowness, in coherence with its measured dielectric permittivity. Direct propagation can be modelled easily with established formulas going from snow bulk properties (dry density and liquid water content) to electromagnetic properties (in-phase and quadrature permittivity) to wave propagation (slowness and attenuation) to measured the properties using RFID tags (phase and received signal strength). Such model predicts a

wave velocity that can be twice slower than in the air, and an attenuation of up to 12 dB/m, in dense and wet snow. In the experiment, however, the attenuation was too small to be measured and the received power was dominated by multipath.

The effect of multipath was shown with the experiment of removing a snow layer on the ground. This had a small effect when removing snow within 1–2 meters of the tag and station antenna due to proximity effects. However, the larger effects happened when removing snow at the reflexion point between the tag and station antenna (-1.6 rad, +6 dB). A multipath model with an 8 cm snow layer with 4% of liquid water content and a dry density of 0.4, resulted in similar results (–1.5 rad, +3.3 dB). The model shows that this effect is controlled by the snow thickness and density, but also by the position of the tag and station antenna and their horizontal or vertical polarization.

Liquid water content strongly influences the snow dielectric permittivity, and therefore all the previously mentioned effects on RFID communication. Superficial snow melting can influence the phase and signal strength of tags placed near the snow surface or within the snowpack. Daily cycles of frost deposition, melting and evaporation on the tag can also influence the phase and signal strength (-0.9 rad, -4 dB).

The models and experiments made approximations and have limits. The proximity effects would strongly depend on the tag design. The snow models ignored many phenomena: snow microstructure, multiple layers, perturbing materials (vegetation, aerosols…), heterogeneity of density and liquid water, rugosity, scattering, and irregular surface. The experiments required a good characterization of the snow, which was not always done (for example when manually placing snow on a tag) and showed the heterogeneity of the snow. Multipath created inaccuracies in any experiment, and prevented measuring the attenuation of direct propagation within snow. The presence of snow seems to create multipath patterns that appear more complex than with just the bare ground. Finally, the multipath experiment would have benefited from a shorter spatial resolution when removing the snow, from the dispatching of multiple tags at different positions. Observing the multipath using both vertical and horizontal polarization would help to understand better the physical phenomena, and could maybe provide a scattering indicator by measuring the depolarization.

Practical conclusions can be drawn, to design an RFID system that could work in snow. Using vertical polarization should reduce the amplitude of multipath interferences due to its smaller reflexion coefficient, particularly near the Brewster angle. Keeping tags above snow should avoid proximity effects, attenuation and small transmission coefficient at high incidence angles, and large phase delay that would create strong localization inaccuracies. Whenever possible, tags should not be installed near the snow surface. A tag below the snow would be easier to read, particularly at a perpendicular incidence. Frost deposition (and melting) on the tag could be minimized using a radiative heat barrier on the tag. Otherwise, measuring this effect with a self-tuning tag could also serve for correcting numerically its influence on the phase.

The main perspective is to measure the snow permittivity with RFID tags, in order to estimate locally the snow dry density, liquid water content and depth using proximity, direct propagation or multipath effects. Proximity effects, such as detuning, are already exploited by dedicated snow instruments. Self-tuning tags could provide the same measurements over large permanent sensor networks. This approach would benefit from using RFID tags: low-cost, wireless, batteryless, small size, small weight and minor heat disturbance. These tags also include temperature sensors, that would be useful to know if snow is dry or wet. Direct propagation of reflected waves is already exploited by ground-based radar, converting the attenuation and time delay into dry density and liquid water content. RFID tags could offer permanent and well-identified scatterers, and the RFID station would be 10x cheaper than a radar. Variations of phase or signal strength could be observed across time, space (multiple or moving station antenna or tags) or frequency (quadrature permittivity is sensitive to frequency). The multipath effect is already exploited to measure the snow height and estimate its water content with permanent GPS stations receiving satellite signals from different directions and under different incident angles. That could be exploited also with RFID using permanent stations and tags, or interrogating the tags from a drone instead of from a satellite. This would allow making measurements on a more restricted area than with GPS, which are obstructed for example by forests or mountains.

Measuring the snow is important for applications such as hydraulic energy, avalanche prediction and meteorology. On landslides, snow melting is a major triggering factor. Estimating the snow depth and density could allow estimating the quantity of infiltrated water and increasing the accuracy of hydrological predictions in

winter (that would be useful for the hydrological analysis presented in chapter 8). Combined with a permanent RFID phase-based displacement monitoring system (presented on the next chapter), the additional cost of installing a few tags for monitoring the snow properties would be ridiculously low. These measurements could also serve for improving the displacement monitoring accuracy by correcting partially the snow effect or providing a confidence value of the measured displacement.

# Chapter 6
# Influence of grass on RFID

**Contents**



## 6.1 Summary


This chapter studies the last major influence observed during the long-term tests outdoors. Grass varies over seasons with growth, decay, or mowing. Its moisture varies both with seasonal and daily cycles, and after rainfalls. This chapter presents experimental results highlighting the influence of grass on RFID phase and signal strength. The expected propagation delay and attenuation due to the vegetation are firstly computed, using formulas from the literature and values of density and moisture content measured on the grass. The expected values for a forward and backward path were 0.67 dB/m of attenuation and 0.56% of additional delay, due to a ray crossing a vegetated volume. Three experiments were made, that exploited the mowing of a vegetated area. Moving a tag vertically before and after mowing, allowed estimating an attenuation factor of 0.26 dB/m and a relative delay increase of 0.27%. Tags placed within the grass while progressively mowing it allowed measuring an attenuation factor of 0.46 dB/m and a relative delay increase of 0.22%

due to the grass. That confirmed the major influence of the propagation within a vegetated volume on the phase and signal strength. However, some results could not be explained by simple ray models, and require studying potential multipath. The last experiment consisted of placing tags above the grass while removing it progressively, to observe only multipath and scattering effects. The limits of the different approximations and of the use of the ray model are then discussed.

## 6.2 Introduction

The usage of Radio-Frequency Identification (RFID) tags in vegetated areas has been recently introduced for precision agriculture (Luvisi et al., 2016; Ruiz-Garcia and Lunadei, 2011) and landslide monitoring (Le Breton et al., 2019; Pichorim et al., 2018). Other usages in potentially vegetated areas include wood tracking (Björk et al., 2011), outdoor sensor nodes (Pozzebon, 2015), buried tags (Abdelnour et al., 2018) or aerial interrogation from drones (Buffi et al., 2017; Casati et al., 2017). Such applications exploit the identification, sensing or localization capabilities of an RFID system. Reading a tag requires the signal strength received by the tag and reader to exceed their respective sensitivities (see appendix 3). Received signal strength is also used for tag localization or for sensing. More recently, monitoring the phase difference of arrival allowed for more accurate localization and sensing, without impacting the readability. Received signal strength and phase appear as an important indicator for sensing and localizing tags outdoor. In this chapter, we investigate the influence of grass on the phase and signal strength during the interrogation of an RFID tag.

Vegetation, including grass, is a complex medium, highly heterogeneous in space. Its height, density and moisture content evolves over days and seasons. Trees deteriorate long-distance radio telecommunications, depending on their height, their species, and the presence of foliage. Forests would also deteriorate the communication between antennas placed 1–2 meters above the ground and at a distance <200 m, which is close to the RFID situation (Smith et al., 2016). However, this study focuses on the effect of lower vegetation, such as grass, which can grow rapidly outdoors. Grass height and moisture would influence the propagation. Indeed, the permittivity of a volume of vegetation is strongly dependent on its moisture. The relative dielectric constant of the dry matrix remains usually between 1.5 and 2.0 (for f=0.5-20 GHz), while the liquid water is around 80, and a mixing theory is presented in (Ulaby and El-rayes, 1987). The difference in the solid matrix, quantity

of water and shapes, leads to different electromagnetic properties between species. Grass may behave differently than corn, soya or grapes, for example. The dielectric constant would also depend on the temperature (El-rayes and Ulaby, 1987), particularly at the transition between liquid and solid water, already presented in the previous chapter. For example, the permittivity of a corn leave would be around 50 above 0 °C, and drop below 5 for a temperature below 0 °C.

Wave propagation in a volume of grass should therefore induce a signal strength attenuation and a phase shift due to the grass properties, and a depolarization due to scattering. The effect of vegetation on radio-frequency measurements are visible with a GPS (Rodriguez-Alvarez et al., 2011a, 2011b; Small et al., 2010). The scattering is measured by ground-based (Y. Kim et al., 2014) or satellite-based polarimetric radars (Bouvet et al., 2009; Steele-Dunne et al., 2017). These emit a wave that is backscattered by the soil and vegetation, leading to backscattering ratio HH, VV, and HV between the emitted and received wave, either at a horizontal or vertical polarization (H or V). The depolarization is expressed by the HV, and the more scattering, the more depolarization. The backscattering coefficient was shown to depend on grazing angle (and therefore slope), soil rugosity, soil moisture and vegetation (Kim and Zyl, 2009). When correcting for these effects, the vegetation waver content per soil surface (typically 0−4 kg/m2) showed a linear relation with a radar vegetation index derived from the backscattering coefficients (Kim et al., 2012). The attenuation of the ground-reflected wave by the vegetation is exploited with GPS methods. The principle is to observe the change of soil reflectivity due to the vegetation: an increase in height, density or moisture content would decrease the amplitude of the ground-reflected pat. That reduces the amplitude of the constructive/destructive interference peaks due to multipath, observed when varying the grazing angle.

The effect of vegetation on RFID—grass specifically—has not been studied yet. However, given the non-RFID studies made at radio frequencies, an increase of grass volume and moisture content should increase the propagation delay and decrease the signal strength of tags placed within the grass. Tags placed above the grass should also be influenced due to scattering and ground-reflected path, with complex effects.

This chapter present experiments made before and after mowing a flat area vegetated with grass. The results highlight the importance of the tag height relatively to the grass, and the control of the grass volume, density and moisture on its effects.

## 6.3 RFID material and grass characterization

The experiments presented observe the effect of mowing a grass field and changing its moisture content, on the phase and signal strength of an RFID system outdoors. Three experiments were made on a large flat grass field at Crolles, France, in 2—4 July 2018. They aimed at estimating the influence of a grass layer on the phase and received signal strength measured by an RFID system. In this goal, measurements were firstly made with the presence of high grass (h=0.8 m), then this grass was progressively removed, and the difference due to removing the grass was observed for tags at different positions. A first experiment consisted of moving a tag vertically above the ground, with and without grass, to see how the height of the tag would influence the measurements. The second experiment consisted of mowing progressively the grass between the tag and antenna, to observe the influence of the grass on the phase and signal strength. Each experiment is described with more details within each appropriate section.


Fig. 6-1: Principle of the experiments presented. A layer of grass was removed, to observe its effect on RFID phase and signal strength. Tags were at different heights above ground and distance from the reader.

The RFID system consisted of an interrogator (SR420 from Impinj) emitting at 865.7 MHz through a Yagi-Uda directive antenna (13 elements), to communicate with one to six tags. The tags were battery-assisted (based on the EM4325 chip) and consisted either of a patch antenna in a hard casing (Confidex Survivor B) or a slot antenna coupled with a loop (Tagsys/Mojix prototype).

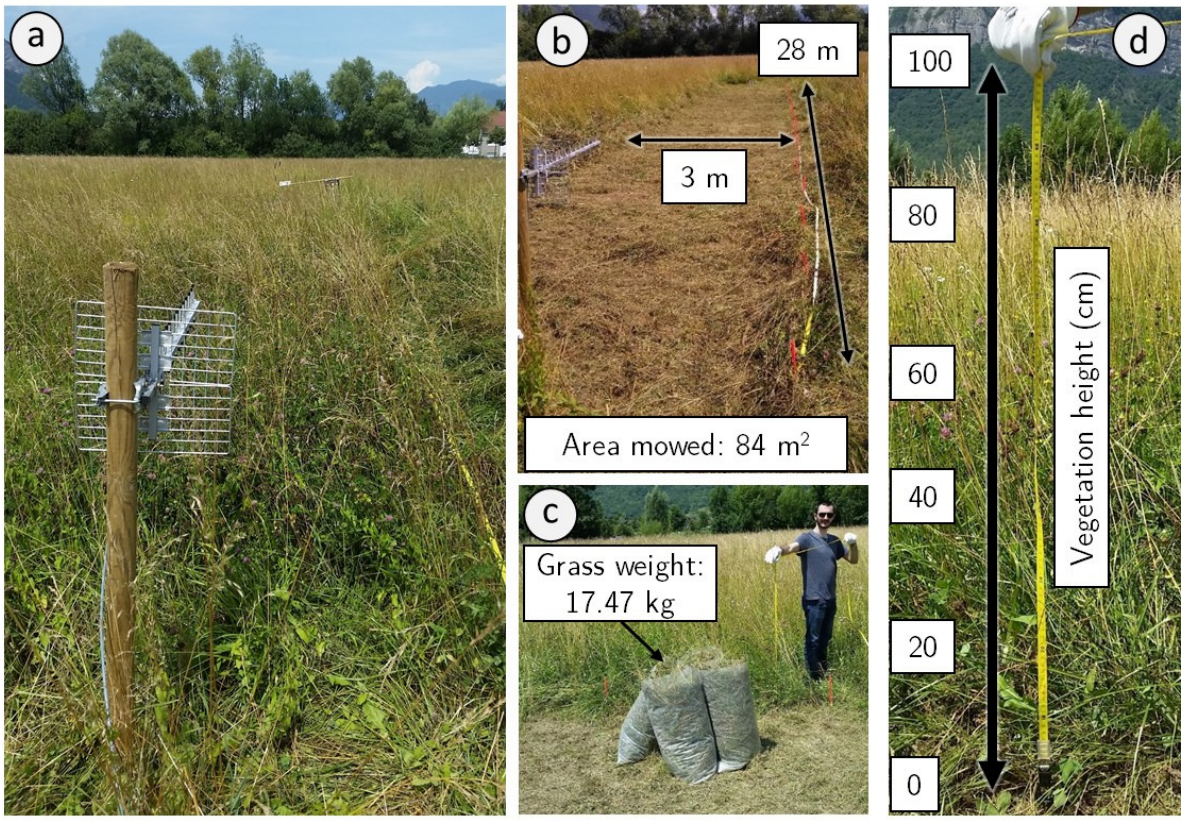


Fig. 6-2: Grass (a) before and (b) after mowing. It was weighted (c) just after mowing, and after 24 hours of oven drying. Its surface density was 0.20 kg/m², with a gravimetric moisture content of 0.65. (d) The mowed grass had a height of 0.8 m.

The grass was characterized, to estimate the wave slowness and attenuation within the volume comprising grass and air. The mowed grass was put in bags just after mowing to avoid its drying, and weighted at the end of the experiment. That allowed for evaluating a surface vegetation mass of 0.20 kg/m². With an average grass height of 0.8 m, the equivalent volume density of the vegetated volume (mix of vegetation material and air) would be 0.25 kg/m³, or $\rho_{\text{vegetated}} = 2.5\times10^{-4} = \rho_v \times \theta_v$. Where $\rho_v$ is the density of the vegetation material and $\theta_v$ the volume ratio of the vegetation material. The grass was then dried in a 100 °C ventilated oven for 24h and weighted again, to compute its gravimetric moisture content $M_g$=0.65. From in situ observation, the grass density and moisture content were higher near the ground than at 0.8 m high. This is considered qualitatively into the interpretation of the results. Similarly, the vegetation was heterogeneous across the mowed area, with different species, height, density and moisture. The measurements over large distances should, however, average this heterogeneity.

The slowness and attenuation are estimated by a linear mixing of air and vegetation material permittivities, based on their volume ratio. The linear mixing approximation is probably biased, but should help to understand several phenomenons. The relative permittivity of the vegetation material $\varepsilon_v$ was estimated using formulas of Ulaby and El-rayes (1987). These formulas depend on $v_{fw}$ the volume fraction of free water, $v_b$ the volume ration of bounded water, $\sigma$ the conductivity of the water inside the vegetation (S/m) and $f$ the frequency (GHz). Most of these variables can be estimated from the gravimetric moisture content of the vegetation $M_g$ (kg/L).

$$\varepsilon_v = \varepsilon_r + v_{fw}\left[4.9 + \frac{75.0}{1 + jf\ /\ 18} - j\frac{18\sigma}{f}\right] + v_b\left[2.9 + \frac{55.0}{1 + \sqrt{jf\ /\ 0.18}}\right] \quad (6\text{-}1)$$

$$\varepsilon_r = 1.7 - 0.74M_g + 6.16M_g^2 \quad (6\text{-}2)$$

$$v_{fw} = M_g(0.55M_g - 0.076) \quad (6\text{-}3)$$

$$v_b = 4.64M_g^2\ /\ (1 + 7.36M_g^2) \quad (6\text{-}4)$$

These formulas assume a bulk dry density $\rho_{bd} = 0.33$ and an average water conductivity $\sigma$=1.27 S/m of corn leaves (Ulaby and El-rayes, 1987). Using the measured gravimetric moisture content $M_g = 0.65$ leads to permittivity of the vegetation material $\varepsilon_v = 27.3 - j \times 10.0 = \varepsilon_v^{'} - j\varepsilon_v^{''}$ .

The vegetated volume contains mostly of air, with a small fraction of vegetation material. We estimate $\varepsilon_{veg}$ the equivalent permittivity of the vegetated volume using a linear mixture of the permittivity of air and vegetation material:

$$\varepsilon_{veg} = \theta_{air}\varepsilon_{air} + \theta_v\varepsilon_v \quad (6\text{-}5)$$

The gravimetric moisture and dry density were used to compute the density of the vegetation material $\rho_v = 0.58$ . With a height of vegetated volume $h_{veg}$=0.8m and a weight of vegetation per surface previously measured as 0.20 kg/m² leads to a volume ratio of vegetation material $\theta_v = 4.28 \times 10^{-4}$ . With an air relative permittivity of one, the mixing ratio finally leads to $\varepsilon_{veg}^{'} = 1.0112$ and $\varepsilon_{veg}^{''} = 0.00430$ . Using equation (5–9) presented in the previous chapter leads to a wave velocity $v_{veg} = c\ /\ 1.0056$ , or a relative slowness increase of 0.56%. Using equations (5–10) and (5–12) would

lead to an intrinsic linear attenuation coefficient of $L = 0.34$ dB/m , or a loss of 0.67 dB/m when considering the forward and backward path in RFID (equation (5–13)).

## 6.4 Experimental results

### 6.4.1 Influence of tag height

To measure the influence of the tag height within and above the grass, a tag was moved over a vertical support, before and after mowing the grass, on July 2 and July 4, respectively. Except for removing the grass, the conditions were almost identical between both experiments: the supporting stick had been installed 19 m away from the station antenna and not moved. However, a rainstorm that occurred between both experiments might have rotated the supporting stick by a few centimeters (see chapter 4 for more details on such problems (Le Breton et al., 2017)). To remove any potential offset, both phase curves were set to zero at their top positions. The signal strength curve was initialized from the highest value of the two curves, of -56 dBm. Finally, the displayed results only consider heights>0.16 m, below which the tag was not read in the presence of vegetation.

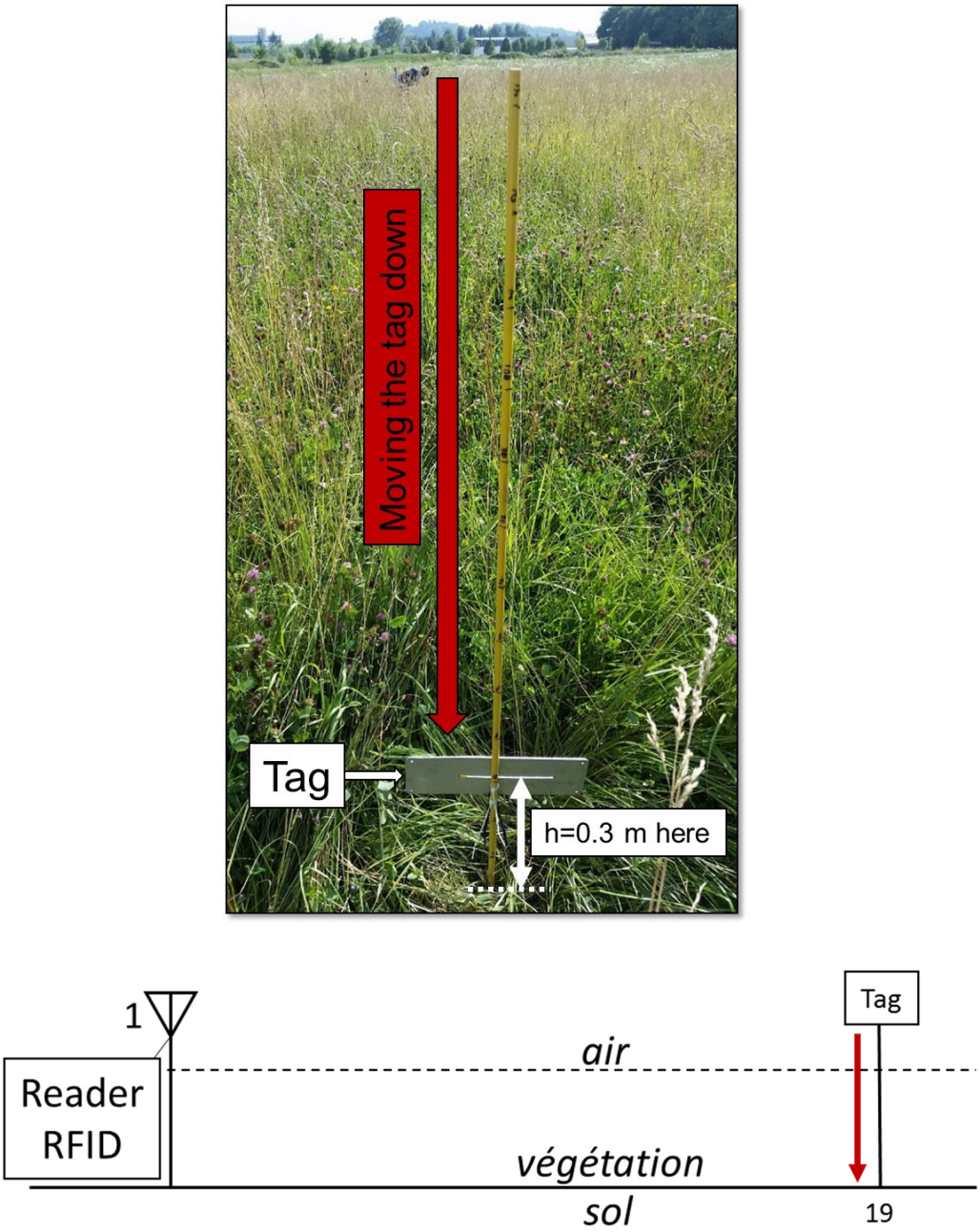


Fig. 6-3: Experiment of moving a tag vertically. (Top) Picture and (bottom) sketching. The experiment was made in the presence of grass, and repeated after mowing the grass.

The resulting variation of the phase and signal strength for both experiments are displayed on Fig. 6-4. The curves without grass show a clear effect when moving the tag close to the ground. The signal strength decreased slowly above 0.5 m (−6.5 dB from 1.25 m to 0.5 m), then started to decrease more rapidly below 0.5 m (−15.5 dB from 0.5 m to 0.16 m). The phase, also, was much influenced by the ground below a height of 0.4 m, with a drop of −1.12 rad from 0.4 m to 0.16 m high. These results highlight the influence of the ground on RFID measurements,

and show that it is better to install tags at least 50 cm above the ground. However, the goal of this chapter is to study the effect of the grass, not the ground.

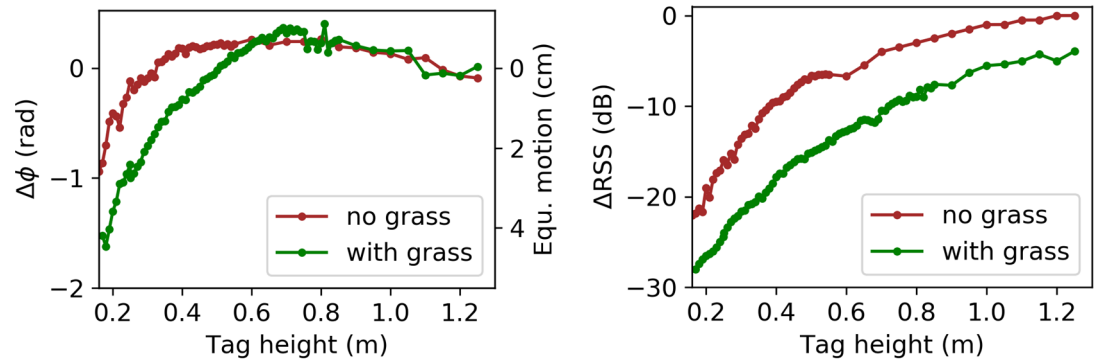


Fig. 6-4: Variations of the (left) phase and (right) signal strength when moving a tag vertically, with grass or not.

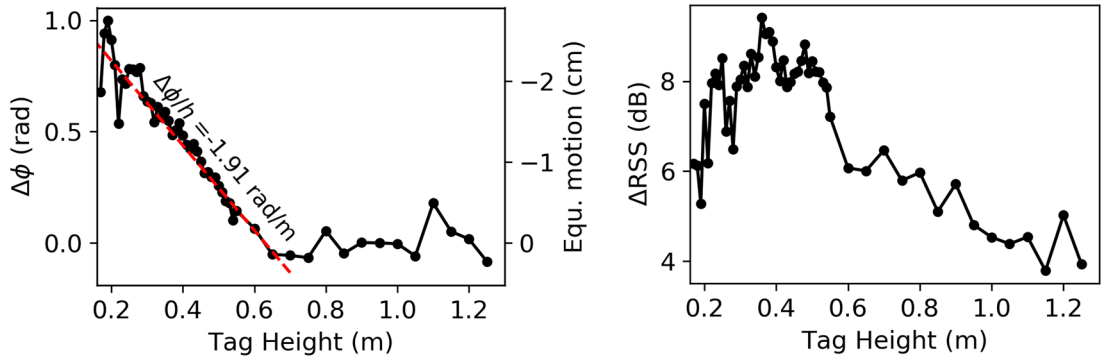


Fig. 6-5: Difference of (left) phase and (right) signal strength, due to removing the grass (i.e. $\Delta\phi = \phi_{\text{no grass}} - \phi_{\text{with grass}}$), to highlight the influence grass depending on the tag height.

To observe only the effect of removing the grass, the difference between both curves $\Delta\phi = \phi_{\text{no grass}} - \phi_{\text{with grass}}$ is displayed on Fig. 6-5.a. This phase difference was stable between 0.65 m and 1.25 m, with only small oscillations between +0.18 rad and −0.08 rad that suggest potential interferences. That suggests that the grass had no major effect between 0.8 m and 0.65 m. That is consistent with the visual observation of a parse and dry grass at this height (see the yellow grass at 0.6–0.8 m of Fig. 6-2.d)

Below 0.65 m, the phase decreased linearly with the height of the tag, at −1.91 rad/m, equivalent to -52 mm/m. After a geometrical conversion (=division by 19), this resulted in a delay per path length of –0.10 rad/m. This is equivalent to a **0.27%** relative velocity decrease, which matches the value of 0.56% estimated in section 6.3. The smaller value (by a factor 2) can be easily explained by the multiple approximations discussed in section 6.5.

The influence of the grass on the signal strength $\Delta RSS = RSS_{\text{no grass}} - RSS_{\text{with grass}}$ is different. Removing the grass increased the RSS by +4 dB at a height of 1.2 m. Then, the signal strength increased from 1.1 m to 0.4 m at 5 dB per meter high. It corresponds to a loss of 0.26 dB per meter of path length. Again, that in the same order of magnitude as the expected value of **0.67 dB/m**, but smaller by a factor 2.5. In addition to the approximations already presented, the attenuation factor could also be affected by the water conductivity, later discussed in section 6.5.1. The signal strength at heights <0.4 m then oscillated around 8 dB and finally seemed to decrease back to 6 dB at h=0.16 m with, however, strong oscillations.

In the ray approximation, the linearity of the phase decrease (and to a lesser extent of the RSS) would suggest the grass to be homogeneous within the height of 0.65−0.2 m. However, in situ observation suggested a vertical gradient of grass density and moisture content. With such gradient, the dependence of the measurements on the depth could also result from the proximity to the grass. The assumption that the variations are caused by the propagation in the grass volume, and not by a proximity effect, should then be verified. That would require modifying the grass at distances far enough from the tag (several wavelengths), to avoid potential proximity effects.

### 6.4.2 Tags below the grass: propagation in the volume

This section measures the effect of high grass placed between a tag and a station, by progressively removing this grass. Two tags were installed on a supporting stick within the grass. The center of the tags was placed at a height of 0.30 m and 0.53 m above the ground (Fig. 6-6). The station antenna was installed 19 m further, 1 m above the ground, slightly above the grass that was approximately 0.8 m high. The installation had slightly flattened the grass just behind the tags. However, the grass between the tag and the station antenna remained almost untouched.

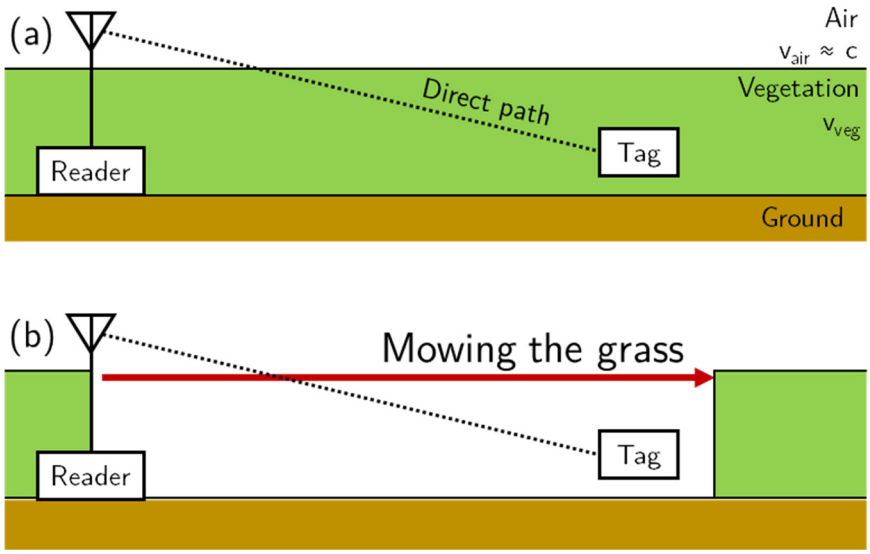


Fig. 6-6: Direct ray propagation for a tag placed in the grass (a) before and (b) after mowing the grass.

The grass was then mowed progressively from the antenna to the tags by steps of one meter and over a band of 3 m width, using a brush cutter (Fig. 6-7). After each mowing step, the grass lying on the ground was pushed on the side of the mown band, and the operator went away from the experiment for one minute to obtain stable RFID data. When reaching the tags, the brush cutter was adjusted to avoid projections on the tag, but still a little bit of grass was projected on the lowest tag (h=0.30 cm) with a larger antenna. The mowing started at 2 m from the station antenna, and ended at a distance of 29 m. The whole experiment was performed on July 4, 2018 between 11:00 a.m. and 12:30 p.m., under a cloudless sky and a strong sun. The experiment was made as rapidly as possible, to reduce the drying of the mown grass lying on the ground. The mown grass was retrieved in plastic bags just after the end of the experiment, for weighting (Fig. 6-2.c)

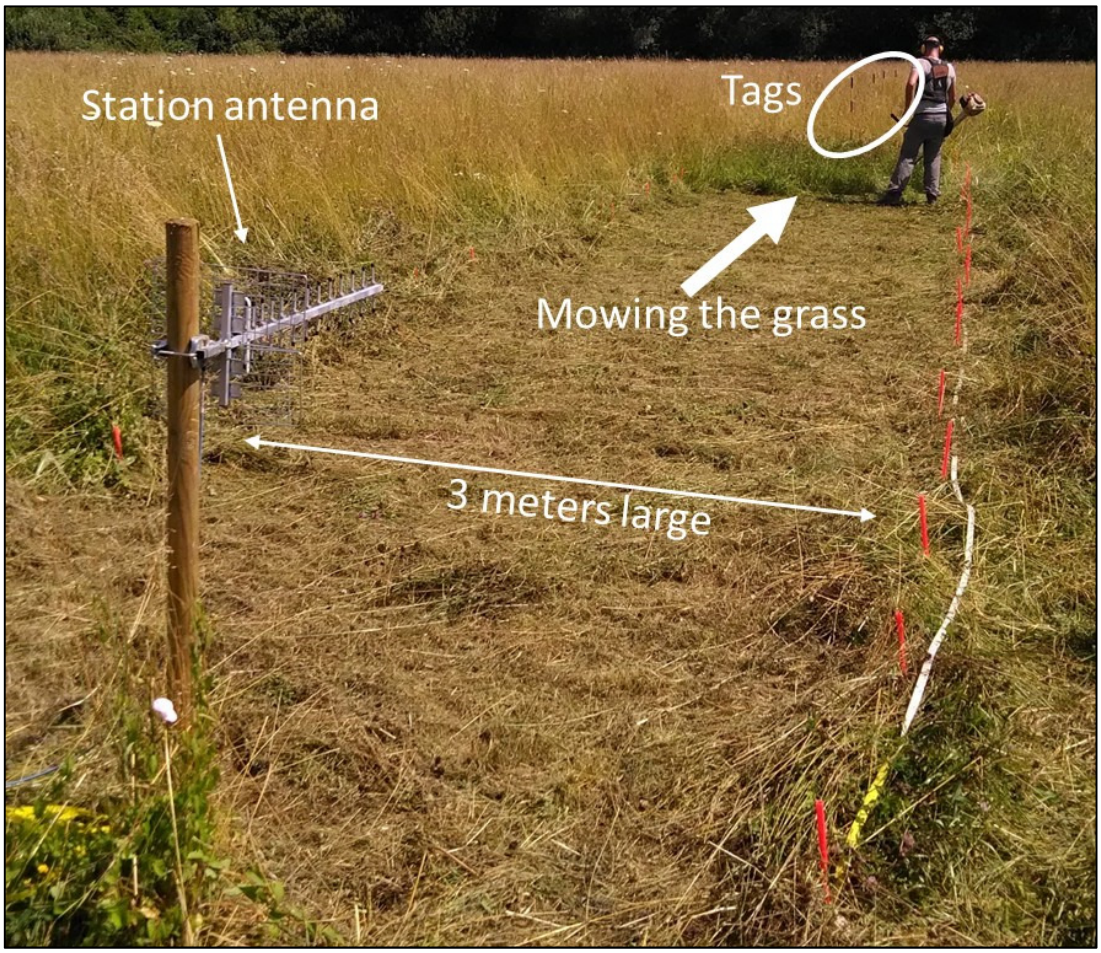


Fig. 6-7: Mowing the grass step by step

Mowing the grass was expected to increase the phase velocity by 0.56%, and to increase the signal strength by 0.67 dB/m (see section 6.3).

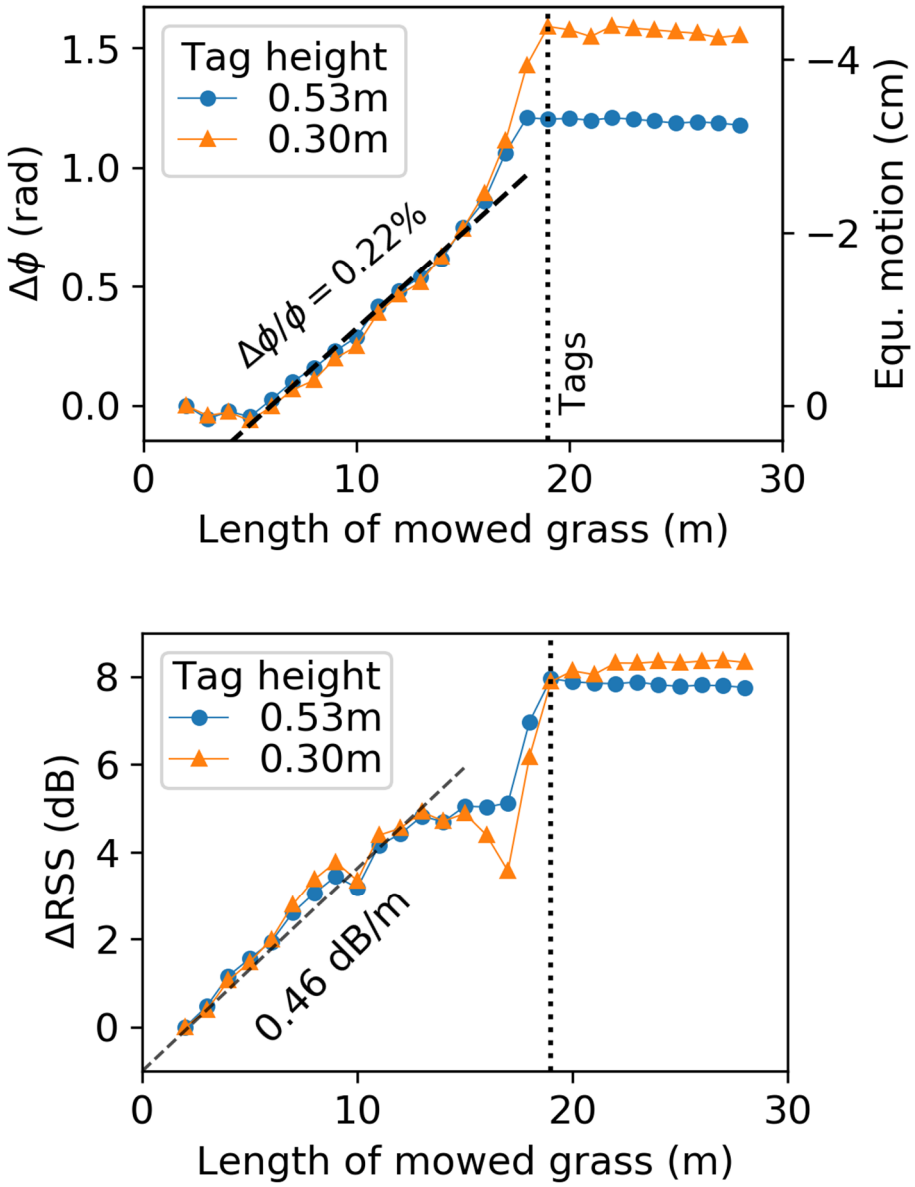


Fig. 6-8: Variations of (top) phase and (bottom) signal strength when mowing the grass, for tags below the grass

The phase variations measured while mowing the grass are shown on Fig. 6-8.a. It was almost the same for both tags, except for the last four meters before reaching the tag. There, phase of the lower tag progressively increased by an additional offset of +0.38 rad. That is consistent with the results from the vertical profile experiment (section 6.4.1), where a increasing the tag height by 0.23 m resulted in an increase of phase of +0.44 rad. The small difference should come from the different tag antennas: there was a vertically symmetric slot antenna at 0.3 m, and an assymetric patch antenna (asymetric in its casing as well due to the battery) at 0.53 m. The results would fit perfectly with placing the upper tag only 3 cm lower.

The variations of signal strength (Fig. 6-8.b) was almost the same for the two tag heights, except for a negative peak of −1 dB and −3 dB two meters before reaching the higher and lower tag, respectively.

Several conclusions can be drawn from the results displayed on Fig. 6-8. The removal of grass displays a linear effect with distance on the phase and signal strength, at distances >5 m from the tag and station antenna. The attenuation is estimated from the slope of the signal strength curve as **0.46 dB/m**. That is close, but lower, than the 0.67 dB/m expected from grass weighting (forward+backward path). The variation of slowness (or velocity) is measured from the phase slope as $\Delta\varphi/\varphi$=**0.22%**. Again, that is in the same order of magnitude, but lower, than the slowness estimated at 0.56% using the measurements of grass density and moisture content (see section 6.3). The possible reasons for the discrepancy are discussed in section 6.5. The lower delay measured with RFID than expected from section 6.3 would be consistent with a vertical gradient of grass density and moisture. Indeed, the slope of the phase curve increased when removing the last four meters of grass in front of the tags. This stronger phase increase near the tag would be qualitatively consistent with a vertical permittivity gradient, under the ray propagation approximation: The direct path would then cross the denser layers of the grass only a few meters before reaching the tag, leading to a faster phase increase when removing the last meters of grass near the tag. The lower tag (h=0.3 m) would be more affected by this effect, leading to a stronger slope than the higher tag (h=0.53 m).

The previous interpretations were based on the approximation of a ray propagation. However, one behavior in the results does not fit to the ray model. Since the station antenna was installed 1 m above the ground (=0.2 m above the grass), the ray close to the antenna should, geometrically, not be affected by the grass before a distance $x_{min}$. A simple geometric ratio estimates this distance as $x_{min}$=14 m to 9 m, for the tags at h = 0.53 m to 0.3 m, respectively. Instead, the phase started to increase at a distance of x = 5 m for both tags. Besides, the RSS increased linearly even earlier, since the first measurement at x = 2 m. This straightforward observation invalidates the ray approximation for explaining the results. A complete explanation would require to consider other effects, such as interferences from scattering and ground multipath, discussed in section 6.5.2

Some results allowed making qualitative hypotheses on the effect of scattering. Removing the grass behind the tag had no major effect on the phase and signal

strength, which suggests that the signal backscattered from the grass to the tag is negligible.

Finally, some observations are difficult to explain. First, the repeated negative peak of signal strength at the distances of 10 m and 17 m could be explained by destructive interferences. Such repetition would require the phase difference between the direct and ground-reflected path to change by $2\pi$ between the two positions. That corresponds to a virtual displacement of 0.34 m, or approximately 5% of the change of grass thickness of 7 m. This value seems too high in comparison with the relative wave slowness of the grass material of 0.2–0.5%. Furthermore, a simple geometric computation expects the multipath negative interferences to be situated at a distance from the station antenna of 13.7 and 4.1 meters for h=0.3 m and 7.9, 4.4 and 2.8 meters for h=0.53 m (destructive interferences at distances $<$ 2m are ignored). That differs from the negative peaks situated at the same distances of 10 m and 17 m for both tag heights. Therefore, those negative peaks may not be explained by simple destructive interferences from ground-reflected paths, and should be further investigated (it should be noted that such peak was not observed when tags remained above the grass, see Fig. 6-10.b). Second, the phase appeared stable when removing the grass at distances of 2–5 m, while the signal strength already increased. That might be caused by a coupling of the antenna with the ground or grass, or by the stronger effect of scattering/backscattering near the station antenna. Third, the total RSS variation after removing all the grass was independent from the tag height, contrarily to the direct path length. That is not consistent with the assumption of direct ray propagation. The next section studies the effect of the tag height with more details.

### 6.4.3 Tags above the grass: multipath interferences

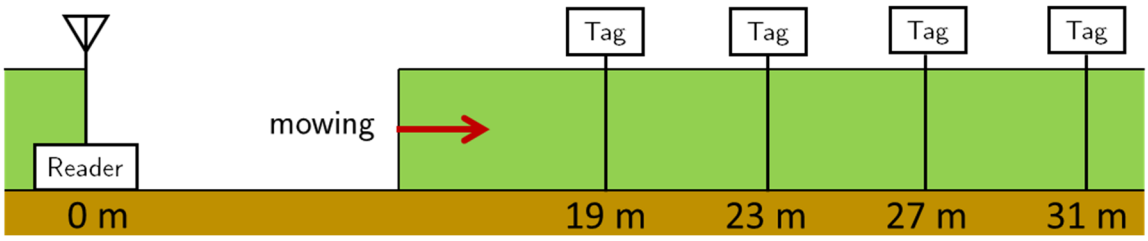


Fig. 6-9: Experiment that consisted of cutting progressively the medium to observe its impact on propagation.

This section studies the influence of the grass for tags placed above the grass, to study the influence of vegetation on multipath and scattering. Four tags were placed 1.23 m above the ground, at distances of x = 19/23/27/31 meters from the

station antenna. The grass was then mowed progressively, following the process already described in section 6.4.2.

The effect on the phase (Fig. 6-10.a) seemed to follow four steps. First, from 2 m to 5 m, the phase decreased almost linearly on the four tags, reaching a minimum between −0.08 rad and −0.13 rad. That would correspond to a relative velocity decrease of 0.07% to 0.12%, respectively. Second, the phase increased irregularly, at an average rate between +36 mrad/m (−0.10%) and +46 mrad/m (−0.13%). Then, at about ¾ of the total distance, the phase encountered a maximum peak, followed by a decrease. This decrease was sharper on the two tags at a shorter distance. Finally, after reaching the tag (marked by a cross), the phase stabilized when the grass was cut behind the tag. That confirms the predominance of the propagation effect relatively to the near-field effect. The differential phase shift when cutting the grass around each tag (the slope of the line that would connect the three crosses on Fig. 6-10.a), show a linear phase increase, with a slope equivalent to a 0.11% slowness decrease.

The overall effect on the phase was unstable, with slope coefficients alternating within ±0.1%. The slope was twice smaller in the "direct" propagation within a vegetated volume, presented in the previous section. Furthermore, the shape of the phase curves were always increasing (or stayed constant in the first 5 m) when removing the grass. The alternation of positive and negative effects is typical of multipath patterns. A tag placed at a larger distance might possibly exhibit more alternation of positive and negative peaks.

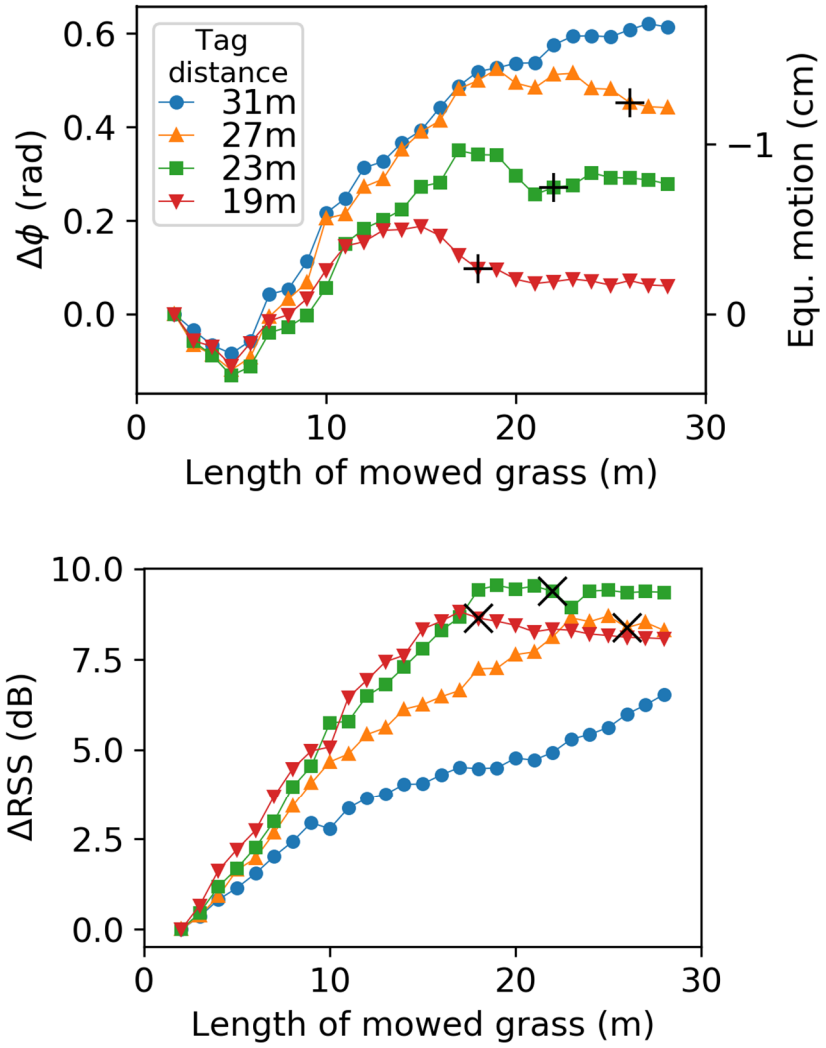


Fig. 6-10: Variations of (top) phase and (bottom) signal strength when mowing the grass, for tags at four distances from the base station. The distance of each tag is indicated by a cross.

The effect on the signal strength is simpler: the signal strength increases regularly until reaching a maximum value of +8 dB to +9.5 dB shortly before removing all the grass between the tag and the station antenna. This increase of signal strength is as strong, or even slightly stronger, than for the tags placed below the grass. The signal strength is usually more sensitive to interferences than the phase. Since no strong peak of signal strength appeared in the curve, the variations of phase might not have been caused by destructive/constructive interferences. The increase of signal strength might be explained by interference patterns that are very broad in space, due to the slightly slower waves that would be reflected on the ground. However, the consistency of the signal strength variation between tags would suggest another possible cause to this effect. At the incidence angles of 83° to 86° of the experiment, and for a soil permittivity of 5−10, the reflexion coefficient in the

vertical polarization would be between +0.42 and +0.70 (using equation 5–15). Such coefficient would result in a gain of 6−9 dB, respectively, due to constructive interferences with nearly null phase shift between the direct and reflected wave. The attenuation due to the propagation within the vegetated volume was measured between 0.26 dB/m and 0.46 dB/m in the previous experiments. Over 20 m, that could attenuate the ground reflected ray by 5−8 dB. Removing the grass could then stop the attenuation on the ground and provide a signal strength increase up to +8 dB.

To conclude, this experiment demonstrates that multipath or scattering plays an important role in the phase and signal strength results, even when the tags are placed above the vegetated volume. The multipath/scattering influence was twice smaller (±0.11%) on the phase, compared to effects due to propagation in the volume (see section 6.4.2). Furthermore, the sign of this influence depends on the position of the grass removed. The influence of the multipath/scattering on the signal strength is of the same amplitude as the variation observed for the propagation in the volume. Finally, the influence of the multipath depends on the tag position.

## 6.5 Discussion on the approximations

### 6.5.1 Average permittivity

The RFID experiments measured a relative slowness increase in the vegetation volume of 0.27% when moving a tag vertically in the grass, and 0.22% when mowing progressively the grass. The two results are very close. However, using the formulas presented in section 6.3 with the grass moisture content and bulk density measured by weighting would result in a relative slowness of 0.56%. The results are in the same order of magnitude, but the estimation from mass weighting is twice higher. That would represent an overestimation of the equivalent in-phase permittivity based on density and moisture. Similarly, the RFID experiment measured a loss of 0.26 dB/m and as 0.46 dB/m, compared to the estimation of 0.67 dB/m from grass mass weighting. That would represent an overestimation of the equivalent quadrature permittivity based on the density and moisture data. The discrepancy could come from the grass itself, due to a vertical gradient and a rainstorm occurrence. It could also come from the formulas used, to compute the bulk grass permittivity and mix it linearly with the air. Given all these assumptions and approximations, a factor of two between the expected and measured value seems acceptable.

A vertical gradient of vegetation density and moisture was observed visually on the vegetation, with a higher density and moisture near the ground. On Fig. 6-2, for example, the grass below 0.6 m was greener than the grass at 0.6–0.8 m. Therefore, the wave slowness and attenuation should be more important near to the ground, and could be negligible on the top layer with a very parse and dry grass. That would correspond very well to the results from the vertical profile, where the influence of the vegetation on the phase started only at a height <0.65 m. This gradient would result in an overestimation of the equivalent permittivity on the top layers, and an underestimation close to the ground. The overestimation is consistent with the experiments, particularly with a ray model for which the direct path would never cross the layers very close to the ground.

A rainstorm occurred between the experiments of the first day (section 6.4.1) and the last day (sections 6.3, 6.4.2 and 6.4.3). It may have changed the moisture content, leading to differences between the results of both sections.

Water in vegetation has a high ionic conductivity, measured for example around on corn leaves (Ulaby and El-rayes, 1987). That results in the conductivity controlling the quadrature permittivity at 868 MHz (see equation (6-1)). However, the conductivity of the grass samples had not been measured, and could have differed from the average value suggested by Ulaby and El-rayes (1987). That should add a strong uncertainty on the estimated attenuation.

The formula used to compute the bulk grass permittivity has an uncertainty measured at ±20% for corn species (Ulaby and El-rayes, 1987), mostly due to the usage of a standard dry bulk density of the vegetation, not measured in our study. However, this uncertainty was for corn leaves. The formulas were supported by a physical mixing theory of dry bulk vegetation material, bounded water and free water. The formulas should therefore work on other species than corn, but probably with a higher uncertainty.

Finally, the approximation of linear mixing of air and bulk grass permittivities (equation (6-5)) was a first-order approximation, not supported by existing studies. Such model should obviously be biased, and increase the error. Furthermore, the assumption of a homogeneous medium should also induce bias, particularly due to the possible scattering effect resulting from the vegetation heterogeneities.

### 6.5.2 Limits of the ray model

The slowness/attenuation estimation was based on a ray propagation approximation. However, some results from the progressive grass mowing experiment, with tags below the snow, showed clear discrepancies with the ray propagation model: the vegetated volume was influencing the results even when it was not crossed by the direct ray. Indeed, in the literature, vegetation is often considered as a scatterer at microwave frequencies, even for thin vegetation at wavelengths >10 cm (Chiu and Sarabandi, 2000; Egido et al., 2014; Kim and Zyl, 2009).

The scattering should also affect a dual ray modeling of the ground-reflected interferences. The ray multipath model — previously used successfully for snow and to simulate interference in a convex topography (see appendix 2) — was tested with this data. However, the modelled results (not shown) could not fit the experimental results. The overall magnitudes were the same in the model as in the experiments (perturbation of ±0.11% due to multipath, that depend on the tag position, with positive/negative alternation, and losses variations of up to 10 dB), but the discrepancy in the values and their sign was too high. Strong perturbations of the model input parameters could lead to correct phase values, but with incorrect signal strength values, and vice versa. A full explanation of these results may require using a different theory than the ray propagation.

If further models were made, they should probably use theories that fit to multi-diffusion scenario, such as modeling wave propagation with multiple heterogeneities, or using radiative transfer theory or diffusion theory. Such theories applied for example in seismology (Obermann et al., 2013b). In the vegetation, models of scattering propagation have been proposed (Brown and Curry, 1982), by modeling for example the leaves with disks (Karam and Fung, 1983) or the vegetation body with cylinders (Huang et al., 2017).

If further experiments were made, they should try to better observe the multipath and scattering effects. Firstly, tags should be dispatched tags over wider distances to observe potential spatial oscillations of the multipath effects. Then, tags should be polarized either horizontally or vertically. Indeed, the vertical shape of the grass could result in different effects depending on the polarization. Finally, the depolarization might be measured by installing tags that are polarized perpendicularly to the station antenna.

## 6.6 Conclusions

This study shows experimental evidence that grass influences the phase and signal strength of an RFID system. The strongest influence should be on the direct wave crossing the vegetated volume. The attenuation and delay seem linear to the distance of vegetated volume. Their value estimated theoretically from the grass density and moisture were close to the values measured with RFID, by a factor 2.5. Measuring the dry grass density should better constrain the estimated delay, and the water conductivity should constrain the attenuation. An improved second order mixing formula should also provide better estimation of the effective slowness and attenuation of a vegetated volume.

Grass would also affect tags placed above the vegetated volume, and direct rays that do not cross the vegetation volume. These effects may occur from the combination of ground multipath and vegetation scattering. A better understanding of these effects might require using multi-diffusion models.

Knowing the effects of grass on direct and indirect propagation could provide an indicator of accuracy for displacement tracking applications. For practical RFID usage outdoors, the vegetation should be kept lower to avoid problems, if possible. Otherwise, tags would be better installed at a height of at least 0.5 m above ground, and above the grass. Tags above the vegetation would still be affected by multipath, with a low influence on the phase but a strong one on signal strength. The loss of RSS due to the grass, of about 8–10 dB, should be taken into account when installing tags. Finally, these effects could be exploited to lead to new applications. For example, the vegetation volume ratio, height, moisture or conductivity, might be measured with an RFID system, for precision agriculture applications.

# Part 3 — Applications to landslide monitoring

# Chapter 7
# Monitoring landslide displacements with RFID

*Published as Le Breton, M., Baillet, L., Larose, E., Rey, E., Benech, P., Jongmans, D., Guyoton, F., Jaboyedoff, M., 2019. Passive radio-frequency identification ranging, a dense and weather-robust technique for landslide displacement monitoring. Engineering Geology 250, 1–10. https://doi.org/10.1016/j.enggeo.2018.12.027 .*

*Patented as Baillet, L., Le Breton, M., Larose, E., Jongmans, D., Rey, E., Guyoton, F., 2018. Procede, systeme et programme d'estimation du deplacement d'une structure geologique et/ou de genie civil susceptible de se deplacer. WO2018197824A1.*

*This work was part of the public exhibition 'Les Mondes Inconnus' at Grenoble Natural History Museum, from October 2018 to July 2019, with 10 000+ visitors.*

*This work received the 'Outstanding Student and Pico Poster Award' at the European Geoscience Union General Assembly 2018 and the 'Best Poster Award' at the Rock Slope Stability Symposium 2018.*

**Contents**



## 7.1 Summary

Ground deformation monitoring at a local scale requires accuracy, along with dense spatio-temporal resolution. Radio-Frequency Identification (RFID) technology is proposed as an alternative to classical geodetic methods for monitoring displacements of a landslide. Passive RFID tags allow for a very dense resolution, both

in time and space, at the scale of a 100-m-long surface. By deploying 19 passive RFID tags on a landslide for 5 months, this study validates the technique by comparison with laser total station and wire extensometer data. The accuracy of the RFID technique was 1 cm during normal weather and up to 8 cm during snow events. The results demonstrate that RFID tag tracking can monitor landslide displacements with multiple sensors at low cost, providing dense spatio-temporal data. This technique could potentially be used for other applications such as monitoring volcanic activity, buildings, unstable rocks or snow cover.

Highlight

- Passive RFID is a new method to monitor surface displacements on a landslide.
- RFID works across vegetation, fog, rain and snowfall.
- This first prototype allows for a wireless monitoring at a range of 60 m.
- Displacement accuracy reaches 1 cm in general and 8 cm with a snow cover.
- Low-cost RFID tag network provides data with high spatio-temporal resolution.

## 7.2 Introduction

Ground deformations are monitored at different scales. On a scale of a few hundred meters, a landslide creates surface displacements that vary in both time and space. Motion monitoring to understand the landslide mechanism requires the best possible spatial and temporal resolution. However, obtaining a high spatial resolution is expensive at the scale of landslides, owing to either the station or the multiple measurement points. Large-zone monitoring techniques, such as ground-based radar interferometers, laser scanners, robotic total stations and fiber optics (Monserrat et al., 2014; Jaboyedoff et al., 2012; Iten et al., 2008) have a high station cost (30–100 k€), which restrict their use in standard applications. Similarly, more localized techniques such as GPS and extensometers have a cost per point (1–10 k€) that make them economically inefficient for a spatially-dense network of sensors (Gili et al., 2000; Angeli et al., 2000). The development of low-cost single-frequency GPS (Benoit et al., 2015) and radio-frequency transponders (Kenney et al., 2009; Intrieri et al., 2018a) reduced the cost to 100–1000 € per point, but each instrument still requires its own power source, which considerably increases the cost of the material, its installation and its maintenance. Satellite Remote sensing techniques

are economically efficient but their best current time resolution is 4–6 days (Intrieri et al., 2018b; Milillo et al., 2014; Lacroix et al., 2018). Similarly, ground-based optical correlation barely exceeds a 1-day resolution (Travelletti et al., 2012) because of low light at night and other luminance variations. Furthermore, some techniques are completely unusable in specific conditions: GPS signal may be blocked by steep slopes and high trees, optical techniques may be hindered by fog, rain, snow and vegetation, and extensometers may be obstructed by snow, ice or animals. In comparison, Radio-Frequency techniques continue to work in the presence of rain, fog, snow and vegetation, although environmental conditions may affect accuracy. Given these facts, Radio-Frequency Identification (RFID) (Heidrich et al., 2010) appears to be a viable alternative in terms of cost, spatio-temporal resolution and weather robustness.

Billions of passive targets, or tags, are produced by the RFID industry every year (Das, 2017) to identify goods remotely, leading to numerous research and business applications (Ngai et al., 2008; Tzeng et al., 2008). Tags typically comprise a passive microcircuit connected to an antenna. They communicate with a station that consists of a reader connected to another antenna. This communication relies on a continuous radio-frequency wave emitted by the station, this wave powers the tag, which then backscatters a modulated wave that encodes its own identification number, and the station reads this number (*EPC Gen2*, 2015). Passive tags and stations currently cost 0.01–20 € and 2–4 k€, respectively, and the reader can identify 30 to 800 tags per second (*EPC Gen2*, 2015; Klair et al., 2010). These advantages have already been exploited in RFID applications in earth-science research, such as to sense soil moisture levels or vibrations (Pichorim et al., 2018; Jayawardana et al., 2016), measure crack openings (Cazeca et al., 2013; Caizzone and DiGiampaolo, 2015), or trace alluvial and coastal sediment (Lamarre et al., 2005; Nichols, 2004). However, continuous displacement monitoring with RFID remains untested outdoors.

Several methods have been developed to locate passive tags (Miesen et al., 2011). These methods usually estimate the 1D range or displacement between a tag and a station antenna, and optionally locate the tag in 2D or 3D using multiple station antennas. These ranging techniques can use the Received Signal Strength (RSS) (Griffin and Durgin, 2009; Ni et al., 2003), the Phase Difference of Arrival (Vossiek and Gulden, 2008; Nikitin et al., 2010) or more recently the Time of Flight (ToF) (Arnitz et al., 2010; Arthaber et al., 2015). Currently, phase-based methods are

compatible with commercial readers and offer the best accuracy. Several studies used the phase to localize tags with an accuracy of one centimeter or less (Scherhäufl et al., 2015; Wang et al., 2016; Zhou and Griffin, 2012)(Akbar et al., 2015a; Miesen et al., 2013a; Scherhäufl et al., 2015; Wang et al., 2016; Zhou and Griffin, 2012)

However, these experiments were of short duration (<1 h), over a short range (<10 m) and were performed indoors. When these techniques are used outdoors, environmental fluctuations could affect their accuracy. A previous study showed that moisture and temperature variations could create a phase drift of up to 20 cm over a year (Le Breton et al., 2017a). Corrections were proposed, which reduced that drift to <2 cm per year, with a temporary reversible error of 7 mm induced by rain. However, the short tag-station distance (6 m) limited the effect of multipath propagation in that study. The effect of multipath propagation may be increased at long range and outdoors and passive RFID has never yet been studied in these conditions.

Hectometer-range outdoor radio-frequency ranging has nevertheless been assessed on landslides using active transponders. The ranging techniques were based either on RSS, ToF or Phase, with displacement accuracies of 100, 5 and 1 cm, respectively (Lucianaz et al., 2015; Intrieri et al., 2018a; Kenney et al., 2009). Since these techniques use the same physical principles as passive techniques, phase-based RFID ranging is also expected to have a displacement accuracy of 1 cm outdoors. As to the maximal range attainable, manufacturers claim ranges of up to 60 m for passive tags (Confidex, 2014); this range may be sufficient for the goals of this study.

The previous studies then suggest that a dense network of passive RFID tags could be deployed on hectometer-scale landslides at low cost, to monitor 1D radial displacements with an accuracy of 1–2 cm in a variety of meteorological conditions. To test the performance of RFID, for five months, we monitored the displacements of 19 tags placed 5 m apart on a medium-sized landslide (Pont-Bourquin, Switzerland) and compared the results to those obtained with total station and extensometer data. We provide an example application that benefit from the RFID technique, studying the relation between the rainfall and the velocity of this landslide, and finally discuss the advantages and limitations of RFID displacement monitoring.

## 7.3 Material and Methods

### 7.3.1 Experimental site: Pont-Bourquin landslide

The Pont-Bourquin landslide lies in the Swiss Pre-Alps, 50 km southeast of Lausanne (Fig. 7-1.a). The landslide crosses a complex geological zone composed of Triassic to Jurassic sediments, including gypsum, cargneule, shale siltstones and black shales, separated by tectonic thrusts (Badoux et al., 1990). Quaternary moraines partially cover the slope. The landslide material thus mixes all these sediments, with a dominant proportion of clay produced by degradation of black shale.

The landslide is about 240 m long, 30 m large (Fig. 7-1.b) and 10 m deep (Jaboyedoff et al., 2009). Its average slope is around 25° facing south. The total landslide volume is approximately 40,000 $m^3$, which includes an active part of around 11,000 $m^3$. The landslide mostly moves translationally, with a slight rotation at its top. Orthophotos from 1995, 1997 and 2004 revealed continuous degradation due to slope movements and erosion in the landslide area. In 2006, a scarp of 0.8 m was observed at the top of the landslide. On 5 July 2007 a sudden earthflow of around 3000 to 6000 $m^3$ occurred after 95 mm of rain fell over a 3-day period (Jaboyedoff et al., 2009). In subsequent years, the landslide permanently moved by a few meters per year, before suddenly accelerating its descent in summer 2010 leading to a mudflow of a few thousand cubic meters that blocked the road downslope on 19 August 2010 (Mainsant et al., 2012b). Due to its continuous activity, this landslide appears to be a good candidate to test the RFID technique over several months.

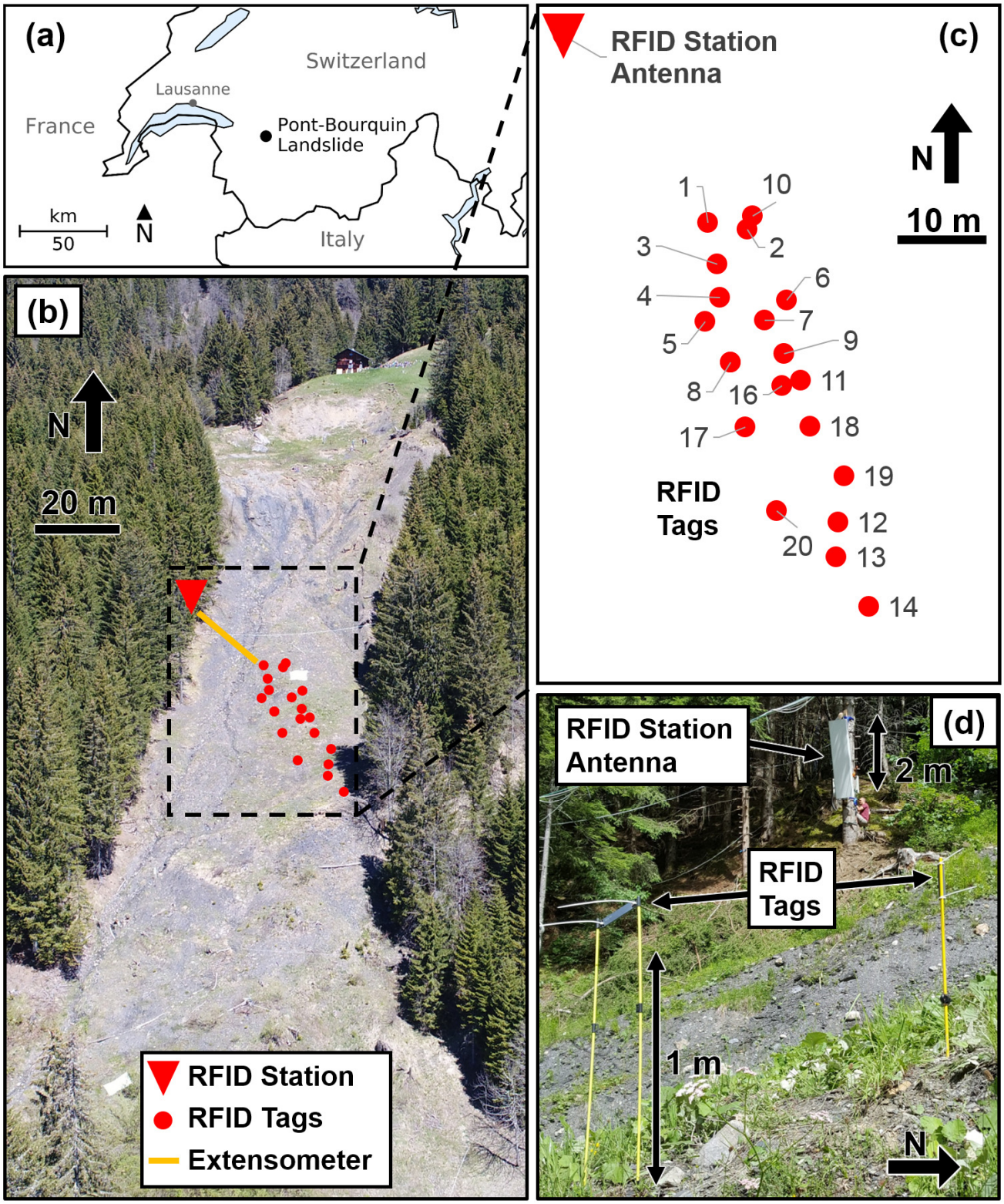


(a) Pont-Bourquin landslide location in Switzerland (46.3518N, 7.1780E), (b) general aerial view of the Pont-Bourquin landslide, (c) the zone where instruments were placed (black rectangle in b), showing the tags and the RFID station, and (d) photograph showing tags No. 10 and No. 2 installed on the landslide, and the station which is placed on a stable zone.

### 7.3.2 Monitoring instruments

On 3 July 2017, the Pont-Bourquin landslide was equipped with the RFID material proposed previously by Le Breton et al., (2017) that reduces the influence of water and temperature on the phase. The acquisition system was composed of a stable station, 19 moving tags, and a remote server. The station was installed on a tree 3 m above the landslide's surface and comprised a reader, an antenna and a computer (SR420 from Impinj and model 80010643 from Kathrein). It typically required 20 W power under continuous operations, which was provided through the Swiss power grid. The station collected about 20 MB of data per day by measuring the phase difference of arrival and the temperature on 30 tags per second, using a randomized tag interrogation order (*EPC Gen2*, 2015). This corresponds to the slowest and most accurate mode of interrogation available on the reader (Dense M8). The reader was chosen because it provided the most precise phase measurements and the best sensitivity (and therefore reading range) and is well adapted for use with slow-moving objects. The phase-shift measured was limited within the range [0, π] (Miesen et al., 2013b). The tags were installed on 0.9-m-high fiber-glass stakes that were planted in the unstable slope (Fig. 7-1.d). The tags were elevated above the ground because preliminary tests indicated that placing tags near the ground considerably reduced the RSS, down to –30 dB at ground-level. These tags were placed within the zone covered by the RFID antenna, which measured approximately 40×10 m (Fig. 7-1.b-c), and remained within the line-of-sight of the station antenna during the experiment. The tags (Survivor B, from Confidex) comprised a solid plastic casing (155 × 26 × 14 mm) protecting a patch antenna (+0.6 dBi effective gain and ± 65 °E / ± 80 °H beam-width at 3 dB) and a battery-assisted microcircuit (EM4325 from EM Microelectronic). While assisted by a tiny button cell to boost their reading range, the tags remain passive: they backscatter the reader carrier wave without amplification, and the exactly same technique works with batteryless tag. In term of lifetime, the tag's battery may last 5 to 20 years under continuous reading, given the cell of 290 mAh and the typical microcircuit current of 1.7–6 µA (*EM 4325 Spec.*, 2015). This lifetime may be shortened by battery aging and by the extra temperature measurements, but still last several years according to the tag manufacturer (Confidex, 2014) and to our own experience.

To validate the RFID measurements, we installed a wire extensometer (ASM WS17KT) between a metallic stake (0.5-m-high, 0.7-m-deep and 1 m away from

tag No. 10) and the bottom of the station antenna. We extended the original 2.5-m Invar wire with a 20-m Kevlar wire. An acquisition card (Campbell CR1000) measured the length of the extensometer wire every minute, representing a radial displacement along the line of sight of the antenna. During processing, the displacement from both the extensometer and the RFID was averaged every hour.

We also measured the 3D coordinates of the tags and base station on 27 July and 6 October using two manual total station surveys (Leica TCR805), to compute the 1D tag-station radial distance and its difference between the two surveys. The positions of the extensometer and tags No. 10 and 11 were measured using a fixed reflector, with an accuracy of ± 5 mm. For the other tags, the manual positioning of the prism resulted in lower accuracy, estimated at ± 2 cm. Hence, the accuracy of the relative displacement between two total station surveys was ± 1 cm for tags No. 10 and 11, and ± 4 cm for the other tags.

Finally, we used data provided by MétéoSuisse related to fresh snow height and total snow height (measured daily at 6 am at Diablerets village, 1 km away), precipitations, humidity, air temperature (every 10 min at Col des Mosses, 6 km away) and pressure (every 10 min at Les Diablerets).

### 7.3.3 RFID ranging methods

This study first compares two absolute ranging techniques (FD-Phase and RSS) with a relative displacement technique (TD-Phase). Firstly, the relative radial displacement of a backscattering tag can be computed in free space using the Time-Domain Phase Difference of Arrival technique (TD-Phase) (Nikitin et al., 2010), as presented in Fig. 7-8, with

$$\delta r = -\frac{v}{4\pi f}\delta\varphi_{\text{air}} \tag{7-1}$$

where

$\varphi_{air}$ phase-shift resulting from propagation through air;

$r$ distance between the station and the tag;

$v$ RF wave velocity in the medium ($\approx 2.998\times10^{8}$ m/s);

$f$ carrier frequency (= 865.7, 866.3, 866.9 or 867.5 MHz as defined by *ETSI-EN 302-208* (2016)).

In this application, the reader measures the phase difference of arrival between [0, π] modulo π. Using Eq. (7-1), this phase interval is equivalent to a distance of 8.6 cm, or ± 4.3 cm. Larger displacements are ambiguous to measure directly and require phase unwrapping, by adding or subtracting 8.6 cm when the difference between two consecutive measurements exceeds ± 4.3 cm.

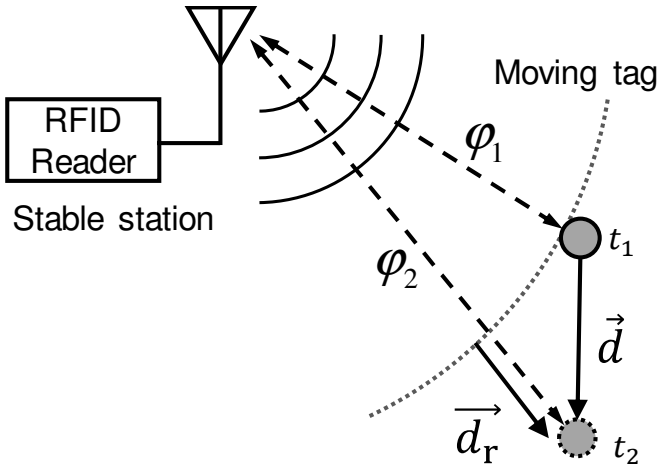


Schematic representation of how tag displacement is tracked by a tation. The phase variation measures the radial displacement $\mathbf{d_r}$ between two acquisitions.

Secondly, the absolute distance r can be computed by measuring the phase at different frequencies, based on the Frequency-Domain Phase Difference of Arrival (FD-Phase) technique (Nikitin et al., 2010) :

$$r = \frac{\delta\varphi_{air}}{\delta f}\frac{v}{4\pi} - r_0 \tag{7-2}$$

where

$\delta\varphi_{air}$ phase difference resulting from the change in carrier frequency;

$\delta f$ difference in frequency between two carrier frequencies (0.6 MHz);

$r_0$ offset due to wave propagation in cables and instruments (11 m).

The resulting distance $r$ was computed for each of the three available frequency intervals and averaged. As long as tags are placed at ≤125 m (minus $r_0$ ) away from the station antenna, this technique provides an absolute distance without ambiguity. The unique offset $r_0$ used on all the tags was initially calibrated from tag No. 10 as 11 m, for which the range to the station (22 m) was measured using the total station on July 27.

Thirdly, the absolute distance $r$ can be estimated from the attenuation of the received power (RSS) over a two-ways propagation (Griffin and Durgin, 2009). As the RSS depends on the station and tag gain, their relative orientation, and the environmental conditions (Dobkin and Weigand, 2005), it requires calibration based on reference tags placed at a known distance (Ni et al., 2003). We computed one virtual reference tag, from the average RSS and total station distances of all the tags over the first month. The absolute range $r_i$ of tag $i$ can then be estimated by comparing its received power $P$ to that of the reference tag, using:

$$r_{\mathrm{i}} \approx r_{\mathrm{ref}} \sqrt[4]{P_{\mathrm{ref}} / P_{\mathrm{i}}} \tag{7-3}$$

These three absolute and relative ranging techniques are compared in section 3.1. The remainder of the article then focuses solely on the TD-Phase relative displacement measurements.

## 7.4 Results

### 7.4.1 Performance of the different RFID ranging techniques

The absolute distance covered by each tag was computed from the Frequency-Domain Phase (using (7-2)) and the RSS (using (7-3)) and compared to the total station laser measurements (Fig. 7-3). The range values were computed every hour and averaged over a 5-month period. The vertical bars represent the drift over this whole period, based on the 90% confidence interval. The curve shows that the RSS-based ranging measurements follow an increasing trend with distance from the station, but that some strong outliers are found, as are large drifts of up to ± 15 m. These datapoints were due to the strong impact of uncontrolled parameters: environmental variations, antenna orientation and ground reflection interference. Therefore, the RSS method cannot be considered reliable. In contrast, the distances obtained with the FD-Phase method gave a good fit with the distances measured with the total station, with a maximum drift of ± 2 m. This level of error is still too high for our monitoring purposes, but it can be reduced by using relative displacement techniques.

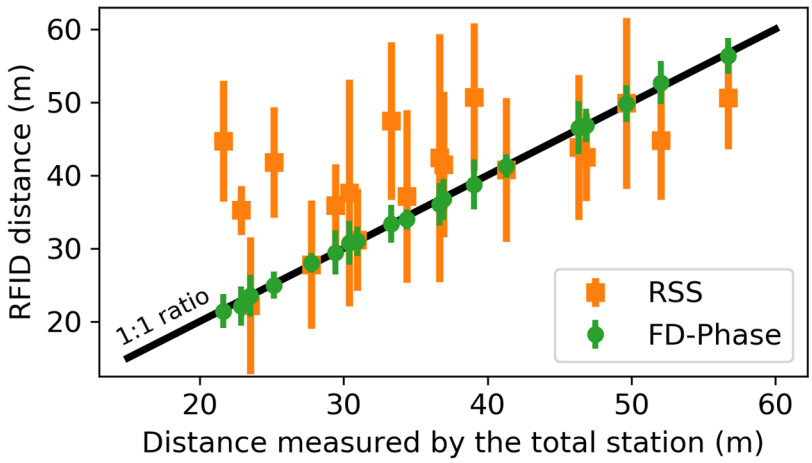


omparison of the radial distances between the tags and the station antenna estimated by ing techniques (RSS and FD-Phase) with this same distance measured by a manual total r the 19 tags deployed. The vertical bars represent the amplitude of the drift over the 5- riod, and the width of the 1:1 ratio line represents the true displacement over 5 months. centimeter-scale total station error is negligible, and was therefore not represented.

The relative displacements of tag No. 10 over time, computed from variations in FD-Phase, RSS, and TD-Phase are compared in Fig. 7-4, along with the total station measurements. The FD-Phase and RSS show significant variations over time, which can be up to 4 m. The drift appear with the same amplitude for FD-Phase and RSS techniques, but that is specific to the tag n°10 (the second smallest distance on Fig. 7-3), as in general the drift is higher using the RSS method as osbserved on last paragraph. In contrast, the TD-Phase measurement appears much more stable and accurate than the RSS and FD-Phase ranging techniques when monitoring relative displacements. Indeed, the relative displacement is more sensitive to phase or frequency errors in Eq. (7-2) (FD-Phase) compared when applying (7-1) (TD-Phase) for two reasons: the FD-Phase is differential across frequencies and it estimates an absolute distance. Indeed, the difference between two frequencies $< 1.8$ MHz represents only 0.2% of the frequency, which magnifies phase and frequency errors. Then, the absolute ranging is more sensitive to a relative phase error $\varepsilon = \Delta\big(\delta\varphi\big)\big/\delta\varphi$ : the resulting displacement error would be $\varepsilon \times r$ (r=20–60 m) and $\varepsilon \times \frac{\lambda}{2}$ ($\frac{\lambda}{2}$=0.17 m) using FD and TD-Phase respectively, leading to 100–300 times more accurate displacements using the TD-Phase technique. The TD-Phase results appear coherent with those provided by the total station, and are

validated in more detail in the next section by comparison with standard ranging techniques.

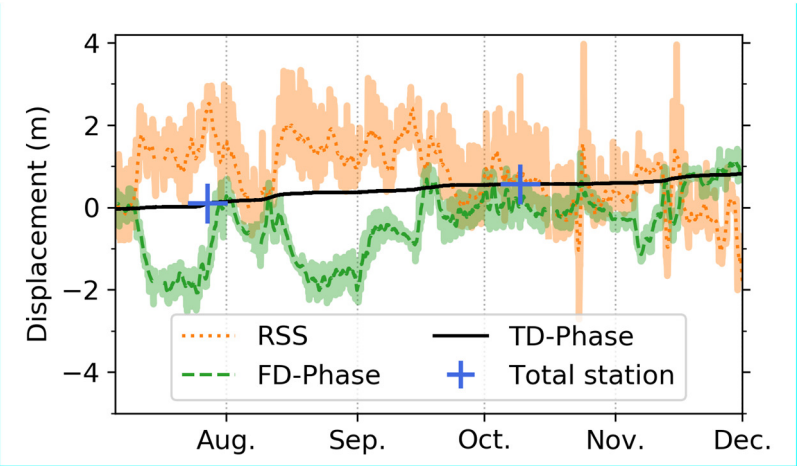


Relative radial displacement between RFID tag No. 10 and the station antenna over a 5-riod, using the Received Signal Strength (RSS), the Frequency-Domain Phase Difference (FD-Phase) and the Time-Domain Phase Difference of Arrival (TD-Phase) techniques, to the radial displacement computed from total station measurements. The darker lines for RSS and FD-Phase represent a 24-h moving averaged.

### 7.4.2 Validation of the TD-Phase RFID technique

The TD-Phase displacements are compared with the automatic wire extensometer measurements over 4 months and with the two manual total station surveys (Fig. 7-5). The tag studied (No. 10) was installed next to the extensometer stake. The RFID curve appears to match the extensometer data although a slight discrepancy appeared in September, which progressively increased to around 5 cm difference at the end of the observation period. The total station data showed that this discrepancy was caused by a true differential displacement between the tag and the extensometer, which were installed on separate stakes. Another difference was that the wire extensometer curve was noisier and exhibited several strong spikes from mid-October, which appear to be linked to snowfall (Fig. 7-5b): snow accumulation bent the wire down, pulling the cable along by several decimeters, such as on October 20. This extra length remained until snowmelt or until the cable was manually dug out from under the snow. RFID tracking thus provided better continuity and accuracy over time than the wire extensometer. In particular, the error due to snowfall was smaller and restricted in time to the precipitation episode.

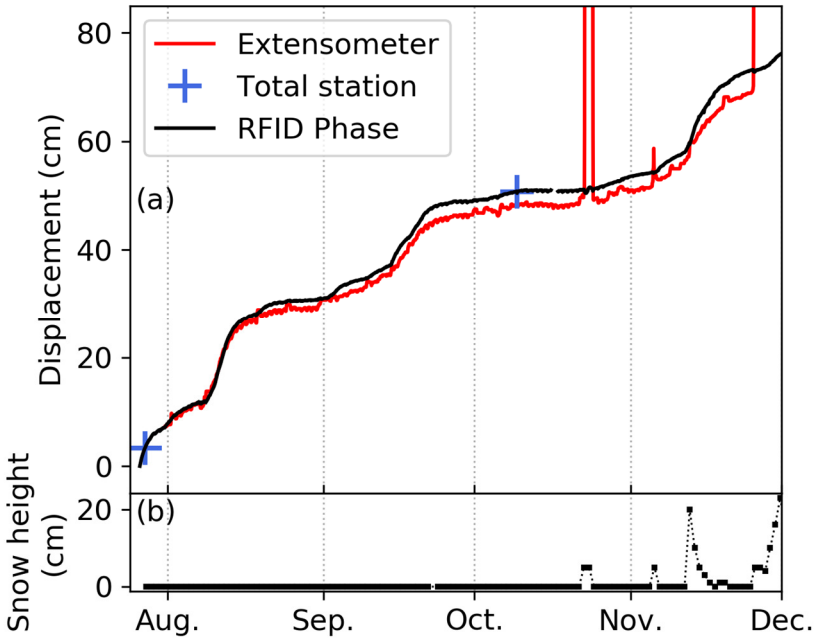


. (a) Cumulative radial displacement measured over 4 months on the Pont-Bourquin
e, using a wire extensometer, the phase of RFID tag No. 10, and a manual laser total
ion. (b) Total snow height. The snow considerably perturb the wire extensometer measurements.

The landslide velocity computed from the RFID (tag No. 10) and the extensometer data are shown in Fig. 7-6.a-b. Each velocity was derived from the displacement, after the application of a low-pass filter (1-day moving average) to reduce the cyclic daily drift. The RFID velocity curve appears more stable than the extensometer velocity curve. Indeed, rain and snow-fall (Fig. 7-6.c-d) created numerous positive and negative peaks on the extensometer velocity curve. That resulted from the additional water or snow weight that temporarily increased curvature in the wire. In comparison, the RFID velocity curve shows almost no perturbation due to rain and the artifact caused by snow was much smaller ($\pm$ 1 cm/day).

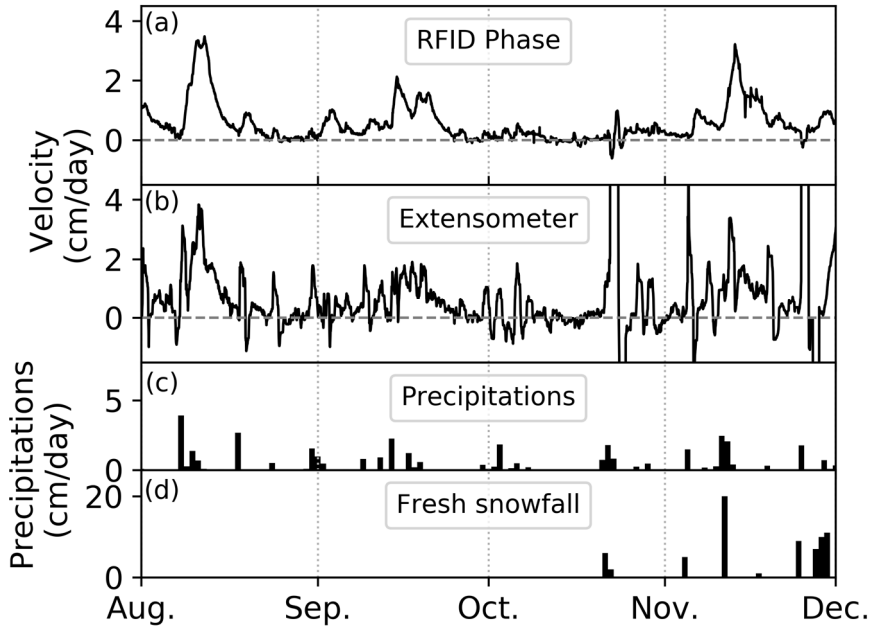


Comparison of radial velocities between (a) RFID tag n°10 and (b) extensometer after filtering for daily variations. (c) Rainfall and (d) fresh snowfall are also shown.

To illustrate its capacity to monitor multiple tags, the RFID cumulative displacement (Fig. 7-7) and the velocity for all tags (Fig. 7-8) were plotted over the 5-month period. The cumulated displacement ranged between 0.69 and 0.94 m (extremes measured for tags No. 12 and No. 7, respectively). The shape of the displacement curves was similar on all tags, suggesting that the zone studied moved in the same way during the observation period. Locally, some displacement measurements may have been affected by a rotational motion of the stick, observed from pictures as ± 7° during the 5-month period. Such motion of the stick would cause a ± 12 cm displacement of the tags, which is the same magnitude as the motion discrepancy between tags. However, the similarity between all the curves indicates that this effect was progressive and smaller than the ground displacement. The velocity for all tags is shown in Fig. 7-8. The curves were ordered according to a noise indicator, computed as the standard deviation of the detrended total displacement, with additional weight for the heavy rainfall recorded between September 30 and October 3. As a result of this ordering, the more accurate curves are placed at the bottom of the figure. Each tag measured the true displacement of the landslide surface, added to an instrumental artifact due to rain. The amplitude of this rain artifact was quite distinct from one tag to another (e.g. between September 30 and October 3) and results in heterogeneous accuracies.

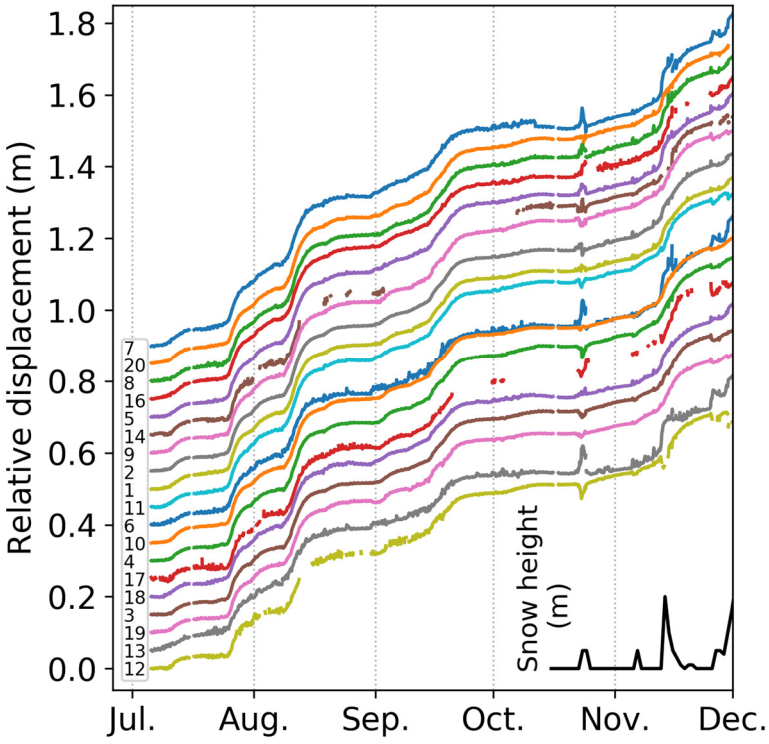


·7. Radial displacement curves for all tags over 5 months. The curves are ordered based on their
ɛ displacement using a vertical offset to facilitate vizualization. The inset indicates the snow height.

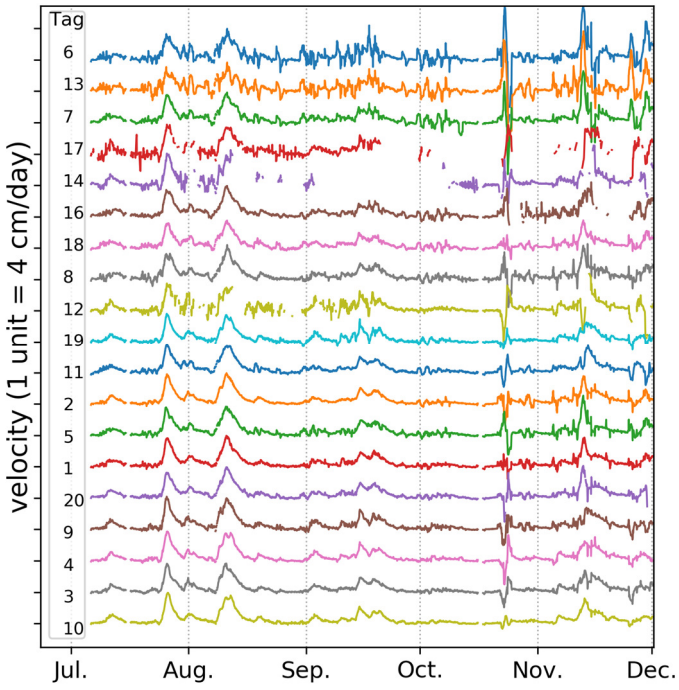


7-8. Radial velocity curves for all tags, ranked by decreasing noise levels from top to bottom.

### 7.4.3 Precision, trueness and robustness of the TD-Phase technique

To determine the validity limits of the RFID TD-Phase technique, we tried to quantify its precision, trueness and robustness from the 5-month experiment. The accuracy indicators are computed from the experimental data and summarized in Table 7-1 for precision and trueness, and Table 7-2 for robustness. The accuracy is then given by the combination of the precision and the trueness.

**Precision**

The precision is given by the random measurement error estimated from the phase standard deviation over one minute, a timespan that is short enough to allow systematic error due to meteorological variations to be neglected. This random measurement error was then plotted against the RSS (Fig. 7-9). The random measurement error appears to obey the relation $\sigma_r = \alpha / \sqrt{P}$ with the received power P, using a reader-dependent coefficient $\alpha$=9.5×10$^{-9}$ m·W$^{1/2}$. The curve obtained is coherent to the phase signal-to-noise ratio observed by Vossiek and Gulden (2008) that depends on the distance. On a single measurement, our random measurement error 3$\sigma$ represents 0.1 to 1.3 cm (Fig. 7-9), for a received power of 10$^{-8.3}$ to 10$^{-6}$ mW. This random error can be statistically decreased to 0.01–0.17 cm by averaging 60 measurements over one minute, it thus becomes negligible compared to the systematic measurement error presented below.

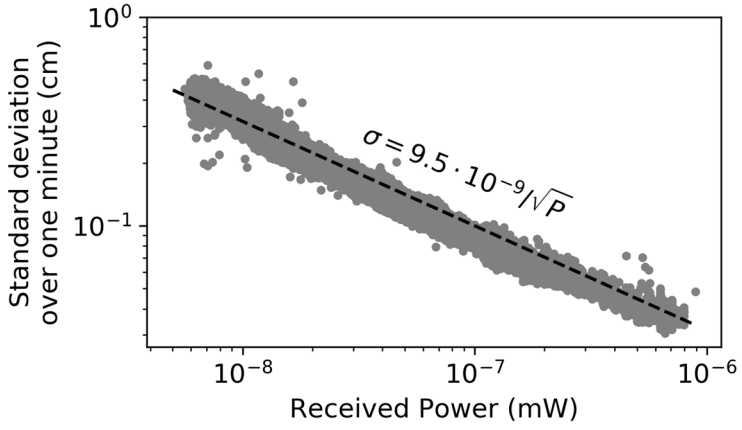


:andom measurement error represented as the standard deviation $\sigma_r$ computed every minute for , plotted against the received power P, on a logarithmic scale. The curve shows a clear linear relation between $\sqrt{P}$ and $\sigma_r$.

Table 7-1: Trueness and precision of the RIFD technique

| | Number of samples | Deviation 99.7% confidence[(a)] (cm) |
|---|---|---|
| Radial Trueness | | |
| Versus total station – all tags | 19 | 5.3 (centered on 0.6) |
| tags No. 10&11 only[(b)] | 2 | 1.0 (centered on –0.05) |
| Versus 24h-smoothed data | 60,000 | 1.1 |
| During the first snowfall[(c)] | 19 | 8.0 |
| Radial Precision | | |
| of a single reading[(d)] | $7x10^7$ | 0.1–1.3 |
| over one minute | $4x10^6$ | 0.01–0.17 |

(a) The 99.7% confidence interval was computed from the Student law when there were ≤2000 samples and directly from the equivalent quantile when there were ≥60,000 samples. The distributions were verified to ensure they were close to a normal law.

(b) Total station surveys were more accurate for tags No. 10 & 11, and their fixation on a single sealed stick was more stable.

(c) The first snow fell between October 21, 18:00 and October 24, midnight, when tags showed a strong measurement bias. This was the worst bias accuracy observed.

(d) The precision of a single reading was linear with the signal amplitude, and followed the law $\sigma_\varphi = \alpha / \sqrt{P}$ , with $\alpha=1\times10^{-8}$ m·$W^{1/2}$

**Trueness**

The trueness is given by the systematic measurement error, estimated as the bias between the true value and the mean of the measured values. It includes the drift over time (days to months) and the inaccuracy over spatial displacements. Table 7-1 shows the displacement accuracy computed from the difference between the RFID technique and the total station surveys used as reference measurements. The average displacement measured for all tags by both methods differed by only 6 mm. Hence, the displacement of all the RFID tags appears coherent and, on average, unbiased compared to the total station data. However, the results are spread statistically over ± 53 mm within the 99.7% confidence interval. This spread mostly corresponds to the error when placing the optical reflector on the tags for the manual total station surveys: we have estimated this survey error to be ± 40 mm for most of the tags. The tags No. 10 and 11 were installed on a single stick, which improved the estimated survey error to ± 10 mm. For these two tags, the difference compared to the RFID measurements remained below 0.5 mm, which, given the small number of samples, corresponds to a potential error of ± 10 mm within the 99.7% confidence interval. In fact, the reference technique – manual total station –

appears as or less accurate than the RFID method that is tested, and thus another method is required to assess the trueness.

The systematic measurement error with RFID is mostly due to environmental variations such as temperature, humidity and moisture, which vary over the course of a day (Le Breton et al., 2017a). To estimate this systematic measurement error, we computed the RFID residual displacement amplitude after removing the 1-day-moving-averaged trend. These calculations showed a daily drift of ≤11 mm 99.7% of the time. Finally, the worst errors were observed during the first snowfall (see photo in Fig. 7-11), which triggered reversible displacement peaks of up to 79 mm, either positive or negative.

Hence, we estimate the trueness of this RFID method to be approximately 1 cm on a real landslide application under mixed meteorological conditions (dry, rain, snow), except for the first snowfall which appeared to limit the trueness to about 8 cm. Because the systematic error is much larger than the random one after averaging, we consider that this trueness also represent the total accuracy.

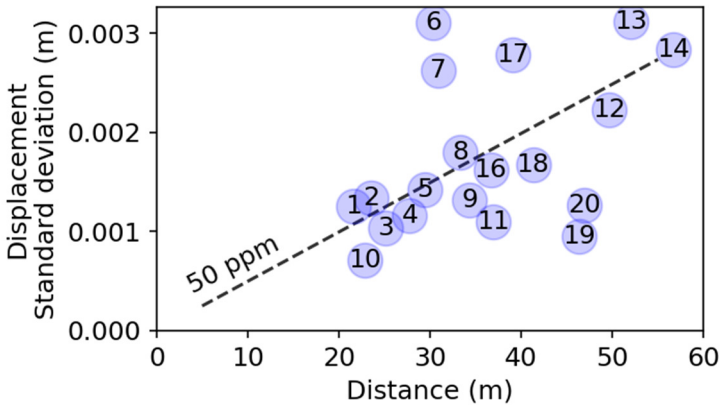


Standard deviation of the 1-hour resampled RFID displacement after trend removal, against the tag radial distance, for each tag. The deviation tends to increase with distance, at a rate of about 50 ppm.

The measurement error could be partly related to the tag-station distance. To verify this relation, the standard deviation was plotted against the distance (Fig. 7-10). This analysis shows that the systematic measurement error tends to increase the measured distance by about 50 ppm, or 150 ppm for 3σ. This trend could be related to the following distance-dependent effects: Firstly, the atmospheric conditions influence on wave velocity (Gage and Balsley, 1980) could induce a ± 3.4 ppm

standard deviation (after detrending), computed from meteorological data. Secondly, the reader frequency instability could result in variations of ± 10 ppm, in line with the regulations (*EPC Gen2*, 2015). Thirdly, the amount of vegetation crossed by ground-reflected waves will increase with the distance, and its properties (such as height or water content) may vary over time and affect the overall signal (Kim et al., 2012). Fourthly, the greater the distance between the tag and the station, the more opportunities for multipathing due to the topography, and therefore potentially the greater the systematic error due to multipathing.

11. Photo illustrating the two main sources of inacurracies in this experiment  the snow
ly the first snowfall) and the angle of the tag supports, which created a temporary error of
(3σ) at the end of October and a slow drift roughly estimated at up to 5 cm per month,
vely. Apart from those two specific problems, the accuracy remained below 1.1 cm (3σ).

**Robustness**

The robustness can be defined as the ratio between the total monitoring time and the time when the RFID is operational. This is an important indicator for operational monitoring. Failure to identify the tags disqualifies the monitoring. Table 7-2 shows the availability ratio for each tag over the observation period; 14 out of 19 tags were available 97.5% of the time. The 2.5% unavailability was the result of software and network errors on the station. The availability of the other tags ranged from 96 to 55%. Snowfall clearly affected communication with tags No. 16 and 20. For other tags, the RSS was close to the limit of reader sensitivity (–83 dBm) due to either their distance (No. 12 and No. 14) or their angle relative to the station's antenna (No. 17). Signal strength may have been reduced by destructive multipath interference at a specific tag position, and increased again once the tag moved forward.

Table 7-2: Overall Measurement Availability

| Tags | ilability[a] | Major cause of problems |
|---|---|---|
| 74% of the tags | 97–98% | Software/network errors |
| No.20 | 96% | Snowfall of 29 Nov. |
| No.16 | 87% | Snowfall |
| No.12 | 82% | Large distance + interferences |
| No.17 | 55% | Station antenna directivity + interferences |
| No.14 | 55% | Largest distance |

## 7.5 Advantages and limitations

The assessment of RFID relative ranging on a landslide has shed light on its advantages and limitations, which will help guide future monitoring applications.

The major advantage identified in this study is that RFID works at night and under all meteorological conditions. Indeed, radio-frequency waves are known to propagate in rain, fog, snow (Monserrat et al., 2014) and vegetation (Intrieri et al., 2018a). Passive RFID in particular has been tested without line-of-sight (Wang and Katabi, 2013), outdoors (Le Breton et al., 2017a) and with snow on the tags (Nummela et al., 2008). This real-world test confirms that RFID adapts very well to natural outdoor areas despite periods of fog and precipitation, although minor accuracy and readability degradations were noted in the presence of snow. This degradation may be due to detuning effects in the vicinity of the tag and station antenna (Dobkin and Weigand, 2005) and to changes in the propagation paths (Kim et al., 2012) due to snow (Larson et al., 2009) or vegetation (Kim et al., 2012). Displacement accuracy outdoors was found to be ± 1 cm with vegetation, precipitations, fog or frost, and in rare cases ± 8 cm after snowfall. The technique is thus well adapted for outdoor applications to measure displacements ranging from 1 cm to several meters.

The second advantage of RFID is its low cost, allowing displacements to be measured with a high spatio-temporal resolution. Current prices are about 20 € per tag and 4 k€ per station. Moreover, the instruments were found to be robust and reliable, requiring little maintenance during the experiment (zero maintenance on the tags, three reboot of the station operated remotely, and one replacement of network cables degraded by animals) and providing a data completeness rate of 97% over five months for most tags. Because of their low cost, a large number of tags can be

deployed on landslides, providing a high spatial resolution to delineate and characterize moving zones. From a technical point of view, unique tag identifiers and anti-collision algorithms make simultaneous reading of hundreds of densely stacked tags possible (Caizzone and Marrocco, 2011) at a rate of up to 800 tags per second (*EPC Gen2*, 2015; Klair et al., 2010). This capacity results in a high spatio-temporal resolution with lightweight time series that are easy to transmit and process almost in real-time. Because of these characteristics, the method could easily be incorporated in an early-warning-system (Intrieri et al., 2012b) and appears to be well suited for low-cost, dense monitoring applications in high-risk environments such as landslides where devices may be destroyed.

The final advantage is the continuous development of tags to become multi-parameter sensors (Zhang et al., 2017). In this study, the tags were equipped with a temperature sensor that we used for phase calibration. Recently, other sensors have been incorporated into tags, to gather data related to tilt (Lai et al., 2018), soil moisture content (Aroca et al., 2018; Pichorim et al., 2018) and vibrations (Jayawardana et al., 2016). All these parameters could be of interest when monitoring landsides, opening new perspectives in dense sensing.

As for the limitations, the first one on landslides is currently the tag's reading range, which was limited to 60 m in this application. However, this limit (Nikitin and Rao, 2008) should rapidly evolve with the development of ultra-sensitive tags (Amato et al., 2018; Durgin, 2016) and directive tag antennas (Kim and Yeo, 2012). Therefore, a range of a few hundred meters seems to be an achievable goal in the near future. This is a critical limit, which would restrict the method today to small landslides. On medium to large landslides (200m to kms), only the zone situated near the landslide boundaries (to install a stable base station) could be monitored, which would diminish the ability to retrieve the spatial heterogeneity of the displacement. New developments to increase the reading range are then critical to be able to use the RFID method over the majority of landslides.

Secondly, the measurement is limited to 1D radial displacement. Measuring a 2D or 3D translational displacement field is technically possible, but would require additional antennas and may alter measurement accuracy (Scherhäufl et al., 2015; Wang et al., 2016). Furthermore, it is not enough to measure a purely translational displacement, as a progressive tilt of the tag's supporting stick can create a discrepancy between the ground and tag displacements that must be accounted for. This

tilt could be measured in real-time by joining multiple tags (Lai et al., 2018) and corrected in the next future.

Finally, the displacements measured are affected by an ambiguity of 8.6 cm that originates from phase difference measurements. To address this problem will require first a high time resolution without missing data to avoid differential displacements exceeding this ambiguity, and second an unwrapping of the phase (Zuo et al., 2016). Unwrapping noisy or incomplete data produced by a tag could be guided by nearby high-quality data if a large number of tags are deployed, or by a previously defined rain-based model such as that presented in the application section.

## 7.6 Conclusions

RFID displacement tracking appears effective for monitoring surface deformations on a landslide, with unpreceded spatio-temporal sampling, at a significantly lower cost than GPS or ground-based radar and with an overall 1-cm accuracy within a range of 60 m including a distance-dependent error of around 150 ppm.

In the future, the technique could be enhanced by monitoring displacements in 3D, increasing the reading range, correcting for tilt of the tag support, and assessing performance in the presence of obstacles (e.g. snow, vegetation, rocks or concrete). New environmental applications could be developed by exploiting sensor tags (e.g. temperature, tilt, soil moisture or vibrations), developing a real-time surveillance system that exploits the rapid time sampling (3–30 ms), measuring very fast displacements, and testing new outdoor applications (e.g. volcanoes, civil infrastructure, rocks, snow or vegetation). Finally, the fast pace of technological developments in RFID should lead to considerable improvements to the technique in the near future.

## 7.7 Acknowledgments

This work has been supported by Géolithe, the ANRT, a grant from Labex OSUG@2020 (Investissements d'avenir – ANR10 LABX56), the VOR program from Univ. Grenoble Alpes, ANR LABCOM GEO3iLAB (17 LCV2 0007 01) and Mojix. The authors thank Benjamin Vial for instrumentation, Antoine Guillemot for field surveys, Christophe Loussert for advices on material, Pascal Lacroix for insights into deformation monitoring techniques, and Hannah Taylor and Maighread Gallagher for proofreading.

# Chapter 8
# Impulse response from rainfall to displacement

*The section 8.3 of this chapter is the "application" section of the published article presented in the previous chapter: Le Breton, M., Baillet, L., Larose, E., Rey, E., Benech, P., Jongmans, D., Guyoton, F., Jaboyedoff, M., 2019. Passive radio-frequency identification ranging, a dense and weather-robust technique for landslide displacement monitoring. Engineering Geology 250, 1–10. https://doi.org/10.1016/j.enggeo.2018.12.027*

**Contents**



## 8.1 Summary


This chapter introduces a method to observe the relation between rainfall and landslide displacements, using a statistical impulse response inversion. The method provides a sharper response function than cross-correlation analysis or than the inversion of infiltration-based mathematical functions. The impulse response shape and lag time computed at different periods on the Pont-Bourquin landslide, suggest that:

1) The landslide response to rain alternates between a stable and transient state. The landslide moves after a rainfall event in both state, but with a different behavior.

2) The switch to the transient state may be caused by rainfall accumulation.

3) In the stable state, the highest displacement rate caused by rainfall would appear after a lag of 1 day, and a rainfall episode would diminish the apparent seismic velocity (at 8-12 Hz) by less than 2% for just a few days.

4) In the transient state, the highest displacement rate caused by rainfall would appear after a lag of 2–3 days, with a broader response in time, and would be accompanied by a strong drop of apparent seismic velocity (>2%) at 8-12Hz that would require a few weeks to return to its former value. The lag of 2–3 days observed in the impulse response could also be caused artificially by the change of state of the landslide.

These hypotheses appear consistent with various displacement sensors (several RFID tags and one extensometer) and various observations (displacements and seismic velocity variations). The activation of the transient state is observed seasonally, in August. The hypotheses are consistent with 2012, 2014 and 2017 data. The two peaks of impulse response could represent a true lag, caused by two different water infiltration paths or by a reaction of the landslide that would depend on depth. Those two peaks may also be induced by the inversion process, to fit to the transition from stable to transient state between two consecutive rainfall events. Such change of state could be caused by rainfall accumulation. The impulse response provides a new method to interpret the processes of a slow-moving landslide that is reactivated by rainfall. It requires only displacement and rainfall data which are very common measurements. However it needs a high enough accuracy and time resolution. The evolution of the impulse response across time could represent a landslide change of state, which could be a precursor to a non-linear rupture.

## 8.2 Introduction

**From Rainfall to displacement**

The displacement of weather-induced landslides are triggered by the infiltration of water that follows precipitation episodes (Iverson, 2000). Landslide monitoring and early warnings are commonly based on displacement (Intrieri et al., 2019) or rainfall data (Guzzetti et al., 2007; Luca and Versace, 2017).

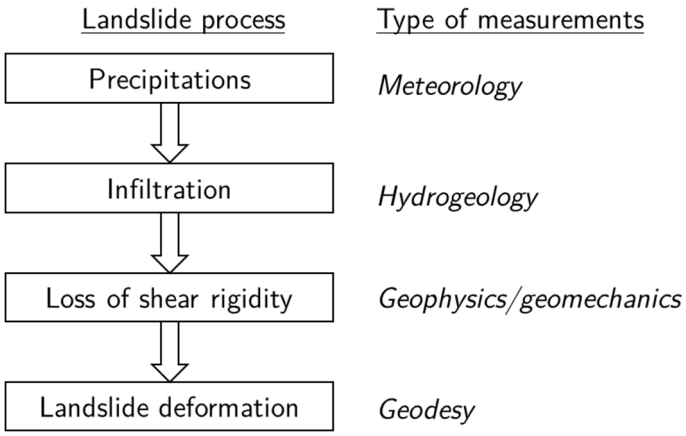


Fig. 8-1: Simplified processes of rainfall-induced landslides, and observation methods.

Rainfall usually causes a displacement through the process described in Fig. 8-1. First, an input of water due precipitations starts to infiltrate in the soil. The quantity of infiltrated water is often well represented by rainfall. However, it can be altered by evapotranspiration (Bievre et al., 2018), water running on the surface, external sources of water, snow melting (Matsuura et al., 2003, 2017), and by soil fracturing caused by ground deformation. The water then progressively infiltrates the ground, with a delay, leading to an elevation of the groundwater level and pore pressure (Iverson, 2000). The displacement of a slow reactivated landslide can be nearly linear with the groundwater level (Corominas et al., 2005), as long as no failure occurs. The groundwater elevation can cause displacement through an increase of shear stress and a rigidity diminution for clayey material (Carrière et al., 2018b; Mainsant et al., 2015, 2012a). Therefore, a relation can be extracted between the quantity of precipitations and the landslide deformation (excluding failures), which includes the infiltration delay.

In practice, the most common measurement data are the surface displacements (Intrieri et al., 2019) and the precipitations. Measuring ground water level and deep deformations requires underground sensors, which are rarely easy to use in a landslide: Slopes are often difficult to access for a drilling machine, the sensors buried in a moving ground are hard to maintain, and multiple sensors are required to catch the slope spatial heterogeneity. Geophysical techniques allow for estimating indirectly the variations of rigidity of the underground layers, by measuring the variations of shear-wave velocity from sensors installed at the surface. That has led to precursor signal to fluidization in rheological tests (Carrière et al., 2018a; Mainsant et al., 2012a) in controlled slope simulation (Mainsant et al., 2015), and on the field (Mainsant et al., 2012b). The resulting displacement can be measured in depth

using inclinometers to determine the slip surface depth, but that requires a costly drilling and maintenance. For these practical reasons, the precipitations and surface displacements are commonly used for landslide monitoring.

Instead of observing precipitations and displacements separately, this study observes their empirical relation. This relation is not used for making a predictive displacement model—these only manage to model linear displacements, not failures—but as an observation in its own with the aim to better constrain the underlying mechanism. Such observed indicator should represent the complexity of the landslide processes, should adapt to its evolution in time, and should be physically relevant and interpretable.

**Complex enough**

Each landslide is complex and unique. Its infiltration and displacement processes are heterogeneous and specific to each landslide (Guzzetti et al., 2007; Montgomery and Dietrich, 1994). Landslide displacements are modeled either with physical, analytical, or statistical models (which are sometimes mixed). Physical models are based on general laws of infiltration and mechanics. But these simple laws hardly represent the complexity of each landslide, and their parameters must be constrained by costly *in situ* measurements.

Analytical models are empiric models based on analytical functions. The model is obtained by convolving a rainfall input with an analytical impulse response function (Sirangelo and Versace, 1996; Helmstetter and Garambois, 2010; Belle et al., 2014) that represent a simple static infiltration process in a homogeneous subsoil. The function is usually defined with a simple mathematical formulation (Helmstetter and Garambois, 2010; Capparelli and Versace, 2011; Sirangelo and Versace, 1996), where a few parameters (1 to 4) are inverted to fit the measured data.

Making these models more complex was shown to provide more accurate models of linear displacements (Belle et al., 2014) and probability of failures (Luca and Versace, 2017). The impulse response function was complexified by summing two analytical functions to account for rapid and slow infiltration (Belle et al., 2014), or by integrating the data from several sensors to account for spatial heterogeneity (Lévy et al., 2017). These models could estimate the slow landslide motions from rainfall data, but could not predict failures (they provide a probability of failure at best). However, simple analytical formulas hardly represent the landslide complexity, and composing custom formulas adapted to each landslide is not appropriate.

Statistical models define the transfer function—including its shape—only from the data. By avoiding simplified analytical laws, they can better represent the complexity of a landslide response to rainfall. Applications on landslides included neural networks (Mayoraz and Vulliet, 2002) and cross-correlation analysis (Belle et al., 2014; Bièvre et al., 2018; Helmstetter and Garambois, 2010). Provided long enough time series, the cross-correlation analysis provides the approximation of an impulse response, but not sufficiently accurate to reconstruct a model since it also contains the fingerprint of the source term. A true reconstitution of the impulse response could be operated with a statistical deconvolution, already used to study the infiltration process on stable grounds (Pinault et al., 2001). The deconvolved impulse response could adapt well to the complexity of each landslide. In mathematical terms, using an impulse response makes the assumption that an output of displacement $y(t)$ is related linearly to an input of rainfall $x(t)$, through the convolution $*$ of an impulse response $\beta(t)$:

$$y(t) = \int_{\tau_{\min}}^{\tau_{\max}} \beta(\tau) x(t-\tau) d\tau = \beta(t) * x(t) \tag{8-1}$$

The impulse response function $\beta(t)$ can be firstly estimated by applying a cross-correlation function $\star$ between the input and output data:

$$\begin{aligned} x(t) \star y(t) &= x(t) \star (\beta(t) * x(t)) \\ &= \underbrace{x(-t) * x(t)}_{\neq \text{Dirac } \delta(t)} * \beta(t) \end{aligned} \tag{8-2}$$

However, the results provide an impulse response convolved with a term of input autocorrelation $x(-t) * x(t)$. To find exactly the impulse response, this term should equal to a Dirac function ($\delta(t) = 1$ for $t = 0$, and 0 otherwise). In practice, the autocorrelation has a main peak centered on zero, with an amplitude different to one, and with a width that blurs the result. This width depends on the width of the correlation time window, compared to the period/frequency observed in the input signal. Shorter time windows increase the peak width, which require large datasets to provide accurate results. Furthermore, this autocorrelation can display secondary peaks related to the periodicity of the input data. The deconvolution techniques aim at estimating the impulse response $\beta(t)$ without this autocorrelation term. However, deconvolutions need a regularization to be stable, which can alter the results.

The timespan of the impulse response $\tau$ is important to consider. It should start at $\tau_{min} = 0$ if the relation from the rainfall to the displacement is causal, and finish at a $\tau_{max}$ that is superior to the true lag of the landslide response and inferior to the data time window. Furthermore, both methods make the assumption that the impulse response is stable within the time window where it is computed, which might not be true when using large time windows.

**Dynamic**

Landslides behavior evolves in time, depending on environmental parameters such as the temperature and water level, and depending on its deformation. However, the behavior of the landslide was considered stationary in most of the studies previously cited. Only a few studies accounted for its evolution, by optimizing the parameters of the response to a moving window of 50 days (Abellán et al., 2015) to 100 days (Bernardie et al., 2015). This adaptation improved the predictive displacement models in the case of slow landslide evolution. However, these do not adapt to rapid evolution of the landslide prior to a failure. In fact, on the shallow landslide of Super-Sauze, a slowly adaptative model (Bernardie et al., 2015) could not directly predict the failure. Yet, a reliable precursor to failure was obtained from the error between the modeled and the measured displacement, which indicated a rapid and non-linear landslide evolution. The present study suggests instead to catch the rapid evolution of the landslide behavior within the impulse response. That would require to use a statistical impulse response, to compute it over a moving window, and to reduce the size of the moving window to be more reactive.

**Understandable and meaningful**

Finally, the provided indicator should be physically relevant and interpretable. The cross-correlation of water input with the displacement rate —used on a slow landslide (Belle et al., 2014; Bièvre et al., 2018) and on a rockslide (Helmstetter and Garambois, 2010)— provides a good signature of the landslide complexity. However it introduces a term of autocorrelation (see equation (2-2)) which smoothes the response and may include secondary peaks due to the periodicity of the input that do not represent the landslide response. On the contrary, black-box neural network can in-fine represent physically meaningful results, but with transfer functions that are hard to interpret. The deconvolution of an impulse response should provide results that are both physically meaningful, and interpretable. However, results should be interpreted with caution, regarding the effect of regularization

and the assumptions of linear and stable landslide behavior within the observed timespan.

**Proposition of this study**

This study introduces an indicator of landslide behavior, based on an impulse response between displacement rate and rainfall computed with a statistical deconvolution (Pinault et al., 2001) over a moving window (Abellán et al., 2015; Bernardie et al., 2015). Such indicator should be complex enough to represent a landslide behavior, dynamic to adapt to a landslide evolution in time, and physically interpretable. It may provide an indicator of the state of instability of a landslide.

The impulse response is firstly computed in a static way, using 5 months of data of the Pont-Bourquin shallow landslide. It is validated by comparing it to the cross-correlation function and by computing a linear predictive displacement model. A dynamic impulse response is then computed on a short 2-week time window, interpreted, and compared with observations of seismic velocity variations to check the consistency of the results. The impulse response is then computed dynamically over several years using historical but less accurate data, to validate the consistency of the observations over several years. Finally, two hypotheses are discussed, to explain the physical process behind the observations.

## 8.3 Pont-Bourquin data

This study is based on data measured at Pont-Bourquin between July 3 and December 1, 2017. The displacement data is obtained using the RFID technique introduced in chapter 7 (Le Breton et al., 2019), based on the low-drift material introduced in chapter 4 (Le Breton et al., 2017a). The displacement rate is the displacement derivative, smoothed with a 1-day moving average filter.

The seismic velocity is obtained using the ambient noise interferometry technique presented in chapter 2. To track the changes of seismic velocity, two short-period vertical seismic sensors (lower frequency of 4.5 Hz broadened up to 0.1 Hz with an analog filter) were installed in January 2012. They were placed on the stable grounds around the zone monitored by the RFID installation. They recorded the ambient seismic noise continuously at a 250 Hz sampling frequency. This noise was processed as described in chapter 2 and (Mainsant et al., 2012b; Bièvre et al., 2018): The hourly traces were equalized in frequency on the broad 4–20 Hz band, then clipped at $3\sigma$ to remove strong noise sources, and finally cross-correlated. After computing the correlations, they were filtered in the [8–12 Hz] frequency, and

stretched in the time window of [-2.5;-0.5]U[0.5;2.5] seconds. The resulting dv/v should be sensitive to depths of 9 m to 20 m that may partly include the active part of the landslide where partial liquefaction was observed during the 2010 event. See (Mainsant et al., 2012b) for further depth sensitivity kernels of surface Rayleigh waves. Each hourly correlation was compared to the average correlation over the period. The resulting *dv/v* was then smoothed with a 2-day centered moving average filter, to remove the instabilities and the daily variations.

The precipitations were measured every hour by an automatic meteorological station of MétéoSuisse (Col des Mosses), six kilometers away but at the same elevation. For quality indicators, the snow depth and precipitation were measured manually by MétéoSuisse operators every morning at 6 a.m., one kilometer away from the landslide. Snow on the ground (starting in October) would strongly disturb the infiltration process and distort the results. The daily precipitations measured close to the landslide were compared to precipitations measured hourly but 6 km further away. Their cross-correlation, after daily resampling, had a maximum coefficient of 0.93 with a lag of 0 day, and visually the data was very coherent. The differences between the two data were negligible, which validated the use of the hourly precipitation data measured at Col des Mosses.

At the end of the chapter, the impulse response is computed from historical data in 2012, 2013 and 2014 (Fig. 8-9). The precipitation data were obtained from a meteorological station installed on Pont-Bourquin. This data was compared to the hourly manual measurements made by MétéoSuisse and the period with discrepancies between both were removed. Similarly, periods with snow on the ground were removed. The displacement data was obtained from a long-range extensometer, and therefore biased during rainfall (see Fig. 8-4). The MétéoSuisse data was available only after 2015, so we used the precipitations measured from a meteorological station installed on the landslide. However, the rainfall collector was regularly obstructed, for example by tree leaves, leading to periods with biased data. This hourly on-site data was validated against the daily manual measurements operated 1 km away by MétéoSuisse, to remove any inconsistent data. The displacement data was obtained from extensometer measurements, in the same zone as the RFID tags. Extensometer data was checked manually to remove artifacts due to snow.

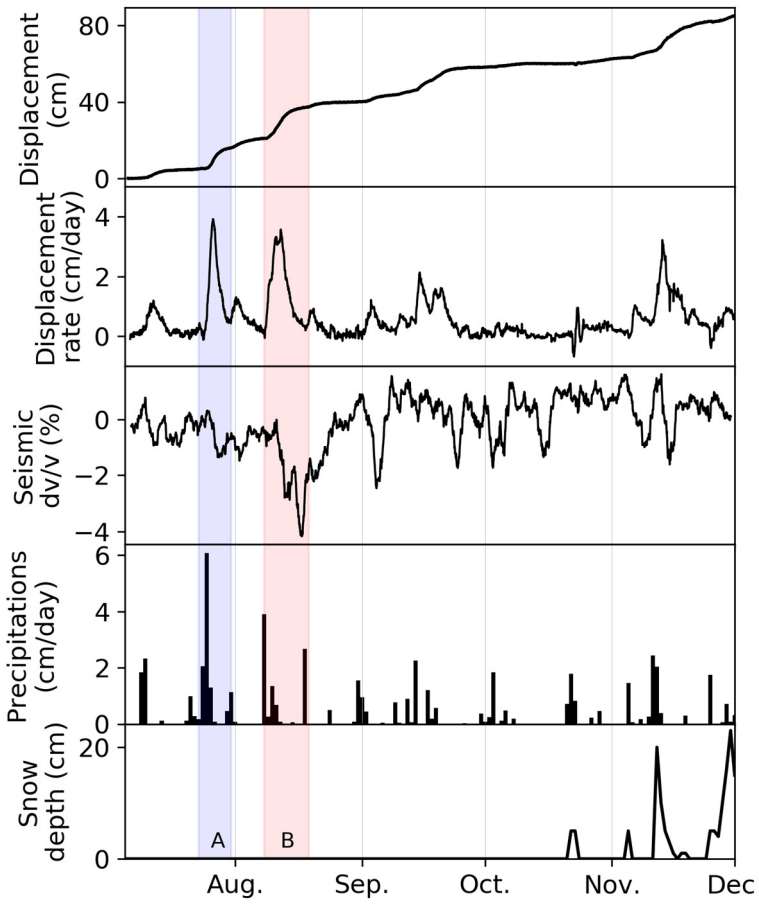


Fig. 8-2: Data measured at Pont-Bourquin in 2017: Displacements are from RFID tag n° 10, seismic velocity variations are in the 8–10 Hz frequency, precipitation and snow depth are from MétéoSuisse. The periods A and B (blue and red), which differ mostly from their seismic velocity, are studied in the section 8.5.1.

## 8.4 Stationary response

### 8.4.1 Impulse response computation

This section studies the stationary relation between rainfall and displacement at Pont-Bourquin. A single impulse response is considered during the whole period, which is approximated to be stable in time. The precipitation/displacement rate curves shown in Fig. 8-2 suggests that this landslide reacts directly to precipitation. This relation is firstly studied by cross-correlating the precipitations with the displacement rate of the tag No. 10, between July 3 and October 1. The tag No. 10 was chosen because it was closer to the station than the other tags, and provided more accurate measurements. The cross-correlation curve on Fig. 8-3 shows a peak rate approximately 1.2 days after the rainfall, followed by a decrease in the displacement rate until days 5–6, as already observed on this site (Bièvre et al., 2018). However, the correlation curve is blurred (by the source autocorrelation) and suggests a reaction of the landslide's displacement before the start of the precipitations,

which is physically unrealistic. To improve this curve, an impulse response (IR) was deconvolved using the linear Lasso regression (Tibshirani, 1996) implemented in the scikit-learn library (Pedregosa et al., 2011), to minimize the following cost function:

$$J = 0.5 \left\| Y - X\beta \right\|_2^2 + \lambda \left\| \beta \right\|_1 \tag{8-3}$$

Where

$\beta$: IR vector; each $\beta_n$ corresponds to the response after $n = 0,1 \ldots N$ hours of lag, N=120 here;

$Y$: displacement rate vector; each $Y_m$ corresponds to the velocity during the $m = 0,1 \ldots M$ hours of the observation period, 3 months here;

$X$: precipitation matrix, where each $X_{m,n}$corresponds to the precipitations measured $m - n$ hours after the start of the observation period;

$\lambda$: regularization parameter, to avoid over-fitting and causing the $\beta$ parameters to tend toward zero. A value of 0.04 was chosen based on preliminary cross-validation tests.

To compute the IR with data that have different amplitudes with a unique regularization parameter, the data can be normalized before the inversion using the following transformation:

$$\begin{aligned} Y_{\mathrm{n}} &= Y \,/\, \left\langle Y \right\rangle^a \\ X_{\mathrm{n}} &= X \,/\, \left\langle X \right\rangle^a \end{aligned} \tag{8-4}$$

Where $\langle\ \rangle$ represents the average function, $X_{\mathrm{n}}$ and $Y_{\mathrm{n}}$ the normalized data, and $a$ an arbitrary factor to control the contribution of small-amplitude data (smaller $a$ increases the regularization on the low-amplitude data, 0.5 was used in this study). After inverting $\beta_n$, the original $\beta$ is retrieved using:

$$\beta = \beta_{\mathrm{n}} \times \frac{\langle Y \rangle^a}{\langle X \rangle^a} \tag{8-5}$$

This process provided a slight underestimation of the IR amplitude because the regularization factor caused the values of $\beta$ to tend toward zero. For this reason, the IR was later corrected by a factor (1.3 in this study) to equalize the measured and modeled velocities (the modeled displacement is presented in the next section).

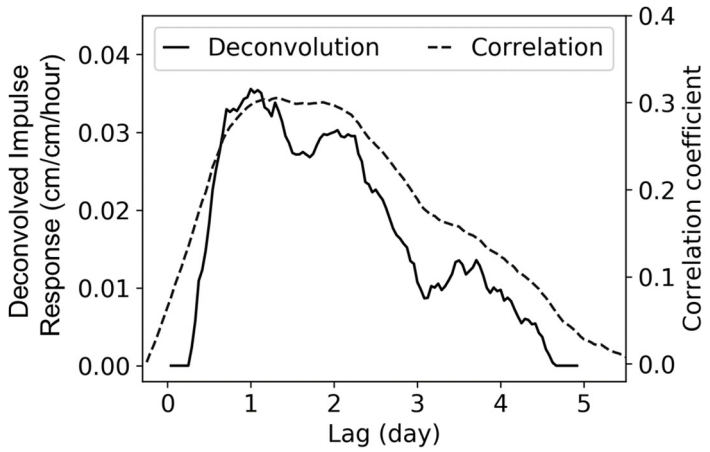


Impulse response of landslide velocity (cm/day) following precipitation estimated by cross-correlation and Lasso regression deconvolution on ll and displacement data from tag No.10 over the 5-month period.

The impulse response (IR), was estimated using data collected from tag No. 10 between July 3 and October 1, before the first snowfalls. It is expressed as a quantity of displacement (cm) per quantity of rainfall (cm) per time sample (hour). The response (Fig. 8-3) appears much sharper than the cross-correlation result, and its amplitude has a physical meaning. This IR suggests that the landslide remained stable for five hours after rainfall, then accelerated rapidly until it reached a peak displacement rate after 18–24 h, and finally returned to a null displacement rate after 4.5 days. This pattern might correspond to an initial infiltration in the superficial layers while the landslide remains stable, followed by a pore pressure increase and then decrease in the aquifer as the landslide accelerates then decelerates. The lag before the peak of displacement rate is consistent with the 20-h delay before the elevation of the water table, measured previously in this zone (Brönnimann, 2011). Besides, the shape of the IR curve looks like a typical water infiltration process (Iverson, 2000).

The impulse response may depend on the instrument and on the location of the measurement. For comparison, the IRs for all tags and for the extensometer are shown in Fig. 8-4. The darkest RFID curves correspond to data that is more accurate and less biased. All the tags exhibit a similar IR, with a discrepancy mostly due to the noise and to the instrumental bias caused by the rain. In contrast, the IR was very different on the extensometer. With this instrument, the IR exhibits a positive peak at the same time as the rain event, then a decrease to a null value

after one day and finally becomes coherent with the RFID curves after two days. This pattern is explained by the dominance of the instrumental response affected by the rain (=cable bending under rain drops weight). This strong instrumental response consequently prevents the extraction of synthetic information from the landslide, such as the IR peak velocity, the lag time before it is reached and the deceleration rate.

To conclude, the deconvolution produces response curves that are sharper and physically more meaningful than the cross-correlation. However, the measured impulse response includes both the landslide and instrumental response. Its correct estimation then requires instruments that are not biased by rainfall, confirming the interest of RFID tags compared to long range cable extensometers.

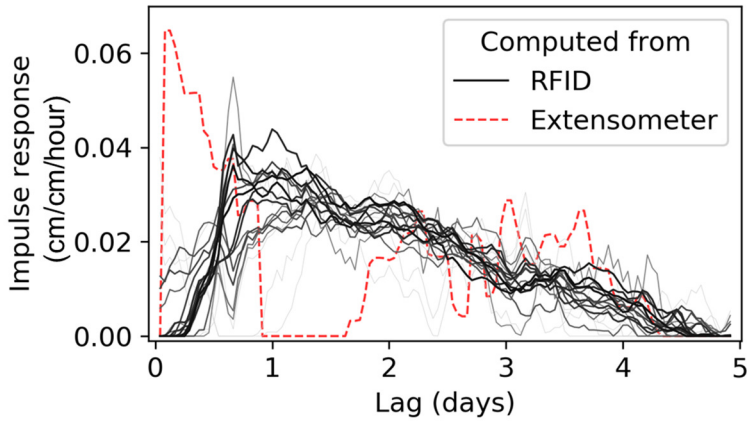


Impulse response of the displacement rate (cm/day) to precipitations (cm/day)
ed using a Lasso regression on the velocity measured by all the RFID tags and the
neter. For the RFID, darker lines represent more accurate tags, presenting lower
noise and a lower sensitivity to rain.

### 8.4.2 Linear displacement rate model

This empiric IR method produced a relatively good fit between the measured and modeled velocity, for which the advantages and limitations are discussed in (Belle et al., 2014; Capparelli and Versace, 2011). This example emphasizes the potential of dense and continuous in situ displacement data, as provided by the RFID technique. As the IR is likely to be heterogeneous across a landslide area, placing multiple sensors enables the delimitation of these zones and provides a redundancy benefit. In this example, continuous data unaffected by rain and fog, with an hourly sampling time and sub-centimetric accuracy was also required to compute the IR.

Observation of how this response changes over time could provide an additional risk indicator, and would require continuous time series covering several months or years. RFID is once again compatible with these measurements because of the low investment necessary and the reduced maintenance cost. This application therefore highlights several advantages of the RFID technique, which will be more fully discussed in the next section.

The convolution of the IR with the precipitations can be used to compute a rain-based velocity model (Belle et al., 2014; Bernardie et al., 2015). Fig. 8-5 shows this velocity model over the whole period, using an impulse response computed during July, superimposed on the velocity measured. Visually, the model appears consistent with the measurements, except on October 23, when the first snowfall was recorded. This coherence is confirmed by the cross-correlation of both curves, which displays a maximum coefficient of 0.77 at a zero-hour delay.

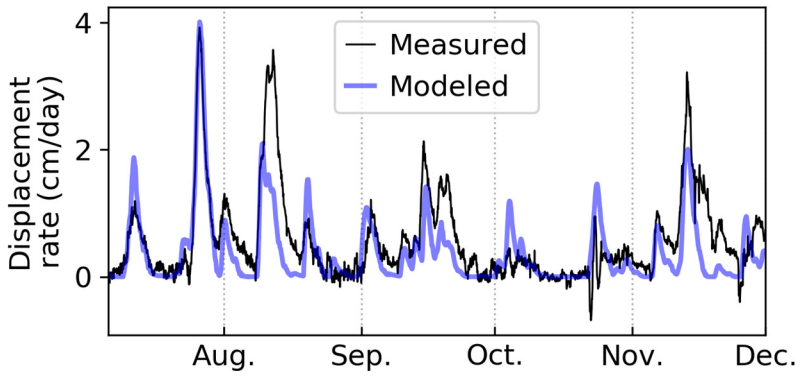


Landslide radial velocity measured from the tag No.10 compared to the model y convolving the precipitation with the impulse response computed in July 2017.

The model could be improved by improving the accuracy of the water input. For example, the effect of evapotranspiration could be estimated and removed (Bievre et al., 2018). Estimating the snow melting (which is a perspective of chapter 5 using RFID tags) would allow using this model continuously, even in the presence of snow during winter.

To conclude, this model can predict linear displacements of the landslide from the rainfall input, or even from rainfall meteorological predictions. However, it would not predict the failures: these are non-linear. The model could serve to compute a probability of failure, based on a threshold value defined by historical rainfall

and failures (Sirangelo and Versace, 1996), using only the rainfall. The most efficient use of such model was to estimate the non-linearity of the behavior, by computing the error of the model compared to the measured velocity (Bernardie et al., 2015). Such non-linearity indicator might also be obtained directly from the impulse response, computed dynamically, which is studied in the next section.

## 8.5 Dynamic response

### 8.5.1 Two states of the impulse responses

The response of a landslide to rainfall should evolve along time, for example after the formation of cracks or the accumulation of groundwater. An impulse response computed over long time windows may average these processes and fail in catching the landslide evolution.

The impulse response is firstly computed over the short period of 23–30 July, for the 19 tags installed at Pont-Bourquin. This period, highlighted in red on Fig. 8-2, is focused around a peak of displacement rate of 4 cm/day, accompanied by only a minor drop of seismic velocity. The corresponding impulse response function (Fig. 8-6.A) exhibits two peaks of displacement, instead of the single peak previously shown when computing the response over several months. A first peak with of about 0.06 cm/cm/hour occurs after 1 day, and a second smaller peak of 0.03 cm/cm/hour occurs after about 2.5 days. These two peaks suggest the existence of two distinct processes causing the landslide displacement, which are discussed later.

The impulse response could evolve along time. The IR computed in the period B (Fig. 8-6.B), between August 08–18, has a different shape than in the period A. The two peaks are still visible after about 1 day and 2.5 days, but their amplitude has switched, with the second peak becoming predominant. The peak amplitude was multiplied by $\times 0.5$ on the first peak (0.06 to 0.03 cm/cm/hour), and by $\times 2.3$ on the second peak (0.03 to 0.07 cm/cm/hour). Furthermore, its width increased by a factor $\times 3$ (from 1 day to 3 days). That suggests a stronger response to rainfall, which lasted longer after the rainfall event. This is consistent with the displacement rate model based on a static impulse response (Fig. 8-5). In July 3–28, the measured displacement rate was always below the model. However, from July 28 to August 18, the measured displacement rate started to overpass the model, both in amplitude and in decrease time. This response might include a bias from the instruments, and particularly from the rotation of the fixation support of the tags caused by a loss of rigidity of the top soil layers. However, in July and August, the

tags had been installed recently and this rotation was minor, particularly in relation to the amplitude peaks of displacement rates of the periods A and B. Furtermore, this rotation, which started to be visible in autumn, moved the tags either further or closer to the station antenna, so its (minor) effect should be averaged when displaying all the tags. Finally, some tags (the n°10 and n°11) were fixed deeper in the ground (0.7 m deep) and showed only a few centimeters of rotational movements. So this effect should be minor in the impulse response. In conclusion, the shape of the impulse response suggests two hypotheses about the Pont-Bourquin landslide: First, rainfall would cause two peaks of displacement rate, after about 1 day and 2.5 days. Second, the landslide response to rain would alternate between a stable and transient state, corresponding to the periods A and B.

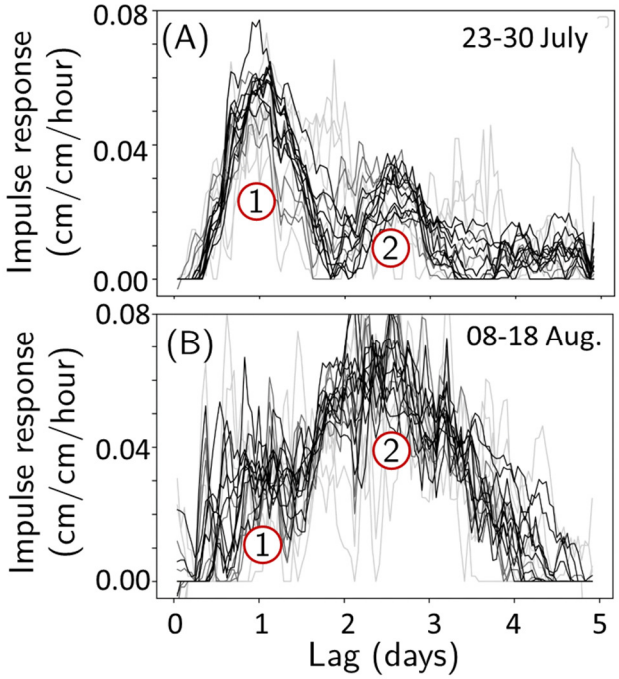


Fig. 8-6: Impulse response computed over the period A and B for all the tags. The gray curves are obtained from noisier data than the black curves. Both curves display two peaks, noted as 1 and 2.

### 8.5.2 Relation with seismic velocity lags

Geophysical techniques are used for monitoring landslide properties at depth without drilling (Jongmans and Garambois, 2007; Whiteley et al., 2018). Seismic ambient noise has been used to observe changes of rigidity loss, by tracking relative variations of surface wave velocity ($dv/v$) (Larose et al., 2015; Mainsant et al., 2012b). This section compares the variations of seismic velocity with the variations of impulse response, to check for potential consistency: a displacement caused by a

rigidity loss in the deformed layers should also exhibit a reduction of *dv/v* , visible at frequencies of 10–14 Hz (Mainsant et al., 2015). The dv/v was observed at 8-12 Hz, following the parameters used by (Bièvre et al., 2018; Carrière, 2016) to study the influence of the environment.

The peaks of displacement rates on Fig. 8-2 correspond visually to negative peaks of *dv/v*. Their cross-correlation over the whole period (not displayed) suggests a *dv/v* lagged by 2.1 days after the displacement, with, however, a weak correlation coefficient of 0.35.

A focus on the periods A and B is displayed on Fig. 8-7. In this period, a drop of dv/v appeared 1 to 1.5 days after the diminution of the velocity, by looking either at the time when the reduction occurs or at the lag between the respective peaks. This suggests that the drop of *dv/v* at 8-12 Hz appeared after the displacement rate increase. This frequency range would be sensitive mostly to depth below 9 m on this site, which explains the larger delay of the observed dv/v. To complete this analysis of the lag, the *dv/v* should be studied at different frequencies. In particular, higher frequencies should be sensitive to layers that are shallower, in which the water should infiltrate with a lower lag.

When looking at the time series of the period B (Fig. 8-7.a), a change seems to occur on August 10, between a state that we will call “stable” and another one that we will call “transient.” The change occurs only two days after the first rainfall. At this time, the measured displacement rate started to strongly exceed the model (calibrated in July 2017). It was twice higher at its peak. At the same time, the *dv/v* started to drop. It continued to decrease for several days, with two minimums, respectively 6 days and 9 days after the first rainfall event. The last peak of dv/v reached –5%. That is a large drop compared to existing studies that exhibited seasonal variations of ±2%, on this site (Larose et al., 2015; Carrière, 2016; Bièvre et al., 2018). However these studies computed the *dv/v* on an hourly basis, while this study uses hourly data.

The existence of two states of the landslide changes the possible interpretation of the two IR peaks (at 1 day and 2.5 days). The computation of the IR assumes the landslide response to be linear and stable within the studied window. The linearity hypothesis seems correct within some time windows, due to the good fit between the modeled and measured displacement rates even with different quantities of rain. However, the response is clearly not stable in time: the displacement caused by rain

was twice higher in the transient state, compared to the stable state. Therefore, an impulse response computed from a period that includes both a transient and stable state, with also several closely spaced rainfall episodes, could display a secondary peak to balance the difference between the two states. Indeed, two minor peaks occurred on the model (highlighted in green on Fig. 8-7.b) on August 11 and 12. Each of these two peaks occurred one day after the respective rainfall events. That is consistent with the impulse response displaying a major peak after one day, in the stable state. However, the same peaks are also visible on the measured data, suggesting that a major importance of the first peak of IR in the transient state could also be possible. More data and more analysis would be required to know if the second IR peak comes from a true dual physical process, or from an artifact due to the change of state of the landslide. In both cases, the indicator would be useful for monitoring landslides: an indicator of a change of state might serve as a precursor signal.

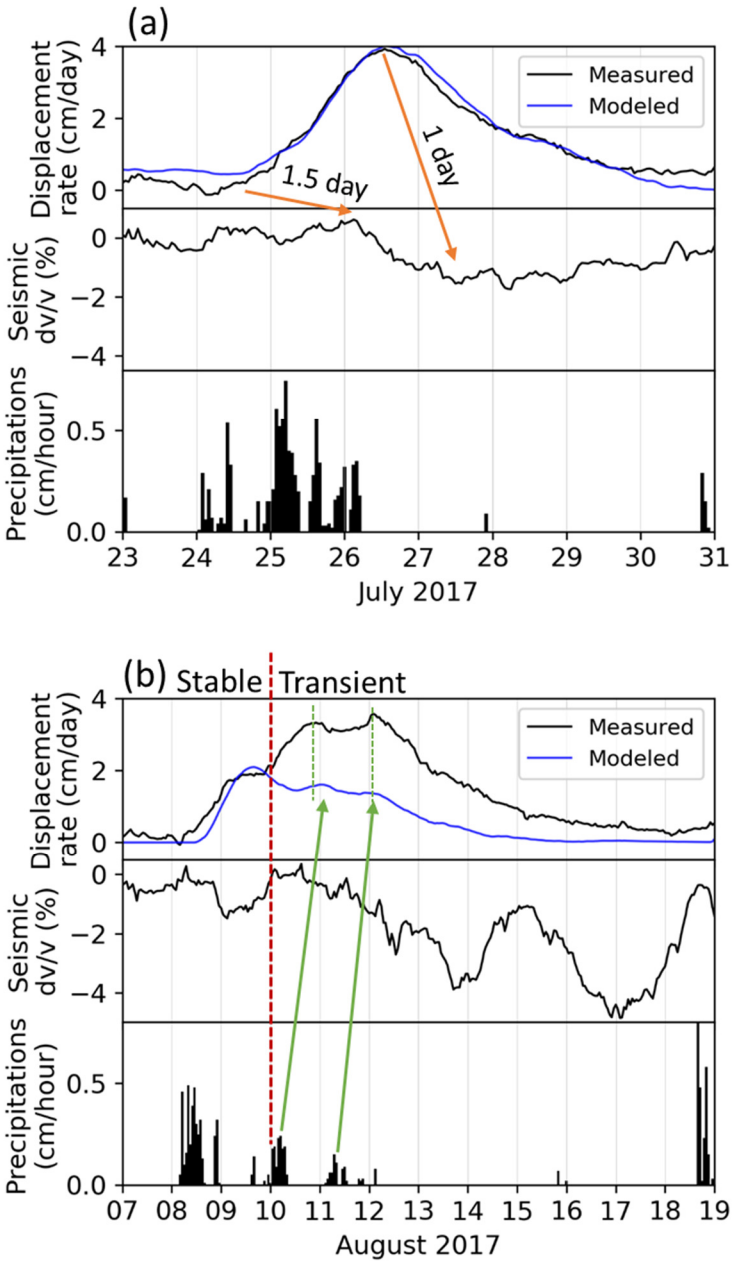


Fig. 8-7: Displacement rate, seismic velocity variations at 8-12 Hz, and precipitations, during (a) the period A and (b) the period B.

### 8.5.3 Evolution of the response over time

To exhibit its evolution in time, the impulse response is computed over a two-weeks-wide moving window during the whole period of observation, using the data from the tag n° 10. The inversion used a regularization factor $\lambda$=0.04 and used normalized data with equations (8-4) and a factor $a$=0.5. The IR matrix then was smoothed with a 3-days moving average filter on the lag axis (vertical) and with a 3-days moving median on the time axis (horizontal). The resulting IR matrix is

shown on (Fig. 8-8), along with the sum of each IR, the displacement and precipitation data used to compute it, and the seismic velocity variations. The IR displayed at a given time is computed from the displacement rate of the two preceding weeks and from the rainfall of the three preceding weeks.

The IR matrix suggests that the landslide response to rainfall can evolve between two states S and T (stable and transient), corresponding to the states already studied in Fig. 8-6. A and B, respectively. The integration of the IR over time (=its discrete sum) represents an indicator of the sensitivity of the landslide to rainfall. For example, a sum of 5 cm/cm would mean that 1 cm of rainfall would produce a cumulated displacement of 5 cm of the landslide. Until August 8, the impulse response is dominated by the first peak (lag=1 day), which we call the stable state (S). During the stable state, the seismic velocity is just below zero in the beginning, then drops to -1.5% after the first strong rainfall event and starts to slowly increase back (shown with a red line). This decrease of velocity suggests that the rainfall event at the end of July induced a long-term change of state in the subsoil. After several days of rainfall and before a full recovery of the seismic velocity, on August 10, the shape of the impulse response changes to the transient state. It is characterized by a broad IR peak centered at 2–2.5 days, and by a decrease of seismic velocity down to –3%. At the beginning of September, the IR returns to the stable state: the main IR peak goes back to a 1–day lag, and the dv/v returns to a more stable value. This alternation between a stable and transient state was also observed by Bontemps et al. (in preparation), in a landslide triggered by rainfall and seismic activity. Starting in October, the impulse response of the landslide is not very clear, and then disturbed by the snow, which prevents its exploitation.

In conclusion, the lag of the IR peak seems to coincide well with the dv/v, with a lag at $2 - 2.5$ days corresponding to a drop of seismic velocity. However, it is unclear whether the IR dual lag is due to a true physical lag, or to a transition between two states occurring within the IR time window. Indeed, the equation (8-1) assumes the landslide response to be linear and stable within the computation window. And we have shown that it is not stable, which could bring an artifact such as a second peak in the IR, to compensate. In that case, the second peak would represent a change of state occurring in the landslide, which could also be a useful indicator.

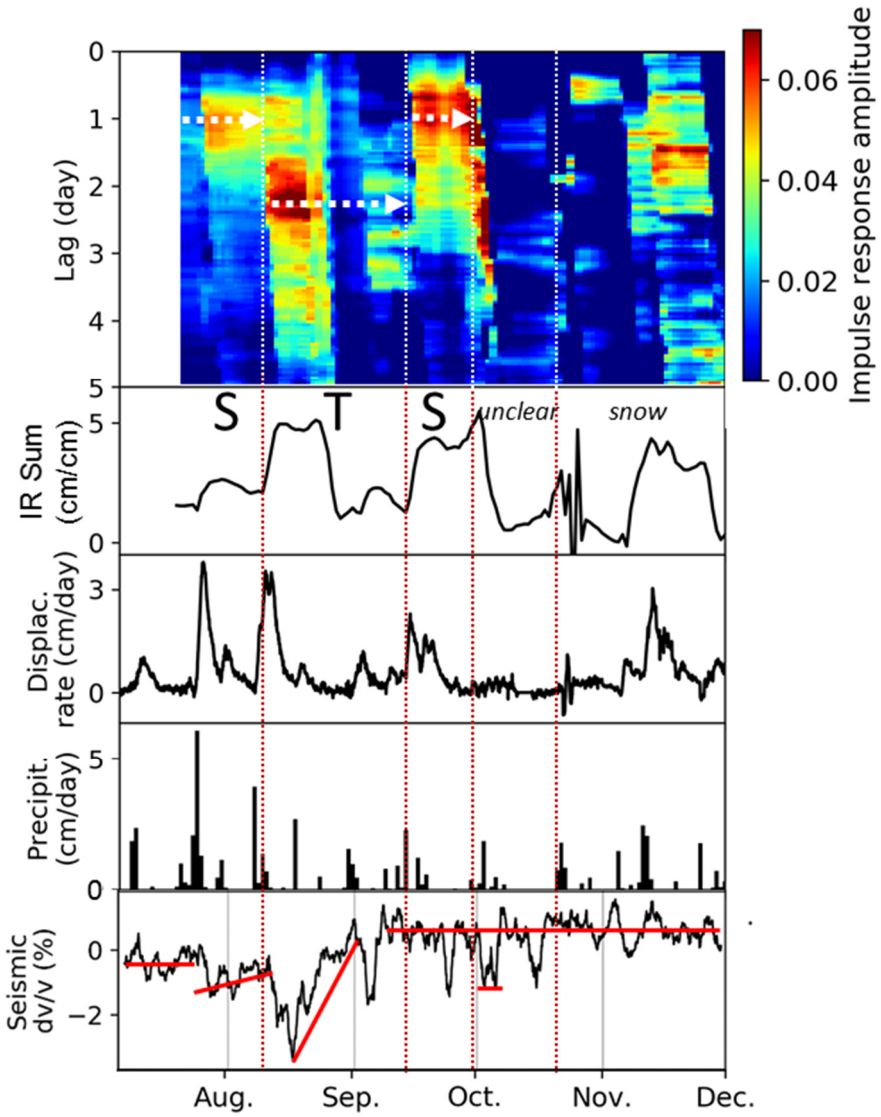


Fig. 8-8: Impulse response computed on a 2-weeks moving average, along with the displacement rate and precipitation curves. The impulse response change its state from stable (S, dominated by the 1-day peak) to transient (T, dominated by a peak at 2–2.5 days) to stable again. Transient state also corresponds to a drop of seismic velocity.

### 8.5.4 Stability and robustness across years

The hypotheses of the previous sections were made from only 5 months of data. To further validate these hypotheses, this section extends the study to 2012–2014. Observing the two IR peaks and the change between a stable and transient state, consistently over the years should strengthen these hypotheses.

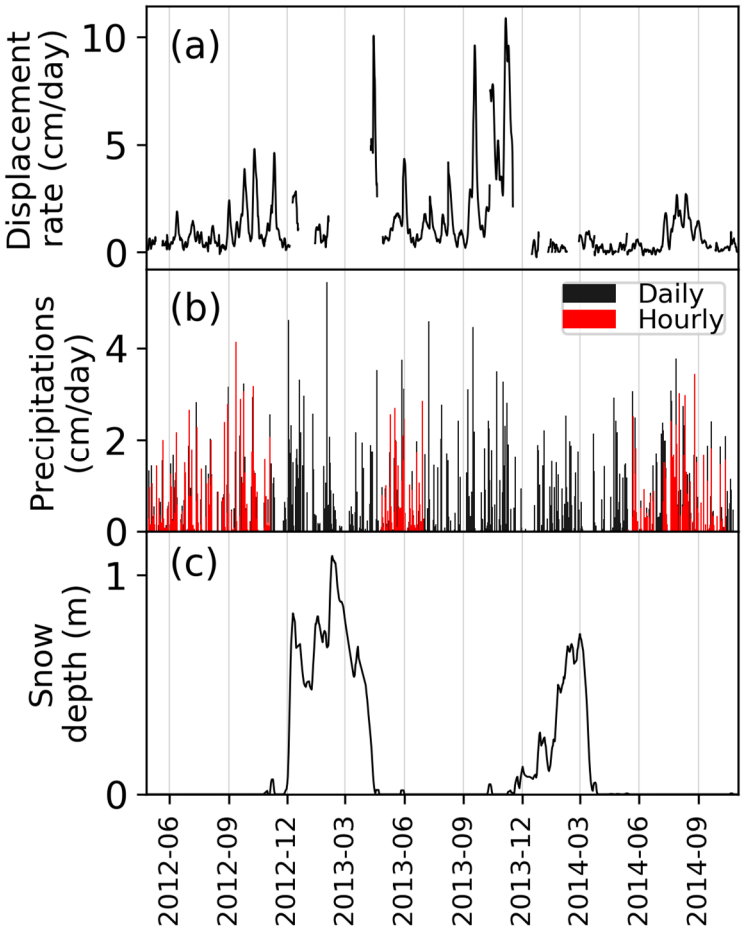


Fig. 8-9: Treated historical data at Pont-Bourquin between 2012-04-27 and 2014-11-01. (a) Displacement data from the extensometer. (b) Rainfall measured every hour from the on-site meteorological station (in red) compared to precipitations measured daily by MétéoSuisse (in black). (c) Snow depth, that strongly affect the water inputs and prohibits the computation of an accurate impulse response.

However, the rainfall and displacement data in 2012–2014 were of lower quality than in 2017, which required adapting the processing. Relevant data was data firstly selected (Fig. 8-2) with the process described in section 8.3 . When snow was present on the ground, the data was removed one week before and after (= length of the IR) . The bias of the rain on the extensometer measurement (see Fig. 8-4 and chapter 7) was smoothed by a 3–day moving average. The impulse response was then computed over a 6-week-large moving window, by steps of 6 weeks. The windows with low rainfall and displacement rate were removed. The regularization factor $\lambda$ was increased iteratively, until the resulting IR was null at the lags t=–1 day and t=+7 days. The IRs with a null value, corresponding to high misfits, were removed from the results. The remaining IRs were then normalized by their maximum amplitudes, to compare the shapes of the IR visually. The resulting IRs are shown in Fig. 8-10.

Dual IR peaks are exhibited in 6 curves, in 2012 and 2014. These exhibit a first peak after around one day, and a second smaller peak after about three days. That is consistent with the dual IR peaks previously shown over 5 months in 2017. Again, these two peaks could either represent a dual process (two infiltration velocities or two deformed layers), or the change of the landslide between two states (the second state being more sensitive to rain).

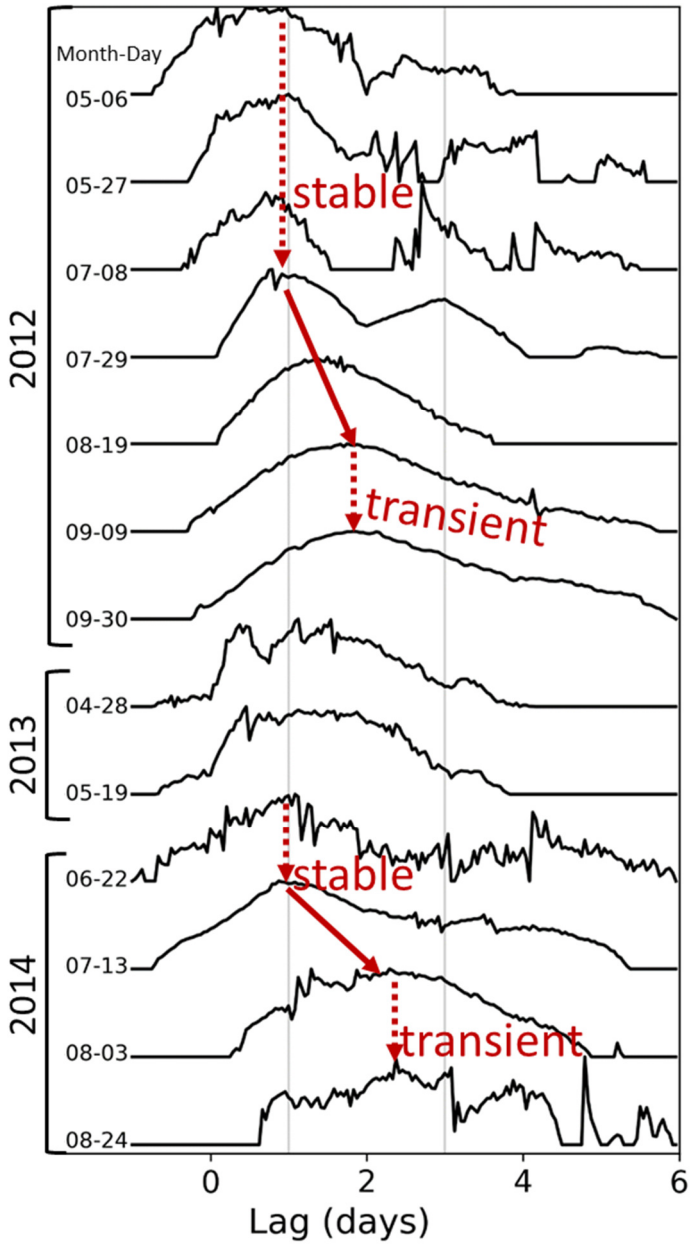


Fig. 8-10: Observation of impulse responses at Pont-Bourquin in 2012, 2013 and 2014, using local rainfall measurement and the displacement data from an extensometer. The impulse response may have a first peak at (a) t=1 day or (b) t=2 to 2.5 days. The transition from stable to transient state happens in August 2012 and 2014.

## 8.6 Discussion on Pont-Bourquin processes

The two IR velocity peaks could have two explanations. First, two distinct processes could indeed occur in the landslide, with two true lags. Second, an increase of sensitivity to water between two consecutive rainfall events could be compensated by an artificially lagged peak in the IR. If that was a true lag, it could be explained by the deformation of layers at two depths, or by two infiltration processes with a different delay. Bievre et al. (2018a) had proposed the hypothesis of two deformed layers after observing the variations of seismic velocities of the Pont-Bourquin landslide. However, the hypothetical two slipping surfaces had not been detected from geophysical surveys nor with an inclinometer (Brönnimann, 2011; Mainsant et al., 2012b).

On the contrary, the hypothesis of a dual infiltration process is supported by a hydrogeological study (Brönnimann, 2011) that observed infiltration delays of 1 to 4 days. The study also suggested that water would both infiltrate directly into the soil, and resurge after passing through the bedrock. Furthermore, this study observed the evolution of the two infiltration delays across time, suggesting a change of state of the landslide after the accumulation of several rainfall episodes. That is consistent with the hypothesis of a water trap where water would accumulate made by Brönnimann (2011).

However, the second IR peak could also be created by a rapid change in the landslide response to rainfall between two rainfall events, represented by the sum of the IR. In this case, the second peak should instead be considered as an indicator that the state of the landslide would be evolving. In both cases, the dominance of the second peak would represent a transient state, which could potentially provide an early indicator of a landslide instability.

## 8.7 Conclusions

Computing an impulse response with statistical deconvolution of the surface displacement data from rain data provides results that are sharper and more physically true than cross-correlating the time series. It also characterizes the landslide complexity with more details than when inverting a simpler analytical impulse response.

The statistical deconvolution allows for making a linear model of the landslide velocity using rainfall data. It seems to work as well as others similar model. The larger number of parameters, compared to analytical impulse responses, results in

noisier impulse responses. But this noise is averaged when convolving the impulse response over a time series of rainfall.

The impulse response seems to evolve over time. The computation of this response over a short time windows provide sharper deconvolved response. At Pont-Bourquin, that led to detecting two peaks in the IR, with lags of 1 day and 2.5 days. This peaks could correspond eitheir to two physical processes, or could be an artifact created during the inversion that represent the change of state of the landslide.

The evolution of the impulse response may reveal changes of behaviors of the landslide. For example, the increase of the second IR peak in August 2017 happened after two strong rain episodes and happened simultaneously to a drop of seismic velocity.

In terms of limits, this approach requires an input (infiltrated water) and an output (displacement). It does not work without rain or landslide movement. The input of infiltrated water and the output of displacement rates must not be biased, and require a time sampling that is below the impulse response length.

This study could be complemented by further analysis. The variations of the impulse response should be compared with the dv/v at different frequencies, to deduce the depth at which the phenomenons occur. To this goal, the historical dv/v should be recomputed at an hourly resolution, using a processing that doesn't require smoothing (see chapter 2). The existence of transient states should be confirmed in the historical data, by looking at the misfit between modeled and measured displacement, and by comparing with the dv/v variations. The results should finally be compared with groundwater data which was sometimes measured at Pont-Bourquin. As a perspective, the method should be applied on a shallow landslide just before its failure: the change of impulse response might provide a precursor to failure.

# Perspectives

Ce travail de thèse offre de nombreuses perspectives, afin 1) d'améliorer les capacités techniques de la mesure de déplacement RFID ; 2) d'exploiter l'interaction de la neige et de la végétation pour améliorer la mesure voire pour développer de nouveaux capteurs ; 3) de développer des techniques d'analyse basées sur de larges quantités de données telles que fournies par la RFID ; et 4) de profiter des avancées techniques de ce travail de thèse pour mieux comprendre l'action de la neige sur les glissements de terrain. Ces thématiques sont discutées ci-dessous.

La technique de mesure de déplacements RFID pourrait être améliorée sur trois aspects. Premièrement, l'augmentation de sa portée de 60 m à 100-200 m la rendrait applicable sur un grand nombre de glissements de terrain et maximiserait le bénéfice du faible coût par tag. Dans ce but, un prototype de tag directif a été testé (portée x2, cf. annexes) et pourrait être amélioré en collaboration avec un laboratoire spécialisé en RFID. La portée sera aussi augmentée dans le futur avec l'amélioration continue de la sensibilité des lecteurs et de puces RFID commerciales. Deuxièmement, mesurer les déplacements et la rotation des tags en 3 dimensions offrirait des données plus complètes. La translation 3D pourrait être mesurée en installant plusieurs antennes côté station afin de réaliser une triangulation. La rotation pourrait être mesurée en installant plusieurs tags à différentes hauteurs sur le même support de fixation afin de mesurer la différence de déplacement entre ces tags. Séparer les composantes de rotation et de translation du déplacement améliorerait la précision des mesures. La mesure de rotation serait doublement utile sur les glissements de terrain rotationnel ou sur les instabilités rocheuses basculantes (écailles), par exemple. Ces mesures de rotation et translation 3D ont été validées en environnement contrôlé lors du stage de Guilhem Scheiblin (Février-Juin 2018) et leur test sur le glissement de terrain de l'Harmalière est prévu en été 2019. Troisièmement, la fiabilité du dispositif de mesure — très convenable pour un premier test de prototype en conditions réelles — doit encore être améliorée avant de l'intégrer dans une surveillance opérationnelle. La chaîne d'acquisition doit intégrer une gestion d'erreurs, et la consommation électrique doit être diminuée par des cycles de mise en veille. Ces travaux d'ingénierie ont été entamés lors du stage d'Axel Pionchon (Mai-Sept. 2018) et continuent au sein du laboratoire commun Geo3i Lab (démarré en 2019). Ils s'intensifieront après la première vente de prototype par la société Géolithe, actuellement en négociation.

Les influences de la neige et de la végétation sur les systèmes RIFD pourraient être exploitées pour mesurer les propriétés physiques de la neige et de la végétation à l'aide d'un réseau de tags. Les mesures de phase, de puissance de signal reçue ou de désaccordage des antennes de tag (effets de proximité) pourraient permettre d'estimer la permittivité efficace de ces milieux. On pourrait alors en déduire leurs propriétés physiques de densité, de contenu en eau liquide ou de salinité. La mesure de densité et de teneur en eau de la végétation pourrait être utile pour l'agriculture de précision. Dans le cas de la neige, ces mesures locales pourraient servir à mieux estimer les risques d'avalanche ou le volume d'eau de fonte qui approvisionne les systèmes hydro-électriques. L'étude des mesures RFID de neige a commencé au cours de la thèse de Guilhem Scheiblin démarrée en septembre 2018. Réciproquement, une bonne connaissance de l'interaction entre le signal radio et ces milieux (neige, végétation) permettrait d'effectuer des corrections de phase pour augmenter la précision des mesures de déformation.

La combinaison de plusieurs types de mesure rend la surveillance de glissements de terrain plus fiable. L'analyse de la relation entre précipitations et déplacements semble prometteuse, mais inefficace en cas de présence d'un manteau neigeux qui perturbe l'infiltration. Comme de nombreux glissements sont provoqués par la fonte de la neige, quantifier cette fonte en ajoutant des tags RFID dédiés à cette mesure améliorerait considérablement la surveillance pour un coût négligeable. Le même constat peut être réalisé avec des capteurs d'humidité de sol. De nombreux tags génèreraient une grande quantité de données ce qui pourrait nécessiter de nouvelles méthodes de traitement et d'analyse. Enfin, la mesure complémentaire des variations de vitesse sismique pourrait améliorer la fiabilité d'une surveillance sur les glissements argileux. Ce travail de thèse a identifié plusieurs verrous à son application en surveillance opérationnelle, qui devront être levés.

Enfin, les travaux effectués dans la thèse offrent une opportunité d'une thématique de recherche visant à mieux étudier l'interaction entre la neige et les glissements de terrain. En effet, la fonte de la neige est un déclencheur majeur de glissements de terrains montagneux (ex. accélération de Pont-Bourqin autour du 1er janvier 2018), qui est paradoxalement peu étudié à cause des difficultés techniques à opérer les mesures adéquates (Matsuura et al., 2017). Les mesures nécessaires incluent le volume équivalent liquide de la neige (dont la variation permet d'estimer précisément la fonte), et aux mesures de déplacement et d'activité du glissement en présence de neige. Or la méthode RFID et l'interférométrie de bruit sismique

fonctionnent toutes deux en présence d'un couvert neigeux. Il semblerait d'ailleurs que la hauteur et la fonte de la neige aient un impact sur la variation de vitesse sismique (Wang et al., 2017) (annexes 4), qui reste à comprendre. De plus, développer des capteurs de neige RFID permettrait de caractériser la fonte avec une haute résolution spatiotemporelle et à faible coût. Ces mesures permettraient d'utiliser la méthode de réponse impulsionnelle fonte –> déplacement, en présence d'un manteau neigeux, et aiderait à mieux comprendre la dynamique de l'effet de la neige au cours du temps. Si j'avais à proposer un projet de recherche à moyen/long terme, il aurait sans doute cet objectif de mieux comprendre l'action de la neige sur les glissements de terrain.

# Appendix 1
# Monitoring Pas de l'Ours using total stations

*The following conference paper presents an implementation of a standard monitoring technique (laser total station) on a real early-warning system, operated by the company Géolithe. Defortis, Simon, Mathieu Le Breton, Quentin Barbier, Lucas Meignan, Fabrice Guyoton, Romain Le Roux-Mallouf, Jean-Marc Verdier, Gilles Delabelle, and Romain Gaucher. "Automatic Monitoring of Landslide Displacements Using Total Station." In Proc. Int. Symp. Rock Slope Stability (RSS), 121–22. Chambéry: C2ROP, 2018. https://www.c2rop.fr/symposium-rss-2018/actes/.*

Landslides are characterized by surface movements with (1) velocity ranging from millimetres to meters and (2) a right of way from meters to tens of kilometres. Detecting the deformation timing and kinematic is a key point in the understanding of the physical causes and to warn possible hazards. Different systems are used to monitor the deformation including differential GPS, optical laser, lidar, radar interferometers (Gili et al., (2000), Abellàn et al., (2009), Herrera et al., (2009), Travelletti et al., (2012)). In this study, we use an automatic survey using total stations to (1) monitor the landslide velocity and kinematic and (2) set up a warning system to close the road, in case of a significant slip which could reach the foothill road.

## 1 STUDY SITE

The Pas de l'Ours landslide is situated in the Queyras valley in France, on the right bank of the Guil, between Aiguilles and Abries cities (Fig. 1).

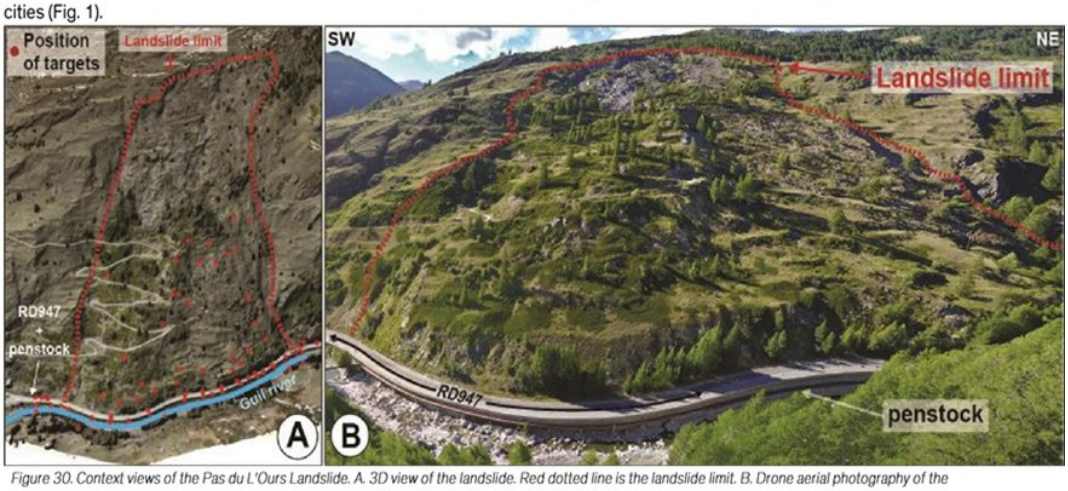


*Figure 30. Context views of the Pas du L'Ours Landslide. A. 3D view of the landslide. Red dotted line is the landslide limit. B. Drone aerial photography of the landslide. Red dotted line is the landslide limit.*

It's one of the largest active slow-moving landslides in the Alps with a width of about 500 m and a high of 400 m and a volume estimated at 15 million cubic meters. The landslides affects the RD947. This road is built in the foothill on excavated soil raised above the Guil River by support structure (Fig. 1). Several issues are concerned by the Pas de l'Ours landslide including the road itself which is the single access to the ski stations of Abries and Ristolas, a penstock or the downstream towns in case of rapid flood caused by breach of a landslide dam. This landslide is monitored since the beginning of 2017 with several facilities such as radar interferometry, GPS, topographic survey, inclinometer measurements (Bornemann et al., 2016, Bornemann et al., 2017, Provost et al., 2017). Since September 2017, the Géolithe Company were assigned to set up an automatic survey of the landslide composed by two total stations (distance measuring systems) and 75 targets located on the road and the landslide (Fig. 2).

## 2 MATERIAL AND METHOD – AUTOMATIC MEASUREMENT DEVICES

The device is composed by 75 targets including 8 reference targets allowing post-treatment corrections. The targets are laid out on the lower part of the landslide between the RD947 at 1480 m to 1640 m of elevation. The two total stations are placed on the opposite hillside and scan the targets with 15-to-45-min frequency.

[1] Géolithe, Crolles, France, corresponding author: romain.lerouxmallouf@geolithe.fr
[2] Institut des Sciences de la Terre, Université Grenoble Alpes, CNRS, Grenoble, France
[3] Département des Hautes-Alpes
[4] Direction interdépartementale des routes méditerranée

## 3 PRELIMINARY RESULTS – MORPHOLOGY AND KINEMATIC OF THE LANDSLIDE

Combine to manual measurement from spring 2017, the automatic measurement (set up in september 2017) monitored two distinct phases of the landslide including (1) a slipping phase (27/04/2017 to 10/07/2017) and (2) remission phase (10/10/2017 to 20/12/2017). This dataset allow us to make assumptions on the landslide kinematic.

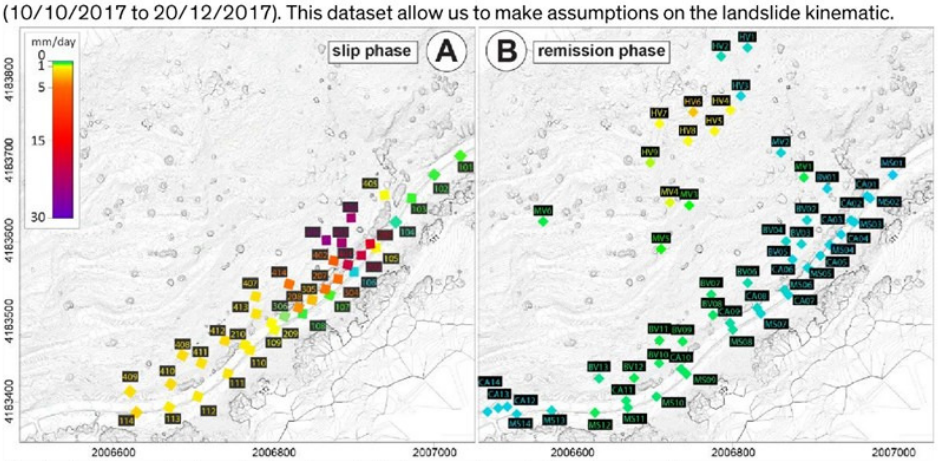


*Figure 2. Average landslide velocities during slip and remission phases. A. Average velocities during the slip phase of the landslide between the 27/04/2017 and 10/07/2017. B. Average velocities during the remission phase between the 10/10/2017 and*

The landslide morphology displays two distinct compartments (west and east).

1. The east part is characterized by rough steep topography without vegetation
2. The west part displays a smoother topography with a vegetal cover.

This lateral variation is clearly visible in the kinematic measurements through a velocity difference during the two phases (remission and slip) between the two compartment feet. The slip phase is characterized by large landslide feet displacement as shown by the figure 2a. This displacement is larger along the east side than the west side. Conversely, during the remission phase, the landslide feet is locked while the automatic measurements show surface displacements (targets HV4 to HV9 in figure 2B).

This lateral variation is associated with a retaining wall built on the landslide east feet, below the road (Fig. 1). The wall is reinforced by horizontal anchored to the ground and is considered as undeformed as shown by the really low values of the targets 103 to 108 (less than 1 mm/day) during the slip phase.

## 4 CONCLUSION

The automatic monitoring of the Pas de l'Ours landslide by an automatic monitoring allows us to better constrain the kinematic of the deformation. Our results show that (1) the landslide can be divided in two distinct part characterized by two different deformation mechanism and (2) the landslide have average displacement rates that can exceed 30 mm per day. Associated with the data acquisition system, we set up a warning system to close the road based on daily velocity threshold to ensure the safety of the road users.

The inverse velocity technique was used on this landslide, which allowed to successfully close the road that was threatened by the landslide two days before a dangerous mudflow (first red cross on Figure A-1)

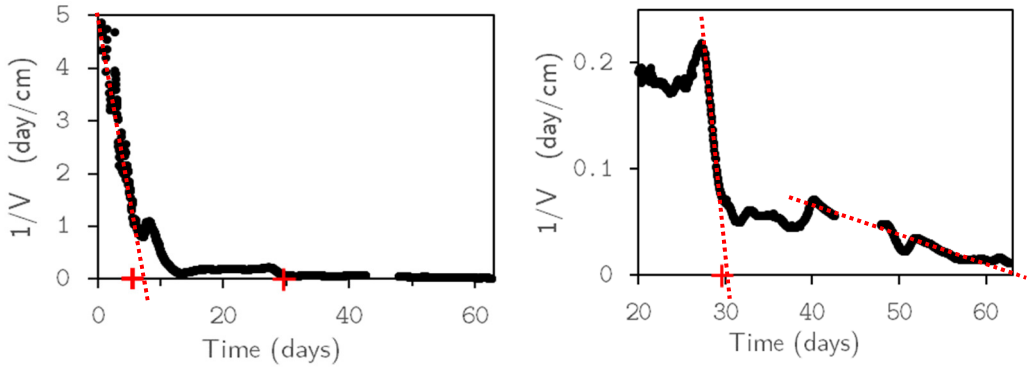


Figure A-1: (top) Inverse velocity at Pas de l'ours landslide and (bottom) zoom. Dashed red lines indicate the regression of the inverse velocity, with a prediction of failure. Red crosses indicate true failures that occurred in another part of the landslide.

# Appendix 2 Interferences from the ground

This section present the interferences from the ground, due to a coupling with the ground at a low elevation of the tag above the ground, and due to multipath interferences in a near-flat and strong-relief terrain. Even if not studied specifically for RFID, the outdoor multipath problem has been already dealt widely for telecommunications in general, and RFID studies indoor had to deal with even stronger interferences. Still, this work highlights the practical interference problems due to terrain relief, and validate the ray model for understanding ground interferences.

The RFID interrogator (SR420 from Impinj) was emitting at 865.7 MHz. The tags were battery-assisted (Tagsys high gain prototype tag with a slot antenna). The station antennas were Yagi-Uda directive antenna (13 elements), except for the 80-meters signal strength profile that used a panel antenna (Kathrein 21 dBi).

The model used the ray approximation presented in the snow chapter, with one direct path and 1 or 2 ground-reflected path. When the ground is not flat, interference patterns can become complex, such as shown on Figure A-4. The impact of the relief was studied at the Vence pass on 22 September 2017.

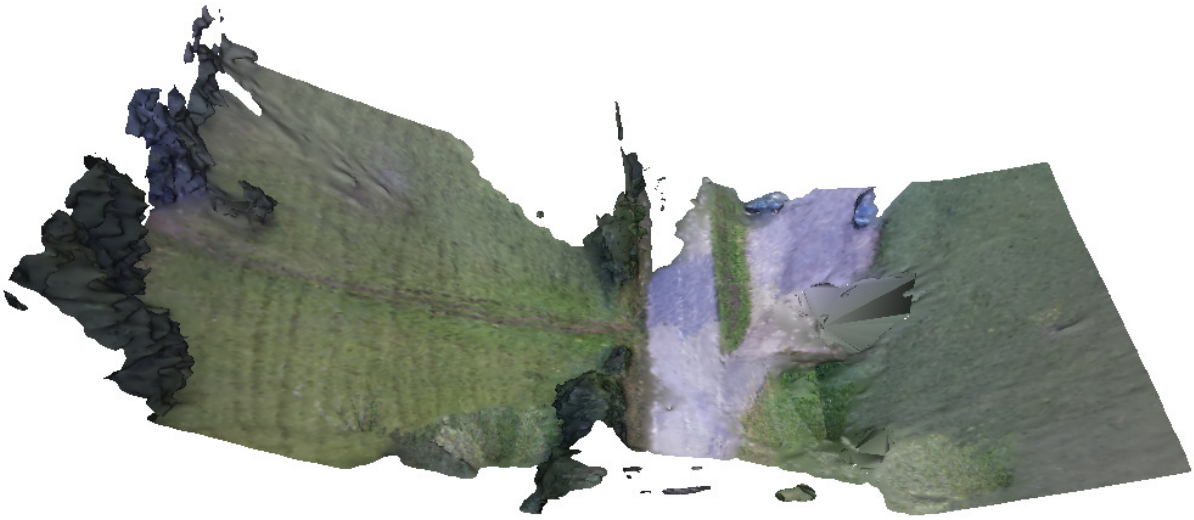

Figure A-2: Numerical 3D model of the Col de Vence field, computed with photogrammetric technique.

Each effect is modeled using a simple model propagating into an isotropic dielectric medium, and reflecting on the ground. The propagation with snow and vegetation use one ray that propagates directly to the tag and one ray that is reflected on the ground. The propagation with a complex relief required to use three rays, for direct propagation, reflexion on the ground near the tag and reflexion in the

middle of the pass (the reflected path of the ground near the station is neglected because of the directivity of the station antenna, and was not necessary to explain the measurements).

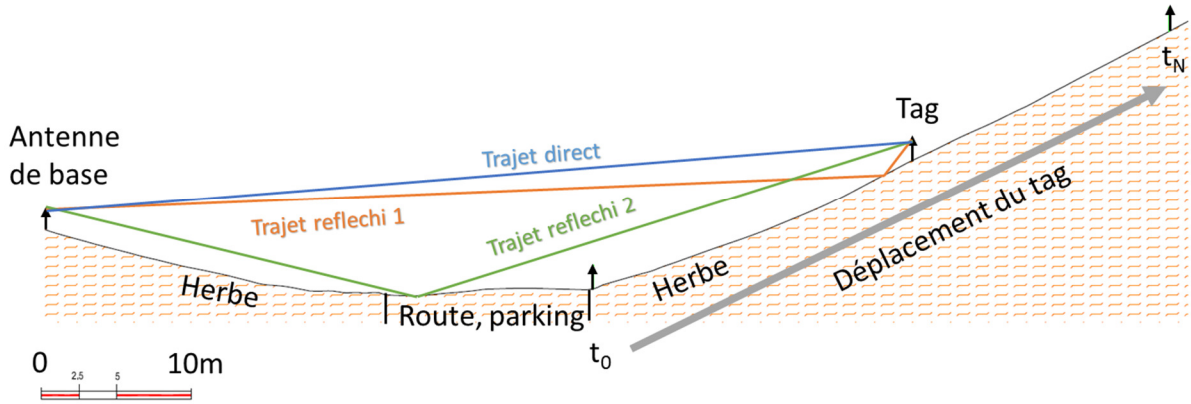


Figure A-3: Model with 3 rays used at Vence pass, to explain the measurements.

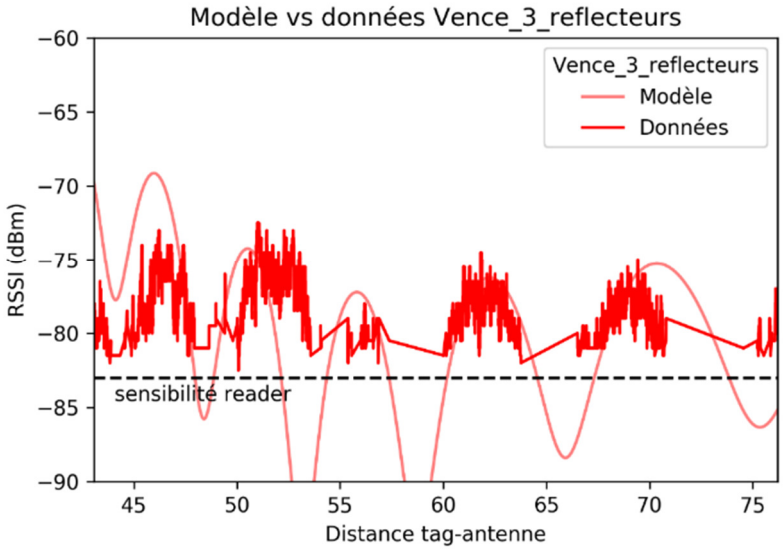


Figure A-4: Modeled and measured multipath interferences on a terrain with a complex topography. (left) the measured signal strength fits rather well with the 3-rays model, validating the model for qualitative understanding.

The interferences from multipathing when moving a tag vertically are however very visible in the context of a complex topography (Figure A-5), with the signal strength varying of at least +/- 12 dB (the lower limit is not measured so the total loss is likely to be stronger). This shows that under a complex topography, the received signal strength and the ability to read a tag strongly dependent on the height of the tag above ground level.

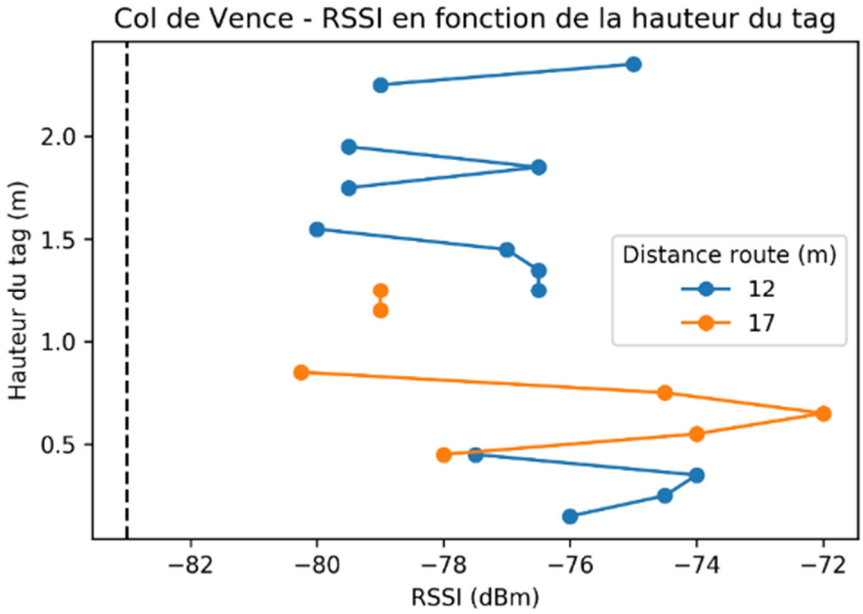


Figure A-5: Multipath interference with a complex topography, depending on the tag height

The interferences due to complex topography induce a succession of positive and negative peak of signal strenght (more than 12 dB). That is challenging when there is little margin for additional path loss, which is often the case in passive RFID (for example when using large range, small tags with small effective gain, or linear depolarization). This effect is even stronger indoors, and has been widely addressed. Because this effect happens at specific location, it is resolved by moving the tag, the station antenna or even the nearby reflectors. Installing multiple antennas may also greatly increase the chance to be read.

# Appendix 3 Increasing the reading range

This appendix shows the work done towards improving the reading range, with a high gain tag. Increasing the range is a key to an effective displacement monitoring system.

## 1. Options to increase the range

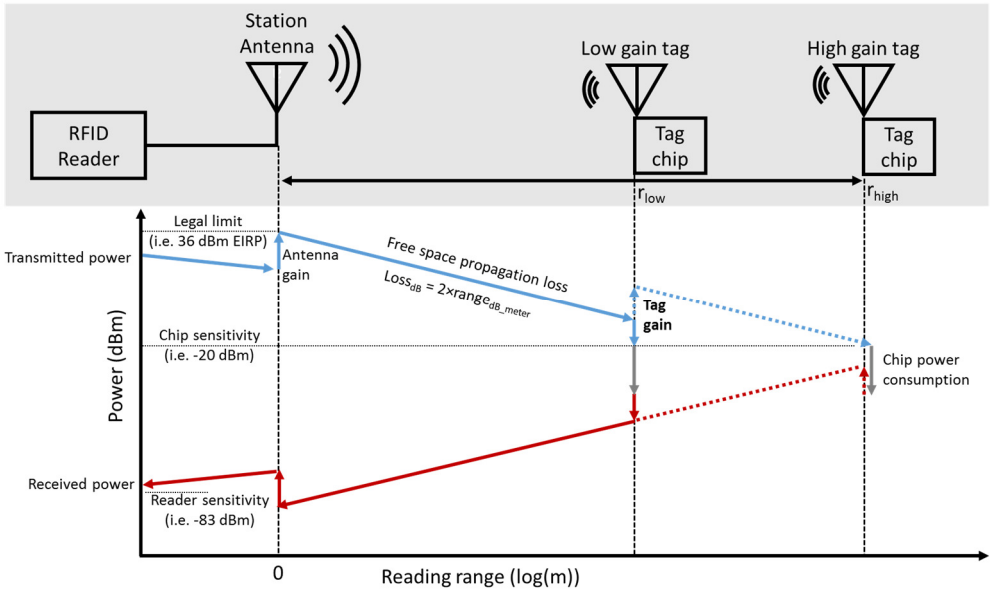


Figure A-6: Diagram of path loss. Modified from (Andia-Vera, 2017)

In part III of this manuscript, the reading range appeared as a critical step to increase the value of the RFID technique on a landslide and in general on outdoor applications. There are several ways to improve this range:

a) **Increase the station antenna gain:** However that is limited by the legislation. Furthermore, that means using large and heavy antennas which are complicated to install on a slope, and that also reduce the aperture of the antenna and therefore the coverage area. It is not a good solution.

b) **Increase the transmitted power:** However, commercial readers rarely transmit above 30 or 33 dBm for legal reasons. Furthermore, increasing the transmitted power would increase the power consumption of the reader, which is also a limiting factor on remote installations. It is not a good solution.

c) **Increase the chip sensitivity**: This was already done by using battery-assisted tags, which resulted in being limited by the reader sensitivity in the present study. Microelectronic research is constantly increasing micro-

circuits sensitivity (Amato et al., 2018; Durgin, 2016), but these are prototypes. Sensitivity is slowly increasing with new generations of robust and low-cost commercial chips. We have to wait.

d) **Increasing the reader sensitivity**: That increase with new generations of readers available on the market. There is not much we can do here. Particularly, we need robust readers, and research prototype would hardly fit the necessity for continuous acquisition in severe conditions outdoors. We have to wait.

e) **Using a bistatic reader**: Using a bistatic reader (with separated reception and emission antennas) increase this sensitivity. However after discussions with the provider of the FX9500, it appeared in the test that the reader could not read the phase, later confirmed by high-level technical support. A bistatic reader could also differentiate the emitting antenna (normal gain) from the reception antenna (high gain) to read high-sensitivity tags, such as in (Amato et al., 2018).

f) **Increasing the tag gain:** Tags are usually designed to be read in whatever directions, so tags on the markets tend to be small, low-cost, and omnidirectional. Increasing the tag gain would require to use a directive antenna, which would increase the tag size and cost and restrict the tag orientation compared to commercial tags. This would require to design a directive antenna such as in (Kim and Yeo, 2012; Zuffanelli et al., 2016), well-tuned with a high-sensitivity microcircuit and a protection for outdoor usage (against snow, rain, insects). The risk is the increase in weight and in windload that would require better tag fixations. The tag high directivity would also reduce slightly the ground multipath, therefore increase the ranging accuracy.

Developing long-range directive tags appears as the only feasible option for increasing the range further. These tags would cost more in terms of fabrication (because of small volumes) and maintenance (to keep the right orientation towards the station antenna), but still 10 to 100 times less than conventional active techniques.

## 2. Improving the range with more efficient tags

Most of the RFID experiments presented in this thesis use the Survivor B tag, from Confidex. This tag has a high chip sensitivity due to its battery assistance, includes a useful temperature sensor and has a hard casing well designed for harsh outdoor usage. However, its datasheet was not excellent, and we had not characterized it in proper condition (ex. anechoic chamber).

The sensitivity of this tag (antenna+chip) was tested by the company Mojix (Figure A-7.a). That measured a tag sensitivity of –24 dBm. That is 4 dB below the chip sensitivity announced to –28 dBm by the chip constructor (EM 4325 Spec., 2015), suggesting an effective gain of the antenna of –4 dB. In free space, within the regulation limits of the emitted power, and with a sufficiently sensitive reader, that would correspond to a reading range of about 23 m. That is much lower to the reading range of 60 m announced by the constructor in the same conditions (Confidex, 2014). Using a more efficient tag, with a higher effective gain, should increase the range.

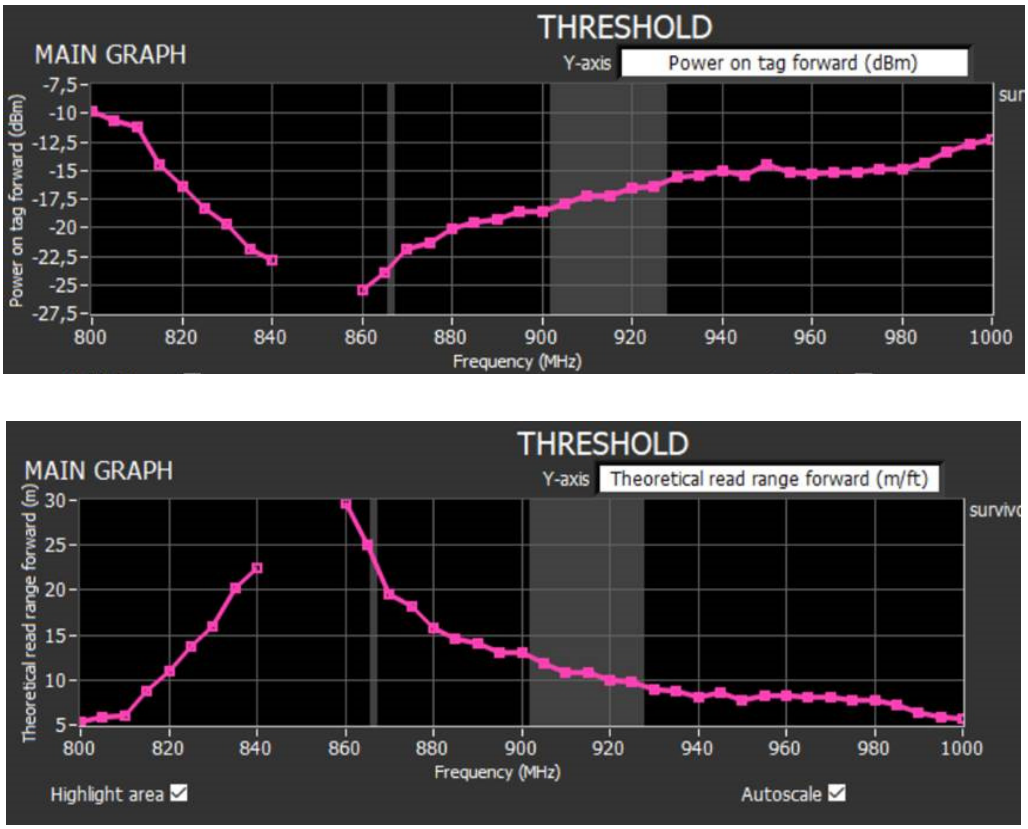


Figure A-7: Test of the Survivor B tag sensitivity depending on the frequency, made by Mojix Company. (top) the maximum reading sensitivity of the tag was −24 dBm, leading to (bottom) a theoretical maximum reading range in free space of 23 m.

A prototype tag was provided by Tagsys (now Mojix), based on the same chip but a different antenna assembly (Figure A-8). Several tests were made on this tag, suggesting a reading range four times higher than the survivor B tag, but in a flat

area. A reading range test was then operated on the Pont-Bourquin landslide, to see the reading limits in real conditions.

Les tests du tag Tagsys sur le site de Pont-Bourquin montrent une augmentation importante de la portée (Figure A-9). La portée latérale est principalement limitée par la forte directivité de l'antenne de la station. La portée dans le sens du glissement est limitée par la topographie du glissement: une forte rupture de pente, indiquée en bleu, bloque le trajet direct. Le gain de portée significatif du prototype de tag Tagsys encourage à développer dans le futur un tag à fort gain, et adapté aux conditions extérieures.

Figure A-8: (left) Survivor B tag, a metal-mount tag with a patch antenna, and (right) a prototype of tag with a higher gain provided by Mojix, using a slot antenna coupled with a magnetic loop.

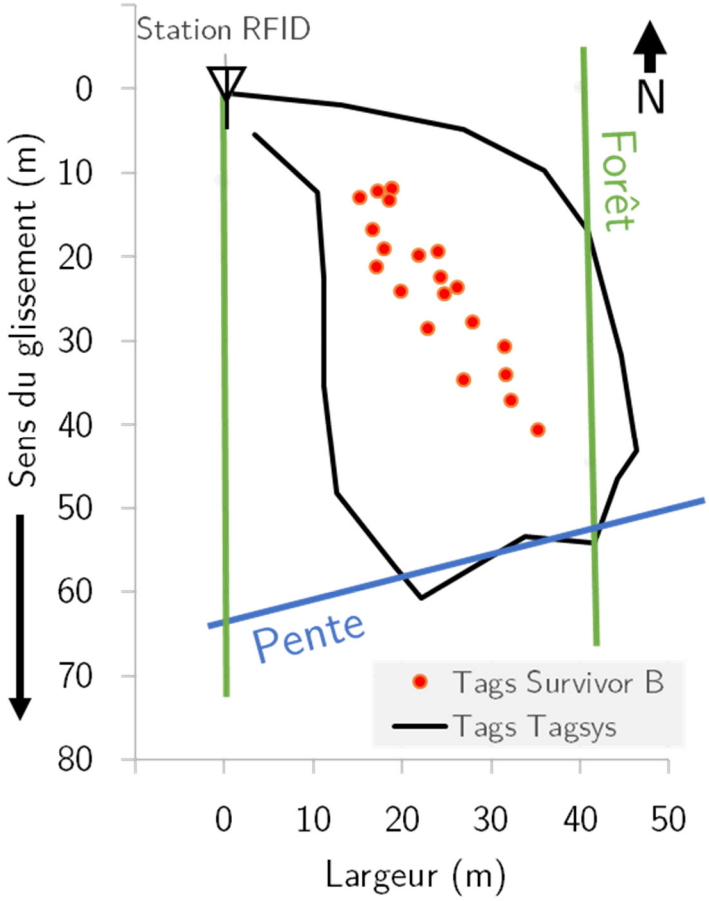


Figure A-9: Portée réelle sur le site de Pont-Bourquin. En rouge, la zone de lecture des tags survivors. En noir, les limites de lecture du tag Tagsys fente. La portée de tag Tagsys est limitée par une forte rupture de pente qui bloque la ligne de vue indiquée en bleu, et par une pente qui remonte vers la zone stable et la forêt, indiquée en vert

# Appendix 4
# Pont-Bourquin data

This appendix, created for the PhD oral defense, presents a synthetic view of the historic available data on Pont-Bourquin (Figure A-10). A specific focus on snow and seismic velocity variations show that snowpack formation and snow melting often happen simultaneously to drops of apparent seismic velocity. This suggests that the yearly correlation between temperature and seismic velocity spotted by (Bièvre et al., 2018) might be indeed caused by snow instead of air temperature, with lower velocity during the cold season due to snowpack formation and melting. This hypothesis would require further studies to confirm.

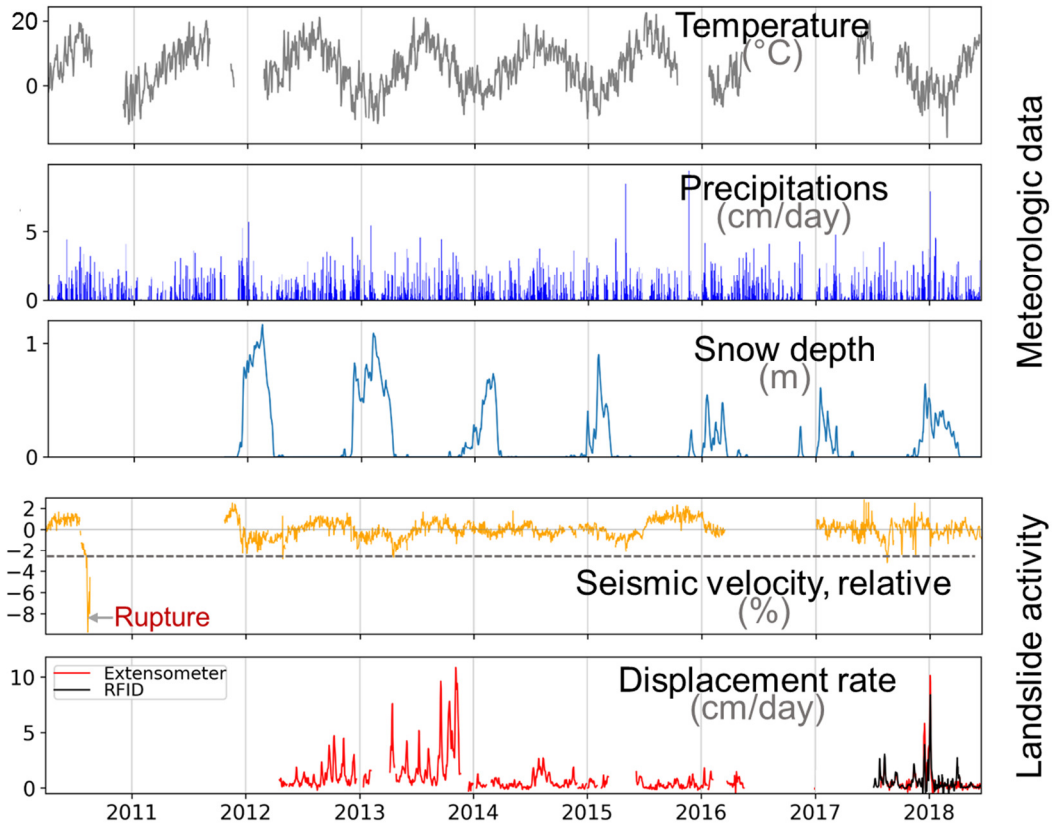


Figure A-10: Meterological data (temperature, precipitation and snow depth) measured near Pont-Bourqin landslide (partly by MeteoSuisse), along with indicators of the landslide activity: seismic velocity variations computed from cross-correlations filtered at 8–14 Hz, and landslide displacement rates in the middle of the landslide, measured by an extensometer and an RFID tag.

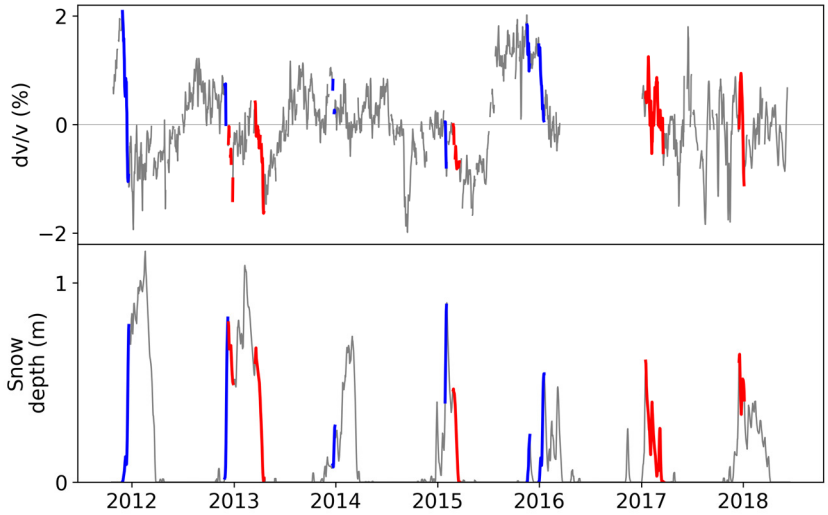


Figure A-11: Comparison of snow depth with variations of apparent seismic velocity (dv/v) after filtering the frequency of the GF at 8–12 Hz. Snowfall and melting events are in red and blue, respectively. These events happen simultaneously as dv/v drops multiple times, suggesting a potential influence of snow on seismic velocity.

# References

Abdelnour, A., Lazaro, A., Villarino, R., Kaddour, D., Tedjini, S., Girbau, D., Abdelnour, A., Lazaro, A., Villarino, R., Kaddour, D., Tedjini, S., Girbau, D., 2018. Passive Harmonic RFID System for Buried Assets Localization. Sensors 18, 3635. https://doi.org/10.3390/s18113635

Abellán, A., Jaboyedoff, M., Oppikofer, T., Vilaplana, J.M., 2009. Detection of millimetric deformation using a terrestrial laser scanner: experiment and application to a rockfall event. Nat. Hazards Earth Syst. Sci. 9, 365–372. https://doi.org/10.5194/nhess-9-365-2009

Abellán, A., Michoud, C., Jaboyedoff, M., Baillifard, F., Demierre, J., Carrea, D., Derron, M.-H., 2015. Velocity Prediction on Time-Variant Landslides Using Moving Response Functions: Application to La Barmasse Rockslide (Valais, Switzerland), in: Lollino, G., Giordan, D., Crosta, G.B., Corominas, J., Azzam, R., Wasowski, J., Sciarra, N. (Eds.), Engineering Geology for Society and Territory - Volume 2. Springer International Publishing, pp. 323–327.

Akbar, M.B., Taylor, D.G., Durgin, G.D., 2015a. Hybrid Inertial Microwave Reflectometry for mm-Scale Tracking in RFID Systems. IEEE Transactions on Wireless Communications 14, 6805–6814. https://doi.org/10.1109/TWC.2015.2460250

Akbar, M.B., Taylor, D.G., Durgin, G.D., 2015b. Amplitude and phase difference estimation bounds for multisensor based tracking of RFID Tags, in: IEEE Int. Conf. RFID. Presented at the 2015 IEEE International Conference on RFID (RFID), San Diego, CA, USA, pp. 105–112. https://doi.org/10.1109/RFID.2015.7113080

Alarcon, J., Saba, R., Egels, M., Pannier, P., 2012. A flexible UHF RFID tag for harsh environments, in: IEEE Int. Conf. RFID Technologies and Applications. Presented at the 2012 IEEE International Conference on RFID-Technologies and Applications (RFID-TA), Nice, France, pp. 267–270. https://doi.org/10.1109/RFID-TA.2012.6404527

Aleotti, P., 2004. A warning system for rainfall-induced shallow failures. Engineering Geology, Rainfall-triggered landslides and debris flows 73, 247–265. https://doi.org/10.1016/j.enggeo.2004.01.007

Alimohammadlou, Y., Najafi, A., Yalcin, A., 2013. Landslide process and impacts: A proposed classification method. CATENA 104, 219–232. https://doi.org/10.1016/j.catena.2012.11.013

Allan, J.C., Hart, R., Tranquili, J.V., 2006. The use of Passive Integrated Transponder (PIT) tags to trace cobble transport in a mixed sand-and-gravel beach on the high-energy Oregon coast, USA. Marine Geology 232, 63–86. https://doi.org/10.1016/j.margeo.2006.07.005

Allen, D., Arthur, S., Wallerstien, N., Blanc, J., Haynes, H., 2015. Provision, transport and deposition of debris in urban waterways. International Journal of Sediment Research 30, 142–149. https://doi.org/10.1016/j.ijsrc.2015.03.006

Amato, F., Torun, H.M., Durgin, G.D., 2018. RFID Backscattering in Long-Range Scenarios. IEEE Transactions on Wireless Communications 17, 2718–2725. https://doi.org/10.1109/TWC.2018.2801803

Amin, E.M., Bhattacharyya, R., Kumar, S., Sarma, S., Karmakar, N.C., 2014a. Towards low-cost resolution optimized passive UHF RFID light sensing, in: WAMICON. Presented at the WAMICON 2014, Tampa, FL, USA, pp. 1–6. https://doi.org/10.1109/WAMICON.2014.6857769

Amin, E.M., Saha, J.K., Karmakar, N.C., 2014b. Smart Sensing Materials for Low-Cost Chipless RFID Sensor. IEEE Sensors Journal 14, 2198–2207. https://doi.org/10.1109/JSEN.2014.2318056

Amitrano, D., Grasso, J.R., Senfaute, G., 2005. Seismic precursory patterns before a cliff collapse and critical point phenomena. Geophysical Research Letters 32. https://doi.org/10.1029/2004GL022270

Amundson, R., Reed, S., 2009. The Feedbacks between Soil and Biota in Vernal Pool Landscapes near Merced, CA 15.

Andia-Vera, G., 2017. Slender and Conformable Passive UHF RFID yarn. Presented at the IEEE Conference on RFID.

Angeli, M.-G., Pasuto, A., Silvano, S., 2000. A critical review of landslide monitoring experiences. Engineering Geology 55, 133–147. https://doi.org/10.1016/S0013-7952(99)00122-2

Arbuthnott, J., Gehm, R., Nevin, J., 1960. Variation of the electrical length of coaxial transmission lines with temperature, in: Annu. Rep. Conf. Electrical Insulation. Presented at the Annual Report Conference on Electrical Insulation, Washington, DC, USA, pp. 187–189. https://doi.org/10.1109/CEI.1960.7461687

Arnitz, D., Muehlmann, U., Witrisal, K., 2010. UWB ranging in passive UHF RFID: proof of concept. Electronics letters 46, 1401–1402. https://doi.org/10.1049/el.2010.1703

Aroca, R.V., Hernandes, A.C., Magalhães, D.V., Becker, M., Vaz, C.M.P., Calbo, A.G., 2018. Calibration of Passive UHF RFID Tags Using Neural Networks to Measure Soil Moisture. Journal of Sensors 2018, 1–12. https://doi.org/10.1155/2018/3436503

Arthaber, H., Faseth, T., Galler, F., 2015. Spread-Spectrum Based Ranging of Passive UHF EPC RFID Tags. IEEE Communications Letters 19, 1734–1737. https://doi.org/10.1109/LCOMM.2015.2469664

Babar, A.A., Elsherbeni, A.Z., Sydänheimo, L., Ukkonen, L., 2013. RFID Tags for Challenging Environments: Flexible High-Dielectric Materials and Ink-Jet Printing Technology for Compact Platform Tolerant RFID Tags. IEEE Microwave Magazine 14, 26–35. https://doi.org/10.1109/MMM.2013.2259391

Babar, A.A., Manzari, S., Sydanheimo, L., Elsherbeni, A.Z., Ukkonen, L., 2012. Passive UHF RFID Tag for Heat Sensing Applications. IEEE Transactions on Antennas and Propagation 60, 4056–4064. https://doi.org/10.1109/TAP.2012.2207045

Badoux, H., Gabus, J.H., Mercanton, C.H., 1990. Les Diablerets, in Swiss Geological Atlas, sheet 1285, Swiss Fed. Off. for Water and Geol., Wabern, Switzerland.

Balanis, C.A., 2012. Advanced Engineering Electromagnetics, Second Edition. ed. John Wiley and Sons.

Baroň, I., Supper, R., 2013. Application and reliability of techniques for landslide site investigation, monitoring and early warning – outcomes from a questionnaire study. Nat. Hazards Earth Syst. Sci. 13, 3157–3168. https://doi.org/10.5194/nhess-13-3157-2013

Bartelt, P., Lehning, M., 2002. A physical SNOWPACK model for the Swiss avalanche warning: Part I: numerical model. Cold Regions Science and Technology 35, 123–145. https://doi.org/10.1016/S0165-232X(02)00074-5

Basher Reid, 2006. Global early warning systems for natural hazards: systematic and people-centred. Philosophical Transactions of the Royal Society A: Mathematical, Physical and Engineering Sciences 364, 2167–2182. https://doi.org/10.1098/rsta.2006.1819

Batchelor, J.C., Rakibet, O.O., Ziai, M.A., Rumens, C.V., Holder, S.J., 2014. Conformal RFID sensing for assisted living, in: 2014 XXXIth URSI General Assembly and Scientific Symposium (URSI GASS). Presented at the 2014 XXXIth URSI General Assembly and Scientific Symposium (URSI GASS), pp. 1–4. https://doi.org/10.1109/URSIGASS.2014.6929402

Bauer-Reich, C., Tan, K.C., Haring, F., Schneck, N., Wick, A., Berge, L., Hoey, J., Sailer, R., Ulven, C., 2014. An investigation of the viability of UHF RFID for subsurface soil sensors, in: IEEE Int. Conf. Electro/Information Technology. Presented at the IEEE International Conference on Electro/Information Technology, Milwaukee, WI, USA, pp. 577–580. https://doi.org/10.1109/EIT.2014.6871828

Baum, R.L., Godt, J.W., 2010. Early warning of rainfall-induced shallow landslides and debris flows in the USA. Landslides 7, 259–272. https://doi.org/10.1007/s10346-009-0177-0

Belle, P., Aunay, B., Bernardie, S., Grandjean, G., Ladouche, B., Mazué, R., Join, J.-L., 2014. The application of an innovative inverse model for understanding and predicting landslide movements (Salazie cirque landslides, Reunion Island). Landslides 11, 343–355. https://doi.org/10.1007/s10346-013-0393-5

Belle, P., Aunay, B., Join, J.-L., Bernardie, S., 2012. An innovative approach for very large landslide dynamic and hydrogeological triggering study by inverse modeling (Grand Ilet landslide, Reunion Island). Presented at the EGU General Assembly 2014.

Benelli, G., Pozzebon, A., Raguseo, G., Bertoni, D., Sarti, G., 2009. An RFID Based System for the Underwater Tracking of Pebbles on Artificial Coarse Beaches, in: 2009 Third International Conference on Sensor Technologies and Applications. Presented at the 2009 Third International Conference on Sensor Technologies and Applications (SENSORCOMM), IEEE, Athens, Greece, pp. 294–299. https://doi.org/10.1109/SENSORCOMM.2009.52

Bennett, G.L., Miller, S.R., Roering, J.J., Schmidt, D.A., 2016. Landslides, threshold slopes, and the survival of relict terrain in the wake of the Mendocino Triple Junction. Geology 44, 363–366. https://doi.org/10.1130/G37530.1

Benoit, L., Briole, P., Martin, O., Thom, C., Malet, J.-P., Ulrich, P., 2015. Monitoring landslide displacements with the Geocube wireless network of low-cost GPS. Engineering Geology 195, 111–121. https://doi.org/10.1016/j.enggeo.2015.05.020

Bernardie, S., Desramaut, N., Malet, J.-P., Gourlay, M., Grandjean, G., 2015. Prediction of changes in landslide rates induced by rainfall. Landslides 12, 481–494. https://doi.org/10.1007/s10346-014-0495-8

Bertoni, D., Grottoli, E., Ciavola, P., Sarti, G., Benelli, G., Pozzebon, A., 2013. On the displacement of marked pebbles on two coarse-clastic beaches during short fair-weather periods (Marina di Pisa and Portonovo, Italy). Geo-Mar Lett 33, 463–476. https://doi.org/10.1007/s00367-013-0341-3

Bertoni, D., Sarti, G., Benelli, G., Pozzebon, A., Raguseo, G., 2010. Radio Frequency Identification (RFID) technology applied to the definition of underwater and subaerial coarse sediment movement. Sedimentary Geology 228, 140–150. https://doi.org/10.1016/j.sedgeo.2010.04.007

Bhattacharyya, R., Floerkemeier, C., Sarma, S., 2010. RFID tag antenna based sensing: Does your beverage glass need a refill?, in: 2010 IEEE International Conference on RFID (IEEE RFID 2010). Presented at the 2010 IEEE International Conference on RFID (IEEE RFID 2010), pp. 126–133. https://doi.org/10.1109/RFID.2010.5467235

Bièvre, G., Franz, M., Larose, E., Carrière, S., Jongmans, D., Jaboyedoff, M., 2018. Influence of environmental parameters on the seismic velocity changes in a clayey mudflow (Pont-Bourquin Landslide, Switzerland). Engineering Geology 245, 248–257. https://doi.org/10.1016/j.enggeo.2018.08.013

Bievre, G., Joseph, A., Bertrand, C., 2018. Preferential Water Infiltration Path in a Slow-Moving Clayey Earthslide Evidenced by Cross-Correlation of Hydrometeorological Time Series (Charlaix Landslide, French Western Alps). Geofluids 2018. https://doi.org/10.1155/2018/9593267

Biron, P.M., Carver, R.B., Carré, D.M., 2012. Sediment Transport and Flow Dynamics Around a Restored Pool in a Fish Habitat Rehabilitation Project: Field and 3d Numerical Modelling Experiments. River Research and Applications 28, 926–939. https://doi.org/10.1002/rra.1488

Björk, A., Erlandsson, M., Häkli, J., Jaakkola, K., Nilsson, Å., Nummila, K., Puntanen, V., Sirkka, A., 2011. Monitoring environmental performance of the forestry supply chain using RFID. Computers in Industry 62, 830–841. https://doi.org/10.1016/j.compind.2011.08.001

Bontemps, N., Lacroix, P., Larose, E., Jara, J., Taipe, E., in preparation. Rain and small earthquakes can maintain a slow moving landslide in critical state.

Bouvet, A., Toan, T.L., Lam-Dao, N., 2009. Monitoring of the Rice Cropping System in the Mekong Delta Using ENVISAT/ASAR Dual Polarization Data. IEEE Transactions on Geoscience and Remote Sensing 47, 517–526. https://doi.org/10.1109/TGRS.2008.2007963

Bradford, J.H., 2007. Frequency-dependent attenuation analysis of ground-penetrating radar data. GEOPHYSICS 72, J7–J16. https://doi.org/10.1190/1.2710183

Bradford, J.H., Harper, J.T., Brown, J., 2009. Complex dielectric permittivity measurements from ground-penetrating radar data to estimate snow liquid water content in the pendular regime: MEASURING SWE WITH GPR. Water Resources Research 45. https://doi.org/10.1029/2008WR007341

Bradley, D.N., 2017. Direct Observation of Heavy-Tailed Storage Times of Bed Load Tracer Particles Causing Anomalous Superdiffusion. Geophysical Research Letters 44, 12,227-12,235. https://doi.org/10.1002/2017GL075045

Bradley, D.N., Tucker, G.E., 2012. Measuring gravel transport and dispersion in a mountain river using passive radio tracers. Earth Surface Processes and Landforms 37, 1034–1045. https://doi.org/10.1002/esp.3223

Brenguier, F., Campillo, M., Hadziioannou, C., Shapiro, N.M., Nadeau, R.M., Larose, E., 2008a. Postseismic Relaxation Along the San Andreas Fault at Parkfield from Continuous Seismological Observations. Science 321, 1478–1481. https://doi.org/10.1126/science.1160943

Brenguier, F., Campillo, M., Takeda, T., Aoki, Y., Shapiro, N.M., Briand, X., Emoto, K., Miyake, H., 2014. Mapping pressurized volcanic fluids from induced crustal seismic velocity drops. Science 345, 80–82. https://doi.org/10.1126/science.1254073

Brenguier, F., Clarke, D., Aoki, Y., Shapiro, N.M., Campillo, M., Ferrazzini, V., 2011. Monitoring volcanoes using seismic noise correlations. Comptes Rendus Geoscience 343, 633–638. https://doi.org/10.1016/j.crte.2010.12.010

Brenguier, F., Rivet, D., Obermann, A., Nakata, N., Boué, P., Lecocq, T., Campillo, M., Shapiro, N., 2016. 4-D noise-based seismology at volcanoes: Ongoing efforts and perspectives. Journal of Volcanology and Geothermal Research 321, 182–195. https://doi.org/10.1016/j.jvolgeores.2016.04.036

Brenguier, F., Shapiro, N.M., Campillo, M., Ferrazzini, V., Duputel, Z., Coutant, O., Nercessian, A., 2008b. Towards forecasting volcanic eruptions using seismic noise. Nature Geoscience 1, 126–130. https://doi.org/10.1038/ngeo104

Brönnimann, C.S., 2011. Effect of Groundwater on Landslide Triggering (Ph.D. Thesis). École Polytechnique Fédérale de Lausanne, Switzerland.

Brown, G.S., Curry, W.J., 1982. A theory and model for wave propagation through foliage. Radio Science 17, 1027–1036. https://doi.org/10.1029/RS017i005p01027

Buffi, A., Nepa, P., Cioni, R., 2017. SARFID on drone: Drone-based UHF-RFID tag localization, in: 2017 IEEE International Conference on RFID Technology Application (RFID-TA). Presented at the 2017 IEEE International Conference on RFID Technology Application (RFID-TA), pp. 40–44. https://doi.org/10.1109/RFID-TA.2017.8098872

Caccami, M.C., Manzari, S., Marrocco, G., 2015. Phase-Oriented Sensing by Means of Loaded UHF RFID Tags. IEEE Transactions on Antennas and Propagation 63, 4512–4520. https://doi.org/10.1109/TAP.2015.2465891

Caccami, M.C., Marrocco, G., 2018. Electromagnetic Modeling of Self-Tuning RFID Sensor Antennas in Linear and Nonlinear Regimes. IEEE Transactions on Antennas and Propagation 66, 2779–2787. https://doi.org/10.1109/TAP.2018.2820322

Caine, N., 1980. The Rainfall Intensity: Duration Control of Shallow Landslides and Debris Flows. Geografiska Annaler. Series A, Physical Geography 62, 23–27. https://doi.org/10.2307/520449

Caizzone, S., DiGiampaolo, E., 2015. Wireless Passive RFID Crack Width Sensor for Structural Health Monitoring. IEEE Sensors Journal 15, 6767–6774. https://doi.org/10.1109/JSEN.2015.2457455

Caizzone, S., DiGiampaolo, E., Marrocco, G., 2014. Wireless Crack Monitoring by Stationary Phase Measurements from Coupled RFID Tags. IEEE Transactions on Antennas and Propagation 62, 6412–6419. https://doi.org/10.1109/TAP.2014.2360553

Caizzone, S., Marrocco, G., 2011. RFID Grids: Part II —Experimentations. IEEE Transactions on Antennas and Propagation 59, 2896–2904. https://doi.org/10.1109/TAP.2011.2158974

Campillo, M., Paul, A., 2003. Long-Range Correlations in the Diffuse Seismic Coda. Science 299, 547–549. https://doi.org/10.1126/science.1078551

Capdevila, S., Jofre, L., Romeu, J., Bolomey, J.C., 2011. Passive RFID based sensing, in: 2011 IEEE International Conference on RFID-Technologies and Applications. Presented at the 2011 IEEE International Conference on RFID-Technologies and Applications, pp. 507–512. https://doi.org/10.1109/RFID-TA.2011.6068592

Capdevila, S., Roqueta, G., Guardiola, M., Jofre, L., Romeu, J., Bolomey, J.C., 2012. Water infiltration detection in civil engineering structures using RFID, in: 2012 6th European Conference on Antennas and Propagation (EUCAP). Presented at the 2012 6th European Conference on Antennas and Propagation (EUCAP), pp. 2505–2509. https://doi.org/10.1109/EuCAP.2012.6206147

Capparelli, G., Versace, P., 2011. FLaIR and SUSHI: two mathematical models for early warning of landslides induced by rainfall. Landslides 8, 67–79. https://doi.org/10.1007/s10346-010-0228-6

Carré, D.M., Biron, P.M., Gaskin, S.J., 2007. Flow dynamics and bedload sediment transport around paired deflectors for fish habitat enhancement: a field study in the Nicolet River. Can. J. Civ. Eng. 34, 761–769. https://doi.org/10.1139/l06-083

Carrière, S., 2016. Recherche de précurseurs géophysiques à la transition solide-fluide dans les glissements-coulées affectant les matériaux argileux. Université Grenoble Alpes, Grenoble, ISTerre.

Carrière, S.R., Bièvre, G., Jongmans, D., Chambon, G., Bellot, H., Lebourg, T., 2018a. Measurement of geophysical parameters on clay samples at the solid–fluid transition. Near Surface Geophysics 16, 1–15. https://doi.org/10.3997/1873-0604.2017039

Carrière, S.R., Jongmans, D., Chambon, G., Bièvre, G., Lanson, B., Bertello, L., Berti, M., Jaboyedoff, M., Malet, J.-P., Chambers, J.E., 2018b. Rheological properties of clayey soils originating from flow-like landslides. Landslides 15, 1615–1630. https://doi.org/10.1007/s10346-018-0972-6

Casagli, N., Frodella, W., Morelli, S., Tofani, V., Ciampalini, A., Intrieri, E., Raspini, F., Rossi, G., Tanteri, L., Lu, P., 2017. Spaceborne, UAV and ground-based remote sensing techniques for landslide mapping, monitoring and early warning. Geoenviron Disasters 4, 9. https://doi.org/10.1186/s40677-017-0073-1

Casati, G., Longhi, M., Latini, D., Carbone, F., Amendola, S., Frate, F.D., Schiavon, G., Marrocco, G., 2017. The Interrogation Footprint of RFID-UAV: Electromagnetic Modeling and Experimentations. IEEE Journal of Radio Frequency Identification 1, 155–162. https://doi.org/10.1109/JRFID.2017.2765619

Cassel, M., Dépret, T., Piégay, H., 2017. Assessment of a new solution for tracking pebbles in rivers based on active RFID. Earth Surface Processes and Landforms 42, 1938–1951. https://doi.org/10.1002/esp.4152

Cazeca, M.J., Mead, J., Chen, J., Nagarajan, R., 2013. Passive wireless displacement sensor based on RFID technology. Sensors and Actuators A: Physical 190, 197–202. https://doi.org/10.1016/j.sna.2012.11.007

Chang, K., Kim, Y.H., Kim, Y.J., Yoon, Y.J., 2007. Functional antenna integrated with relative humidity sensor using synthesised polyimide for passive RFID sensing. Electronics Letters 43, 259–260.

Chapuis, M., Bright, C.J., Hufnagel, J., MacVicar, B., 2014. Detection ranges and uncertainty of passive Radio Frequency Identification (RFID) transponders for sediment tracking in gravel rivers and coastal environments: DETECTION RANGES AND UNCERTAINTY OF PASSIVE RFID TRANSPONDERS. Earth Surface Processes and Landforms 39, 2109–2120. https://doi.org/10.1002/esp.3620

Chapuis, M., Dufour, S., Provansal, M., Couvert, B., de Linares, M., 2015. Coupling channel evolution monitoring and RFID tracking in a large, wandering, gravel-bed river: Insights into sediment routing on geomorphic continuity through a riffle–pool sequence. Geomorphology 231, 258–269. https://doi.org/10.1016/j.geomorph.2014.12.013

Chiu, T., Sarabandi, K., 2000. Electromagnetic scattering from short branching vegetation. IEEE Transactions on Geoscience and Remote Sensing 38, 911–925. https://doi.org/10.1109/36.841974

Chtouki, T., Vergne, J., Provost, F., Malet, J.-P., Burtin, A., Hibert, C., 2017. Ambient seismic noise monitoring of the Super-Sauze landslide from a very dense temporary seismic array. Presented at the EGU General Assembly Conference Abstracts, p. 8678.

Clements, T., Denolle, M.A., 2018. Tracking Groundwater Levels Using the Ambient Seismic Field. Geophysical Research Letters 45, 6459–6465. https://doi.org/10.1029/2018GL077706

Colombero, C., Baillet, L., Comina, C., Jongmans, D., Larose, E., Valentin, J., Vinciguerra, S., 2018. Integration of ambient seismic noise monitoring, displacement and meteorological measurements to infer the

temperature-controlled long-term evolution of a complex prone-to-fall cliff. Geophys J Int 213, 1876–1897. https://doi.org/10.1093/gji/ggy090

Confidex, 2014. Survivor B Datasheet.

Corominas, J., Moya, J., Ledesma, A., Lloret, A., Gili, J.A., 2005. Prediction of ground displacements and velocities from groundwater level changes at the Vallcebre landslide (Eastern Pyrenees, Spain). Landslides 2, 83–96. https://doi.org/10.1007/s10346-005-0049-1

Croux, D., Vangerven, T., Broeders, J., Boutsen, J., Peeters, M., Duchateau, S., Cleij, T., Deferme, W., Wagner, P., Thoelen, R., De Ceuninck, W., 2013. Molecular imprinted polymer films on RFID tags: a first step towards disposable packaging sensors. Phys. Status Solidi A 210, 938–944. https://doi.org/10.1002/pssa.201200743

Cruden, D.M., Varnes, D.J., 1996. Landslide Types and Processes, in: Turner AK, Schuster RL (Eds) Landslides Investigation and Mitigation. Transportation research board, US National Research Council. Special Report, Washington, DC, pp. 36–75.

Curtiss, G.M., Osborne, P.D., Horner-Devine, A.R., 2009. Seasonal patterns of coarse sediment transport on a mixed sand and gravel beach due to vessel wakes, wind waves, and tidal currents. Marine Geology 259, 73–85. https://doi.org/10.1016/j.margeo.2008.12.009

Czuba, K., Sikora, D., 2011. Temperature stability of coaxial cables. Acta Phys. Pol. A 119, 553–557.

Dai, F.C., Lee, C.F., Ngai, Y.Y., 2002. Landslide risk assessment and management: an overview. Engineering Geology 64, 65–87. https://doi.org/10.1016/S0013-7952(01)00093-X

Das, R., 2017. RFID Forecasts, Players and Opportunities 2017-2027. IDTechEx.

Dell'Agnese, A., Brardinoni, F., Toro, M., Mao, L., Engel, M., Comiti, F., 2015. Bedload transport in a formerly glaciated mountain catchment constrained by particle tracking. Earth Surface Dynamics 3, 527–542. https://doi.org/10.5194/esurf-3-527-2015

Denoth, A., 1989. Snow dielectric measurements. Advances in Space Research 9, 233–243.

Denoth, A., 1980. The Pendular-Funicular Liquid Transition in Snow. Journal of Glaciology 25, 93–98. https://doi.org/10.3189/S0022143000010315

Dépret, T., Gautier, E., Hooke, J., Grancher, D., Virmoux, C., Brunstein, D., 2017. Causes of planform stability of a low-energy meandering gravel-bed river (Cher River, France). Geomorphology 285, 58–81. https://doi.org/10.1016/j.geomorph.2017.01.035

Dhawan, S.K., 1992. Understanding effect of Teflon room temperature phase transition on coax cable delay in order to improve the measurement of TE signals of deuterated polarized targets. IEEE Transactions on Nuclear Science 39, 1331–1335. https://doi.org/10.1109/23.173201

Dickson, M.E., Kench, P.S., Kantor, M.S., 2011. Longshore transport of cobbles on a mixed sand and gravel beach, southern Hawke Bay, New Zealand. Marine Geology 287, 31–42. https://doi.org/10.1016/j.margeo.2011.06.009

Dobkin, D., Weigand, S., 2005. Environmental effects on RFID tag antennas, in: IEEE MTT-S Int. Microwave Symp. Dig. Presented at the IEEE MTT-S International Microwave Symposium Digest, Long Beach, CA, USA, pp. 135–138. https://doi.org/10.1109/MWSYM.2005.1516541

Dobkin, D.M., 2008. The RF in RFID: passive UHF RFID in practice, Communications engineering series. Elsevier / Newnes, Amsterdam ; Boston.

Doesken, N.J., Judson, A., 1997. The snow booklet, 2nd edition. ed. Colorado State University, Colorado.

Dong, Y., Lu, N., 2016. Dependencies of Shear Wave Velocity and Shear Modulus of Soil on Saturation. Journal of Engineering Mechanics 142, 04016083. https://doi.org/10.1061/(ASCE)EM.1943-7889.0001147

Droin, A., Taverdet, J.L., Vergnaud, J.M., 1988. Modeling the kinetics of moisture adsorption by wood. Wood Science and Technology 22, 11–20.

Durgin, G.D., 2016. RF thermoelectric generation for passive RFID, in: 2016 IEEE International Conference on RFID (RFID). Presented at the 2016 IEEE International Conference on RFID (RFID), pp. 1–8. https://doi.org/10.1109/RFID.2016.7488025

Egido, A., Paloscia, S., Motte, E., Guerriero, L., Pierdicca, N., Caparrini, M., Santi, E., Fontanelli, G., Floury, N., 2014. Airborne GNSS-R Polarimetric Measurements for Soil Moisture and Above-Ground Biomass Estimation. IEEE Journal of Selected Topics in Applied Earth Observations and Remote Sensing 7, 1522–1532. https://doi.org/10.1109/JSTARS.2014.2322854

El-rayes, M.A., Ulaby, F.T., 1987. Microwave Dielectric Spectrum of Vegetation-Part I: Experimental Observations. IEEE Transactions on Geoscience and Remote Sensing GE-25, 541–549. https://doi.org/10.1109/TGRS.1987.289832

EM 4325 Spec. (Technical Specifications No. 420005-A01, 2.0), 2015. . EM Microelectronic - Marin SA.

EPC (tm) Radio-Frequency Identity Protocols Generation-2 UHF RFID (Standard No. 2.0.1), 2015. . EPCglobal Inc.

ETSI EN 302-208 (Standard No. 3.1.0), 2016. . ETSI.

Favorskaya, M.N., Jain, L.C., 2017. Overview of LiDAR Technologies and Equipment for Land Cover Scanning, in: Handbook on Advances in Remote Sensing and Geographic Information Systems. Springer International Publishing, Cham, pp. 19–68. https://doi.org/10.1007/978-3-319-52308-8_2

Federico, A., Popescu, M., Elia, G., Fidelibus, C., Internò, G., Murianni, A., 2012. Prediction of time to slope failure: a general framework. Environ Earth Sci 66, 245–256. https://doi.org/10.1007/s12665-011-1231-5

Fierz, C., Amstrong, R.L., Durand, Y., Etchevers, P., Greene, E., McClung, D.M., Nishimura, K., Satyawali, P.K., Sokratov, S.A., 2009. The International Classification for Seasonal Snow on the Ground (No. IHP-VII Technical Documents in Hydrology N°83, IACS Contribution N°1). UNESCO-IHP, Paris.

Fiolleau, S., Jongmans, D., Bièvre, G., Helmstetter, A., Lacroix, P., Baillet, L., 2018. Seismic characterization of clay- block ruptures in the Harmalière landslide (French Western Alps). Presented at the EGU General Assembly Conference Abstracts, p. 13201.

Fiolleau, S., Jongmans, D., Bièvre, G., Helmstetter, A., Lacroix, P., Baillet, L., in preparation. Seismic characterization of a clay-block rupture in the Harmalière landslide (French Western Alps).

Flores Orozco, A., Bücker, M., Steiner, M., Malet, J.-P., 2018. Complex-conductivity imaging for the understanding of landslide architecture. Engineering Geology 243, 241–252. https://doi.org/10.1016/j.enggeo.2018.07.009

Ford, M.R., 2014. The application of PIT tags to measure transport of detrital coral fragments on a fringing reef: Majuro Atoll, Marshall Islands. Coral Reefs 33, 375–379. https://doi.org/10.1007/s00338-014-1131-8

Froment, B., Campillo, M., Chen, J.H., Liu, Q.Y., 2013. Deformation at depth associated with the 12 May 2008 MW 7.9 Wenchuan earthquake from seismic ambient noise monitoring. Geophysical Research Letters 40, 78–82. https://doi.org/10.1029/2012GL053995

Froude, M.J., Petley, D.N., 2018. Global fatal landslide occurrence from 2004 to 2016. Natural Hazards and Earth System Sciences 18, 2161–2181. https://doi.org/10.5194/nhess-18-2161-2018

Fukuzono, T., 1985. A new method for predicting the failure time of a slope., in: Proc. IV Th Int. Conf. and Field Workshop on Landslides. pp. 145–150.

Fuschini, F., Piersanti, C., Paolazzi, F., Falciasecca, G., 2008. On the Efficiency of Load Modulation in RFID Systems Operating in Real Environment. IEEE Antennas and Wireless Propagation Letters 7, 243–246. https://doi.org/10.1109/LAWP.2008.921354

Gage, K.S., Balsley, B.B., 1980. On the scattering and reflection mechanisms contributing to clear air radar echoes from the troposphere, stratosphere, and mesophere. Radio Sci. 15, 243–257. https://doi.org/10.1029/RS015i002p00243

Gallistl, J., Weigand, M., Stumvoll, M., Ottowitz, D., Glade, T., Orozco, A.F., 2018. Delineation of subsurface variability in clay-rich landslides through spectral induced polarization imaging and electromagnetic methods. Engineering Geology 245, 292–308. https://doi.org/10.1016/j.enggeo.2018.09.001

Gao, J., Siden, J., Nilsson, H.E., 2011. Printed Electromagnetic Coupler With an Embedded Moisture Sensor for Ordinary Passive RFID Tags. IEEE Electron Device Letters 32, 1767–1769. https://doi.org/10.1109/LED.2011.2170616

Gariano, S.L., Guzzetti, F., 2016. Landslides in a changing climate. Earth-Science Reviews 162, 227–252. https://doi.org/10.1016/j.earscirev.2016.08.011

Gassenmeier, M., Sens-Schönfelder, C., Delatre, M., Korn, M., 2015. Monitoring of environmental influences on seismic velocity at the geological storage site for CO2 in Ketzin (Germany) with ambient seismic noise. Geophys J Int 200, 524–533. https://doi.org/10.1093/gji/ggu413

Ghahremani, A., Fu, Q., Baiya, D., Simpson, J., Fathy, A.E., 2016. Performance of flexible antennas with protective super-hydrophobic coating layers at RF frequencies, in: IEEE Radio and Wireless Symp. Presented at the IEEE Radio and Wireless Symposium (RWS), Austin, TX, USA, pp. 32–35. https://doi.org/10.1109/RWS.2016.7444356

Gilet, L., Gob, F., Virmoux, C., Touche, J., Harrache, S., Gautier, E., Moës, M., Thommeret, N., Jacob-Rousseau, N., 2018. Suivi de l'évolution morphologique et sédimentaire de l'Yonne suite à la première phase du démantèlement du barrage de Pierre Glissotte (Massif du Morvan, France). Géomorphologie : relief, processus, environnement 24, 7–29. https://doi.org/10.4000/geomorphologie.11946

Gili, J.A., Corominas, J., Rius, J., 2000. Using Global Positioning System techniques in landslide monitoring. Engineering Geology 55, 167–192. https://doi.org/10.1016/S0013-7952(99)00127-1

Gonçalves, R., Rima, S., Magueta, R., Pinho, P., Collado, A., Georgiadis, A., Hester, J., Carvalho, N.B., Tentzeris, M.M., 2015. RFID-Based Wireless Passive Sensors Utilizing Cork Materials. IEEE Sensors Journal 15, 7242–7251. https://doi.org/10.1109/JSEN.2015.2472980

Goseberg N., Nistor I., Mikami T., Shibayama T., Stolle J., 2016. Nonintrusive Spatiotemporal Smart Debris Tracking in Turbulent Flows with Application to Debris-Laden Tsunami Inundation. Journal of Hydraulic Engineering 142, 04016058. https://doi.org/10.1061/(ASCE)HY.1943-7900.0001199

Graff, K., Viel, V., Carlier, B., Lissak, C., Madelin, M., Arnaud-Fassetta, G., Fort, M., 2018. Traçage sédimentaire d'une lave torrentielle dans le bassin de la Peyronnelle (Queyras, Alpes françaises du Sud). Géomorphologie : relief, processus, environnement 24, 43–57. https://doi.org/10.4000/geomorphologie.11967

Grasegger, K., Strapazzon, G., Procter, E., Brugger, H., Soteras, I., 2016. Avalanche Survival After Rescue With the RECCO Rescue System: A Case Report. Wilderness & Environmental Medicine 27, 282–286. https://doi.org/10.1016/j.wem.2016.02.004

Greco, G., Lucianaz, C., Bertoldo, S., Allegretti, M., 2015a. A solution for monitoring operations in harsh environment: A RFID reader for small UAV, in: 2015 International Conference on Electromagnetics in Advanced Applications (ICEAA). Presented at the 2015 International Conference on Electromagnetics in Advanced Applications (ICEAA), pp. 859–862. https://doi.org/10.1109/ICEAA.2015.7297235

Greco, G., Lucianaz, C., Bertoldo, S., Allegretti, M., 2015b. Localization of RFID tags for environmental monitoring using UAV, in: IEEE 1st Int. Forum Research and Technologies for Society and Industry. Presented at the 2015 IEEE 1st International Forum on Research and Technologies for Society and Industry (RTSI), Turin, Italy, pp. 480–483. https://doi.org/10.1109/RTSI.2015.7325144

Griffin, J.D., Durgin, G.D., 2009. Complete Link Budgets for Backscatter-Radio and RFID Systems. IEEE Antennas and Propagation Magazine 51, 11–25. https://doi.org/10.1109/MAP.2009.5162013

Griffin, J.D., Durgin, G.D., Haldi, A., Kippelen, B., 2006. RF Tag Antenna Performance on Various Materials Using Radio Link Budgets. IEEE Antennas and Wireless Propagation Letters 5, 247–250. https://doi.org/10.1109/LAWP.2006.874072

Grosinger, J., Görtschacher, L., Bösch, W., 2016. Passive RFID Sensor Tag Concept and Prototype Exploiting a Full Control of Amplitude and Phase of the Tag Signal. IEEE Transactions on Microwave Theory and Techniques 64, 4752–4762. https://doi.org/10.1109/TMTT.2016.2623610

Guillemot, A., Baillet, L., Helmstetter, A., Larose, É., Mayoraz, R., in preparation. Seismic monitoring of the Gugla-Breithorn rock glacier (Switzerland).

Gutierrez, A., Nicolalde, F.D., Ingle, A., Hochschild, W., Veeramani, R., Hohberger, C., Davis, R., 2013. High-frequency RFID tag survivability in harsh environments, in: IEEE Int. Conf. on RFID. Presented at the 2013 IEEE International Conference on RFID (RFID), Penang, Malaysia, pp. 58–65. https://doi.org/10.1109/RFID.2013.6548136

Guzzetti, F., Carrara, A., Cardinali, M., Reichenbach, P., 1999. Landslide hazard evaluation: a review of current techniques and their application in a multi-scale study, Central Italy. Geomorphology 31, 181–216. https://doi.org/10.1016/S0169-555X(99)00078-1

Guzzetti, F., Peruccacci, S., Rossi, M., Stark, C.P., 2007. Rainfall thresholds for the initiation of landslides in central and southern Europe. Meteorol. Atmos. Phys. 98, 239–267. https://doi.org/10.1007/s00703-007-0262-7

Hadziioannou, C., 2011. Ondes sismiques en milieu complexe : mesure des variations temporelles des vitesses (phdthesis). Université de Grenoble.

Hadziioannou, C., Larose, E., Coutant, O., Roux, P., Campillo, M., 2009. Stability of monitoring weak changes in multiply scattering media with ambient noise correlation: Laboratory experiments. The Journal of the Acoustical Society of America 125, 3688–3695.

Hallikainen, M.T., Ulaby, F.T., Dobson, M.C., El-rayes, M.A., Wu, L., 1985. Microwave Dielectric Behavior of Wet Soil-Part 1: Empirical Models and Experimental Observations. IEEE Transactions on Geoscience and Remote Sensing GE-23, 25–34. https://doi.org/10.1109/TGRS.1985.289497

Harba, P., Pilecki, Z., 2017. Assessment of time–spatial changes of shear wave velocities of flysch formation prone to mass movements by seismic interferometry with the use of ambient noise. Landslides 14, 1225–1233. https://doi.org/10.1007/s10346-016-0779-2

Hasan, A., Bhattacharyya, R., Sarma, S., 2015. Towards pervasive soil moisture sensing using RFID tag antenna-based sensors, in: IEEE Int. Conf. RFID Technologies and Applications. Presented at the 2015 IEEE International Conference on RFID Technology and Applications (RFID-TA), Tokyo, Japan, pp. 165–170. https://doi.org/10.1109/RFID-TA.2015.7379812

Heidrich, J., Brenk, D., Essel, J., Schwarzer, S., Seemann, K., Fischer, G., Weigel, R., 2010. The Roots, Rules, and Rise of RFID. IEEE Microwave Magazine 11, 78–86. https://doi.org/10.1109/MMM.2010.936075

Helmstetter, A., Garambois, S., 2010. Seismic monitoring of Séchilienne rockslide (French Alps): Analysis of seismic signals and their correlation with rainfalls. Journal of Geophysical Research: Earth Surface 115. https://doi.org/10.1029/2009JF001532

Herrera, G., Fernández-Merodo, J.A., Mulas, J., Pastor, M., Luzi, G., Monserrat, O., 2009. A landslide forecasting model using ground based SAR data: The Portalet case study. Engineering Geology 105, 220–230. https://doi.org/10.1016/j.enggeo.2009.02.009

Higuchi, K., Fujisawa, K., Asai, K., Pasuto, A., Marcato, G., 2005. APPLICATION OF NEW LANDSLIDE MONITORING TECHNIQUE USING OPTICAL FIBER SENSOR AT TAKISAKA LANDSLIDE, JAPAN 10.

Hillers, G., Ben-Zion, Y., Campillo, M., Zigone, D., 2015a. Seasonal variations of seismic velocities in the San Jacinto fault area observed with ambient seismic noise. Geophys J Int 202, 920–932. https://doi.org/10.1093/gji/ggv151

Hillers, G., Campillo, M., Ma, K.-F., 2014. Seismic velocity variations at TCDP are controlled by MJO driven precipitation pattern and high fluid discharge properties. Earth and Planetary Science Letters 391, 121–127. https://doi.org/10.1016/j.epsl.2014.01.040

Hillers, G., Retailleau, L., Campillo, M., Inbal, A., Ampuero, J.-P., Nishimura, T., 2015b. In situ observations of velocity changes in response to tidal deformation from analysis of the high-frequency ambient wavefield. Journal of Geophysical Research: Solid Earth 120, 210–225. https://doi.org/10.1002/2014JB011318

Hobiger, M., Wegler, U., Shiomi, K., Nakahara, H., 2016. Coseismic and post-seismic velocity changes detected by Passive Image Interferometry: comparison of one great and five strong earthquakes in Japan. Geophys J Int 205, 1053–1073. https://doi.org/10.1093/gji/ggw066

Huang, H., Tsang, L., Njoku, E.G., Colliander, A., Liao, T.H., Ding, K.H., 2017. Propagation and Scattering by a Layer of Randomly Distributed Dielectric Cylinders Using Monte Carlo Simulations of 3D Maxwell Equations With Applications in Microwave Interactions With Vegetation. IEEE Access 5, 11985–12003. https://doi.org/10.1109/ACCESS.2017.2714620

Hufnagel, J., 2016. Flume Construction and RFID Tracking Techniques for Fluvial Sediment Transport Studies.

Hungr, O., Leroueil, S., Picarelli, L., 2014. The Varnes classification of landslide types, an update. Landslides 11, 167–194. https://doi.org/10.1007/s10346-013-0436-y

Ilma, R., 2016. Antenna arrays model [WWW Document]. URL https://nbviewer.jupyter.org/github/rilma/Antenna-Pattern/blob/master/AntennaArray.ipynb

Intrieri, E., Carlà, T., Gigli, G., 2019. Forecasting the time of failure of landslides at slope-scale: A literature review. Earth-Science Reviews. https://doi.org/10.1016/j.earscirev.2019.03.019

Intrieri, E., Gigli, G., Casagli, N., Nadim, F., 2013. Brief communication "Landslide Early Warning System: toolbox and general concepts." Natural Hazards and Earth System Sciences 13, 85–90. https://doi.org/10.5194/nhess-13-85-2013

Intrieri, E., Gigli, G., Gracchi, T., Nocentini, M., Lombardi, L., Mugnai, F., Frodella, W., Bertolini, G., Carnevale, E., Favalli, M., Fornaciai, A., Marturià Alavedra, J., Mucchi, L., Nannipieri, L., Rodriguez-Lloveras, X., Pizziolo, M., Schina, R., Trippi, F., Casagli, N., 2018a. Application of an ultra-wide band sensor-free wireless network for ground monitoring. Engineering Geology 238, 1–14. https://doi.org/10.1016/j.enggeo.2018.02.017

Intrieri, E., Gigli, G., Mugnai, F., Fanti, R., Casagli, N., 2012a. Design and implementation of a landslide early warning system. Engineering Geology 147–148, 124–136. https://doi.org/10.1016/j.enggeo.2012.07.017

Intrieri, E., Gigli, G., Mugnai, F., Fanti, R., Casagli, N., 2012b. Design and implementation of a landslide early warning system. Engineering Geology 147–148, 124–136. https://doi.org/10.1016/j.enggeo.2012.07.017

Intrieri, E., Raspini, F., Fumagalli, A., Lu, P., Del Conte, S., Farina, P., Allievi, J., Ferretti, A., Casagli, N., 2018b. The Maoxian landslide as seen from space: detecting precursors of failure with Sentinel-1 data. Landslides 15, 123–133. https://doi.org/10.1007/s10346-017-0915-7

Iten, M., Puzrin, A.M., Schmid, A., 2008. Landslide monitoring using a road-embedded optical fiber sensor, in: Proc. of SPIE. Presented at the Smart Sensor Phenomena, Technology, Networks, and Systems, International Society for Optics and Photonics, p. 693315. https://doi.org/10.1117/12.774515

Iverson, R.M., 2000. Landslide triggering by rain infiltration. Water Resour. Res. 36, 1897–1910. https://doi.org/10.1029/2000WR900090

Jaboyedoff, M., Oppikofer, T., Abellán, A., Derron, M.-H., Loye, A., Metzger, R., Pedrazzini, A., 2012. Use of LIDAR in landslide investigations: a review. Nat Hazards 61, 5–28. https://doi.org/10.1007/s11069-010-9634-2

Jaboyedoff, M., Pedrazzini, A., Loye, A., Oppikofer, T., Güell i Pons, M., Locat, J., 2009. Earth flow in a complex geological environment: the example of Pont Bourquin, Les Diablerets (Western Switzerland), in: Proceedings of the International Conference on Landslide Processes. Strasbourg, France, pp. 131–137.

James, S.R., Knox, H.A., Abbott, R.E., Screaton, E.J., 2017. Improved moving window cross-spectral analysis for resolving large temporal seismic velocity changes in permafrost. Geophysical Research Letters 44, 4018–4026. https://doi.org/10.1002/2016GL072468

James, W.L., 1975. Dielectric Properties of Wood and Hardboard: Variation with Temperature, Frequency, Moisture Content, and Grain Orientation. Forest Products Laboratory Research Paper.

Jayawardana, D., Kharkovsky, S., Liyanapathirana, R., Zhu, X., 2016. Measurement System With Accelerometer Integrated RFID Tag for Infrastructure Health Monitoring. IEEE Transactions on Instrumentation and Measurement 65, 1163–1171. https://doi.org/10.1109/TIM.2015.2507406

Jochner, M., Turowski, J.M., Badoux, A., Stoffel, M., Rickli, C., 2015. The role of log jams and exceptional flood events in mobilizing coarse particulate organic matter in a steep headwater stream. Earth Surface Dynamics 3, 311–320. https://doi.org/10.5194/esurf-3-311-2015

Jongmans, D., Garambois, S., 2007. Geophysical investigation of landslides : a review. Bulletin de la Société Géologique de France 178, 101–112. https://doi.org/10.2113/gssgfbull.178.2.101

Karam, M.A., Fung, A.K., 1983. Scattering from randomly oriented circular discs with application to vegetation. Radio Science 18, 557–565. https://doi.org/10.1029/RS018i004p00557

Keefer, D.K., Wilson, R.C., Mark, R.K., Brabb, E.E., Brown, W.M., Ellen, S.D., Harp, E.L., Wieczorek, G.F., Alger, C.S., Zatkin, R.S., 1987. Real-Time Landslide Warning During Heavy Rainfall. Science 238, 921–925. https://doi.org/10.1126/science.238.4829.921

Kenney, J.D., Poole, D.R., Willden, G.C., Abbott, B.A., Morris, A.P., McGinnis, R.N., Ferrill, D.A., 2009. Precise positioning with wireless sensor nodes: Monitoring natural hazards in all terrains, in: IEEE Int. Conf. Systems, Man and Cybernetics. Presented at the IEEE International Conference on Systems, Man and Cybernetics, San Antonio, TX, USA, pp. 722–727. https://doi.org/10.1109/ICSMC.2009.5346714

Kim, D., Yeo, J., 2012. Dual-Band Long-Range Passive RFID Tag Antenna Using an AMC Ground Plane. IEEE Transactions on Antennas and Propagation 60, 2620–2626. https://doi.org/10.1109/TAP.2012.2194638

Kim, E., Pyeon, M., Kang, M.-S., Park, J., 2006. A Management System of Street Trees by Using RFID, in: Carswell, J.D., Tezuka, T. (Eds.), Web and Wireless Geographical Information Systems, Lecture Notes in Computer Science. Presented at the International Symposium on Web and Wireless Geographical Information Systems, Springer Berlin Heidelberg, pp. 66–75. https://doi.org/10.1007/11935148_7

Kim, S., Le, T., Tentzeris, M.M., Harrabi, A., Collado, A., Georgiadis, A., 2014. An RFID-enabled inkjet-printed soil moisture sensor on paper for “smart” agricultural applications, in: IEEE SENSORS Proc. Presented at the IEEE SENSORS 2014 Proceedings, Valencia, Spain, pp. 1507–1510. https://doi.org/10.1109/ICSENS.2014.6985301

Kim, Y., Jackson, T., Bindlish, R., Hong, S., Jung, G., Lee, K., 2014. Retrieval of Wheat Growth Parameters With Radar Vegetation Indices. IEEE Geoscience and Remote Sensing Letters 11, 808–812. https://doi.org/10.1109/LGRS.2013.2279255

Kim, Y., Jackson, T., Bindlish, R., Lee, H., Hong, S., 2012. Radar Vegetation Index for Estimating the Vegetation Water Content of Rice and Soybean. IEEE Geoscience and Remote Sensing Letters 9, 564–568. https://doi.org/10.1109/LGRS.2011.2174772

Kim, Y., Zyl, J.J. van, 2009. A Time-Series Approach to Estimate Soil Moisture Using Polarimetric Radar Data. IEEE Transactions on Geoscience and Remote Sensing 47, 2519–2527. https://doi.org/10.1109/TGRS.2009.2014944

Kinar, N.J., Pomeroy, J.W., 2015. Measurement of the physical properties of the snowpack. Reviews of Geophysics 53, 481–544. https://doi.org/10.1002/2015RG000481

Klair, D.K., Kwan-Wu Chin, Raad, R., 2010. A Survey and Tutorial of RFID Anti-Collision Protocols. IEEE Communications Surveys & Tutorials 12, 400–421. https://doi.org/10.1109/SURV.2010.031810.00037

Koelle, A.R., Depp, S.W., Freyman, R.W., 1975. Short-range radio-telemetry for electronic identification, using modulated RF backscatter. Proceedings of the IEEE 63, 1260–1261. https://doi.org/10.1109/PROC.1975.9928

Kurri, M., Huuskonen, A., 2008. Measurements of the Transmission Loss of a Radome at Different Rain Intensities. Journal of Atmospheric and Oceanic Technology 25, 1590–1599. https://doi.org/10.1175/2008JTECHA1056.1

Lacroix, P., Bièvre, G., Pathier, E., Kniess, U., Jongmans, D., 2018. Use of Sentinel-2 images for the detection of precursory motions before landslide failures. Remote Sensing of Environment. https://doi.org/10.1016/j.rse.2018.03.042

Lahokallio, S., Kiilunen, J., Frisk, L., 2014. Performance of passive RFID tags in a high temperature cycling test, in: Electronics System-Integration Technology Conf. Presented at the Electronics System-Integration Technology Conference (ESTC), 2014, Helsinki, Finland, pp. 1–5. https://doi.org/10.1109/ESTC.2014.6962848

Lai, X., Cai, Z., Xie, Z., Zhu, H., 2018. A Novel Displacement and Tilt Detection Method Using Passive UHF RFID Technology. Sensors 18, 1644. https://doi.org/10.3390/s18051644

Lamarre, H., MacVicar, B., Roy, A.G., 2005. Using Passive Integrated Transponder (PIT) Tags to Investigate Sediment Transport in Gravel-Bed Rivers. Journal of Sedimentary Research 75, 736–741. https://doi.org/10.2110/jsr.2005.059

Lamarre, H., Roy, A.G., 2008. The role of morphology on the displacement of particles in a step–pool river system. Geomorphology 99, 270–279. https://doi.org/10.1016/j.geomorph.2007.11.005

Lanza, V.L., Herrmann, D.B., 1958. The density dependence of the dielectric constant of polyethylene. J. Polym. Sci. 28, 622–625. https://doi.org/10.1002/pol.1958.1202811813

Larose, E., 2004. Imaging from one-bit correlations of wideband diffuse wave fields. Journal of Applied Physics 95, 8393. https://doi.org/10.1063/1.1739529

Larose, E., Carrière, S., Voisin, C., Bottelin, P., Baillet, L., Guéguen, P., Walter, F., Jongmans, D., Guillier, B., Garambois, S., Gimbert, F., Massey, C., 2015. Environmental seismology: What can we learn on earth surface processes with ambient noise? Journal of Applied Geophysics 116, 62–74. https://doi.org/10.1016/j.jappgeo.2015.02.001

Larose, E., Montaldo, G., Derode, A., Campillo, M., 2006. Passive imaging of localized reflectors and interfaces in open media. Applied Physics Letters 88, 104103. https://doi.org/10.1063/1.2186112

Larson, K.M., 2016. GPS interferometric reflectometry: applications to surface soil moisture, snow depth, and vegetation water content in the western United States. Wiley Interdisciplinary Reviews: Water 3, 775–787. https://doi.org/10.1002/wat2.1167

Larson, K.M., Braun, J.J., Small, E.E., Zavorotny, V.U., Gutmann, E.D., Bilich, A.L., 2010. GPS Multipath and Its Relation to Near-Surface Soil Moisture Content. IEEE Journal of Selected Topics in Applied Earth Observations and Remote Sensing 3, 91–99. https://doi.org/10.1109/JSTARS.2009.2033612

Larson, K.M., Gutmann, E.D., Zavorotny, V.U., Braun, J.J., Williams, M.W., Nievinski, F.G., 2009. Can we measure snow depth with GPS receivers? Geophys. Res. Lett. 36, L17502. https://doi.org/10.1029/2009GL039430

Lauth, T.J., Papanicolaou, A.N., 2008. Experimental/Feasibility Study of Radio Frequency Tracers for Monitoring Sediment Transport and Scour around Bridges, in: World Environmental and Water Resources Congress 2008. Presented at the World Environmental and Water Resources Congress 2008, American Society of Civil Engineers, Honolulu, Hawaii, United States, pp. 1–10. https://doi.org/10.1061/40976(316)345

Le Breton, M., Baillet, L., Larose, E., Rey, E., Benech, P., Jongmans, D., Guyoton, F., 2017a. Outdoor UHF RFID: Phase Stabilization for Real-World Applications. IEEE Journal of Radio Frequency Identification 1, 279–290. https://doi.org/10.1109/JRFID.2017.2786745

Le Breton, M., Baillet, L., Larose, E., Rey, E., Benech, P., Jongmans, D., Guyoton, F., 2017b. Outdoor meteorological effects on UHF RFID phase shift: Experimental simulations, in: 2017 IEEE International Conference on RFID (RFID). Presented at the 2017 IEEE International Conference on RFID (RFID), Phoenix, AZ, USA, pp. 103–109. https://doi.org/10.1109/RFID.2017.7945594

Le Breton, M., Baillet, L., Larose, E., Rey, E., Benech, P., Jongmans, D., Guyoton, F., Jaboyedoff, M., 2019. Passive radio-frequency identification ranging, a dense and weather-robust technique for landslide displacement monitoring. Engineering Geology 250, 1–10. https://doi.org/10.1016/j.enggeo.2018.12.027

Lecocq, T., Longuevergne, L., Pedersen, H.A., Brenguier, F., Stammler, K., 2017. Monitoring ground water storage at mesoscale using seismic noise: 30 years of continuous observation and thermo-elastic and hydrological modeling. Scientific Reports 7, 14241. https://doi.org/10.1038/s41598-017-14468-9

Lesage, P., Reyes-Dávila, G., Arámbula-Mendoza, R., 2014. Large tectonic earthquakes induce sharp temporary decreases in seismic velocity in Volcán de Colima, Mexico. Journal of Geophysical Research: Solid Earth 119, 4360–4376. https://doi.org/10.1002/2013JB010884

Lévy, C., Baillet, L., Jongmans, D., Mourot, P., Hantz, D., 2010. Dynamic response of the Chamousset rock column (Western Alps, France). Journal of Geophysical Research 115. https://doi.org/10.1029/2009JF001606

Li, H., Chan, G., Wong, J.K.W., Skitmore, M., 2016. Real-time locating systems applications in construction. Automation in Construction 63, 37–47. https://doi.org/10.1016/j.autcon.2015.12.001

Li, S., Li, N., Calis, G., Gerber, B.B., 2011. Impact of Ambient Temperature, Tag/Antenna Orientation, and Distance on the Performance of Radio Frequency Identification in Construction Industry. Computing in Civil Engineering 85.

Liébault, F., Bellot, H., Chapuis, M., Klotz, S., Deschâtres, M., 2012. Bedload tracing in a high-sediment-load mountain stream. Earth Surface Processes and Landforms 37, 385–399. https://doi.org/10.1002/esp.2245

Luca, D.L.D., Versace, P., 2017. A comprehensive framework for empirical modeling of landslides induced by rainfall: the Generalized FLaIR Model (GFM). Landslides 14, 1009–1030. https://doi.org/10.1007/s10346-016-0768-5

Lucianaz, C., Greco, G., Bertoldo, S., Allegretti, M., 2015. Real time outdoor localization of buried RFID tags through statistical methods, in: Int. Conf. on Electromagnetics in Advanced Applications. Presented at the International Conference on Electromagnetics in Advanced Applications (ICEAA), pp. 1152–1154. https://doi.org/10.1109/ICEAA.2015.7297299

Lucieer, A., Jong, S. de, Turner, D., 2013. Mapping landslide displacements using Structure from Motion (SfM) and image correlation of multi-temporal UAV photography. Progress in Physical Geography 0309133313515293. https://doi.org/10.1177/0309133313515293

Luttrell, K., Sandwell, D., 2010. Ocean loading effects on stress at near shore plate boundary fault systems. Journal of Geophysical Research 115. https://doi.org/10.1029/2009JB006541

Luvisi, A., Panattoni, A., Materazzi, A., 2016. RFID temperature sensors for monitoring soil solarization with biodegradable films. Computers and Electronics in Agriculture 123, 135–141. https://doi.org/10.1016/j.compag.2016.02.023

Machacca, R., Lesage, P., Larose, E., Lacroix, P., 2017. Towards Forecasting Explosive Volcanic Eruptions Using Ambient Noise Correlation: Ubinas Volcano Peru (Master thesis). Université Grenoble Alpes.

Machacca, R., Lesage, P., Larose, E., Lacroix, P., Ancassi, R., 2019. Detection of pre-eruptive seismic velocity variations at an Andesitic volcano using noise correlation on 3-components seismic stations: Ubinas volcano, Peru. JVGR in revision.

MacVicar, B.J., Piégay, H., Henderson, A., Comiti, F., Oberlin, C., Pecorari, E., 2009. Quantifying the temporal dynamics of wood in large rivers: field trials of wood surveying, dating, tracking, and monitoring techniques. Earth Surface Processes and Landforms 34, 2031–2046. https://doi.org/10.1002/esp.1888

Mainsant, G., Chambon, G., Jongmans, D., Larose, E., Baillet, L., 2015. Shear-wave-velocity drop prior to clayey mass movement in laboratory flume experiments. Engineering Geology 192, 26–32. https://doi.org/10.1016/j.enggeo.2015.03.019

Mainsant, G., Jongmans, D., Chambon, G., Larose, E., Baillet, L., 2012a. Shear-wave velocity as an indicator for rheological changes in clay materials: Lessons from laboratory experiments. Geophys. Res. Lett. 39, L19301. https://doi.org/10.1029/2012GL053159

Mainsant, G., Larose, E., Brönnimann, C., Jongmans, D., Michoud, C., Jaboyedoff, M., 2012b. Ambient seismic noise monitoring of a clay landslide: Toward failure prediction. J. Geophys. Res. 117, F01030. https://doi.org/10.1029/2011JF002159

Manzari, S., Caizzone, S., Rubini, C., Marrocco, G., 2014a. Feasibility of wireless temperature sensing by passive UHF-RFID tags in ground satellite test beds, in: 2014 IEEE International Conference on Wireless for Space and Extreme Environments (WiSEE). Presented at the 2014 IEEE International Conference on Wireless for Space and Extreme Environments (WiSEE), pp. 1–6. https://doi.org/10.1109/WiSEE.2014.6973074

Manzari, S., Catini, A., Pomarico, G., Natale, C.D., Marrocco, G., 2014b. Development of an UHF RFID Chemical Sensor Array for Battery-Less Ambient Sensing. IEEE Sensors Journal 14, 3616–3623. https://doi.org/10.1109/JSEN.2014.2329268

Manzari, S., Marrocco, G., 2014. Modeling and Applications of a Chemical-Loaded UHF RFID Sensing Antenna With Tuning Capability. IEEE Transactions on Antennas and Propagation 62, 94–101. https://doi.org/10.1109/TAP.2013.2287008

Manzari, S., Occhiuzzi, C., Nawale, S., Catini, A., Natale, C.D., Marrocco, G., 2012. Humidity Sensing by Polymer-Loaded UHF RFID Antennas. IEEE Sensors Journal 12, 2851–2858. https://doi.org/10.1109/JSEN.2012.2202897

Mao, L., Dell'Agnese, A., Comiti, F., 2017. Sediment motion and velocity in a glacier-fed stream. Geomorphology, SEDIMENT DYNAMICS IN ALPINE BASINS 291, 69–79. https://doi.org/10.1016/j.geomorph.2016.09.008

Mao, S., Campillo, M., Hilst, R.D. van der, Brenguier, F., Stehly, L., Hillers, G., 2019. High Temporal Resolution Monitoring of Small Variations in Crustal Strain by Dense Seismic Arrays. Geophysical Research Letters 46, 128–137. https://doi.org/10.1029/2018GL079944

Marano, K.D., Wald, D.J., Allen, T.I., 2010. Global earthquake casualties due to secondary effects: a quantitative analysis for improving rapid loss analyses. Nat Hazards 52, 319–328. https://doi.org/10.1007/s11069-009-9372-5

Marrocco, G., 2010. Pervasive electromagnetics: sensing paradigms by passive RFID technology. IEEE Wireless Communications 17, 10–17. https://doi.org/10.1109/MWC.2010.5675773

Marshall, H.-P., Koh, G., 2008. FMCW radars for snow research. Cold Regions Science and Technology 52, 118–131. https://doi.org/10.1016/j.coldregions.2007.04.008

Matrosov, S.Y., 1998. A Dual-Wavelength Radar Method to Measure Snowfall Rate. J. Appl. Meteor. 37, 1510–1521. https://doi.org/10.1175/1520-0450(1998)037<1510:ADWRMT>2.0.CO;2

Matrosov, S.Y., 1992. Radar reflectivity in snowfall. IEEE Transactions on Geoscience and Remote Sensing 30, 454–461. https://doi.org/10.1109/36.142923

Matsuura, S., Asano, S., Okamoto, T., Takeuchi, Y., 2003. Characteristics of the displacement of a landslide with shallow sliding surface in a heavy snow district of Japan. Engineering Geology 69, 15–35. https://doi.org/10.1016/S0013-7952(02)00245-4

Matsuura, S., Okamoto, T., Asano, S., Osawa, H., Shibasaki, T., 2017. Influences of the snow cover on landslide displacement in winter period: a case study in a heavy snowfall area of Japan. Environ Earth Sci 76, 362. https://doi.org/10.1007/s12665-017-6693-7

Mayoraz, F., Vulliet, L., 2002. Neural Networks for Slope Movement Prediction. International Journal of Geomechanics 2, 153–173. https://doi.org/10.1080/15323640208500177

Mazur, M., Marynowski, W., Kusiek, A., Zieniutycz, W., 2014. Effect of time varying measurement conditions on antenna pattern in near field measurement and its correction procedure, in: 20th Int. Conf. Microwave,

Radar, and Wireless Communication. Presented at the 2014 20th International Conference on Microwaves, Radar, and Wireless Communication (MIKON), Gdansk, Poland, pp. 1–4. https://doi.org/10.1109/MIKON.2014.6899882

Meier, U., Shapiro, N.M., Brenguier, F., 2010. Detecting seasonal variations in seismic velocities within Los Angeles basin from correlations of ambient seismic noise. Geophysical Journal International 181, 985–996. https://doi.org/10.1111/j.1365-246X.2010.04550.x

Mercer, A.J., James, R.K., Bennett, G., Patel, P., Johnston, C., Cai, J., 2011. RFID testing and evaluation for an RF-harsh environment, in: IEEE Int. Conf. RFID Technologies and Applications. Presented at the 2011 IEEE International Conference on RFID-Technologies and Applications (RFID-TA), Sitges, Spain, pp. 95–102. https://doi.org/10.1109/RFID-TA.2011.6068622

Merilampi, S.L., Virkki, J., Ukkonen, L., Sydänheimo, L., 2014. Testing the effects of temperature and humidity on printed passive UHF RFID tags on paper substrate. International Journal of Electronics 101, 711–730. https://doi.org/10.1080/00207217.2013.794491

Miao, Y., Shi, Y., Wang, S.-Y., 2018. Temporal change of near-surface shear wave velocity associated with rainfall in Northeast Honshu, Japan. Earth Planets Space 70, 204. https://doi.org/10.1186/s40623-018-0969-3

Miesen, R., Ebelt, R., Kirsch, F., Schäfer, T., Li, G., Wang, H., Vossiek, M., 2011. Where is the Tag? IEEE Microwave Magazine 12, S49–S63. https://doi.org/10.1109/MMM.2011.942730

Miesen, R., Kirsch, F., Vossiek, M., 2013a. UHF RFID Localization Based on Synthetic Apertures. IEEE Transactions on Automation Science and Engineering 10, 807–815. https://doi.org/10.1109/TASE.2012.2224656

Miesen, R., Parr, A., Schleu, J., Vossiek, M., 2013b. 360° carrier phase measurement for UHF RFID local positioning, in: 2013 IEEE International Conference on RFID-Technologies and Applications (RFID-TA). Presented at the 2013 IEEE International Conference on RFID-Technologies and Applications (RFID-TA), pp. 1–6. https://doi.org/10.1109/RFID-TA.2013.6694499

Milillo, P., Fielding, E.J., Shulz, W.H., Delbridge, B., Burgmann, R., 2014. COSMO-SkyMed Spotlight Interferometry Over Rural Areas: The Slumgullion Landslide in Colorado, USA. IEEE Journal of Selected Topics in Applied Earth Observations and Remote Sensing 7, 2919–2926. https://doi.org/10.1109/JSTARS.2014.2345664

Miller, I.M., Warrick, J.A., Morgan, C., 2011. Observations of coarse sediment movements on the mixed beach of the Elwha Delta, Washington. Marine Geology 282, 201–214. https://doi.org/10.1016/j.margeo.2011.02.012

Monserrat, O., Crosetto, M., Luzi, G., 2014. A review of ground-based SAR interferometry for deformation measurement. ISPRS Journal of Photogrammetry and Remote Sensing 93, 40–48. https://doi.org/10.1016/j.isprsjprs.2014.04.001

Montgomery, D.R., Dietrich, W.E., 1994. A physically based model for the topographic control on shallow landsliding. Water Resources Research 30, 1153–1171. https://doi.org/10.1029/93WR02979

Mordret, A., Mikesell, T.D., Harig, C., Lipovsky, B.P., Prieto, G.A., 2016. Monitoring southwest Greenland's ice sheet melt with ambient seismic noise. Science Advances 2, e1501538. https://doi.org/10.1126/sciadv.1501538

Moreau, L., Stehly, L., Boué, P., Lu, Y., Larose, E., Campillo, M., 2017. Improving ambient noise correlation functions with an SVD-based Wiener filter. Geophys J Int 211, 418–426. https://doi.org/10.1093/gji/ggx306

Moreiras, S.M., 2005. Climatic effect of ENSO associated with landslide occurrence in the Central Andes, Mendoza Province, Argentina. Landslides 2, 53–59. https://doi.org/10.1007/s10346-005-0046-4

Morgan, G.C., Rawlings, G.E., Sobkowicz, J.C., 1992. Evaluating total risk to communities from large debris flows, in: Proceedings of 1st Canadian Symposium on Geotechnique and Natural Hazards. BiTech Publishers, Vancouver, BC, Canada, pp. 225– 236.

Murray, F.W., 1967. On the Computation of Saturation Vapor Pressure. J. Appl. Meteor. 6, 203–204. https://doi.org/10.1175/1520-0450(1967)006<0203:OTCOSV>2.0.CO;2

Nakata, N., Boué, P., Brenguier, F., Roux, P., Ferrazzini, V., Campillo, M., 2016. Body and surface wave reconstruction from seismic noise correlations between arrays at Piton de la Fournaise volcano. Geophysical Research Letters 43, 1047–1054. https://doi.org/10.1002/2015GL066997

Nakata, N., Snieder, R., 2012. Estimating near-surface shear wave velocities in Japan by applying seismic interferometry to KiK-net data. Journal of Geophysical Research: Solid Earth 117. https://doi.org/10.1029/2011JB008595

Ngai, E.W.T., Moon, K.K.L., Riggins, F.J., Yi, C.Y., 2008. RFID research: An academic literature review (1995–2005) and future research directions. International Journal of Production Economics, Special Section on RFID: Technology, Applications, and Impact on Business Operations 112, 510–520. https://doi.org/10.1016/j.ijpe.2007.05.004

Ni, L.M., Liu, Y., Lau, Y.C., Patil, A.P., 2003. LANDMARC: indoor location sensing using active RFID, in: Proceedings of the First IEEE International Conference on Pervasive Computing and Communications, 2003. (PerCom 2003). Presented at the Proceedings of the First IEEE International Conference on Pervasive Computing and Communications, 2003. (PerCom 2003), pp. 407–415. https://doi.org/10.1109/PERCOM.2003.1192765

Ni, L.M., Zhang, D., Souryal, M.R., 2011. RFID-based localization and tracking technologies. IEEE Wireless Communications 18, 45–51. https://doi.org/10.1109/MWC.2011.5751295

Nichols, M.H., 2004. A Radio Frequency Identification System for Monitoring Coarse Sediment Particle Displacement. Applied Engineering in Agriculture 20, 783–787. https://doi.org/10.13031/2013.17727

Niethammer, U., James, M.R., Rothmund, S., Travelletti, J., Joswig, M., 2012. UAV-based remote sensing of the Super-Sauze landslide: Evaluation and results. Engineering Geology, Integration of Technologies for Landslide Monitoring and Quantitative Hazard Assessment 128, 2–11. https://doi.org/10.1016/j.enggeo.2011.03.012

Nikitin, P.V., Martinez, R., Ramamurthy, S., Leland, H., Spiess, G., Rao, K.V.S., 2010. Phase based spatial identification of UHF RFID tags, in: IEEE Int. Conf. RFID. Presented at the IEEE International Conference on RFID, IEEE, Orlando, FL, USA, pp. 102–109. https://doi.org/10.1109/RFID.2010.5467253

Nikitin, P.V., Rao, K.V.S., 2008. Antennas and propagation in UHF RFID systems. Presented at the IEEE International Conference on RFID, Las Vegas, USA, pp. 277–288. https://doi.org/10.1109/RFID.2008.4519368

Niklewski, J., Fredriksson, M., Isaksson, T., 2016. Moisture content prediction of rain-exposed wood: Test and evaluation of a simple numerical model for durability applications. Building and Environment 97, 126–136. https://doi.org/10.1016/j.buildenv.2015.11.037

Nummela, J., Ukkonen, L., Sydänheimo, L., 2008. Passive UHF RFID tags in arctic environment. International Journal of Communications 2, 135–142.

Obermann, A., Planès, T., Larose, E., Campillo, M., 2013a. Imaging preeruptive and coeruptive structural and mechanical changes of a volcano with ambient seismic noise. Journal of Geophysical Research: Solid Earth 118, 6285–6294. https://doi.org/10.1002/2013JB010399

Obermann, A., Planès, T., Larose, E., Sens-Schönfelder, C., Campillo, M., 2013b. Depth sensitivity of seismic coda waves to velocity perturbations in an elastic heterogeneous medium. Geophys J Int 194, 372–382. https://doi.org/10.1093/gji/ggt043

Occhiuzzi, C., Amendola, S., Nappi, S., D'Uva, N., Marrocco, G., 2018. Sensing -oriented RFID tag Response in High Temperature Conditions, in: 2018 3rd International Conference on Smart and Sustainable Technologies (SpliTech). Presented at the 2018 3rd International Conference on Smart and Sustainable Technologies (SpliTech), pp. 1–4.

Occhiuzzi, C., Caizzone, S., Marrocco, G., 2013. Passive UHF RFID antennas for sensing applications: Principles, methods, and classifcations. IEEE Antennas and Propagation Magazine 55, 14–34. https://doi.org/10.1109/MAP.2013.6781700

Occhiuzzi, C., Cippitelli, S., Marrocco, G., 2010. Modeling, Design and Experimentation of Wearable RFID Sensor Tag. IEEE Transactions on Antennas and Propagation 58, 2490–2498. https://doi.org/10.1109/TAP.2010.2050435

Oguchi, T., 1983. Electromagnetic wave propagation and scattering in rain and other hydrometeors. Proceedings of the IEEE 71, 1029–1078. https://doi.org/10.1109/PROC.1983.12724

Olinde, L., Johnson, J.P.L., 2015. Using RFID and accelerometer-embedded tracers to measure probabilities of bed load transport, step lengths, and rest times in a mountain stream. Water Resour. Res. 51, 7572–7589. https://doi.org/10.1002/2014WR016120

Olinde, L.J., 2015. Displacement and entrainment behavior of bedload clasts in mountain streams (Thesis). https://doi.org/10.15781/T21P7X

Olivier, G., Brenguier, F., de Wit, T., Lynch, R., 2017. Monitoring the stability of tailings dam walls with ambient seismic noise. The Leading Edge 36, 350a1-350a6. https://doi.org/10.1190/tle36040350a1.1

Osborne, P.D., Macdonald, N., Curtiss, G., 2011. Measurements and Modeling of Gravel Transport under Wind Waves, Vessel-Generated Waves, and Tidal Currents. Journal of Coastal Research 165–172. https://doi.org/10.2112/SI59-017.1

Pedregosa, F., Varoquaux, G., Gramfort, A., Michel, V., Thirion, B., Grisel, O., Blondel, M., Prettenhofer, P., Weiss, R., Dubourg, V., Vanderplas, J., Passos, A., Cournapeau, D., 2011. Scikit-learn: Machine Learning in Python. Journal of Machine Learning Research 12, 2825–2830.

Petley, D.N., Hearn, G.J., Hart, A., Rosser, N.J., Dunning, S.A., Oven, K., Mitchell, W.A., 2007. Trends in landslide occurrence in Nepal. Nat Hazards 43, 23–44. https://doi.org/10.1007/s11069-006-9100-3

Picard, G., Sandells, M., Löwe, H., 2018. SMRT: an active–passive microwave radiative transfer model for snow with multiple microstructure and scattering formulations (v1.0). Geoscientific Model Development 11, 2763–2788. https://doi.org/10.5194/gmd-11-2763-2018

Pichorim, S., Gomes, N., Batchelor, J., 2018. Two Solutions of Soil Moisture Sensing with RFID for Landslide Monitoring. Sensors 18, 452. https://doi.org/10.3390/s18020452

Piegay, H., Arnaud, F., Cassel, M., Dépret, T., Alber, A., Michel, K., Rollet, A.-J., Vaudor, L., 2016. Suivi par RFID de la mobilité des galets : retour sur 10 ans d'expérience en grandes rivières. BSGLg.

Pinault, J.-L., Plagnes, V., Aquilina, L., Bakalowicz, M., 2001. Inverse modeling of the hydrological and the hydrochemical behavior of hydrosystems: Characterization of Karst System Functioning. Water Resources Research 37, 2191–2204. https://doi.org/10.1029/2001WR900018

Planès, T., Mooney, M.A., Rittgers, J.B.R., Parekh, M.L., Behm, M., Snieder, R., 2016. Time-lapse monitoring of internal erosion in earthen dams and levees using ambient seismic noise. Géotechnique 66, 301–312. https://doi.org/10.1680/jgeot.14.P.268

Planès, T., Rittgers, J.B., Mooney, M.A., Kanning, W., Draganov, D., 2017. Monitoring the tidal response of a sea levee with ambient seismic noise. Journal of Applied Geophysics 138, 255–263. https://doi.org/10.1016/j.jappgeo.2017.01.025

Plumb, B., 2017. Impacts of Hydromodification and Sediment Supply Alterations on Bedload Transport and Bed Morphology in Urbanizing Gravel-bed Rivers.

Polivka, M., Svanda, M., Hudec, P., Zvanovec, S., 2009. UHF RF Identification of People in Indoor and Open Areas. IEEE Transactions on Microwave Theory and Techniques 57, 1341–1347. https://doi.org/10.1109/TMTT.2009.2017305

Pozar, D.M., 2000. Microwave and Rf Design of Wireless Systems. Wiley.

Pozzebon, A., 2015. Integrating RFID Transponders as Data Loggers in Wireless Sensor Nodes for Outdoor Remote Monitoring Operations. Int J Wireless Inf Networks 22, 399–406. https://doi.org/10.1007/s10776-015-0291-y

Prasad, S., Ghahfarokhi, S.S., Tayari, D., 2011. Impact of Moisture Content on RFID Antenna Performance for Wood-Log Monitoring, in: 3rd RF Measurement Technology Conf. Presented at the RF Measurement Technology Conference, Gävle, Sweden.

Preiswerk, L.E., Walter, F., 2018. High-Frequency (>2 Hz) Ambient Seismic Noise on High-Melt Glaciers: Green's Function Estimation and Source Characterization. Journal of Geophysical Research: Earth Surface 123, 1667–1681. https://doi.org/10.1029/2017JF004498

Preradovic, S., Karmakar, N.C., 2010. Chipless RFID: Bar Code of the Future. IEEE Microwave Magazine 11, 87–97. https://doi.org/10.1109/MMM.2010.938571

Qiao, Q., Zhang, L., Yang, F., Yue, Z., Elsherbeni, A.Z., 2013. UHF RFID temperature sensor tag using novel HDPE-BST composite material, in: IEEE Antennas and Propagation Soc. Int. Symp. Presented at the 2013 IEEE Antennas and Propagation Society International Symposium (APSURSI), Orlando, FL, USA, pp. 2313–2314. https://doi.org/10.1109/APS.2013.6711815

Rainato, R., Mao, L., Picco, L., 2018. Near-bankfull floods in an Alpine stream: Effects on the sediment mobility and bedload magnitude. International Journal of Sediment Research 33, 27–34. https://doi.org/10.1016/j.ijsrc.2017.03.006

Raso, T., 2017. The Impacts of Stormwater Management on Hydromodification and Bedload Sediment Transport in a Gravel-bed Stream.

Ravazzolo, D., Mao, L., Garniga, B., Picco, L., Lenzi, M.A., 2013. Displacement length and velocity of tagged logs in the tagliamento river. 1. https://doi.org/10.4081/jae.2013.251

Razavi, S.N., Haas, C.T., 2011. Using reference RFID tags for calibrating the estimated locations of construction materials. Automation in Construction, Selected papers from the 26th ISARC 2009 20, 677–685. https://doi.org/10.1016/j.autcon.2010.12.009

Reigber, A., Scheiber, R., 2003. Airborne differential SAR interferometry: first results at L-band. IEEE Transactions on Geoscience and Remote Sensing 41, 1516–1520. https://doi.org/10.1109/TGRS.2003.814610

Renalier, F., Bièvre, G., Jongmans, D., Campillo, M., Bard, P.-Y., 2010a. Clayey Landslide Investigations Using Active and Passive VS Measurements, in: Advances in Near-Surface Seismology and Ground-Penetrating Radar. Society of Exploration Geophysicists, American Geophysical Union, Environmental and Engineering Geophysical Society, pp. 397–413. https://doi.org/10.1190/1.9781560802259.ch24

Renalier, F., Jongmans, D., Campillo, M., Bard, P.-Y., 2010b. Shear wave velocity imaging of the Avignonet landslide (France) using ambient noise cross correlation. Journal of Geophysical Research: Earth Surface 115. https://doi.org/10.1029/2009JF001538

Revil, A., Le Breton, M., Niu, Q., Wallin, E., Haskins, E., Thomas, D.M., 2017a. Induced polarization of volcanic rocks – 1. Surface versus quadrature conductivity. Geophys J Int 208, 826–844. https://doi.org/10.1093/gji/ggw444

Revil, A., Murugesu, M., Prasad, M., Le Breton, M., 2017b. Alteration of volcanic rocks: A new non-intrusive indicator based on induced polarization measurements. Journal of Volcanology and Geothermal Research 341, 351–362. https://doi.org/10.1016/j.jvolgeores.2017.06.016

Richter, T., Sens-Schönfelder, C., Kind, R., Asch, G., 2014. Comprehensive observation and modeling of earthquake and temperature-related seismic velocity changes in northern Chile with passive image interferometry. Journal of Geophysical Research: Solid Earth 119, 4747–4765. https://doi.org/10.1002/2013JB010695

Rivet, D., Brenguier, F., Clarke, D., Shapiro, N.M., Peltier, A., 2014. Long-term dynamics of Piton de la Fournaise volcano from 13 years of seismic velocity change measurements and GPS observations. Journal of Geophysical Research: Solid Earth 119, 7654–7666. https://doi.org/10.1002/2014JB011307

Rivet, D., Campillo, M., Shapiro, N.M., Cruz-Atienza, V., Radiguet, M., Cotte, N., Kostoglodov, V., 2011. Seismic evidence of nonlinear crustal deformation during a large slow slip event in Mexico. Geophysical Research Letters 38. https://doi.org/10.1029/2011GL047151

Rodriguez-Alvarez, N., Bosch-Lluis, X., Camps, A., Aguasca, A., Vall-llossera, M., Valencia, E., Ramos-Perez, I., Park, H., 2011a. Review of crop growth and soil moisture monitoring from a ground-based instrument implementing the Interference Pattern GNSS-R Technique. Radio Science 46. https://doi.org/10.1029/2011RS004680

Rodriguez-Alvarez, N., Camps, A., Vall-llossera, M., Bosch-Lluis, X., Monerris, A., Ramos-Perez, I., Valencia, E., Marchan-Hernandez, J.F., Martinez-Fernandez, J., Baroncini-Turricchia, G., Perez-Gutierrez, C., Sanchez, N., 2011b. Land Geophysical Parameters Retrieval Using the Interference Pattern GNSS-R Technique. IEEE Transactions on Geoscience and Remote Sensing 49, 71–84. https://doi.org/10.1109/TGRS.2010.2049023

Rorato, O., Greco, G., Bertoldo, S., Lucianaz, C., Allegretti, M., Curtaz, M., Roasio, A., Barone, S., Perona, G., 2014. An ad-hoc RFID tag for glaciers monitoring, in: IEEE-APS Topical Confe. on Antennas and Propagation in Wireless Communications. Presented at the IEEE-APS Topical Conference on Antennas and Propagation in Wireless Communications (APWC), Palm Beach, Aruba, pp. 864–867.

Rose, N.D., Hungr, O., 2007. Forecasting potential rock slope failure in open pit mines using the inverse-velocity method. International Journal of Rock Mechanics and Mining Sciences 44, 308–320. https://doi.org/10.1016/j.ijrmms.2006.07.014

Ruiz-Garcia, L., Lunadei, L., 2011. The role of RFID in agriculture: Applications, limitations and challenges. Computers and Electronics in Agriculture 79, 42–50. https://doi.org/10.1016/j.compag.2011.08.010

Saarinen, K., Björninen, T., Ukkonen, L., Frisk, L., 2014. Reliability Analysis of RFID Tags in Changing Humid Environment. IEEE Transactions on Components, Packaging and Manufacturing Technology 4, 77–85. https://doi.org/10.1109/TCPMT.2013.2278182

Sadiku, M.N.O., 1985. Refractive index of snow at microwave frequencies. Appl. Opt., AO 24, 572–575. https://doi.org/10.1364/AO.24.000572

Saito, M., 1965. Forecasting the time of occurrence of a slope failure. Proc. 6 th Int. Conf. Soil Mechanics and Foundation Eng. 537–541.

Salazar, J.L., V. CHANDRASEKAR, JORGE M. TRABAL, PAUL SIQUERA, RAFAEL MEDINA, ERIC KNAPP, DAVID J. MCLAUGHLIN, 2014. A Drop Size Distribution (DSD)-Based Model for Evaluating the Performance of Wet Radomes for Dual-Polarized Radars. Journal of Atmospheric and Oceanic Technology 31, 2409–2430.

Santos, A.S., Puhlmann, H.F., Avanço, L., Miranda, M.J.A.C., Jacon, M., Noda, M.K., Brazolin, S., Yojo, T., Mancini, V.A., Cugnasca, C.E., Pinto, J.K.C., Martinelli, V.E., Santos, A.C., 2014. Challenges to the use of RFID in wood crossties, in: 2014 IEEE Brasil RFID. Presented at the 2014 IEEE Brasil RFID, pp. 25–27. https://doi.org/10.1109/BrasilRFID.2014.7128957

Schenk, E.R., Moulin, B., Hupp, C.R., Richter, J.M., 2014. Large wood budget and transport dynamics on a large river using radio telemetry. Earth Surface Processes and Landforms 39, 487–498. https://doi.org/10.1002/esp.3463

Scherhäufl, M., Pichler, M., Stelzer, A., 2015. UHF RFID Localization Based on Phase Evaluation of Passive Tag Arrays. IEEE Transactions on Instrumentation and Measurement 64, 913–922. https://doi.org/10.1109/TIM.2014.2363578

Schneider, J., Hegglin, R., Meier, S., Turowski, J.M., Nitsche, M., Rickenmann, D., 2010. Studying sediment transport in mountain rivers by mobile and stationary RFID antennas. River Flow 2, 1301–1308.

Scott, K.M., Macias, J.L., Naranjo, J.A., Rodriguez, S., McGeehin, J.P., 2001. Catastrophic debris flows transformed from landslides in volcanic terrains : mobility, hazard assessment and mitigation strategies (Report No. 1630), Professional Paper. USGS.

Senfaute, G., Duperret, A., Lawrence, J.A., 2009. Micro-seismic precursory cracks prior to rock-fall on coastal chalk cliffs: a case study at Mesnil-Val, Normandie, NW France. Natural Hazards and Earth System Science 9, 1625–1641. https://doi.org/10.5194/nhess-9-1625-2009

Sens-Schönfelder, C., Larose, E., 2008. Temporal changes in the lunar soil from correlation of diffuse vibrations. Phys. Rev. E 78, 045601. https://doi.org/10.1103/PhysRevE.78.045601

Sens-Schönfelder, C., Wegler, U., 2006. Passive image interferometry and seasonal variations of seismic velocities at Merapi Volcano, Indonesia. Geophys. Res. Lett. 33, L21302. https://doi.org/10.1029/2006GL027797

Shahmirzadi, E., Sumi, T., Ishida, H., 2016. Field experiments on coarse-sediment displacement upstream of flood mitigation dams. Water Harvesting Research 1, 32–43. https://doi.org/10.22077/jwhr.2017.375

Shapiro, N.M., Campillo, M., 2004. Emergence of broadband Rayleigh waves from correlations of the ambient seismic noise. Geophysical Research Letters 31. https://doi.org/10.1029/2004GL019491

Siden, J., Zeng, X., Unander, T., Koptyug, A., Nilsson, H.E., 2007. Remote Moisture Sensing utilizing Ordinary RFID Tags, in: IEEE Sensors Conf. Presented at the 2007 IEEE Sensors, Atlanta, GA, USA, pp. 308–311. https://doi.org/10.1109/ICSENS.2007.4388398

Simpson, J.T., Hunter, S.R., Aytug, T., 2015. Superhydrophobic materials and coatings: a review. Reports on Progress in Physics 78, 086501. https://doi.org/10.1088/0034-4885/78/8/086501

Sirangelo, B., Versace, P., 1996. A real time forecasting model for landslides triggered by rainfall. Meccanica 31, 73–85. https://doi.org/10.1007/BF00444156

Skolnik, M.I. (Ed.), 2008. Radar handbook, 3rd ed. ed. McGraw-Hill, New York.

Slack, D., 2017. Minimizing Temperature Induced Phase Errors in Coaxial Cables. Microwave Journal 60.

Small, E.E., Larson, K.M., Braun, J.J., 2010. Sensing vegetation growth with reflected GPS signals. Geophysical Research Letters 37. https://doi.org/10.1029/2010GL042951

Smith, D.P., Messier, G.G., Wasson, M.W., 2016. Boreal Forest Low Antenna Height Propagation Measurements. IEEE Transactions on Antennas and Propagation 64, 4004–4011. https://doi.org/10.1109/TAP.2016.2583490

Snieder, R., Larose, E., 2013. Extracting Earth's Elastic Wave Response from Noise Measurements. Annual Review of Earth and Planetary Sciences 41, 183–206. https://doi.org/10.1146/annurev-earth-050212-123936

Solheim, F.S., Vivekanandan, J., Ware, R.H., Rocken, C., 1999. Propagation delays induced in GPS signals by dry air, water vapor, hydrometeors, and other particulates. Journal of Geophysical Research: Atmospheres 104, 9663–9670. https://doi.org/10.1029/1999JD900095

Song, J., Haas, C.T., Caldas, C.H., 2007. A proximity-based method for locating RFID tagged objects. Advanced Engineering Informatics 21, 367–376. https://doi.org/10.1016/j.aei.2006.09.002

Squarzoni, C., Delacourt, C., Allemand, P., 2005. Differential single-frequency GPS monitoring of the La Valette landslide (French Alps). Engineering Geology 79, 215–229. https://doi.org/10.1016/j.enggeo.2005.01.015

Steele-Dunne, S.C., McNairn, H., Monsivais-Huertero, A., Judge, J., Liu, P.W., Papathanassiou, K., 2017. Radar Remote Sensing of Agricultural Canopies: A Review. IEEE Journal of Selected Topics in Applied Earth Observations and Remote Sensing 10, 2249–2273. https://doi.org/10.1109/JSTARS.2016.2639043

Stockman, H., 1948. Communication by Means of Reflected Power. Proceedings of the IRE 36, 1196–1204. https://doi.org/10.1109/JRPROC.1948.226245

Suwalak, R., Lertsakwimarn, K., Phongcharoenpanich, C., Krairiksh, M., Torrungrueng, D., 2012. Effects of tag location on light weight concrete for an RFID sensor application, in: 2012 9th International Conference

on Electrical Engineering/Electronics, Computer, Telecommunications and Information Technology. Presented at the 2012 9th International Conference on Electrical Engineering/Electronics, Computer, Telecommunications and Information Technology, pp. 1–4. https://doi.org/10.1109/ECTICon.2012.6254309

Taira, T., Brenguier, F., 2016. Response of hydrothermal system to stress transients at Lassen Volcanic Center, California, inferred from seismic interferometry with ambient noise. Earth, Planets and Space 68, 162. https://doi.org/10.1186/s40623-016-0538-6

Takano, T., Nishimura, T., Nakahara, H., Ohta, Y., Tanaka, S., 2014. Seismic velocity changes caused by the Earth tide: Ambient noise correlation analyses of small-array data. Geophysical Research Letters 41, 6131–6136. https://doi.org/10.1002/2014GL060690

Techel, F., Pielmeier, C., 2011. Point observations of liquid water content in wet snow – investigating methodical, spatial and temporal aspects. The Cryosphere 5, 405–418. https://doi.org/10.5194/tc-5-405-2011

Tedesco, M., 2015. Remote Sensing of the Cryosphere, 1st ed, The Cryosphere Science Series. Wiley.

Tedjini, S., Ghesquier, N., Martin, T., Nespoulous, A., 2015. Système RFID UHF de surveillance du charriage de cours d'eau. Esisar INP Grenoble, EDF.

Tibshirani, R., 1996. Regression Shrinkage and Selection via the Lasso. Journal of the Royal Statistical Society. Series B (Methodological) 58, 267–288.

Tiuri, M., Sihvola, A., Nyfors, E., Hallikaiken, M., 1984. The complex dielectric constant of snow at microwave frequencies. IEEE Journal of Oceanic Engineering 9, 377–382. https://doi.org/10.1109/JOE.1984.1145645

Todd, B., Phillips, M., Schultz, S.M., Hawkins, A.R., Jensen, B.D., 2009. Low-Cost RFID Threshold Shock Sensors. IEEE Sensors Journal 9, 464–469. https://doi.org/10.1109/JSEN.2009.2014410

Toivonen, M., Björninen, T., Sydänheimo, L., Ukkonen, L., Rahmat-Samii, Y., 2013. Impact of Moisture and Washing on the Performance of Embroidered UHF RFID Tags. IEEE Antennas and Wireless Propagation Letters 12, 1590–1593. https://doi.org/10.1109/LAWP.2013.2293334

Travelletti, J., Delacourt, C., Allemand, P., Malet, J.-P., Schmittbuhl, J., Toussaint, R., Bastard, M., 2012. Correlation of multi-temporal ground-based optical images for landslide monitoring: Application, potential and limitations. ISPRS Journal of Photogrammetry and Remote Sensing 70, 39–55. https://doi.org/10.1016/j.isprsjprs.2012.03.007

Tremblay, P., Leconte, R., Jay Lacey, R.W., Bergeron, N., 2014. Multi-day anchor ice cycles and bedload transport in a gravel-bed stream. Journal of Hydrology 519, 364–375. https://doi.org/10.1016/j.jhydrol.2014.06.036

Tsai, V.C., 2011. A model for seasonal changes in GPS positions and seismic wave speeds due to thermoelastic and hydrologic variations. Journal of Geophysical Research: Solid Earth 116. https://doi.org/10.1029/2010JB008156

Tsakiris, A.G., Papanicolaou, A.N. (Thanos), Moustakidis, I.V. (Danny), Abban, B.K., 2015. Identification of the Burial Depth of Radio Frequency Identification Transponders in Riverine Applications. Journal of Hydraulic Engineering 141, 4015007–1. https://doi.org/10.1061/(ASCE)HY.1943-7900.0001001

Tsang, L., Pan, J., Liang, D., Li, Z., Cline, D.W., Tan, Y., 2007. Modeling Active Microwave Remote Sensing of Snow Using Dense Media Radiative Transfer (DMRT) Theory With Multiple-Scattering Effects. IEEE Transactions on Geoscience and Remote Sensing 45, 990–1004. https://doi.org/10.1109/TGRS.2006.888854

Tzeng, S.-F., Chen, W.-H., Pai, F.-Y., 2008. Evaluating the business value of RFID: Evidence from five case studies. International Journal of Production Economics 112, 601–613. https://doi.org/10.1016/j.ijpe.2007.05.009

Uhlemann, S., Smith, A., Chambers, J., Dixon, N., Dijkstra, T., Haslam, E., Meldrum, P., Merritt, A., Gunn, D., Mackay, J., 2016. Assessment of ground-based monitoring techniques applied to landslide investigations. Geomorphology 253, 438–451. https://doi.org/10.1016/j.geomorph.2015.10.027

Ulaby, F.T., El-rayes, M.A., 1987. Microwave Dielectric Spectrum of Vegetation - Part II: Dual-Dispersion Model. IEEE Transactions on Geoscience and Remote Sensing GE-25, 550–557. https://doi.org/10.1109/TGRS.1987.289833

UNISDR, 2016. Report of the open-ended intergovernmental expert working group on indicators and terminology relating to disaster risk reduction. United Nations Office for Disaster Risk Reduction.

Valero, E., Adán, A., 2016. Integration of RFID with other technologies in construction. Measurement 94, 614–620. https://doi.org/10.1016/j.measurement.2016.08.037

Valero, E., Adán, A., Cerrada, C., 2015. Evolution of RFID Applications in Construction: A Literature Review. Sensors 15, 15988–16008. https://doi.org/10.3390/s150715988

Vera, G.A., Abdelnour, A., Sarkis, M., Georgiadis, A., Kaddour, D., Tedjini, S., 2016. Passive RFID-enabled proximity sensor, in: 2016 IEEE MTT-S International Microwave Symposium (IMS). Presented at the 2016 IEEE MTT-S International Microwave Symposium (IMS), pp. 1–3. https://doi.org/10.1109/MWSYM.2016.7539961

Vibert, C., Arnould, M., Cojean, R., Le Cleach, M., 1988. Essai de prevision de rupture d'un versant montaineaux, in: Proceedings of Fifth International Symposium on Landslides. Lausanne, pp. 789–92.

Virtanen, J., Ukkonen, L., Bjorninen, T., Elsherbeni, A.Z., Sydänheimo, L., 2011. Inkjet-Printed Humidity Sensor for Passive UHF RFID Systems. IEEE Transactions on Instrumentation and Measurement 60, 2768–2777. https://doi.org/10.1109/TIM.2011.2130070

Voisin, C., Garambois, S., Massey, C., Brossier, R., 2016. Seismic noise monitoring of the water table in a deep-seated, slow-moving landslide. Interpretation 4, SJ67–SJ76. https://doi.org/10.1190/INT-2016-0010.1

Voisin, C., Guzmán, M.A.R., Réfloch, A., Taruselli, M., Garambois, S., 2017. Groundwater Monitoring with Passive Seismic Interferometry. Journal of Water Resource and Protection 09, 1414. https://doi.org/10.4236/jwarp.2017.912091

Vora, S., Dandekar, K., Kurzweg, T., 2015. Passive RFID tag based heart rate monitoring from an ECG signal, in: 2015 37th Annual International Conference of the IEEE Engineering in Medicine and Biology Society (EMBC). Presented at the 2015 37th Annual International Conference of the IEEE Engineering in Medicine and Biology Society (EMBC), pp. 4403–4406. https://doi.org/10.1109/EMBC.2015.7319371

Vossiek, M., Gulden, P., 2008. The Switched Injection-Locked Oscillator: A Novel Versatile Concept for Wireless Transponder and Localization Systems. IEEE Transactions on Microwave Theory and Techniques 56, 859–866. https://doi.org/10.1109/TMTT.2008.918158

Walter, F., Roux, P., Roeoesli, C., Lecointre, A., Kilb, D., Roux, P.-F., 2015. Using glacier seismicity for phase velocity measurements and Green's function retrieval. Geophys J Int 201, 1722–1737. https://doi.org/10.1093/gji/ggv069

Wang, Baoshan, Zhu, P., Chen, Y., Niu, F., Wang, Bin, 2008. Continuous subsurface velocity measurement with coda wave interferometry. Journal of Geophysical Research: Solid Earth 113. https://doi.org/10.1029/2007JB005023

Wang, J., Katabi, D., 2013. Dude, Where's My Card?: RFID Positioning That Works with Multipath and Non-line of Sight, in: Proceedings of the ACM SIGCOMM 2013 Conference on SIGCOMM, SIGCOMM '13. ACM, New York, NY, USA, pp. 51–62. https://doi.org/10.1145/2486001.2486029

Wang, Q.-Y., Brenguier, F., Campillo, M., Lecointre, A., Takeda, T., Aoki, Y., 2017. Seasonal Crustal Seismic Velocity Changes Throughout Japan. Journal of Geophysical Research: Solid Earth 122, 7987–8002. https://doi.org/10.1002/2017JB014307

Wang, Z., Ye, N., Malekian, R., Xiao, F., Wang, R., 2016. TrackT: Accurate tracking of RFID tags with mm-level accuracy using first-order taylor series approximation. Ad Hoc Networks 53, 132–144. https://doi.org/10.1016/j.adhoc.2016.09.026

Want, R., 2004. Enabling ubiquitous sensing with RFID. Computer 37, 84–86. https://doi.org/10.1109/MC.2004.1297315

Watkins, S.E., Swift, T.M., Molander, M.J., 2007. RFID Instrumentation in a Field Application, in: IEEE Region 5 Technical Conf. Presented at the 2007 IEEE Region 5 Technical Conference, Fayetteville, AR, USA, pp. 400–403. https://doi.org/10.1109/TPSD.2007.4380343

Weaver, R.L., Hadziioannou, C., Larose, E., Campillo, M., 2011. On the precision of noise correlation interferometry. Geophys J Int 185, 1384–1392. https://doi.org/10.1111/j.1365-246X.2011.05015.x

Weaver, R.L., Lobkis, O.I., 2001. Ultrasonics without a Source: Thermal Fluctuation Correlations at MHz Frequencies. Phys. Rev. Lett. 87, 134301. https://doi.org/10.1103/PhysRevLett.87.134301

Wegler, U., Sens-Schönfelder, C., 2007. Fault zone monitoring with passive image interferometry. Geophys J Int 168, 1029–1033. https://doi.org/10.1111/j.1365-246X.2006.03284.x

Whiteley, J.S., Chambers, J.E., Uhlemann, S., Wilkinson, P.B., Kendall, J.M., 2018. Geophysical monitoring of moisture-induced landslides: a review. Reviews of Geophysics 0. https://doi.org/10.1029/2018RG000603

Yadav, R.K., Kishor, J., Yadava, R.L., Yadav, R.K., Kishor, J., Yadava, R.L., 2013. Effects of Temperature Variations on Microstrip Antenna. International Journal of Networks and Communications 3, 21–24.

Yang, F., Qiao, Q., Zhang, L., Yue, Z., Elsherbeni, A.Z., 2014. High-sensitivity RFID sensing antennas: From sensing mechanism selections to antennas structure designs, in: 31th URSI General Assembly and Scientific Symp. Presented at the 31th URSI General Assembly and Sci. Symp., Beijing, China, pp. 1–4. https://doi.org/10.1109/URSIGASS.2014.6929407

Yang, L., Cao, J., Zhu, W., Tang, S., 2015. Accurate and Efficient Object Tracking Based on Passive RFID. IEEE Transactions on Mobile Computing 14, 2188–2200. https://doi.org/10.1109/TMC.2014.2381232

Yu, X., Yu, Y., Wang, D., Qian, K., Liu, J., Zhao, Z., 2016. A Novel Temperature Control System of Measuring the Dynamic UHF RFID Reading Performance, in: 6th Int. Conf. Instrumentation Measurement, Computer, Communication and Control. Presented at the Sixth International Conference on Instrumentation Measurement, Computer, Communication and Control (IMCCC), Harbin, China, pp. 322–326. https://doi.org/10.1109/IMCCC.2016.16

Yuan, M., Chahal, P., Alocilja, E.C., Chakrabartty, S., 2015. Sensing by growing antennas: A novel approach for designing passive RFID based biosensors, in: 2015 IEEE International Symposium on Circuits and Systems (ISCAS). Presented at the 2015 IEEE International Symposium on Circuits and Systems (ISCAS), pp. 2121–2124. https://doi.org/10.1109/ISCAS.2015.7169098

Zhang, C.-C., Zhu, H.-H., Liu, S.-P., Shi, B., Zhang, D., 2018. A kinematic method for calculating shear displacements of landslides using distributed fiber optic strain measurements. Engineering Geology 234, 83–96. https://doi.org/10.1016/j.enggeo.2018.01.002

Zhang, G., Nakaoka, S., Kobayashi, Y., 1997. Millimeter wave measurements of temperature dependence of complex permittivity of dielectric plates by the cavity resonance method, in: Proc. Asia-Pacific Microwave Conf. Presented at the Proceedings of 1997 Asia-Pacific Microwave Conference, Hong Kong, Hong Kong, pp. 913–916 vol.3. https://doi.org/10.1109/APMC.1997.656347

Zhang, J., Tian, G.Y., Marindra, A.M.J., Sunny, A.I., Zhao, A.B., 2017. A Review of Passive RFID Tag Antenna-Based Sensors and Systems for Structural Health Monitoring Applications. Sensors 17, 265. https://doi.org/10.3390/s17020265

Zhenzhong, L., Nezih, M., George, X., Yuu, O., Guocheng, L., Dayan, B., 2011. Effects of temperature and Humidity on UHF RFID performance, in: CANSMART Workshop Smart Materials & Structures. Presented at the CANSMART workshop for Smart Materials & Structures, NDT Canada, Montreal, Canada.

Zhou, C., Griffin, J.D., 2012. Accurate phase-based ranging measurements for backscatter RFID tags. IEEE Antennas Wirel. Propag. Lett 11, 152–155. https://doi.org/10.1109/LAWP.2012.2186110

Zuffanelli, S., Aguila, P., Zamora, G., Paredes, F., Martin, F., Bonache, J., 2016. A High-Gain Passive UHF-RFID Tag with Increased Read Range. Sensors 16, 1150. https://doi.org/10.3390/s16071150

Zuo, C., Huang, L., Zhang, M., Chen, Q., Asundi, A., 2016. Temporal phase unwrapping algorithms for fringe projection profilometry: A comparative review. Optics and Lasers in Engineering 85, 84–103. https://doi.org/10.1016/j.optlaseng.2016.04.022

# Glossary

**Abreviations**

| | |
|---|---|
| CC | Correlation Coefficient. |
| CCF | Cross-Correlation Function. |
| EPC Gen2 | Electronic Product Code. Standard communication protocol for RFID. |
| ETSI | European Telecommunication Standard Institute. |
| ETSI EN 302-208 | Norm defining open frequency bands usable by RFID. |
| FD-Phase | Frequency-Domain Phase difference of arrival. Absolute ranging. |
| GB-SAR | Ground-Based Synthetic Aperture Radar. Remote displacement sensing. |
| GF | Green Function. |
| GNSS | Global Navigation Satellite System (see GPS). |
| GPS | Global Positionning System. |
| H/V | Geophysical method. Ratio of horizontal over vertical wave frequency. |
| HF | High Frequency (3−30 MHz). |
| IR | Impulse Response of a landslide displacement to rainfall (m/m/hour) |
| InSAR | Inverse Synthetic Aperture Radar. |
| LIDAR | Distance measurement with a pulsed laser light, often used as a scanner. |
| LF | Low Frequency (30−300 kHz). |
| PIT | Passive Integrated Transponder. Another name for RFID tag. |
| PTFE | Polytetrafluoroethylene, commonly called Teflon©. |
| Radar | Radio Detection And Ranging. |
| RH | Relative Humidity of the air (%). Partial over saturation vapor pressure. |
| RF | Radio-Frequency (20 Hz−300 GHz). |
| RFID | Radio-Frequency Identification. |
| RMSE | Root Mean Square Error. |
| RSS$I$ | Received Signal Strength *Indicator*. Signal power received by the reader (dBm). |
| SDK | Software Development Kit. |
| SVD | Single Value Decomposition. |
| SNR | Signal to Noise Ratio (unitless). |
| S | Stable state. |

| | |
|---|---|
| T | Transient state. |
| TD-Phase | Time Domain Phase difference of arrival. Relative ranging technique. |
| ToF | Time of Flight ranging technique. |
| UAV | Unmanned Aerial Vehicle, also called “drone”. |
| UHF | Ultra-High Frequency (300 MHz−3 GHz). |
| X-Pol | Two antennas assembled together polarized at +45°/−45°. |
| 1D-3D | Translational displacements in space. |
| Brewster angle | Incident angle at an interface, at which the reflexion coefficient is null. |
| Yagi-Uda | A type of directive array antenna. |

**Letters and operators**

| | |
|---|---|
| $\alpha$ | Attenuation factor of an electromagnetic wave (rad/m); or<br>Empiric noise coefficient (chapter 7). |
| $\beta$ | Velocity factor of an electromagnetic wave (rad/m, in chapter 5); or<br>Inversion parameter (days, in chapter 2); or<br>Inversed impulse response parameters (m/m/hour, in chapter 8). |
| $\delta$ | Small variation; or<br>Dirac function. |
| $\varepsilon$ | Relative dielectric permittivity (unitless) compared to vacuum $\varepsilon_0$. |
| $\theta$ | Volume ratio of a material (unitless). |
| $\lambda$ | Wavelength (m); or<br>Regularization term of a regression (unitless). |
| $\mu$ | Relative magnetic permeability (=1 here) compared to vacuum $\mu_0$. |
| $\rho$ | Density of a material ($10^3$×kg/m$^3$); or<br>Equivalent density of this material in a mixing of multiple materials. |
| $\sigma$ | Electrical conductivity (S/m); or<br>Standard deviation (chapter 7) |
| $\tau$ | Lag time (hours). |
| $\phi, \varphi$ | Phase (rad). |

| | |
|---|---|
| $\omega$ | Pulsation (rad/s). |
| $a$ | Arbitrary factor (no unit) |
| $A$ | Amplitude coefficient. |
| $c$ | Light velocity in vacuum ($\approx 2{,}998 \times 10^8$ m/s). |
| $C$ | Constant, eliminated in a calculus. |
| $d$ | Displacement between two points (m). |
| dv/v | Variation of apparent relative velocity of a radio or seismic wave (%) |
| $e$ | Water vapor pressure (hPa). |
| $E$ | Electric field (Volt / m) |
| $f$ | Carrier frequency of radio waves (MHz); or |
| | Seismic signal frequency (Hz). |
| $G$ | Gain of an antenna in a direction (unitless). |
| $h$ | Transfer function in the time domain; Height above ground (m). |
| $i$ | Angle of incidence of a ray (rad). Zero = Perpendicular; or |
| | Indice for any variable. |
| $i'$ | Angle compared to the direction of maximal radiation (rad). |
| $j$ | Imaginary number; or |
| | Indice for any variable. |
| $J$ | Cost function, minimized in an inversion. |
| $L$ | Power loss due to linear attenuation (dB/m); or |
| | Tag modulation efficiency (dB) |
| $n$ | Ratio of wave velocity between two mediums (unitless); or |
| | Indice for discrete time series. |
| P | Power (in dB, dBm or Watt); or |
| | Atmospheric pressure (Pa, in chapter 4.4.4). |
| $r$ | Radial distance between two points, in spherical coordinates (m). |
| $R_H$ $R_V$ | Reflexion coefficient, at a horizontal or vertical polarization. |
| $R^2$ | Normalized residual of a regression (unitless). |
| $S, s$ | Signal waveform. |

| | |
|---|---|
| $t$ | Time (second, hour or day). |
| $T$ | Temperature (°C); or |
| | Period ($m^{-1}$, in chapter 2). |
| $T_H$ $T_V$ | Transmission coefficient, at a horizontal or vertical polarization. |
| $v$ | Velocity of an electromagnetic or seismical wave (m/s); or |
| | Displacement rate of a lanslide (m/s). |
| $V$ | Voltage (Volts); or |
| | Volume of a material ($m^3$). |
| $x$ | Horizontal distance between a tag and a station antenna (m); or |
| | Input of rainfall time series (cm/day). |
| $y$ | Output of displacement time series (cm/day). |
| $Z$ | Impedance (Ohm). Ratio of tension/current, or electric/magnetic field. |
| ' and " | In-Phase and Quadrature (= Real and Imaginary) terms of $\varepsilon, \sigma, \mu$. |
| $\langle\ \rangle$ | Average function. |
| $*$ | Convolution operator. |
| $\star$ | Cross-correlation operator. |

**Organization, companies and products**

ISTerre, UGA, ANRT, ANR, CNRS, IEEE, ETSI, VOR, EGU, RSS.

Géolithe, Myotis, Mojix, Tagsys, Time Domain, Confidex, Impinj, Kathrein.

ASM WS17KT, Campbell CR1000, EM4325, Confidex Survivor B, RECCO, SENTINEL, Octane SDK Java, Impinj SR420, Impinj Threshold, RG58, PhaseTrack LS240, PT240, Kathrein 80010643, Riegl VZ 400, Leica TCR805, Davis Vantage Pro 2.